# Land Conversion in Amazonia and Northern South America; Influences on Regional Hydrology and Ecosystem Response



by

Ryan Gary Knox

B.S.E., University of Connecticut (2002)

Submitted to the Department of Civil and Environmental Engineering
in partial fulfillment of the requirements for the degree of

Doctor of Philosophy in the Field of Hydrology

at the

MASSACHUSETTS INSTITUTE OF TECHNOLOGY

February 2013



Author .....
Department of Civil and Environmental Engineering
September 26, 2012

Certified by .....
Rafael L. Bras
Professor Emeritus of Civil and Environmental Engineering
Provost and Executive Vice President for Academic Affairs, Georgia Institute of Technology
Thesis Supervisor

Accepted by .....
Heidi Nepf
Chair, Departmental Committee for Graduate Students

# Land Conversion in Amazonia and Northern South America; Influences on Regional Hydrology and Ecosystem Response

by

Ryan Gary Knox

Submitted to the Department of Civil and Environmental Engineering
on September 26, 2012, in partial fulfillment of the
requirements for the degree of
Doctor of Philosophy in the Field of Hydrology

## Abstract

A numerical model of the terrestrial biosphere (Ecosystem Demography Model) is compbined with an atmospheric model (Brazilian Regional Atmospheric Modeling System) to investigate how land conversion in the Amazon and Northern South America have changed the hydrology of the region, and to see if those changes are significant enough to produce an ecological response. Two numerical realizations of the structure and composition of terrestrial vegetation are used as boundary conditions in a simulation of the regional land surface and atmosphere. One realization seeks to capture the present day vegetation condition that includes human deforestation and land-conversion, the other is an estimate of the potential structure and composition of the region without human influence. Model output is assessed for consistent and significant differences in hydrometeorology. Locations that show compelling differences are taken as case studies. The seasonal biases in precipitation at these locations are then used to create perturbations to long-term climate datasets. These perturbations then drive long-term simulations of dynamic vegetation to see if the climate consistent with a potential regional vegetation could elicit a change in the vegetation equilibrium at the site. Results show that South American land conversion has had consistent impacts on the regional patterning of precipitation. At some locations, changes in precipitation are persistent and constitute a significant fraction of total precipitation. Land-conversion has decreased mean continental evaporation and increased mean moisture convergence. Case study simulations of long term vegetation dynamic indicate that a hydrologic climate consistent with regional potential vegetation can indeed have significant influence on ecosystem structure and composition, particularly in water limited growth conditions.

Thesis Supervisor: Rafael L. Bras
Title: Professor Emeritus of Civil and Environmental Engineering
Provost and Executive Vice President for Academic Affairs, Georgia Institute of Technology

# Acknowledgments

I would like to start by thanking Rafael Bras; my thesis advisor, friend, mentor and confident. Rafael allowed me the freedom to be my own scientist, kept me focused on the big picture, challenged me to ask intelligent questions and gave me the flexibility to take on curiosities that arose. For his support I owe him a debt of gratitude.

I would like to acknowledge my doctoral thesis committee, Paul Moorcroft, Dara Entekhabi and Elfatih Eltahir. My committee was an example of people who truly enjoy the scientific process, its discussion and I thank them for sharing this and interacting with me. In particular, I would like to thank Paul Moorcroft who has given me a significant amount of his time, care and friendship to guide me through the field of terrestrial ecology.

When I first came to Cambridge I was hesitant to form new relationships with colleagues and student, perhaps I had anticipated a culture fraught with icy competition. After several years of living in the Parsons Laboratory for Environmental Science and Engineering here at MIT, and visiting the department of Organismic and Evolutionary Biology at Harvard, I have made wonderful friends of some truly extraordinary and warm people. I would like to personally thank several individuals for both their friendship and for their time hovering over computer screens and white-boards helping me along my way: Gajan Sivandran, Marcos Longo, Amy Mueller, Gautam Bisht, Jingfeng Wang, Naomi Levine, David Medvigy, Michael Dietze, Anthony Parolari, Chiara Lepore, Rebecca Gianotti, Ben Scandella, Alejandro Flores, Homero Flores, Abby Swann, and Victoria Murphy. To Susan, thank for making me smile, cheering me on through the home stretch, and for being just plain wonderful. To my friends at Parsons, past and future Bras groupers, and EDM developers, all the best and thanks for the memories.

In final, I would like to thank my family for their love and support. My family, particularly my parents, have given me more than I could ever dream to repay, so I will start be dedicating this thesis to them.

# Contents

# List of Figures

# List of Tables

# Chapter 1

# Introduction

This work addresses how deforestation affects the regional scale interaction between land surface vegetation and climate in the Amazon basin. It substantiates its conclusions primarily through the use of two tools. The first tool is the statistical analysis of satellite rainfall data. The second is the use of a computer model that numerically represents the physical processes of the terrestrial biosphere and atmosphere. Focus will be on the dynamics of the Amazon and its neighboring region, without looking beyond its coastlines to the potential connections deforestation may have on the entire globe. On a similar note, there is an inherent difficulty in studying the terrestrial forest and climate dynamics of an entire region, in that we are dealing with inordinate number of variables and physical processes that would ideally be resolved at the smallest of scales. For instance, it is impossible to numerically represents the flux of water vapor emanating from individual stomata, on individual leaves, from individual trees in a such a large full three dimensional space over our period of interest. Only so much information can be held in computer memory, only so many floating point operations can be conducted in a reasonable length of time. Most importantly, only so much information is known and data is available, to thus infer the parameters of the system. However, as will become apparent, significant effort went into utilizing massive computer systems, and designing research tools specifically to utilize these systems and resolve domains with increased realism. Despite the improved spatial and time resolution of the modeling efforts, approximations were needed, leaps from the physical into the conceptual, and

both spatial and temporal averaging. In the end, the results are tested against other observations and data to show that the modifications and conceptual mechanics are sound.

### 1.0.1 Brief Introduction to the Regional Climate of the Amazon

Yearly rainfall in the Amazon varies from several meters in the western headwaters to lows that can periodically dip close to one meter in the southern and eastern portions of the basin. This is however rare, as the entire basin typical receives at least one and a half meters of yearly rainfall. A strong peak in spatial rainfall can be seen over the Amazon River's delta region. Panel A in Figure 1-1 shows a map of the mean annual rainfall accumulations of northern South America from 1998 through 2007. This estimate is taken directly from the Tropical Rainfall Measurement Mission's (TRMM) 3B42 product. This is a gridded composite based on the TRMM satellite's Precipitation Radar and Microwave Imager, as well as visible and infrared cloud images from GOES geostationary satellites and bias correcting rain-gages on the surface.

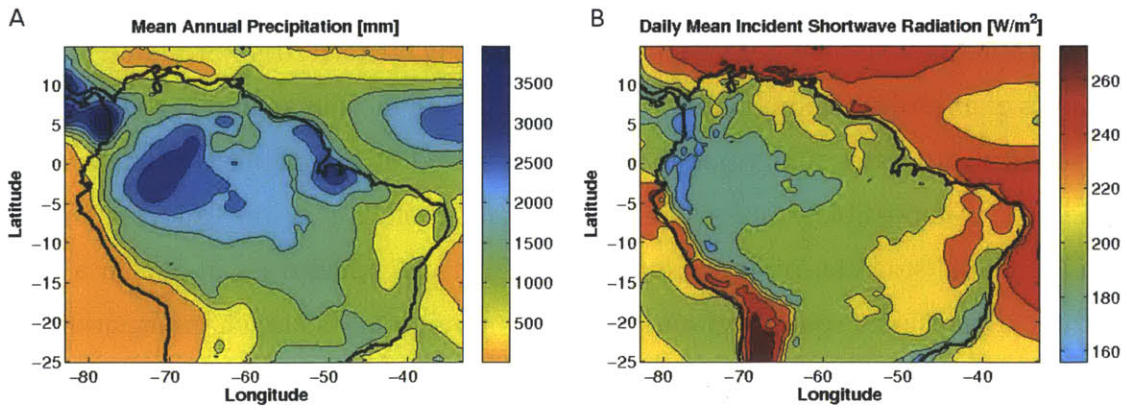


Figure 1-1: A. Mean annual precipitation derived from a composite product with satellite rainfall (TRMM 3B43) 1998-2007. B. Mean daily incident solar radiation at the surface derived from Surface Radiation Budget dataset, 1986-2001.

The seasonal variability of rainfall is captured by a set of raingage measurement stations distributed throughout the basin. These are intensive environmental study sites

including a range of instrumentation based on an eddy flux tower; they will be referred to in greater depth during the validation phase of this study. The point-like nature of raingages makes them less suited for detecting spatial patterns of rainfall, but their direct volumetric measurements and high sampling frequency make them ideal for analyzing temporal variability. Figure 1-2 shows the change in mean rainfall from month to month for a selection of rain gauges across the basin. The Manaus station shows relatively high monthly rainfall accumulations, as it is centrally situated in the basin at 2 degrees south. The highest monthly accumulation is at the Jaru station, which is located in the state of Rondônia in southwestern Brazil. Along with the high accumulations in January, there is also very strong seasonality where little to no rainfall is recorded during the dry season months of June through August. It also shows that wet and dry season precipitation varies significantly across each of these locations.

In the central Amazon the wet season peaks roughly in phase with the austral summer (Dec-Feb). The raingage stations indicate that peak rainfall occurs later in the austral summer, leading into April. Likewise, the dry-season seems coincident with the austral Winter (Jun-Aug). Perhaps a better picture of how the inter-seasonal timing of peak and minimum rainfall varies from place to place, can be found in the gridded data of the European Center For Medium Range Weather Forecasting's (ECMWF) 40 year reanalysis product (ERA-40). The ERA-40 dataset is the assimilation of a wide range of environmental observations (radiosondes, atmospheric radiances,etc) with a grid-based numerical weather model. The mean monthly rainfall can be retrieved over a grid covering South America, and evaluated to determine when the wet and dry seasons peak for the various locations. Figure 1-3 associates each month of the year with a color, and maps the month of the year where different locations experience maximum and minimum monthly rainfall. It confirms rainfall peaks are in phase with the summer and winter, and that southern Brazil shares similar seasonality with the Amazon basin south of the equator. There is a more stark contrast in the peak seasonal rainfall between the southern Amazon and the northern continental regions such as Colombia and Venezuela where the dry season occurs in January.

Rainfall in the Amazon is typically convective, and therefore often coincides with the

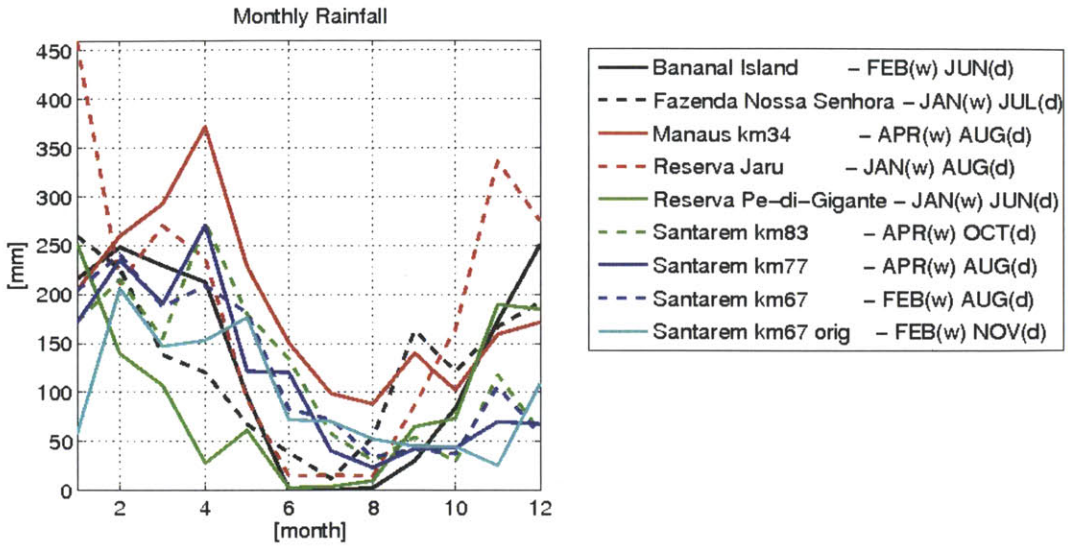


Figure 1-2: Mean monthly rainfall accumulations of several rainfall gaging stations throughout Brazil. Most gage data was available over a period of 2-3 years continuously. The set spans from 1999-2004. The legend on the right panel indicates the month of peak wet season (w) and dry season (d).

afternoon when surface heating due to solar radiation has created thermal instability and mixing in the planetary boundary layer. From a regional perspective, the downward shortwave radiation at the land surface follows an inverse pattern with precipitation. Clouds coincident with areas of high rainfall occlude light from reaching the surface. This is evident by comparing the TRMM rainfall map in Panel A of Figure 1-1 with map of mean down-welling shortwave radiation derived from the Surface Radiation Budget (SRB) product in Panel B. The highest rates of incident solar radiation can be found at the Andean Altiplano $25^oS - 68^oW$. This is partly due to the high elevation and a relatively thin, cloudless atmosphere. The whole of the Amazonian basin receives distinctly less solar radiation than the areas of eastern and southern Brazil. In Eastern Brazil, where precipitation is rather sparse, daily insolation is quite high. The lowest levels of solar radiation can be found in the basin headwaters in the far west.

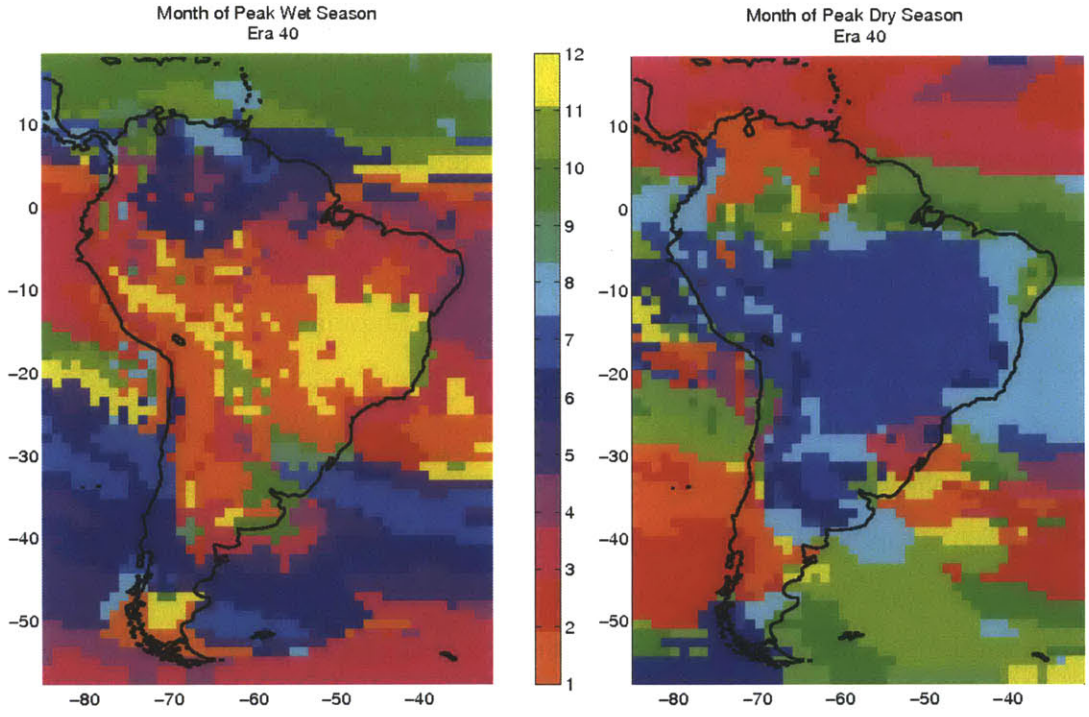


Figure 1-3: Color maps depicting the month of the year when maximum (left) and minimum (right) rainfall accumulation occurs. Rainfall accumulations are derived from the ECMWF ERA-40 dataset from 1980-1999.

### 1.0.2 Governance of Regional Climate

In the broadest sense, climate is controlled by the sun's position over various (inter-annual, seasonal and diurnal) time-scales, the changes in the chemical composition of the atmosphere, biosphere and oceans, the rotation of the earth and the features of the continental land masses. The topography of South America is typified by three major structures, the continuous South American Cordilleras (including Andes mountains) which extends along the north-south axis of the continent on its western edge, the interior lowlands and the continental shield, see Figure 1-4. The presence of a land mass imposes lateral boundaries to the circulations of the oceans and their air-masses. The combination of these boundaries with the rotational Coriolis force drives cyclonic gyres in the atmosphere above the sub-tropical oceans in the southern hemisphere. Accordingly, the Cordillera serves as an almost impenetrable boundary to winds in the mid to lower troposphere. On the western side of this mountain chain, the climate of this thin strip of land is dominated by the low level south-westerlies of the South Pacific gyre crossing the cold waters of the southern South Pacific Ocean. On the eastern side of the divide, which comprises the great majority of the continent's area, climate is dominated by the interaction of the gyre over the South Atlantic's sub-tropical high pressure center and the southern polar gyre as they oscillate over their seasonal modes. This thesis is particularly interested on the land-atmosphere connections mitigated by changes in the Amazon land cover, and is therefore concerned with the latter two motions of air and circulation patterns directly connected with the Amazon basin.

The cyclonic winds of the sub-tropical Atlantic high is a consistent inter-seasonal feature, whose winds on its northern side emerge as the easterly trade-winds at the equator. As the trade winds cross inland, the boundary of the Andes mountains force the Easterlies in the mid and lower troposphere to turn northerly and then northwesterly at about 20°S near the Bolivian Andes. This is especially true during the austral Summer (December, January and February) when the sun and the Inter Tropical Convergence Zone is at its northward position. At this time the sub-tropical high is slightly weaker and shifts to a more eastern position than during the austral winter months (June July

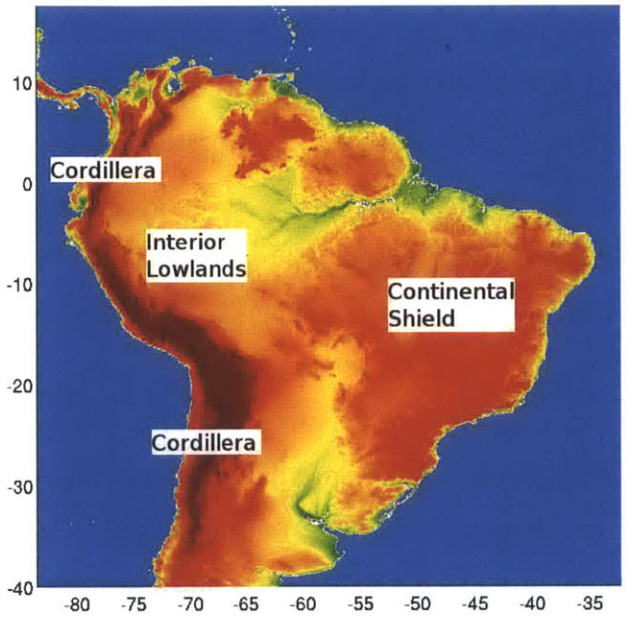


Figure 1-4: Topographic relief map, presented in natural log scale. The natural log scaling helps to preserve the texture of the continental shield and lowlands which would otherwise be completely shadowed by the scale of the Andes mountains. For reference, average elevation of the Altiplano is roughly 3 kilometers, while Andean peaks reach 6 kilometers.

August). In the winter, the sub-tropical high is stronger and deeper west where it nears the eastern coast of southern Brazil. An estimate of the mean seasonal geopotential and wind vectors at 925 millibars was compiled from the ERA-40 dataset and is shown in Figure 1-5. Satyamurty and co-authors discuss the South American climate system and analyze the seasonal tendencies of atmospheric pressure, wind vectors, outgoing longwave radiation and precipitation using the National Center for Environmental Prediction's (NCEP) 50 year reanalysis product [Satyamurty *et al.*, 1998]. Zhou and Lau first argued that the this seasonal shifting of the atmospheric circulation defined what is called the South American Monsoon System (SAMS) [Zou and Lau, 1998].

The active monsoon system is defined by a periodic and definitive shift in prevailing wind patterns [Gan *et al.*, 2004], associated with other atmospheric qualities such as moisture convergence, convective activity [Kousky, 1988] and precipitation [Marengo *et al.*, 2001]. The result of this shift is evident in the negative anomaly in seasonal Outgoing Longwave Radiation (OLR), which acts as a proxy for convective activity. Figure 1-6 is excerpted from the work of Satyamurty and co-authors (1998) and shows a smooth Northeast to Southwest seasonal oscillation in convective activity. In the winter (JJA), convective activity migrates northwest with greatest activity occurring over the northern parts of Colombia and Panama. Eastern and northeastern Brazil show particular lack of cloudiness and convective activity over the Winter period. It is during this period that the trade winds show a distinct lack of northerly component.

In addition to the westerly shift of the Atlantic sub-tropical high, the onset of SAMS is coincident with the following features: 1) greater moisture convergence, particularly from the northeasterly trade-winds over the northern coast of South America, 2) a moisture laden northwesterly wind regime in southwestern Brazil that ultimately converges with easterlies on the western flank of the sub-tropical high as they reach areas of southern Brazil and the combinations of 3) divergent descending winds over Bolivia (known as the Bolivian high, which is associated with anti-cyclonic motions in the upper troposphere) and the general ascending air mass of the Amazon basin [Raia and de Albuquerque Cavalcanti, 2008]. The ascension of Amazonian air is associated with the convective re-stabilization of the atmosphere and its upward transport and release

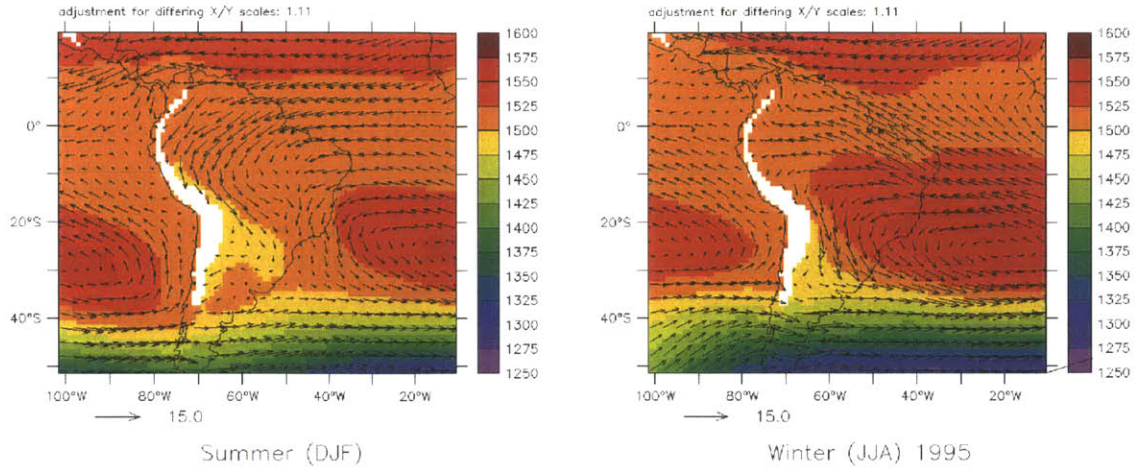


Figure 1-5: Mean seasonal geopotential (meters) and wind vectors (m/s) at 925mb. Data taken from the ECMWF ERA-40 during the year of 1995.

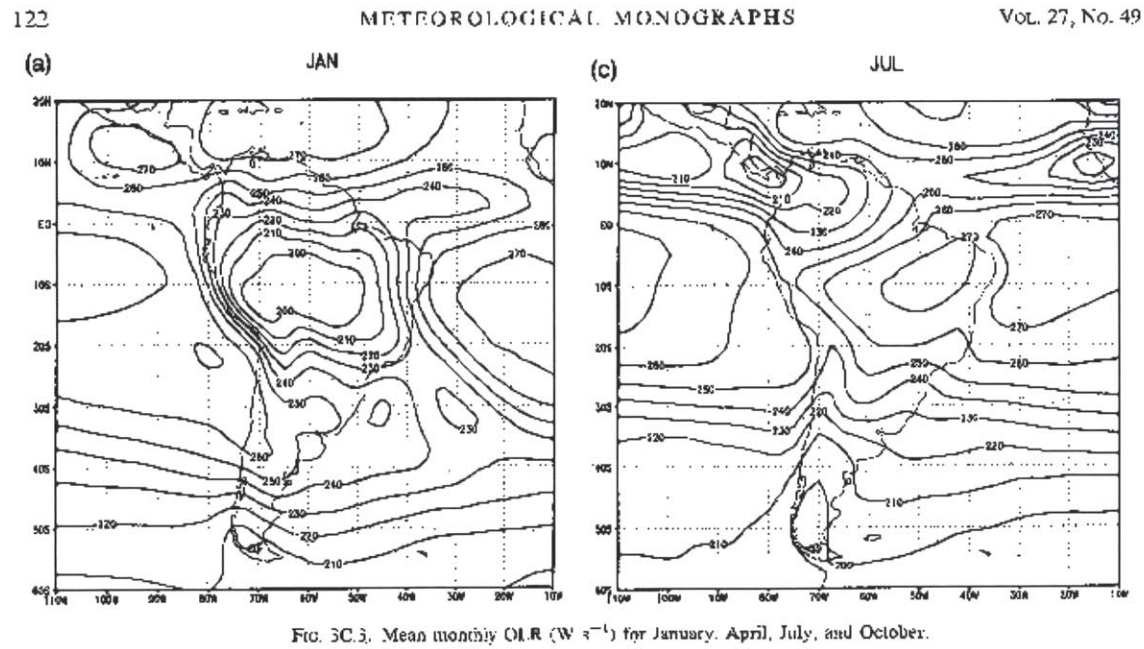


FIG. 3C.3. Mean monthly OLR (W $s^{-1}$) for January, April, July, and October.

Figure 1-6: Excerpted from Satyamurty et al. (1998). Outgoing longwave radiation, lower values indicate heightened convective activity and deep clouds.

of latent heat.

A feature of the summer monsoon is the periodic presence of a convective band extending from southwestern Amazonia to the Atlantic coast at roughly 20S (South American Convergence Zone). Convective activity in this band reaches its maximums during the summer periods, and usually persists over roughly 10 day intervals. Figueroa and co-authors identified the key ingredients that drive its formation as the diabatic heating of the Amazon basin and central Brazil, and the steep Andean topography that redirects the easterly trade-winds towards this zone of convergence [Figueroa *et al.*, 1995]. It is argued here that the South American Convergence Zone (SACZ) is critically linked to the forest ecosystems of the Amazon basin, in that it is a product of the converging air masses of the Amazon's north-westerlies and the easterlies associated with the south Atlantic sub-tropical high's western flank. Rainfall is sustained in the SACZ due to several processes, including the frontal waves from the Southern gyre, but mostly due to the the moisture convergence of these north-westerlies. An example of an active and non active SACZ is excerpted from Herdies and co-authors (2002), see Figure 1-7. The evapotranspiration of the Amazonian forests has a significant impact on the moisture flux of these north-westerlies and therefore couples the ecosystems of Amazonia with those of South Eastern Brazil, Paraguay and northern Argentina. Perhaps this coupling is most prominent through the South American Low Level Jet (SALLJ). As the transcontinental trade-winds encounter the Andes and progress from northerly to northwesterly, they compress against the mountains into a very localized and thin band of high velocity air that resides below 850mb directly on the eastern foothills of Bolivia, transporting moisture and momentum to the Southern Brazil, Northern Argentina and Paraguay [Vera and co authors, 2006]. The presence and strength of the jet has covariance with the hydrological climate of these regions, as well as the patterning and development of mesoscale convective systems (MCS) [Salio *et al.*, 2007].

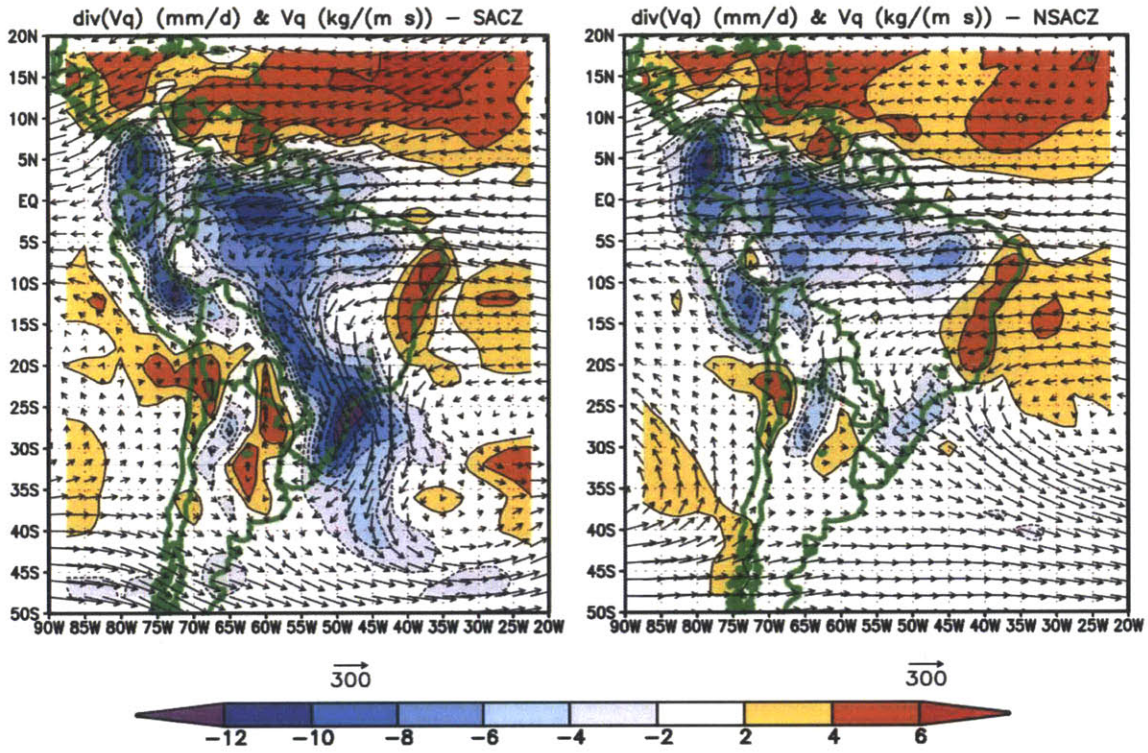


**Figure 5.** Vertically integrated regional moisture flux (vectors) and moisture flux divergence (shaded) for (a) SACZ period and (b) NSACZ period from GEOS-2 data set. The units for vectors is kg/(ms) and divergence in units of mm/day.

Figure 1-7: Excerpted from Herdies et al. (2002). Maps of moisture convergence and wind vectors during period where the South Atlantic Convergence Zone is active (SACZ) and not active (NSACZ)

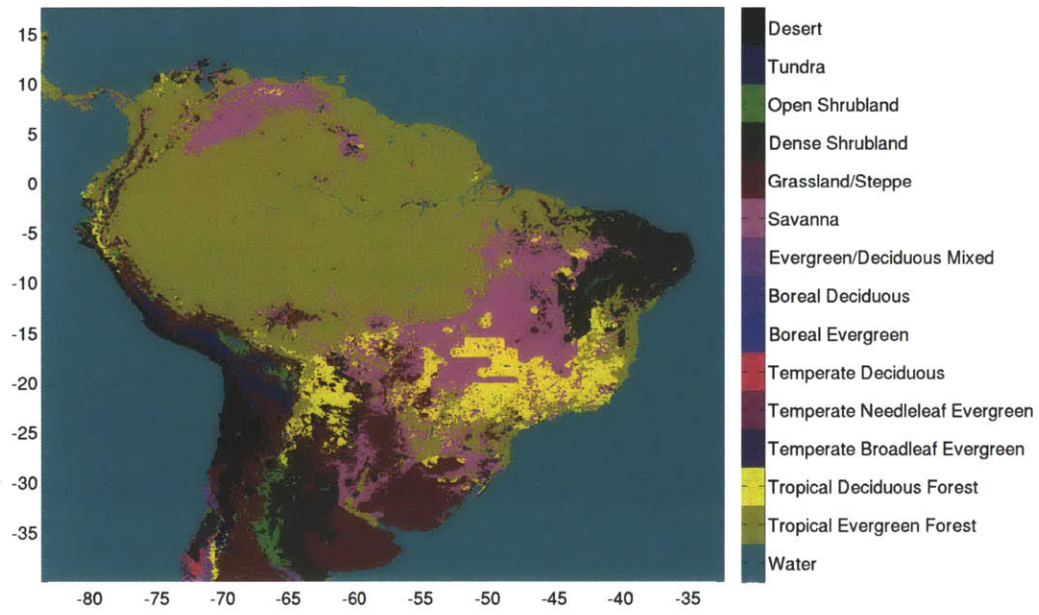


Figure 1-8: Map of potential vegetation land classification from the DISCover database in the EROS data center. Classification follows the Olson Global Ecosystem Framework [Olson, 1994].

### 1.0.3 The Forests of Amazonia Terra-Firma

Laurance (2001) provides a nice ecological review of the forests of the Central Amazon, based on his analysis of the fractionated forests of the Biological Dynamics of Forest Fragments Project (BDFFP) in the Distrito Agropecuario, a 500,000 ha site for agricultural research and development north of Manaus Brazil (central Amazon) [Laurance, 2001]. The central Amazonian primary forests were described as having exceedingly diverse floristic composition, as Western and Central Amazonia are generally thought to house the greatest diversity of tree species in the world. Oliveira and Moori estimate that mean species richness hovers around 280 species per hectare in these regions [Oliveira and Mori, 1999]. Extensive heterogeneity in tree speciation in the forests near Distrito Agropecuario was observed personally as well. Likewise, massive trunk diameters were present but uncommon.

Identifying age distributions in tropical forests is relatively difficult due to the uncertainties in the relationship between ring structure and the progression of time. Carbon dating has however revealed that old growth Central Amazonian trees reach maximums of 1400 years old (Cariniana micrantha) [Chambers *et al.*, 2001]. Chambers and co-authors determined that tree age was only weakly (but positively) correlated with tree diameter. This may be part of the reason why the primary forests, while incredibly old (estimated at 4500 years since the last major disturbance) did not contain a large fraction of the population with diameters above 150 cm. For instance, two of the Cariniana micrantha with a base diameter of 180 centimeters differed in age by 900 years [Laurance, 2001].

Through personal observation, the canopy structure of the Central Amazonian forests had an almost continuous strata of sub-canopy crown layering. Like any forest, the emergents and the top layer of the canopy contained a large fraction of leaf biomass, but the significant undergrowth and variable canopy layering existed within. This differed strongly with experience in the island tropical rainforests of Puerto Rico, which was primarily composed of three tree species (Tabanuco, Trumpets and Palms). In that case, the forest was composed of nearly monoculture patchworks. Two photographs

of the forest under-story from Luquillo National Forest Puerto Rico and an old growth Central Amazonian forest near Manaus are compared in Figure 1-9. The consolidating thread is that Central and Western Amazonian old growth forests are variable in vegetation composition and structure in all three dimensions.

The soils of Amazonian rainforests are traditionally described as poor to extremely poor, dominated by sandy and clayey latosols derived from alluvial deposits of the Tertiary period [Beinroth, 1975]. Chauvel, Lucas and Boulet (1987) described Central Amazonian soils as being acidic, high in toxic aluminum, and containing low quantities of plant essential nutrients such as calcium, phosphorus and potassium [Chauvel *et al.*, 1987]. Silver and co-authors (2000) described the eastern Amazonian soils of the Tapajos National Forest (Brazil) also as nutrient poor clay oxisols with pockets of sandy utisols [Silver *et al.*, 2000]. Both soils are low in organic carbon content and nutrient "ion-exchange capacity". Perhaps due to their harsh nature, Amazonian soils have been observed to exact controls over speciation. It is very common to find swaths of shrub based demography inhabiting sandy soils with characteristically higher toxic Aluminum, whereas total above ground biomass abounds in sites based in clays with sources of phosphorus and nitrogen [Laurance, 2001]. Laurance (2001) cites an estimate that one third of the variance in Amazonian above ground biomass is attributed to soil composition.

There is a distinct lack of mammalian fauna in the Central Amazon's Distrito Agropecuario, bearing testament to the nutrient conservation strategy of the system. It is hypothesized that the lack of fauna is a symptom of local vegetation. Laurance described the demography as being relatively devoid of fruit bearing, nut bearing and flowering species. More so, the undergrowth is understood to contain less desirable qualities such as tannins. These characteristics are associated with nutrient conservation strategies, enabling biomass to abound in a weak soil nutrient environment, warding away potential foragers. The vegetation in the Amazon rainfall basin has been described by many as a marvel of genetic adaptation, generating phenotypes that squeeze the greatest utility out of those resources which are scarce, and effectively thriving and competing for those resources which abound.

Figure 1-9: Photographs of the lower forest canopy. The upper panel is from the Ducke Reservation in Central Amazonia (near Manaus, Brazil). The lower panel is from Luquillo National Forest, Puerto Rico

Perhaps the only apt generalization of composition and structure for the forests of the Amazon rainfall basin is only that it is highly variable. Typified by vastness and species richness; this short preamble is intended only to give a quick reference to some of its sampled characteristics. Hopefully it conveys that it is an interesting place, one who's preservation has implicit and local benefits. Stepping back it becomes clear that the Amazon is an large player in the global exchange of carbon. It is estimated that 40% of the global storage of carbon in terrestrial biomass happens in the forests of the Amazon [Dixon *et al.*, 1994]. Large changes to the structure of the Amazonian forests have even been found to have "teleconnections" or effects on climate signatures on the other side of the world [Avissar and Werth, 2004].

### 1.0.4 The Nature of Amazonian Deforestation

Over the last several decades Amazonian deforestation has gained visibility through a combination of dedicated scientific analysis, improved observational technology and a social awareness stemming through progress in the former. In January of 2007, National Geographic featured a cover story "Amazon Forest to Farms" encapsulating the socio-eco-environmental challenge of managing what was once thought of as Brazil's seemingly inexhaustible 450 million hectares of natural resource. It is estimated that agricultural practices in 1995 accounted for over 48 million hectares of land in the Brazilian Amazon (roughly 11% of the total area) [Cardille and Foley, 2003]. Some 23 million ( 5%) of those hectares were attributed to non-natural pasture-lands, i.e., croplands and cleared pastures resulting from deforestation. There are varying statistics on the total amount of forest land that has been cleared or converted. Skole and Tucker estimated that 6% of the Amazon had been deforested as of 1988 [Skole and Tucker, 1993]. The Instituto Nacional de Pesquisas Espaciais (INPE) reported that as of 2001, 15% of the Amazon had been deforested [de Pesquisas Espaciais INPE, 2003]. They reported that over 7 million new hectares ( 2%) of agricultural lands were created in the Brazilian Amazon between 1980 and 1995. Regionally, the majority of Amazonian deforestation practices are concentrated in an arc on the southeastern fringe. The total

deforestation from 1980 to 1990 varied significantly among different states; total agriculture decreased by $6\%$ in the states of Tocantis and Goias and increased by roughly $300\%$ in the Southwest state of Rondônia.

Figure 1-10: Photograph of the canopy top at Ducke Reservation (near Manaus Brazil).

Deforestation rates are strongly coupled to the development of infrastructure. More than two-thirds of deforestation in the Amazon is within 50km of a major paved highway [Nepstad *et al.*, 2001]. Various deforestation predictive models have made use of socio-economic data and projection, and have tested their hypotheses in case studies [Geist and Lambin, 2002][Laurance *et al.*, 2001][Nepstad *et al.*, 2001]. Soares-Filho estimated that by 2050, only 53% of pre-anthropogenic closed canopy forest stands would remain [Soares-Filho *et al.*, 2006]. Of this, eight of the Amazon's twelve major hydrologic basins would lose more than half of their forest cover to deforestation.

### 1.0.5 Stand Structure and Deforestation

According to Skole and Tucker, in addition to the $6\%$ of Amazon forest stands cleared as of 1988, more than $15\%$ of forested canopies were said to have been affected by deforestation. The rate of tropical deforestation in the Amazon from 1978 to 1988 was $15,000km^2$ per year, but the rate of forest fragmentation and degradation was $38,000km^2$ per year [Skole and Tucker, 1993]. Selective logging, or removal practices that target single trees, is estimated to account for a large fraction of the Amazon's total deforested area. However, it is difficult to get an accurate estimate of regional selective logging. Continuous regional observations necessitate the use space-born remote sensing strategies which often do not have sensor resolutions capable of capturing fragmentation at such fine scales. Degraded and fragmented landscapes appear to represent a significant portion of total deforestation practices. And although there are inherent difficulties in accurately measuring its progress, fragmentation may have significant influences on its surrounding ecosystems, and perhaps the land-atmosphere coupled system.

The effects of controlled human disturbance on surrounding ecosystems have been documented. Several studies have found correlations between controlled patches of deforestation and mortality rates in adjoining forest stands [Skole and Tucker, 1993][Laurance *et al.*, 1998]. The edges of intact forests adjoining completely deforested areas can be influenced by deforestation at depths up to one kilometer. Laurence et al. (1998) detected a bias in mortality rate that increases with proximity to the forest edge. He attributed mechanisms of increased wind-throw, changes in micro-climate and competition with invasive species to name a few.

### 1.0.6 The Regional Vegetation-Climate Connection

The idea that land surface vegetation could influence regional to global scale atmospheric dynamics was pioneered by Charney in 1975 [Charney, 1975]. A number of important studies followed in the late 1980s and early 90s using coupled numerical models of general circulation and land surface energy exchange. Early models treated the

land-surface conditions with permanence, and generally applied land-use patterns uniformly or at coarse resolutions. These seminal modeling studies cited that widespread deforestation would lead to local reductions in precipitation, evaporation and moisture convergence, with slight increases in surface temperature [Henderson-Sellers *et al.*, 1993][Nobre *et al.*, 1991][Lean and Warrilow, 1989][Dickinson and Henderson-Sellers, 1998]. For instance Nobre and co-authors (1991) and Lean and Warrilow (1989) predicted widespread deforestation would elicit regional average precipitation decreases by as much as 1.76 and 1.34 mm/day respectively. These works varied however in their predicted magnitudes and in the sign of the change in total runoff. Discrepancies were attributed to a lack of understanding the mechanics and contributions of moisture flux convergence.

Some of the first-order hydrologic mechanisms that connect terrestrial tropical forests to the regional climate system can be identified. Firstly, stems and leaves absorb light over different portions of the visible and thermal spectrum and at different magnitudes compared to bare earth, typically resulting in a lower surface albedo (reflectance) and higher levels of net surface radiation. Another truth is that forest leaf surfaces increase the area of interception for precipitation, potentially effecting total runoff and evaporation rates. Forest leaf surfaces also increase the effective area contributing to transpiration, which *depending* on the resistance to transport of water vapor from the stomatal enclosures into the atmospheric boundary layer, has an effect on the timing and magnitudes of water vapor flux. Below the canopy crown, litter-fall and forest floor vegetation combine with leaf interception to enhance overall retention of water from runoff both on the surface and through the soil matrix. Consider further that canopy structure changes the surface topography and therefore the drag surface incident on the winds and eddy structures of the planetary boundary layer, thereby modifying the vertical transport of heat, momentum and water vapor. Below the surface, forest root layers can redirect soil moisture stores through the plant tissues to the canopy air space.

The rate of precipitation recycling, i.e., the amount of precipitation coming immediately from land-surface evaporated water in that region, is reflective of the strength of the dynamic between climate and vegetation. Eltahir and Bras estimated that the basin

average recycling rate of water vapor is approximately 25% [Eltahir and Bras, 1993]. To clarify, 25% of the rainfall is sedimented from water that evapotranspired within its borders while the other 75% is transported into the basin laterally in the atmosphere. Salati and Vose argued that deforestation threatens to reduce the water vapor exchange of the land-surface with the atmospheric boundary layer, and that the subsequent losses to recycling would likely be the most important factor in regional climate change [Salati and Vose, 1984].

Eltahir and Bras proposed that widespread Amazonian deforestation would, as direct consequence, increase surface temperature and reduce tropospheric heating [Eltahir and Bras, 1993]. Higher surface temperatures are a result of a the decreases or losses in evapotransipirative cooling from the leaf surfaces in cleared vegetation. The reduction in atmospheric heating follows losses in the heat released through precipitating (condensing) atmospheric water, an assumed consequence of reduced land-atmosphere vapor transport. There are secondary and potentially compensatory feedback effects associated with deforestation as well. While increased surface temperature anomalies induce convergent circulations coincident with a decrease in surface pressure, decreased precipitation heating anomalies reduce tendency towards convergence. Eltahir followed by identifying that while surface temperatures are potentially higher in deforested areas, there would necessarily be a decrease in total surface energy flux as a direct result of an increased surface albedo [Eltahir, 1996].

Kleidon and Heimann theorized that deep rooted vegetation would have several pronounced feedback effects on water cycle dynamics [Kleidon and Heimann, 2000]. Deep rooted vegetation (up to 18 meters) exists throughout the Amazon basin [Nepstad *et al.*, 1994]. These deep root systems increase the storage capacity and access of the land surface's evapotranspiration system. Increased storage capacity would theoretically yield larger transpiration rates year round (especially in the dry season when precipitation is at a low), which would in turn increase the latent heat flux. Latent heat flux could potentially strengthen convective tendencies. Stronger convection would positively feedback by increasing convergence in the region, driving more vigorous circulations.

It has already been identified that convective heating generates a regionally consistent ascending and converging flow above the basin [Figueroa *et al.*, 1995]. However, there are competing negative feedbacks. Increased convection leads to increased cloud presence, which strongly decreases surface shortwave radiation and to a lesser extent increases down-welling longwave radiation. During daylight, net surface radiation and therefore the available energy for sensible and latent heat fluxes decreases. Note also that cloud induced reductions in solar radiation can potentially inhibit plant photosynthesis in light limited growth conditions. During night hours, increased cloud cover due to convective activity warms the surface by trapping thermal radiation.

The transport of water through the root system also has an influence on the timing of land-atmosphere energy exchange. Recall that the central/southern Brazilian winter lacks the strong northerly transport of moisture laden air. Deep root systems can potentially dampen the seasonal depression of vertical moisture transport by lifting water from the lower soil layers. In this regard, deep roots have a mitigating effect on the seasonal water exchange signal by stimulating continued latent heat release, water recycling and cloud formation. Scenarios of deforestation potentially break this seasonal link.

Pielke reviewed the influence of vegetation and soil moisture patterns on thunderstorms and their teleconnections with large scale systems, a rough summary of these concepts is described here [Peilke, 2005]. Alterations in vegetation potentially change the surface albedo thereby altering the net radiative flux and subsequent heating rates, similar to Eltahir's findings. Vegetation influences both the albedo and the bowen ratio, thereby directly modifying sensible heat flux. Changes in sensible heat flux can alter boundary layer growth and subsequently the initiation of thunderstorms. Latent heat flux is critical to the atmospheric profiles of moist static energy, which is analogous to the fuel to sustain thunderstorm growth. Pielke acknowledges there is an apparent tradeoff in the influencing effects of latent and sensible heat flux on thunderstorm growth. Increased soil moisture or standing leaf water (associated with forested areas) can be viewed as a source of convective available potential energy (CAPE). However *if* net radiation remains unchanged and total heat flux is conserved (which is not necessarily the

case, but is a possibility) increased evapotranspiration necessitates a decreased Bowen ratio and consequently reduced sensible heat flux. Sensible heat flux drives boundary layer entropy, growth and its vertical turbulent air motions. Decreasing sensible heat flux and associated weak planetary boundary layer height could arguably stunt cumulus convection. According to Pielke (2001), sensible heat drives the large thermal motions that stimulate boundary layer growth and are likewise needed to trigger convection [Pielke, 2001]. Large thermal motions and rapid boundary layer growth are very often seen as a necessary mechanism for convection, where eddy circulations will give air parcels the energy to periodically lift above the top of the atmospheric boundary layer and penetrate the level of free convection.

### 1.0.7 Spatial Qualities of Amazonian Deforestation

Recall that actual Amazonian deforestation is patterned and selective, the discussion thus far has been conceptual in nature, related to analytical models or dealing with regional phenomena. Real deforestation has spatial structure, and likewise the land-atmosphere dynamical processes have spatial quality as well. Chagnon and Bras [Chagnon and Bras, 2005] reported a seasonal shift in rainfall patterns associated with specific zones of dense Amazonian deforestation. They used satellite born rainfall measurements and land-cover mappings to detect precipitation bias over deforested versus forested patches of land. Chagnon and co-authors [Chagnon *et al.*, 2004] found a statistical spatial correlation between deforested areas in the Amazon and the presence of low clouds. The fragmentation of actual deforestation creates differential heating and roughness characteristic of the land-surface. It is theorized that this drives a locally enhanced energy circulation between the land and atmosphere, potentially effecting cloud formations. This concept will be discussed further in Chapter 2.

Physical model studies have shown that spatially heterogeneous land-use changes can induce coherent changes in weather. Wang et al. (2000) observed pronounced seasonal differences in the effect of land-surface heterogeneity stimulating convergence and weather events [Wang *et al.*, 2000]. They found that wet season weather events

were dominated by synoptic forcing. Yet, dry season mesoscale circulations and associated convective precipitation events were influenced by land-surface heterogeneity. Coherent land surface patterns may strengthen convergence zones on the surface, creating vertical wind triggers to thunderstorms. Avissar and Werth (2004) [Avissar and Werth, 2004] introduced that coherent land surface patterns transfer heat, moisture and wave energy to the higher latitudes through thunderstorm activity. These changes "teleconnect" with distant areas by affecting the ridge and trough patterns associated with the polar jet stream. Thunderstorms are viewed as an effective agent of teleconnection from the tropics to mid latitudes, because they export vast amounts of heat and energy pole-ward via the mid to upper atmosphere. Avissar and Werth [Avissar and Werth, 2004] tested the existence of teleconnections using ensembles of global land-atmosphere simulations of widespread deforestation in the Amazon, Central Africa and Indonesia (separate and simultaneous). They identified that regions non-local to the deforestation in the upper, mid and lower-latitudes were impacted, generating a significantly different precipitation climatology. Some regions in Central Asia and the Arabian Peninsula showed changes of up to $40\%$.

### 1.0.8 Vegetation disturbance dynamics

Initially studies looked at vegetation as a "passive respondent" to changes in climate and weather. Salati and Vose were among the first to suggest that the land-surface of the Amazon was not influencing the local climate but changing with it [Salati and Vose, 1984]. Shukla and co-authors were among the first to suggest that decreased precipitation and increased surface temperatures resulting from deforestation could result in a new equilibrium in the state of Amazonian vegetation [Shukla *et al.*, 1990]. These climate-ecosystem transitions have been clearly observed in other regions. The Sahel of Western Africa is an excellent case of disturbance shock initiating a significant, intransitive and stable shift in the vegetation-climate equilibrium [Wang and Eltahir, 2000a]. Wang and Eltahir used the ZonalBAM model to investigate the rebounding of the vegetation-climate equilibrium under land surface disturbance conditioning [Wang

and Eltahir, 2000b]. They proposed that initial degradation of the land surface, created a distinctive change in albedo and roughness, slowing down water cycling and moving the entire land-atmosphere system into an arid regime.

While there is no overwhelming evidence that an equilibrium shift has occurred in the Amazon thus far, certain studies have attempted to elucidate its pathways and potentials under various deforestation scenarios. Perhaps to considering the dynamic feedback, one must consider vegetation's immediate yet potentially differential responses to disturbance. Botta and Foley have used off-line land-surface model ensembles to argue that disturbance magnitude influences the relative biomass partitioning between under-story and upper-story vegetation [Botta and Foley, 2002]. For instance low disturbance rates were ineffective in changing the upper canopy enough to significantly alter the light levels penetrating the lower canopy thus inhibiting grass growth leaving more water available for tree seeding; while simultaneously the lower canopy disturbance opened up the the grass dominated under-story giving tree seedlings an opportunity to take root. However, at disturbance rates larger than $0.5\%/yr$, the reduction in alive biomass in the upper canopy was significant enough to create canopy openings, enabling sufficient light for opportunistic grasses.

Fire is perhaps the greatest contributor to Amazonian deforestation. Fire exerts tremendous influence over vegetation dynamic, and is likewise itself shaped by vegetation and hydro-climatological conditions. Of course, fire frequency is shaped to a large degree by synoptic factors. For instance the El Nino year of 1997 was an extremely active fire year in the Amazon basin. But Nepstad suggests there are several important local modulators of fire and flammability [Nepstad *et al.*, 2001]. Recently burned lands are more susceptible to re-burn. Dense tall canopies act as fire retardants because they are litter (fuel) resistant. Selective logging and other practices that open up the vegetation canopy can increase fire disturbance rate. Open canopies allow sunlight to penetrate the under-stories, creating desiccation. Dry litter makes excellent fuel to start fires. Logging practices create the debris component of wild-fire fuel.

Forest fires can even create positive feedbacks on themselves; Nepstad outlines three modes [Nepstad *et al.*, 2001]. Firstly, post-fire environments may be drier, and desic-

cated biomass increases fire fuel. Secondly, fires release smoke into the atmosphere. It can be argued that smoke reduces rainfall rates promoting drought, which promotes more fires. The rationale is that smoke saturates the atmosphere with so many condensation nuclei that cloud water droplets form too readily, and weekly distribute the available moisture such that cloud droplets do not grow large enough to sediment into rainfall [Rosenfeld, 1998]. The third fire feedback mode suggests that fires "open up" plant canopies, allowing sunlight to penetrate and dessicate under-stories. The fourth feedback cycle involves human response. The lack of control of undesired fires, prompts discourage in land-managers' ability to manage their lands without fire, setting a tone of increased fire use as a management tool [Nepstad *et al.*, 2001].

Most of the discussion thus far has focused on the interactions between vegetation and climate mitigated by water and heat. But it would be premature to ignore other pathways, particularly carbon exchange. The conversion of tropical forests to croplands and pastures, especially through burning, creates a net flux of carbon dioxide into the atmosphere [Skole and Tucker, 1993][Botta and Foley, 2002]. Some have estimated that increased atmospheric carbon could potentially feedback on tropical vegetation through water use efficiency (i.e., altering the stomatal exchange rates of water-vapor and carbon dioxide). Effectively, this reduces transpiration and could possibly drive a precipitation feedback cycle toward more arid conditions [Cox *et al.*, 2000]. The climatological impacts of increased CO2 concentrations through warming effects is obviously a key discussion piece in contemporary culture [Solomon *et al.*, 2007].

## 1.1 Science Questions and Experimental Design

This thesis is most interested in uncovering the non-local feedbacks and sensitivities of hydrologic climate in response to deforestation in the Amazon and conversion of lands in the region. This is approached from two directions: 1) via data analysis of precipitation patterns over a selected location of structured Amazonian deforestation and 2) through a a regional modeling approach. The latter encompasses the bulk of the thesis research. The Ecosystem-Demography Model 2 (EDM2), a spatially distributed

dynamic terrestrial model of plant structure and composition, succession, disturbance and biophysics, is coupled with the Brazilian Regional Atmospheric Model (BRAMS). BRAMS is a three dimensional physical model of the atmosphere, it uses a finite volume integration of the fluid momentum equations and a host of physics parameterizations; turbulent closure, convection, radiative transfer, etc.

Given that human derived ecosystem disturbance exceeds the ecosystem disturbance rates of natural history, we may start to ask if certain aspects of the Amazonian vegetation-climate system has undergone shifts in equilibrium. This thesis poses two questions:

1. How has land conversion in the Amazon and surrounding regions changed regional hydrology?

2. Are the changes in regional hydrology significant enough to produce an ecological response?

### 1.1.1 Design of the Model Experiment

The objective of the modeling experiment is to isolate differences in regional hydrology that are attributed to the land-conversion feedback processes, and to see if these differences have the potential to influence the equilibrium state of ecosystem structure and composition. The step-by step process of the experiment is described as follows:

1. Create a realization of regional terrestrial vegetation with the EDM2 model. This uses an off-line climate driver to dynamically evolve vegetation from a near bare-ground condition until ecosystem structure reaches a steady state equilibrium with climate. Use a modern estimate of atmospheric carbon dioxide, 370ppm but do not apply any anthropogenic disturbance events. Save the resulting regional structure and composition, this is called the "Potential Vegetation(PV)" condition.

2. Continue the offline simulation over a period of several decades. Apply human land-conversion derived from external datasets. Save the resulting regional structure and composition, this is called the "Actual Vegetation (AV)" condition.

3. Perform two coupled EDM-BRAMS simulations. The simulations are identical with the exeption of using the "potential" and "actual" ecosystems as the lower boundary condition. The lateral boundary conditions, model parameters, initialization of heat and moisture and timing are all identical. Observe the differences in the patterns of seasonal hydrologic variables such evaporation, temperature, vapor pressure and most importantly precipitation.

4. Identify locations that show interesting differences in seasonal hydrology generated by the two cases. Create a monthly mean perturbation to precipitation that reflects this difference.

5. Run offline ecosystem simulations at the locations of interest. Run one control simulation using the original climate data that produced the current equilibrium. Also run test simulations where the climate driver data is perturbed according to the coupled model results.

### 1.1.2 Thesis Outline

Chapter 2 presents an approach of satellite rainfall analysis in the southwestern Amazon and the statistics of rainfall relative to the transition between forests and non-forests. Chapters 3 will cover some of the biophysical theory behind the EDM2 model and its coupling with the BRAMS model. Chapter 4 covers the preparation of the regional vegetation demographic initial condition. Chapter 5 assesses the validity of the coupled model system to re-produce realistic atmospheric conditions and surface fluxes such as radiation and precipitation. Chapter 6 covers the results of the coupled model simulation. The differences observed in the two test cases and highlighted and potential mechanisms behind the differences are discussed. Chapter 7 evaluates the offline climate perturbation experiment. Additional information regarding technical matters of the modeling system can be found in the Appendices.

# Chapter 2

# Precipitation Variability over the Forest to Non-Forest Transition in Southwestern Amazonia

## 2.1 Introduction

There is theoretical support for the idea that land-cover heterogeneities drive solenoidal circulations [Atkinson, 1981], [Pielke, 1984], [Pielke, 2001], [Renno and Ingersoll, 1996]. Updrafts can be analytically related to near surface heat flows across dissimilar patches of land, the plumes themselves occurring over the deforested patches with higher surface temperatures. Low level forest to pasture momentum fluxes and high level pasture to forest momentum fluxes have been observed in the southwestern Amazon [Souza *et al.*, 2000]. Assuming that deforested patches are indeed warmer, the high sensible heat flux influences vigorous boundary layer development [Pielke, 2001]. The combination of boundary layer development and convergent lifting winds provides mechanical energy necessary to lift air parcels to the level of free convection.

There is some general agreement that land-cover length scales on the order of tens of kilometers, or perhaps the Rossby radius, are most optimal for promoting solenoidal circulations [Pielke, 2001], [Dalu *et al.*, 1996]. Heterogeneity scales larger than 100

km cannot produce significant gradients in surface temperatures, while at scales smaller than several kilometers diffusion processes tend to homogenize thermal properties thereby destroying the thermal gradients that drive circulation [Baldi *et al.*, 2008], [Anthes, 1984], [Dalu and Pielke, 1993]. Ambient winds can potentially strengthen or ameliorate updrafts depending on various factors including wind strength and plume tilting.

Thus far, uncovering the water cycling effects of structured deforestation in the Amazon have been elusive. D'Almeida and coauthors [D'Almeida and co authors, 2007] found agreement among experiments with General Circulation Models that widespread Amazonian deforestation promotes a weakened water-cycle. Although, there is inconsistency in results at finer scales and more realistic land-use scenarios. A land-atmosphere model inter-comparison at the 2008 Moore-NSF workshop on Amazonian Savannization [Nepstad and Coe, 2008] provided evidence that more realistic deforestation scenarios [Soares-Filho *et al.*, 2006] alter patterns of hydrologic energy including rainfall, yet results differed regarding the sign of mean precipitation anomalies at various locations under different land-use scenarios. Other meso-scale numerical simulation experiments have found that increased deforestation leads to reduced precipitation, preferentially reduced over the deforested areas themselves [Silva *et al.*, 2008]. Some have shown increased convective precipitation resultant from various scales of forest/non-forest heterogeneities, particularly over deforested areas thus creating positive re-growth conditions [Avissar and Liu, 1996].

It has already been observed that dry season afternoon shallow cumulus clouds show a positive bias over deforested areas of the region [Cutrim *et al.*, 1995], [Rabin and co authors, 1990], [Chagnon *et al.*, 2004]. Wang and co-authors (2009) found the opposite was true for high cold clouds, which were more prevalent over intact forests. Correspondingly, both Convective Available Potential Energy and Convective Inhibition were typically weaker over non-forests and stronger over intact forests, suggesting that non-forested land-covers are associated with relatively rapid boundary layer development but lesser ability to generate deep convection.

The objective here is to use observations from the Tropical Rainfall Measurement Mission's Precipitation Radar to further elucidate the precipitation component of this

relationship between the land-cover of the southwestern Amazon and its hydrometeors, and consider its current and potential implications to the local ecohydrology. This continues the focus of previous papers on dry-season (June through October) afternoon precipitation events. The methodology of matching precipitation with land-cover and forming comparative statistics is presented first. The results from three tests are then analyzed: (1) the comparison of precipitation fractions over forested and non-forested landscapes, (2) the comparison of precipitation fraction over interior non-forest regions with both forested and forest edge regions and (3) the three-way comparison of precipitation fraction over interior forests, interior non-forests and transition zones between the two.

## 2.2 Methods

Three experiments were performed and will be explained in more detail. The experiments were common in that a series of TRMM rainfall maps were observed, and counted the cells with rainfall keeping a record of which type of land-cover (forested or not) was present beneath it. All experiments derived the condition of forestation from the same dataset, they differ in how this dataset was ultimately processed.

### 2.2.1 Datasets - MODIS 12Q1 and TRMM 2A25

Forest coverage in Rondônia Brazil was retrieved from the MODIS Land Cover Type product MCD12Q1, a yearly product providing land-cover classifications from 2001 to 2008 on a 500 meter sinusoidal grid. This data was re-projected via nearest neighbor, to an equal angle 4 kilometer grid that roughly matches the resolution of the TRMM 2A25 product. The land-cover classes follow the International Geosphere-Biosphere Programme (IGPB) standard. Cells identified as evergreen needle-leaf, evergreen broad-leaf, deciduous needle-leaf, deciduous broad-leaf and mixed-forested were deemed "forested", while the remainder were deemed "non-forested". This binary 4 kilometer map of forested and non-forested cells was used as the basis for comparing rainfall

measurements in the following experiments.

The non-forested portion of the binary map was drawn from crop-lands, urban areas, permanent wet-lands, grasslands, savannas, woody savannas, closed shrub-lands and water. A map of these coverage types are shown in Figure 2-1. In 2001, 75% of the grid was composed of broad-leaf evergreen forests, 3% by mixed forests, 2% woody savanna, 10% savanna, 2% grasslands and 5% crop-lands. The remainder summed to roughly 3% of total coverage. By 2007, broad-leaf evergreen forests accounted for 71% of land-cover while mixed forests decreased to a little over 1% and the coverage of savannas increased to roughly 13% of the total area. While "forested" landscapes by and large refer to broad-leaf evergreen forests, the variability of the physical properties across non-forested land-covers is not trivial. In the most extreme case, compare the heating rate and energy flux properties of water bodies versus dry lands with shallow rooting depths; the partitioning of total net radiation into sensible, latent and earthward energy flux components could differ significantly. It is argued here that non-forested landscapes in this domain of study are strongly reflective of savanna and grassland type ecosystems, which in general have consistently higher albedo, lower leaf area index, lower surface layer roughness and drag coefficients, and shallower rooting depths than forests. While water bodies, permanent wetlands and irrigated crop-lands may have higher potential evaporation rates and increased thermal inertia due to standing water, they only account for less than 10% of the total non-forested area and can only marginally influence statistics. Regarding terra-firma, forests of the region typically have higher potential evaporation rates than grasslands, savannas and crop-lands. While there has been open discussion on how the evpotranspiration rates of the region's forested and non-forest ecosystems respond to stomatal control, eddy covariance measurements indicate evaportranspiration rates for pastures (Fazenda Nossa Senhora) are on average lower than intact forests (Jaru) in both wet and dry seasons [Hasler and Avissar, 2007].

The binary mapping of forest cover was then used as a common grid to geo-reference TRMM 2A25 precipitation measurements. The 2A25 is a swath based near instantaneous measurement of rainfall converted from backscattered reflectivity by the TRMM precipitation radar[Kummerow *et al.*, 1998]. The estimated rainfall is not without

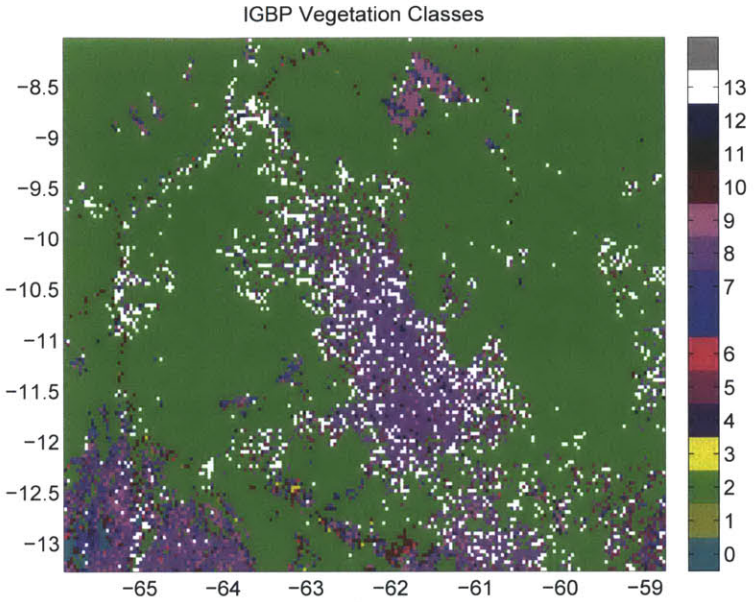


Figure 2-1: Land cover classifications per the International Geosphere-Biosphere Programme (IGPB) standard, 2001 Rondônia Brazil. 0-Water 1-Evergreen Needleleaf Forest 2-Evergreen Broadleaf Forest 3-Decidous Needleleaf Forest 4-Decidous Broadleaf Forest 5-Mixed Forest 6-Closed Shrubland 7-Woody Savanna 8-Savanna 9-Grassland 10-Permanent Wetland 11-Cropland 12-Urban 13-Cropland (classes open shrubland, barren and snow were not represented)

its uncertainties, considering for example its known biases over the region of interest[Rozante *et al.*, 2010], patterned bias in sampling frequency and its limited ability to measure the diurnal cycle or rainfall at fine scales[Negri *et al.*, 2002]. Likewise with any remote sensing product, there are non-negligable instances of missed detections, estimated at rates of 15% or less compared to validating rain gauges over 5 minute integrations[Wang and Wolff, 2010]. As will be discussed in greater detail, the interest in this study lies in making relative comparisons of rainfall detection, and formulates its statistics irrespective of the swath footprint, swath coverage frequency or the accumulations or temporal trends in rainfall. It is acknowledged however, that the analysis of the TRMM PR data only reflects the statistics of the window of interest (afternoon), and not the whole diurnal spectrum of rainfall.

The orbital swaths of TRMM 2A25 precipitation that intersected the study domain were archived during an extended dry season (June through October) from 2001 through 2007 falling between the hours of 11AM and 6PM local time, 199 rainfall producing swaths were used. The rainfall estimate is a three dimensional product, providing a ground resolution of five kilometers in a 247 kilometer swath width at a vertical layering resolution of 250 meters. Perhaps a TRMM product rendering surface rainfall alone would be simpler to use, but the 2A25 product was already available in-house after an extensive pre-analysis and comparison with other products such as the TRMM 2A12 and GOES VIS/IR. The swath based precipitation measurements were matched to the land-cover grid via the nearest neighbor method. The study domain is 600km wide in the North-South and 800km East-West (150x200 pixels), see Figure 2-2A.

### 2.2.2 Data Analysis Framework

There was concern that multiple environmental covariates to precipitation were present in the area of interest, thus making it difficult to confidently discern how the linkage between land-cover and precipitation exists in this area. Two obvious factors are topographic elevation and weather patterns. While the southwestern portion of the study domain does not quite reach the lower slopes of the Bolivian Andes, orographic weather

effects and the persistent weather patterns associated with the South American Low Level Jet and South American Circulation cannot be ignored. In order to neutralize the spatial biases imposed by topography or climate, the sampling strategy is randomized and the analysis is carried out over a series of smaller sub-domains. More specifically, the statistical techniques (to be discussed) were applied to each sub-domain independently and then the average behavior across the sub-domains was recorded for each event. These sub-domains are each 50 pixels wide (200x200 km) and their locations were selected randomly by seeding an offset tiling the domain. An example of how the sub-domains are tiled relative to an offset is shown in Figure 2-2B. Notice that the sub-domains are depicted with rounded corners in the figure, this is only to help the viewer differentiate sub-domains and areas that were rejected. Sub-domains were rejected from the analysis if both forested and deforested pixels did not each cover at least $10\%$ of the total area. The number of sub-domains varies from year to year as the land-cover influences the balance of forested to non-forested pixels.

### 2.2.3 Experiment 1

Here the question is asked, "Given a land-cover, forest or non-forest, what is the likelihood precipitation will be detected above it?". This is similar to and based on Wang and co-authors (2009) question, "Given a cloud, what is the likelihood it is found above a forest or pasture?". During each TRMM overpass, the precipitation fraction is calculated for each forested $PF^{for}$ and non-forested $PF^{nf}$ land-cover for each the sub-domains. This is simply the number of pixels with precipitation $P$ above their respective land cover type, normalized by the number of that land-cover's pixels $N$ contained in that sub-domain.

$$PF^{nf} = \frac{P^{nf}}{N^{nf}}, \; PF^{for} = \frac{P^{for}}{N^{for}} \tag{2.1}$$

In the same way, Chagnon and Bras [Chagnon and Bras, 2005] used cloud fractions to calculate a binary exceedance $(e)$ which describes the tendency of the cloud fractions over a series of events. In this case, if the sub-domain precipitation fraction is greater

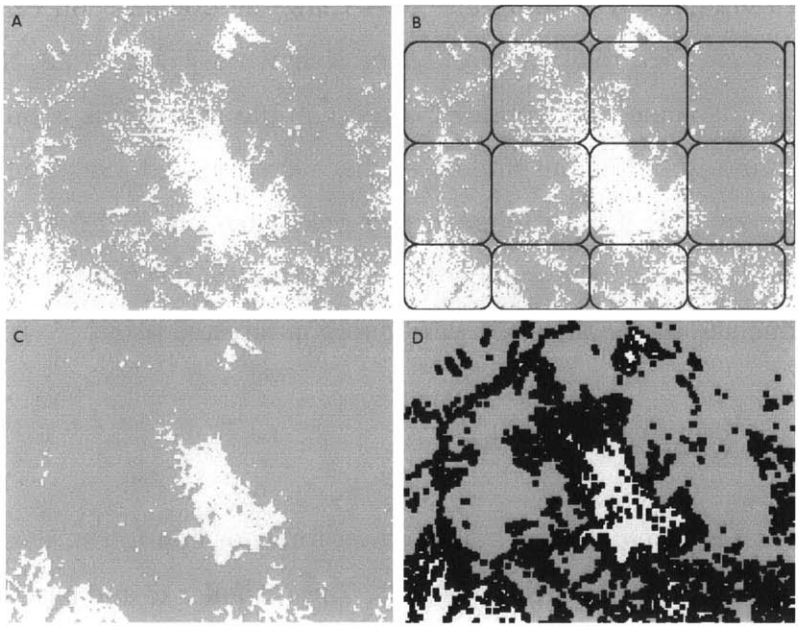


Figure 2-2: A) Binary mapping of the forested and non-forested grid converted from MODIS MCD12Q1 IGBP classes for the year 2001. B) An example of sub-domains that have been tiled out from a random offset. C) The binary map with a 1-cell encroachment as used in experiment 2. D) Mapping of the forested, non-forested and an 8 kilometer band on the forest to non-forest transition, as used in experiment 3.

over the non-forested areas, a binomial count of one is assigned. A zero is assigned for the alternative.

$$e = \begin{cases} 1 & \text{if } PF^{nf} - PF^{for} > 0, \\ 0 & \text{if } PF^{nf} - PF^{for} < 0 \end{cases} \tag{2.2}$$

The event based binary exceedance $\epsilon_i$ is simply the mode of the exceedance across each of the sub-domains for that event. The exceedance count $(EC)$ is then defined as the sum of the event exceedances over $M$ total events.

$$EC = \sum_{i=1}^{M} \epsilon_i \tag{2.3}$$

This is analogous to a coin flip. If there is no tendency for either of the land-covers to have higher precipitation fractions, the expectancy of this counting statistic is half of the total number of swaths (events,coin flips, etc). A posterior binomial counting distribution is constructed about the observed exceedance count ratio [Wang and co authors, 2009]. If the expected random exceedance count ratio of $1/2$ lies outside the confidence interval of the posterior distribution, then it can be said with significance that the observed precipitation fractions differ. A leftward shift from center indicates precipitation fractions are generally greater over forested landscapes. The opposite is true for a rightward shift.

The natural first question is to identify if precipitation fractions tend to be greater over intact forests or non-forests. The satellite overpasses are grouped by month and the exceedance counts calculated, see Figure 2-3. Notice several features in the plots. The central vertical line is the expectancy. The dashed vertical lines are the two sided $90\%$ confidence boundaries on the posterior binomial distribution centered on the observed exceedance count ratio. Although there is some slight indication of precipitation favoring deforested areas in some months, the confidence range of the posterior distribution encompasses the expectancy, therefore the precipitation fractions show no significant deviation from an unbiased binomial. Statistically, both land-coverages as a whole have

similar precipitation fractions.

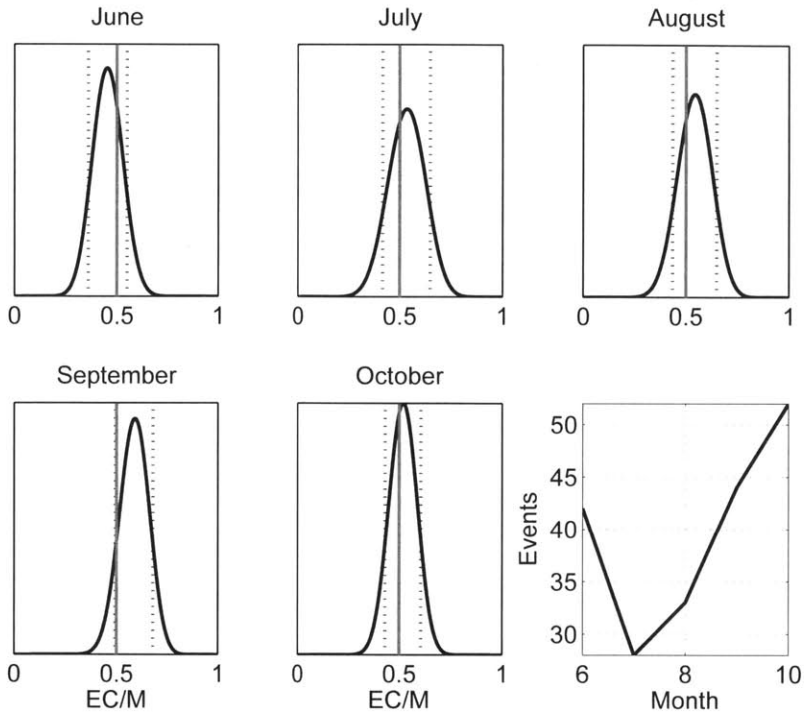


Figure 2-3: Probability density functions (black line) of precipitation fraction exceedance count ratios between forests and non-forests. The central vertical line at 0.5 is the expectancy. The dashed vertical lines are the two sided 90% confidence boundaries. The number of precipitation events contributing to the statistic is shown in the lower right panel.

### 2.2.4 Experiment 2

The next objective was to identify if there were differences in precipitation fractions observed in the deep interior regions of non-forested landscapes, as compared to the remainder (forested lands and also those non-forested lands bordering forested lands). This was done by creating a modified land-cover map. Starting with the original binary forest coverage map, the non-forested pixels bordering the forest were incrementally changed into forested pixels. Each increment encroached on the non-forests by 4 km. After encroaching 5 times (20 km), there were too few non-forested pixels in the modified map to enable robust samples. The same binomial counting exercise carried out in

experiment 1 was then applied to the modified maps for each succession of encroachment. An example of the binary forest map encroached 1 time is provided in Figure 2-2C. It is apparent in results of this image that much of the deforestation in this region is fractionated, at least at averaging scales of 4 kilometers.

The exceedance ratio is calculated in the same fashion as in the first experiment, using the modified land-covers. Figure 2-4 presents the binomial counting statistics after three encroachments (12 km). These plots also show the posterior binomial counting distribution from the original map (dashed curved line) for reference against the distributions based on the encroached land-cover (solid line). In each case, the distribution shifted to the left. The leftward shift indicates that the modified forest landscapes typically have higher precipitation fractions. The observed exceedance count ratio in the months of June, August, September and October are significantly different than the expectancy (0.5). In July, the 90% confidence interval still encompasses the expectancy.

The spectrum of observed exceedance count ratios for each level of encroachment are shown in Figure 2-5. Results are broken down by month (line markers) and with the mean across months (solid dark line). For reference, the y-intercept reflects an exceedance ratio for an un-modified forest cover (forest vs. non-forest, compare Figure 2-3); the exceedance count ratios shown in Figure 2-4 are reflected at x=12. As the effective interior non-forest region is encroached upon, the mean observed exceedance count ratio decreases from the expected outcome (0.5) to roughly 0.30 at an encroachment of 16 kilometers. This indicates that relative precipitation fraction progressively decreases towards the center of the domain's large deforestation structure.

### 2.2.5 Experiment 3

Given the first two exercises, it is still not clear how precipitation fraction changes on the forest edge. Results so far seem to indicate that the differentiation of precipitation fractions between forest and non-forest regions is accentuated as the transition areas between the two are reassigned to the forested region. In doing so, it is understood that the interior deforested areas are drier. However, because the first experiment indicates

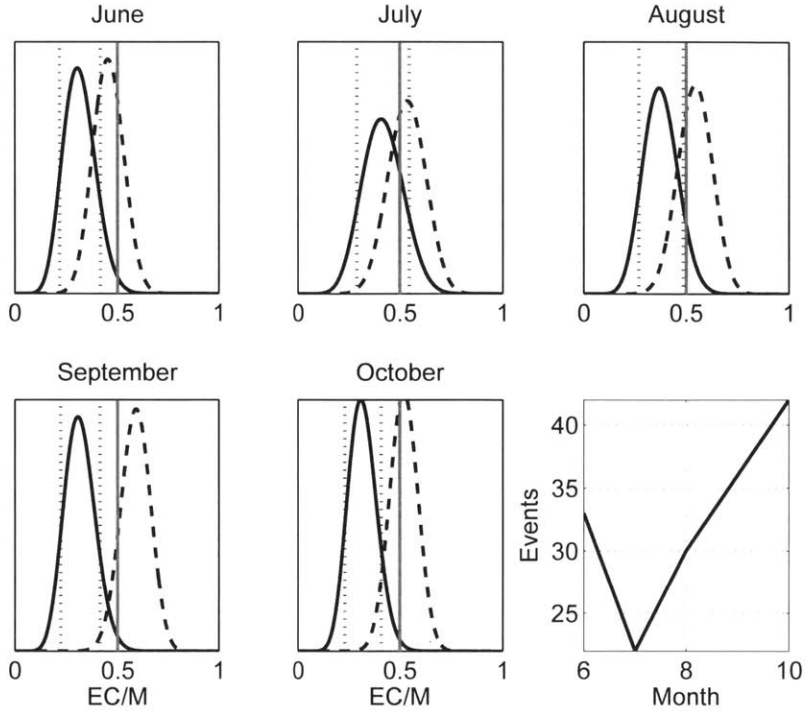


Figure 2-4: Probability density functions (black line) of precipitation fraction exceedance count ratios between interior non-forests and expanded forested regions by encroaching 12 km of non-forested adjacent regions. The probability density functions of forest versus non-forests from Figure 2-3 are provided for reference (dashed curved line). Again, vertical dashed lines show the $90\%$ confidence boundaries of the probability density function.

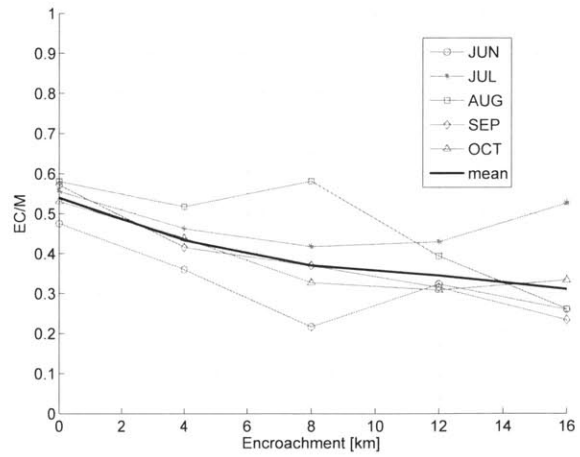


Figure 2-5: Observed exceedance count ratios as a function of encroachment in experiment 2, grouped by month.

that precipitation is balanced between the forested and non-forested land-covers as a whole, there must be a compensatory effect. To elucidate this result compare the precipitation fractions above (1) interior forests, (2) forest edges (transition bands) and (3) interior non-forests simultaneously. A transition band is defined here as those locations where forested pixels adjoin non-forested pixels. Both forested and non-forested pixels on each side of the transition are considered part of the band, and is therefore at least 8 km wide on the whole. Correspondingly, a 16 km transition band extends one more pixel on each side. An example of an 8 km transition band is shown in Figure 2-2D.

A three-way comparison cannot be done with the binary exceedance statistic. Instead, for each event, the precipitation fractions above each of the three land-covers are compared, and the superlative is logged. The superlative counts using both 8 and 16 kilometer transition bands are shown in Figure 2-6. With the exception of July, precipitation fractions are highest above the 8 kilometer transition band more times than compared to interior forests and interior non-forests. The precipitation fractions above the broader 16 kilometer transition were much more likely to be higher than the interior forested and interior non-forested zones. In summary, precipitation fractions were greatest above the transition region the most number of times, as compared to the other two. In the same vein, interior forest regions typically had greater precipitation fractions than interior non-forest regions.

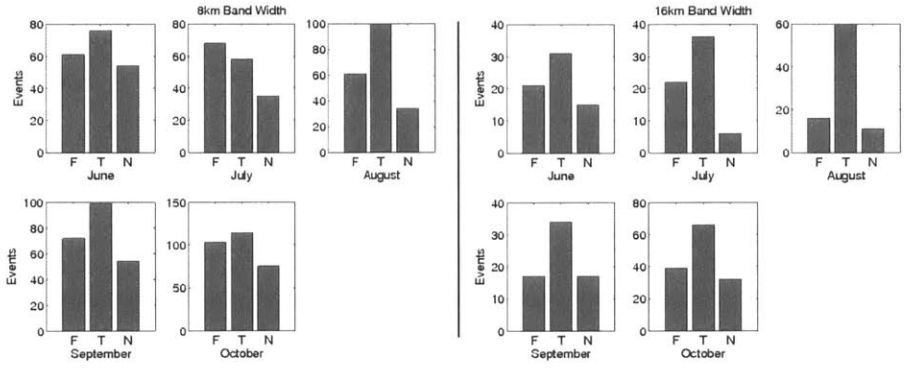


Figure 2-6: Number of events in which precipitation fractions over each land-cover type were superlative. Forests $(F)$ refer to interior forest land-covers and non-forests $(N)$ are interior non-forests. The left panel shows transition bands $(T)$ which are 8 km wide, the right panel shows when transition bands are 16 kilometers wide.

## 2.3 Discussion and Conclusions

Consider a transect originating in the forest interior, crossing the transition region, and ending in the non-forest interior. Interpretations of the results from the three exercises on this theoretical transect are provided in Figure 2-7. Experiment one suggested that precipitation fractions were somewhat balanced, perhaps marginally biased towards the the non-forested side of the transect (see upper left panel). Experiment two suggested that precipitation fractions were less over the interior non-forest regions, compared with all other landscapes (see upper right panel). The third experiment showed that the transition bands had the greatest precipitation fractions (see lower left panel) while the interior forested regions had greater precipitation fractions than the interior non-forests. The three experiments fit together as pieces of a puzzle, rendering a cohesive picture along this transect. Because precipitation fractions on each side of the forest edge balance, and because deep interior non-forests have low precipitation fraction, there must be a compensatory effect over the edge. The compensation is that precipitation fraction above the non-forest side of the forest edge must be high.

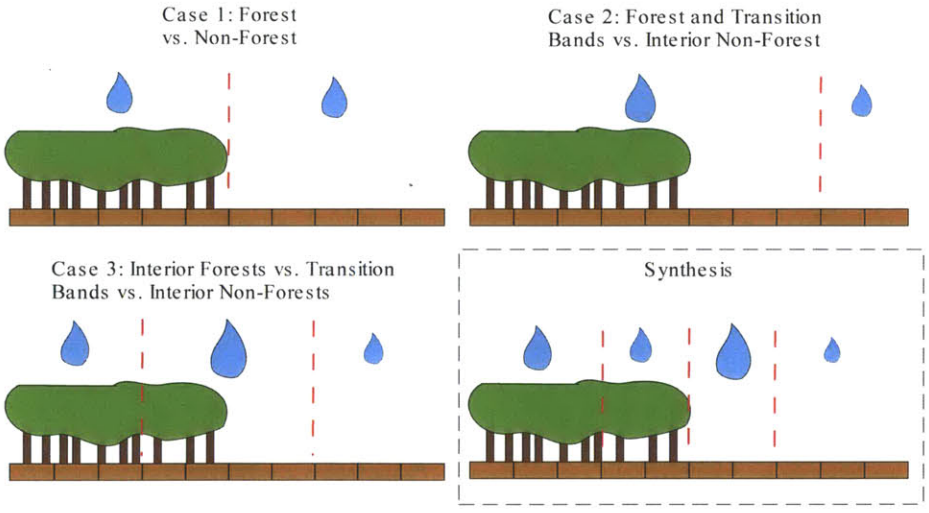


Figure 2-7: Diagram of a transect from the forest interior to the non-forest interior. An representation of an intact forest stand is on the left side, non-forests are on the right. Rain drops size qualitatively represents the relative differences in precipitation fraction across the different land-covers of interest.

Non-forests (grasslands, savannas, crop-lands, etc) in the southwestern Amazon are

typically associated with higher surface temperatures, rapidly developing atmospheric boundary layers and subsequently lower convective inhibition [Wang and co authors, 2009]. At certain heterogeneity scales, this convective focus can create convergence zones and solenoidal circulations [Atkinson, 1981], [Pielke, 1984], [Pielke, 2001], [Renno and Ingersoll, 1996]. Situated on the forest edges, there is corresponding subsidence over the forest canopies which serve as sources of moisture to the up-welling air on the non-forest edge. This moist static energy contributes to the convective available potential energy needed for deep convective precipitating clouds. The subsidence over the forested side of the transition band would inhibit precipitation at that location. The resulting precipitation trend along the transect from forest to non-forest features high precipitation fraction above the interior forest, lessened precipitation above the forest side of the transition, highest precipitation fractions over the non-forest side of the transition and low precipitation fraction over the interior non-forest region. This synthesis is shown in the lower right panel of Figure 2-7.

Mean areal precipitation fraction is synonymous with mean precipitation frequency at point locations within the statistically representative space and time. Shifting terminology, it can be stated that precipitation frequency shows decline towards the interior of non-forests. In cases where non-forests are the result of exogenous disturbance, there is potential for a drought-based feedback cycle of desertification. The evidence also poses some questions as to ecosystem response on the forest edge. Two observations are possible. The subsidence-based decrease in precipitation frequency on the intact side poses a drying threat to forest ecosystem stability. Alternatively, the enhanced precipitation frequency on the non-forest side could conceivably stimulate forest regrowth by minimizing drought stress. These competing theories are dependent on many factors; including the holistic community responses to precipitation changes regarding growth rates, mortality rates, coupled effects with soil and nutrient composition, and endogenous disturbance. There is evidence, though, that the Amazon rainforest shows a basin-wide general sensitivity to drought stress [Phillips and co authors, 2009].

While it is difficult to quantify the potential canopy biophysical affects of changes in precipitation frequency, the effects of forcibly excluding precipitation through-fall

have been observed in the central-eastern Amazon. When precipitation through-fall was forcibly reduced by 50% of depth over the first half of the year, significant changes were seen in canopy openness, leaf area index and above ground biomass production [Nepstad and co authors, 2002]. The results presented in this study cannot provide similar seasonal precipitation accumulations due to the inconsistent orbital nature of the satellite measurement system, however they do indicate that existing large scale Amazonian deforestation structures can modify precipitation fractions and frequency on the orders of ten(s) of a percent.

The generalized tendencies discussed here are applicable to afternoon, dry season events in southwestern Amazonia. However there is no reason these results could not extrapolate to other regions of the world. The key for this to occur depends on the fact that precipitation is convectively driven and that there exists meso-scale land-cover heterogeneity (several to tens of kilometers) with associated differential heating rates. It is also clear that certain ambient conditions constrain the likelihood of stimulating land-surface influenced precipitation. It was shown analytically through a stochastic analysis that the mesoscale circulations driven by heterogeneous land surface heating rates are strongest when ambient winds are at their lowest[Wang *et al.*, 1996]. Wet season precipitation in Rondônia features frontal based precipitation and wide-spread meso-scale convective complexes that often spawn convective cells triggered from the down drafts of other cells [Lima and Wilson, 2008]. These types of non-locally stimulated events were not completely filtered out from this study, but perhaps future analysis could utilize more intelligent storm recognition to make restrictions. However, a signal was detected even among such noise, signifying that the precipitation tendencies driven by land-cover induced phenomena are not insignificant among the whole.

# Chapter 3

# Regional Coupling of Amazonian Hydrologic Climate - The Modeling System

The Ecosystem Demography Model (EDM2) and Brazilian Regional Atmospheric Modelling System (BRAMS) simulate the physical interactions between the atmosphere and terrestrial biosphere. These are the central tools used in the second part of this thesis.

The two models (EDM2 and BRAMS) can exist independently. An atmospheric model can rely on simplified lower boundary conditions to reflect atmospheric radiation as well as produce drag and fluxes of heat and moisture. An ecosystem model can exist independently when driven with previously derived datasets of precipitation, down-welling radiation, atmospheric humidity, temperature, air pressure and windspeed. This chapter reviews the origins of these two models and how they were put together. The process of coupling the two models was based on the methods Robert Walko constructed in LEAF-RAMS [Walko *et al.*, 2000].

The atmospheric model BRAMS is maintained by its own set of developers. Its evaluation will be brief, with special emphasis placed on a discussion of the parameterization of cumulus clouds and precipitation. There is special emphasis placed on the mechanics of the ED2 model, as various development efforts have been motivated at least partially by the goals of this thesis and that of other researchers. Much of the model physics has

been documented in [Moorcroft *et al.*, 2001] and [Medvigy, 2006]. A comprehensive discussion of EDM2 biophysics is provided in the appendices, this chapter will cover basic concepts behind model coupling, land-surface biophysics, and then a briefing on the key contributions this thesis work has made to the EDM2 system.

## 3.1 Brazilian Regional Atmospheric Model (BRAMS)

The Brazilian Regional Atmospheric Modeling System (BRAMS) is an adaptation of the Regional Atmospheric Modeling system (RAMS) [Pielke *et al.*, 1992], with special modifications to accommodate the climate regime of the tropics and key research issues in the area (such as carbon exchange, influence of industrial areas, and Lagrangian dispersion tracking of scalar quantities). BRAMS could be generalized as a limited-area three-dimensional physical model of the atmosphere. It is limited in area because it uses pre-derived lateral boundary conditions. The atmospheric dynamics are constructed around the full set of primitive dynamical equations of atmospheric motion. The equations of mean momentum are integrated forward in time via explicit finite difference (numerically achieved via leap-frog stepping), incorporating advection, Coriolis, pressure, gravity, diffusion of internal energy, and second order viscous effects. The dynamic equations are supported by a suite of parameterizations for turbulent diffusion, solar and thermal radiation, moist processes including the formation of multi-phase clouds and precipitating hydrometeors, sensible and latent heat exchange between the land and atmosphere, drag effects of terrain and cumulus convection. Cumulus convective clouds are responsible for a significant portion of tropical rainfall. Convective heating materializes in the form of plumes and jets containing high levels of moist static energy. At fine scales on the order of hundreds of meters, differencing schemes can resolve the spatial variability in these convective structures, allowing buoyancy gradients to drive convective restabilization. However, this thesis research uses meso-scale (resolutions of several kilometers) resolutions where grid-scale convective structures cannot be resolved. Convective parameterization seeks to estimate the average effects of these sub-grid scale convective processes. The BRAMS methodology of parameterizing uses

Grell [Grell *et al.*, 1995] cumulus parameterization, designed to create conceptual cloud updrafts, downdrafts and environmental feedbacks, with options of different methods to dynamically control the mass fluxes associated with the updrafts and downdrafts. A more thorough discussion of Grell's cumulus parameterization is covered in Appendix A.

## 3.2 Ecosystem Demography Model (EDM)

### 3.2.1 EDM Version 1 (EDM1)

In its first incantation, the Ecosystem Demography Model [Moorcroft *et al.*, 2001] was designed to simulate the ecological dynamics of terrestrial vegetation. Referred to as EDM1 or ED, it accounts for the biogeochemical fluxes of carbon and nitrogen in the soil, woody biomass and leafy biomass. These fluxes modulate the dynamical processes of mortality, reproduction and growth. Its central design philosophy is the stochastic representation of all plants into Size and Age Structured (SAS) communities. These communities are differentiated into *patches* of land, which are principally defined by the time since the last disturbance. Each patch contains an array of plant *cohorts*, which are plant groups of similar properties. The properties unique to each cohort include Plant Functional Type (PFT), size and allometry, leaf biomass, stem biomass, below ground carbon, biomass for recruitment and phenological status, among other characteristics. For a complete and thorough description of the model please consult the original paper by Moorcroft, [Moorcroft *et al.*, 2001], and its appendices.

### 3.2.2 ED Version 2.0 (EDM2)

The model's second version, the Ecosystem Demography Model 2 (EDM2), was expanded to conserve and account for mass and energy transfer [Medvigy, 2006].[1] Struc-

[1]Similar descriptions of these processes can be found in David Medvigy's thesis [Medvigy, 2006] according to his original formulations. This section in particular acknowledges efforts of the EDM2 code development team (term 2005-2010): Paul Moorcroft, David Medvigy, Marcos Longo, Michael Dietze, Yeonjoo Kim, Jeff Chun-Fung Lo, Naomi Levine, Thomas Powell, Abby Swann and myself.

turally, the model was given a layered soil column and a vertically distributed layering of crowns within a continuous and encompassing canopy airspace. Perhaps most importantly, this second version accounted for the biophysical processes of heat and mass transfer (water) between these entities. The system of scaling from large scale to fine scale processes has remained largely intact from its origins with EDM1.

There are four scales of information the model accounts for; each scale of information may have multiple branches of child scales. As alluded to in the introduction of EDM1, these scales (from parent to child) are called *Polygon*, *Site*, *Patch* and *Cohort*. They are ordered from large to small in terms of the size of the geographical area, and from small to large in terms of complexity and density of information.

- *Polygons* define a bounded region of space, within which there are uniform external atmospheric conditions (precipitation, upper air temperature and humidity, pressure, etc.), and an association with a geographic location. Each polygon retains the fractional cover of dry land and aqueous environments, the geographic coordinates of its center point and mean topographical elevation. Polygons line up with the discrete grid-points of the atmospheric model's lowest level.

- *Sites* define areas of geomorphic specificity within the polygon. A site could have unique qualities of soil texture, aspect, slope, depth to bedrock, etc., however the geographic position of a site does not have precision greater than the center of its bounding polygon because sites are not necessarily associated with specific landscape features. For example, the geographic center of "all areas with clay-loam soils" is rather meaningless if clay loam soils are pocketed among the polygon; the same goes for "all areas that share the same aspect". Conversely it is also possible that a site could be associated with a hydrologic basin within a polygon's boundaries, an explicitly geographically-located feature. There *can* be several sites within each polygon, however for purposes of this thesis, only 1 site per polygon was used. The site within each polygon used the soil texture with greatest spatial area, an average slope, and contained no lateral hydrologic routing. The ED model was operated in the vertical dimension only.

- *Patches* define a canopy space where vegetation, soil and air can conserve the exchange of radiation, heat, water and carbon. Plants co-exist in a vertically distributed canopy. They interact, compete and facilitate the use of light, moisture and nutrients. The interactions dictate that patches function conceptually at the gap scale (a gap is roughly thought of as the surface area encapsulated by the crown of a large tree), however a *Patch* does not indicate only one gap in the canopy. Rather, it is thought of as a statistical fraction of the land area typified by the gap it describes. *Patches* are further defined by their age, synonymously the time since the disturbance event that created it. Of course a landscape has a whole strata of disturbance based age history, and therefore many *Patches* are found in each *Site*. Like sites, they are not associated with an exact geographic location but are amorphously assigned a fraction of the total area within the site.

  Mechanistically, EDM2 creates new patches every year based on an assessment of the disturbance events that had occurred to the existing patches in that site, including fire events, tree-fall and land conversion. In this process, the percentage area of the existing patch is decreased based on the severity of the event, and the new area defines the size of the newly created patch. The new patch may reflect a new demographic of surviving/introduced plants (explained below) associated with the repercussions of that event. To save memory, a census of the new patch and cohort (see next) structure is taken each time new patches are created, and the most similar patches and cohorts are fused together sequentially until their total numbers are reduced to levels that are computationally suitable.

- *Cohorts* define the groups of plants inside the *Patches*. The plants of a cohort all have the same functional attributes, such as size, shape, phenotype, phenology and thermodynamic state. In this respect a cohort can be viewed as a group of clones. Cohorts have number density, which is the number of plants per square meter of soil. The ED model has a database of parameters and functional traits for the following tropical plant groups of South America: subtropical C3 grass, C4 grass, early successional tropical broad-leaf evergreens, mid successional tropical

broad-leaf evergreens and late successional tropical broad-leaf evergreens.

There may be any number of cohorts found in each patch. For instance, an arid grassland defined by a monoculture would likely have only one plant functional type and so little diversity in plant size to merit more than one cohort to explain the system. On the other hand, tropical rain-forests typified by multi-layered canopies, rich species diversity and complex competition modes could merit uncountable cohorts to completely define the system. While ED does not have limits on how many groups can be used, computer resources limit the model to operationally use on the order of tens of cohorts per patch.

New cohorts are created through reproduction and recruitment. Their number density decreases over time based on mortality functions. An example of one mortality function is the evaluation of the cohort's ability to take in carbon. The per-plant biomass of each cohort changes based on the balance of carbon gains associated with respiration, photosynthesis, litter-fall, conversion to structural biomass, storage in seed biomass and leaf extension.

A visualization of the polygon, patch and cohort scales is shown in Figure 3-1. Polygons are used to associate geospatial coverage and the forcing of the climate. They are represented in the figure as a grid. The patches, having unique disturbance ages, are visualized here as a pie-chart. Fire, tree-fall, human disturbance and potentially other disturbances are applied to patches based on information updated every month (although their time integrated effects are applied yearly to create a new strata of patches). An example of the vegetation strata for a patch shows that it is inhabited by several different plant functional types, each with different number densities, phenologic status and physiology.

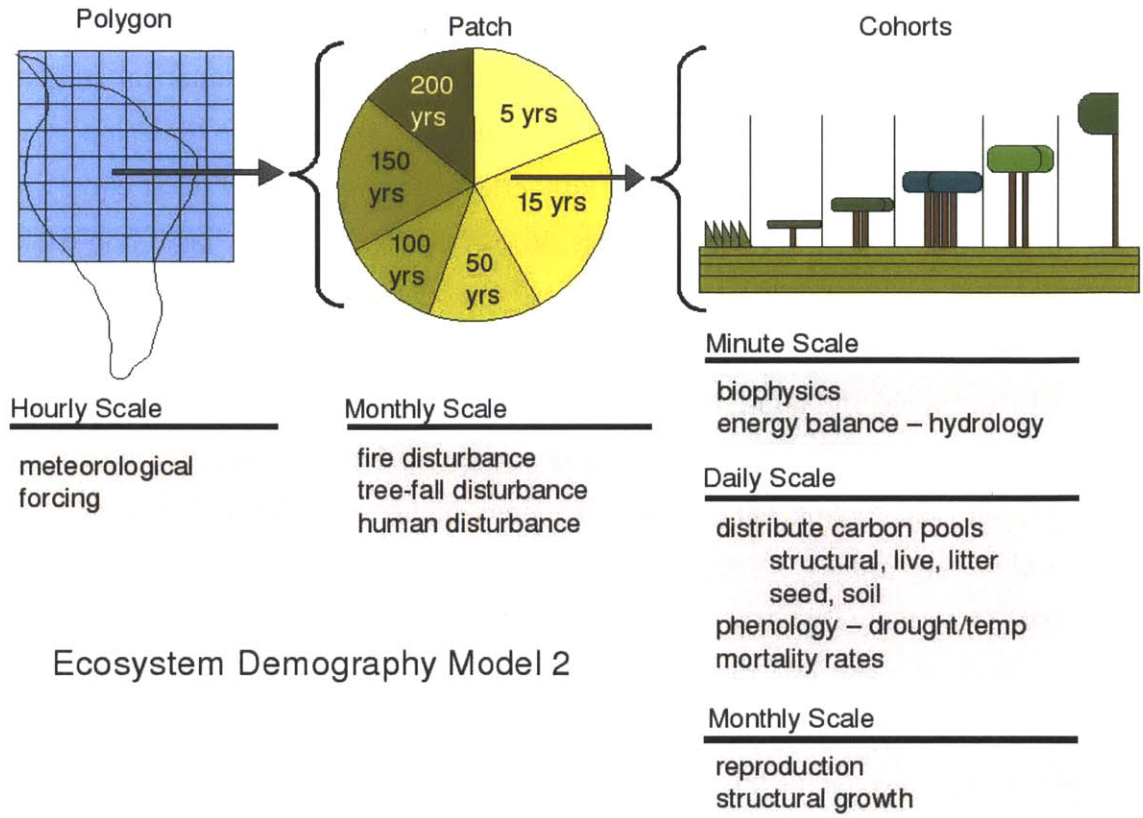


Figure 3-1: Visualization of the EDM2.1 memory and scales at which different processes are conducted.

## 3.3 Model Coupling Strategy

The atmospheric and land surface models communicate asynchronously. The atmosphere (BRAMS) provides information at the beginning of the EDM forward step, while EDM assumes this information is constant over the duration of its forward step and makes a time average of the fluxes during the step to return. The information bounces back and forth between the two models, waiting for one process to complete before it is sent back to the other. If the time-steps of each model are very small compared to the derivative of the variables exchanged, then asynchronicity is not an issue. For instance the radiation, precipitation, wind-speed and temperature that is evaluated by the atmospheric model at 11:55 AM is likely to be a suitable approximation for surface forcing one minute later. This may not be the case if the the models are 1-hour out of phase.

Meso-scale atmospheric models at spatial resolutions of tens of kilometers typically perform integrations on the order of tens of seconds to maintain numerical stability and convergence. The simulations in this thesis used an atmospheric time-step of 30 seconds. Ideally, the land surface and atmospheric models would operate at equal and short time-steps. For crude surface models this is feasible, but EDM has a non-trivial computational overhead. Ultimately, the EDM2.1 model used a 300 second time-step while coupled to BRAMS.

In both a coupled and non-coupled "off-line" mode, atmospheric information is provided to EDM2 at a reference height. It is suggested that the reference height for the meteorological forcing data is tens of meters higher than the tallest vegetation cohort (which are usually 30-40 meters for tropical evergreens). This is required because EDM2 internally calculates turbulent transport of heat, moisture and momentum through the canopy and into the inertial sub-layer of the lower atmosphere. The inertial sub-layer is found in the first hundred meters or so above the canopy and is often observed to have a constant flux profile typified by a logarithmic decay of wind-speed. The canopy top acts as a rough wall which imposes drag on the lower boundary layer, and the resulting shear creates a region where the energy in the turbulent spectrum is prominent at small eddy scales (as well as large eddy structures). A list of the variables required to drive EDM2 is provided in Table 3.1.

| | | |
|---|---|---|
| $u_x$ | $[m/s]$ | Zonal wind speed |
| $u_y$ | $[m/s]$ | Meridional wind speed |
| $T_a$ | $[K]$ | Air temperature |
| $q_a$ | $[kg/kg]$ | Air specific humidity |
| $\dot{m}_{pcp}$ | $[kg/s]$ | Precipitation mass rate |
| $z_{ref}$ | $[m]$ | Height of the reference point |
| $R_{ld}$ | $[w/m^2]$ | Downward longwave radiation |
| $R_{vb}$ | $[w/m^2]$ | Downward shortwave radiation, visible beam |
| $R_{vd}$ | $[w/m^2]$ | Downward shortwave radiation, visible diffuse |
| $R_{nb}$ | $[w/m^2]$ | Downward shortwave radiation, near infrared beam |
| $R_{nd}$ | $[w/m^2]$ | Downward shortwave radiation, near infrared diffuse |

Table 3.1: Atmospheric boundary conditions driving the EDM2.1 model.

The ED model passes boundary fluxes at the polygon scale to the atmospheric surface layer as an area-weighted average across patches and sites. There are three groups of

| | | |
|---|---|---|
| $\overline{(u'w')}$ | $[m^2/s^2]$ | Average vertical flux of horizontal wind velocity perturbations |
| $\overline{(w'w')}$ | $[m^2/s^2]$ | Average vertical flux of vertical wind velocity perturbations |
| $\overline{(t'w')}$ | $[mK/s^2]$ | Average vertical flux of temperature perturbations |
| $\overline{(q'w')}$ | $[kg/m^2/s^2]$ | Average vertical flux of moisture perturbations |
| $\overline{(c'w')}$ | $[\mu mol/m^2/s^2]$ | Average vertical flux of carbon perturbations |
| $\chi_s$ | [-] | Average total shortwave albedo |
| $\chi_l$ | [-] | Average total longwave albedo |
| $R_{lu}$ | $[w/m^2]$ | Average up-welling longwave radiation |

Table 3.2: EDM2.1 flux variables providing the lower boundary condition for the atmospheric model.

information the land surface must provide the atmosphere model. Firstly, it provides the topography which governs the geometry of the atmosphere's coordinate system. Secondly, the land surface model must provide the atmosphere with a lower boundary condition for turbulent closure, i.e., the vertical velocity perturbations of momentum, heat, moisture and carbon. Fluxes are presented as the time average of the sub-scale perturbations of vertical wind velocity and the associated perturbation terms they have covariance with. Thirdly, the land surface model must provide a lower boundary to atmospheric radiation. These variables are listed in Table 3.2.

For any generic variable $S$, at a polygon with $N$ sites of fractional area $A_{site}$, each of which contain $M$ patches of area $A_{patch}$, the area averaged quantity is straight forward.

$$S_{poly} = \sum_{i}^{N} S_{site,i} A_{site,i} \tag{3.1}$$

$$S_{site} = \sum_{j}^{M} S_{patch,j} A_{patch,j} \tag{3.2}$$

where

$$\sum_{i}^{N} A_{site,i} = 1 \tag{3.3}$$

$$\sum_{j}^{M} A_{patch,j} = 1 \tag{3.4}$$

## 3.4 Summary of Biophysical Processes

The mass and energy balance of the vegetation system starts with a definition of the prognostic state variables. These represent the energy and mass state of several clearly defined control volumes: (1) the vegetation system, (2) the canopy air, (3) the soil matrix and (4) transient surface water pools. The integration is handled numerically as either a Runga-Kutta fourth order (RK4), Runge-Kutta second-order, forward Euler or a hybrid forward-backwards Euler (FE-BDF2) process. The RK4 process is arguably the more accurate of methods because it can estimate its own step truncation error (the errors associated with assuming constant rather than continuous derivatives over step period) and reduce step-size accordingly (a benefit of using multiple sub-steps). The hybrid process, while not having the benefit of estimating error, is relatively fast and stable. A detailed description of its implementation in ED2 is explained in Appendix H.

A list of the prognostic biophysical variables is provided in Table 3.3. Note that the enthalpy of the vegetation $H_v$, soil $H_g$, surface water pools $H_{sfc}$ and canopy air space $H_c$ are all expressed directly in energy units. Enthalpy is equivalent to internal energy for materials other than compressible-fluids, as there is no pressure work term. In depth discussion on the use of enthalpy as a conservative state variable is provided in Appendix C.

| | | |
|---|---|---|
| $H_c$ | $[J/m^2]$ | Enthalpy of the moist canopy air |
| $q_c$ | $[kg/kg]$ | Specific humidity of the canopy air |
| $CO2_c$ | $[\mu mol/mol]$ | Carbon dioxide concentration of the canopy air |
| $w_{g(z)}$ | $[m^3/m^3]$ | Volumetric soil water content (ground) |
| $H_{g(z)}$ | $[J/m^3]$ | Enthalpy or internal energy of the moist soil matrix |
| $m_{sfc(k)}$ | $[kg/m^2]$ | Mass of surface water |
| $H_{sfc(k)}$ | $[J/m^2]$ | Enthalpy or internal energy of surface water |
| $m_v$ | $[kg/m^2]$ | Mass of water on the vegetation |
| $H_v$ | $[J/m^2]$ | Enthalpy or internal energy of the vegetation and its standing water |

Table 3.3: Prognostic variables in the EDM2 integrator.

A diagram of the prognostic state and flux variables of hydrologic mass is provided in Figure 3-2. Likewise, a similar diagram of the enthalpy fluxes and prognostic states is provided in Figure 3-3.

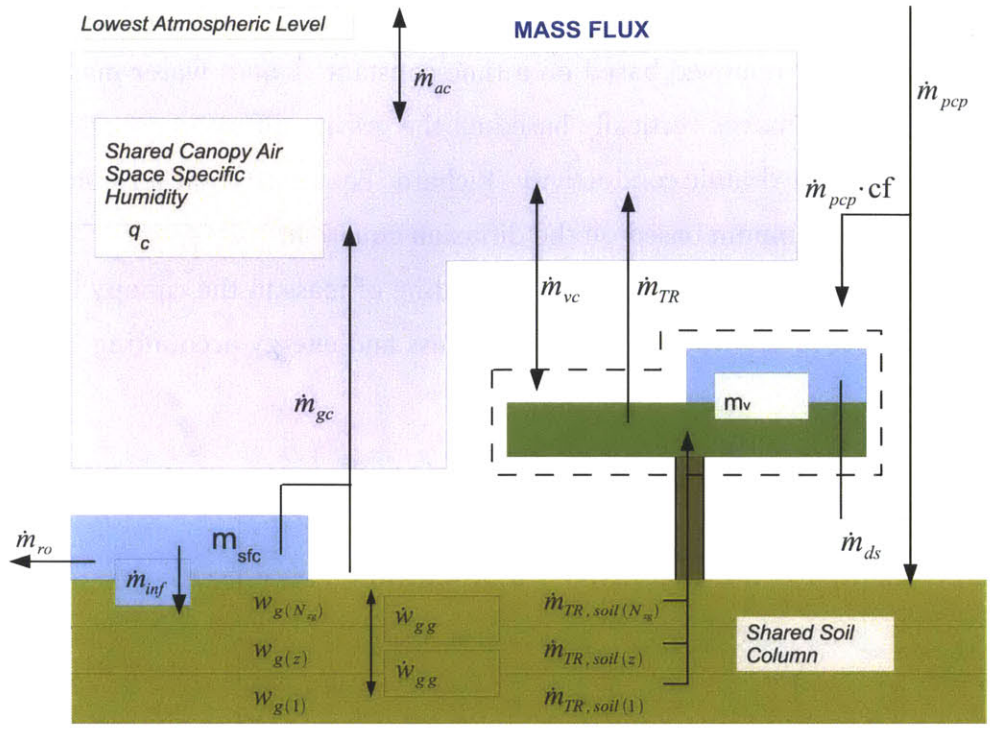


Figure 3-2: Schematic of the hydrologic mass flux between the soil, vegetation and canopy air control volumes. Refer to Table 3.3 and the glossary for variable definitions. Over dots indicate fluxes between pools. Subscripts associate the variable with the pool, $g$ for ground, $c$ for canopy air, $a$ for atmosphere, $v$ for vegetation, $sfc$ for surface (ponded water), $ro$ for runoff, $TR$ for transpiration and $ds$ for drip-and-stem flow. Crown fraction is shown with $cf$. NOTE: Only one cohort is shown for compactness. Many cohorts may exist, each one exchanging independently with the soil, canopy air and precipitation interception. Cohorts have no direct exchange with each other.

Mass and energy are exchanged across the following flux boundaries: the ground surface to canopy air $(gc)$ (which may or may not have ponded surface water), the vegetation to canopy air $(vc)$, between soil layers $(gg)$, and between the atmospheric boundary layer and the canopy air $(ac)$. Each cohort acts as a control volume exchanging mass and energy within the shared canopy air-space. Likewise, leaf surfaces and the soil surface can intercept and hold precipitation. Precipitation enters the top of the canopy, where the leaf surfaces are wetted until a holding capacity is exceeded and excess rainfall is routed into stem-flow to the ground surface. The surface water pool

infiltrates the top layer of the soil column until saturation; un-infiltrated surface water is potentially and partially removed based on a time-constant. Liquid water mass and energy in the soil column moves vertically based on the gravity diffusion equation using matric potentials and hydraulic conductivity (Richards Equation). Soil sensible heat transfers vertically in the column based on the diffusion equation.

A more comprehensive explanation of the accounting of mass in the canopy is provided in Appendix B. A review of the soil column mass and energy accounting is provided in Appendix E.

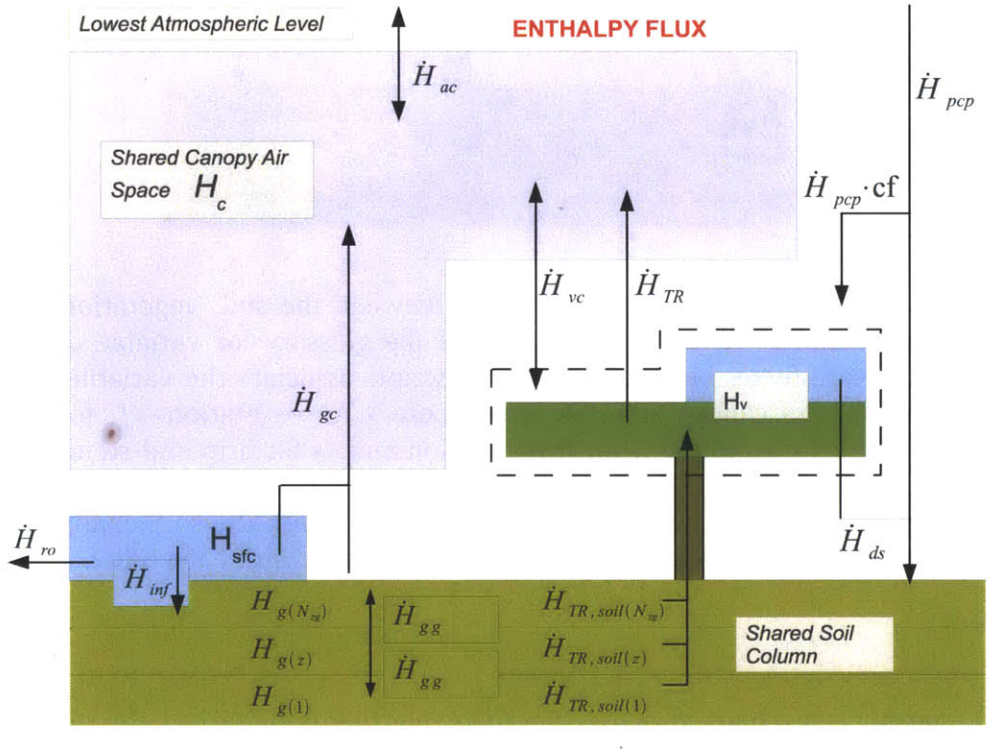


Figure 3-3: Schematic of the enthalpy flux between the soil, vegetation and canopy air control volumes. Subscripting follows the same conventions as in Figure 3-2.

The vegetation and soil surface can scatter, absorb and emit (thermal) radiation. The ED2 model is one of the more advanced large scale land surface models in that it uses its size structured cohort data to represent a vertical profile of leaf and stem

scattering elements. The model has no information regarding the relative positions of actual plants, so it cannot employ ray-tracing scattering models. Yet parameterizations based on the statistical mean qualities of canopy crown size allow for a two-stream radiation model [Sellers *et al.*, 1992]. A diagram of the radiative fluxes are shown in Figure 3-4. The leaves and stems of the cohorts do not exchange energy or mass with each other through direct means such as conduction or liquid mass flows. Rather they do so indirectly as mediated through the heat and moisture of the soil and air, and of course, through radiation. The plant surfaces use physical parameterizations of photosynthesis based on limiting factors of light, carbon, metabolism and soil moisture [Collatz *et al.*, 1991]. Stomatal resistance, which governs transpiration, root water uptake and carbon assimilation are likewise affected by soil moisture availability. These mechanics are explained further in Appendix D.

The turbulent transport of scalar quantities such as heat, mass and momentum is regulated mainly through gradient/resistance parameterizations analogous to an electrical circuit. The resistances are calculated based on an assessment of the mechanical and buoyant production of eddy transport. The gradients often require an assessment of the representative scalar quantities at the edge of the boundary layers surrounding each of these control volumes. An in depth review of the resistance calculation from turbulent transport is provided in Appendix F.

### 3.4.1 Biophysics Submodules

This chapter has served as a general overview of the model system concepts and general design philosophy. While most all of the physics modules in the EDM system are relevant to the goals of this thesis, a selection of key biophysical processes are covered in more detail in the Appendices.

- Appendix B: Vegetation System Mass Balance
- Appendix C: Enthalpy Flux and Conservation in the Canopy Air Space

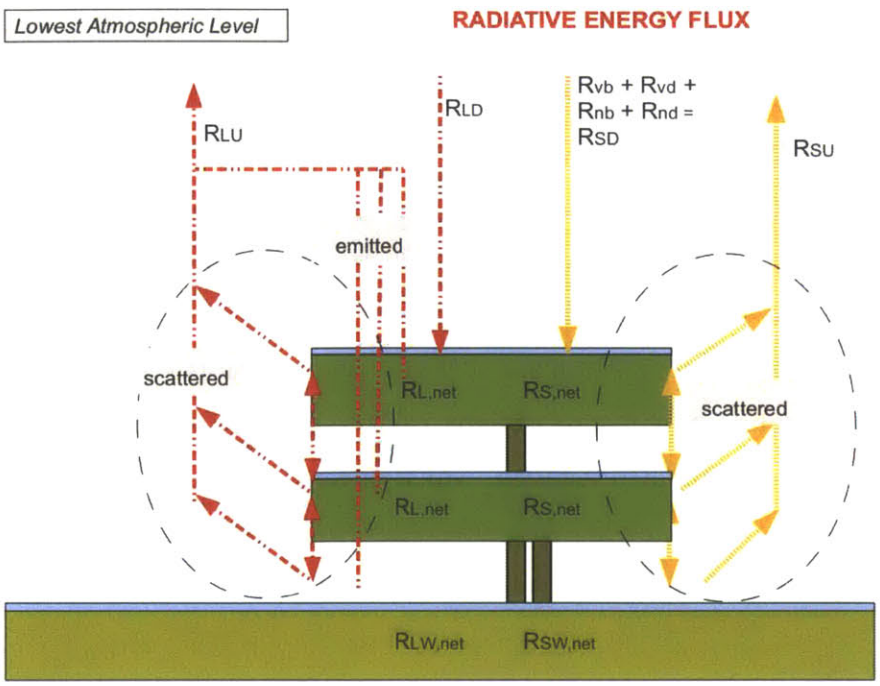


Figure 3-4: Schematic of the radiative flux between the soil, vegetation and upper air. Radiative scattering is calculated via a two-stream radiation process [Sellers *et al.*, 1992]. Long and shortwave radiation heat and cool the canopy leaves over their vertical depth, transient surface water pools and the surface soil layer. Subscripting follows the same conventions as in Figure 3-2. Radiation flux $[W/m2]$ is designated as variable $R$ with the following subscripts: visible-beam $(vb)$, visible-diffuse $(vd)$, near-infrared beam $(nb)$, near-infrared diffuse $(nd)$, longwave $(L)$, shortwave $(S)$, up-welling $(U)$ and down-welling $(D)$. Subscript $(net)$ indicates the net balance of incoming and outgoing radiation that is absorbed into warming the tissue and creating light reactions.

- Appendix D: The Photosynthetic Pathway and Transpiration Demand
- Appendix E: Soil System Mass and Energy Balance
- Appendix F: Turbulent Canopy Processes
- Appendix G: Bulk Resistance of Scalar Transport from Leaf Surfaces
- Appendix H: Hybrid Numerical Integration

## 3.5 Significant Contributions to the Modeling System

This section details significant contributions to the EDM2 modeling system as part of this thesis work. It must be stated that improvement of the model involved a team of individuals. In particular, Mr. Marcos Longo contributed to many small and large projects.

### 3.5.1 The Process of Coupling the Models

The process of coupling EDM2 and BRAMS was the first major tasks of the thesis. ED2.0 had been already coupled with the RAMS 4.0 model by Dr. David Medvigy as part of his thesis work. His work provided a reference template to work from. Major differences exist between BRAMS and RAMS-4.0 and between EDM2.0 (the version David Medvigy spear-headed) and EDM2.1 (the modern version that is coupled with BRAMS). At the time of implementing the coupled model, EDM2.1 was undergoing major changes to its memory structure, how it is "tiled" for parallelization and how the model polygons are initialized with information regarding thermodynamic state and the structure and composition of biomass. These factors and many others influenced the re-design of the model coupling strategy, which essentially motivated a ground-up approach to many new sub-routines that couple the models together.

Part of this process included building new modules for non-land boundary conditions to the atmospheric model. This module constrained water surface temperatures directly from external datasets. The ocean/lake module implements a sub-layer above the water surface with prognostic enthalpy and humidity. Exchange of sensible and latent heat is governed by gradient resistance theory using tabular drag coefficients for oceans and lakes. The water surface albedo is governed by lookup tables as well. The sub-layer enthalpy and humidity is integrated forward with explicit Euler integration.

### 3.5.2 EDM Software Architecture Re-Design

Core elements in EDM software were re-designed. These elements are not related to model physics. These elements were motivated by model usability and functionality. They are broken down considering previous conditions, motivations and changes.

**Vectorization** *Previous Condition:* EDM previously used "linked-lists" to handle the model memory. Each unique entity (polygon, site, patch, cohort) was a single unit of structured memory, which contained a pointer to an adjacent entity. For instance, a cohort structure contained scalars describing traits of a single cohort, as well as a pointer to the memory location of the next tallest and next shortest cohorts in the patch. *Motivation:* While linked lists were intuitive and naturally suited to handle the creation and removal of patches and cohorts, linked lists can not reap the benefits of vectorization and loop optimizations. *Change:* Main model memory was changed to utilize structured arrays. In this implementation for instance, cohort biophysical traits would be stored as vector data in a patch structure. The location of the patch memory is contained in one of the indices of a pointer vector in a higher level site structure. Where, that site structure would also contain arrays that also describe the biophysical traits of those patches. An example of model code for the linked list and structured arrays are shown below.

```
cpoly => first_polygon
do while(associated(cpoly))

   csite => cpoly%first_site
   do while(associated(csite))

      cpatch => cpatch%oldest_patch
      do while(associated(cpatch))

         ccohort => cpatch%tallest_cohort
         do while(associated(ccohort))

            print*,"HERE IS AN EXAMPLE OF LISTING THE TEMPERATURE"
            print*,"OF VEGETATION IN ALL COHORTS IN THE MODEL STATE"

            print*,ccohort%veg_temp

            !or

            print*,cpoly%csite%cpatch%ccohort%veg_temp


            ccohort => ccohort%younger
         enddo
         cpatch => cpatch%younger
      end do
      csite => csite%next_site
   end do
   cpoly => cpoly%next_polygon
end do
```

Figure 3-5: An excerpt of legacy code traversing the state variable hierarchy.

```
do ipy = 1,cgrid%npolygons

   cpoly => cgrid%polygon(ipy)
   do isi = 1,cpoly%nsites

      csite => cpoly%site(isi)
      do ipa = 1,csite%npatches

         cpatch => csite%patch(ipa)
         do ico = 1,cpatch%ncohorts

            print*,"HERE IS AN EXAMPLE OF LISTING THE TEMPERATURE"
            print*,"OF VEGETATION IN ALL COHORTS IN THE MODEL STATE"

            print*,cpatch%veg_temp(ico)

            !or

            print*,cgrid%polygon(ipy)%site(isi)%patch(ipa)%veg_temp(ico)

         enddo
      enddo
   enddo
enddo
```

Figure 3-6: An excerpt of the new code using structured arrays traversing the state variable hierarchy.

**Hierarchical Data Format 5 (HDF5) Model Output** *Previous Condition:* EDM previously used text files to store all input and output data, including structure and composition of forests, climate and biophysical information. *Motivation:* Text formated input and output files are not compressed and take up far more space than compressed data. Text based input and output is the slowest form of reading and writing data to storage. The EDM model also has a vast set of variables that combine to completely describe the state of the model at any given time. Writing a file that completely describes the model state would be far too cumbersome to implement using text based I/O. This made restarting the model exactly as it left off impossible. *Change:* A registry was added to all global variables which described the variable type, dimensionality, size and which kinds of files they should be written to. All requisite input and output datasets were converted to use HDF5 which is compressed, allows meta-data tagging, and allows for parallel writing and reading of irregularly shaped variable arrays called "hyper-slabs".

**Overhaul of the Model Parallelization** *Previous Condition:* The linked-list memory structure and text-based input and output played an influential role in how the EDM2 model was originally parallelized. *Changes:* The fact that memory and file writing was fundamentally changed in EDM2 necessitated a re-working of parallelization via the message passing interface (MPI) protocols. File input and output has also been re-worked to allow reading and writing to the a file shared by multiple tasks distributed over multiple machines. One of the benefits of the new design is that the tasks (different computers working in parallel) operate without a master coordinating them and distributing information. They read and write to jointly accessible datasets independently, and thus reduce latency by eliminating the bulk of network message passing.

It is difficult to quantify the benefits of the general software overhaul that started the change of the EDM model from version 2.0 to 2.1. Much of the benefits are related to functionality. A user now has much greater control over the model output. The model can now be stopped and restarted. Periodic testing has shown that model restarts

have reproducibility at extremely high precision (nearly binary reproducibility). The vectorization of model memory indeed improved model run-time performance. In short, the model looks completely different from a software perspective.

When the memory structure was being migrated from linked-lists to structured arrays, both types existed in the same model environment for a short period of time. This was done to ensure that the new structured array memory types generated the same results as the linked lists. Another benefit was that a profile on performance was created. The gprof profiling tool identifies and sorts the computation time is dedicated to each subroutine, as well as how many times each subroutine is called. Figure 3-7 shows this information as percentage of model runtime. Note that subroutines that use the structured arrays have the suffix "ar" (denoting use of arrays). Understand also that this profile was assessed extremely early in the development of structured arrays, and does not reflect the overall performance or usability improvements.

```
Each sample counts as 0.01 seconds.
  %   cumulative   self              self     total
 time   seconds   seconds    calls   s/call   s/call  name
 15.36     85.00    85.00 1236239813     0.00     0.00  quad4ci_
 10.81    144.00    59.00 39549868     0.00     0.00  inc_rk4_patch_
  9.52    197.51    52.71 58215821     0.00     0.00  zbrent_c3_
  6.18    231.73    34.23  9809678     0.00     0.00  leaftw_derivs_
  5.92    264.50    32.77  9816111     0.00     0.00  leaftw_derivs_ar_
  4.70    290.52    26.02  9816111     0.00     0.00  canopy_derivs_two_ar_
  4.64    316.18    25.67 39576328     0.00     0.00  inc_rk4_patch_ar_
  4.63    341.82    25.64 1178023992     0.00     0.00  residual_c3_
  3.09    358.94    17.13  9809678     0.00     0.00  canopy_derivs_two_
  3.09    376.04    17.10 15478909     0.00     0.00  copy_rk4_patch_ar_
  2.99    392.60    16.56 15470246     0.00     0.00  copy_rk4_patch_
  2.66    407.33    14.73 333047093     0.00     0.00  rslf_
  2.49    421.09    13.76  1182600     0.00     0.00  canopy_photosynthesis_ar_
  2.30    433.82    12.74  1182600     0.00     0.00  canopy_photosynthesis_
  1.57    442.52     8.70 1236239812     0.00     0.00  aflux_c3_
  1.03    448.22     5.71 65639774     0.00     0.00  zbrak_c3_
  0.72    452.21     3.99  1182600     0.00     0.00  __lsm_driver__initp2modelp
  0.67    455.90     3.69 280194953     0.00     0.00  qwtk_
  0.66    459.53     3.63                              malloc
  0.63    463.03     3.51 1236239812     0.00     0.00  csc_c3_
  0.63    466.51     3.48  1182600     0.00     0.00  __rk4_driver_ar__initp2modelp_ar
  0.62    469.97     3.46 51935280     0.00     0.00  lphysiol_full_
  0.62    473.39     3.42  9914854     0.00     0.00  __rk4_stepper_ar__lsm_sanity_check_ar
  0.60    476.72     3.33  9907950     0.00     0.00  __lsm_integ_rk__lsm_sanity_check
  0.57    479.89     3.17                              free
  0.54    482.87     2.98    96148     0.00     0.00  sw_twostream_clump_
  0.53    485.78     2.91 51935280     0.00     0.00  prep_lphys_solution_
  0.46    488.34     2.56 21990989     0.00     0.00  ed_stars_
  0.46    490.87     2.54  1182600     0.00     0.00  soil_respiration_ar_
  0.44    493.33     2.46   384592     0.00     0.00  mprove_
  0.41    495.60     2.27 207741120     0.00     0.00  arrhenius_
  0.41    497.85     2.25  1182600     0.00     0.00  copy_patch_init_
  0.39    500.01     2.17 12647178     0.00     0.00  redistribute_snow_
  0.38    502.14     2.13 21991403     0.00     0.00  ed_grndvap_
  0.38    504.26     2.12  1042496     0.00     0.00  banbks_
  0.38    506.34     2.08 65639774     0.00     0.00  solve_open_case_c3_
```

Figure 3-7: A profile of EDM subroutine calls early in the development phase of structured array memory handling. The profile was created using gprof during a prototype, single site EDM simulation. This model build contained both linked lists and structured arrays simultaneously. Subroutines using structured arrays have suffix "ar".

### 3.5.3 Mass Based Leaf Internal Energy

In earlier formulations of EDM, the extensive heat capacity of vegetation biomass, $C_{vb}$, was calculated as a function of the cohort's leaf area index, $LAI_c$, weighted fraction of the patch leaf area, $LAI_p$, canopy height, $h_c$, minimum allowable height, $h_{min}$, and a reference heat capacity of vegetation, $c_{ref}$. The reference heat capacity of vegetation was 3000. Patch leaf area is the cohort sum leaf area of all cohorts in the patch.

$$C_{vb}(old) = c_{ref} max(h, h_{min}) \frac{\text{LAI}}{\sum \text{LAI}} \tag{3.5}$$

The previous formulation is empirically based and useful because the distribution of heat capacities are typically an order of magnitude higher than those that are calculated based on mass and tissue densities. Higher heat capacities were thought to promote stable integration because the temperature fluctuations would be dampened. However it was physically inconsistent because the amount of vegetation in the plant community $\sum$ LAI influenced the heat capacity of individual plants (this has no physical basis).

The current formulation bases the extensive heat capacity of plant tissue directly on carbon and water content. Leaf biomass is a constant scale of leaf carbon, using a biomass multiplier $C2B$ (which is typically around 2). It uses literature derived estimates of specific heat capacity of dry green leaf biomass, $c_{dgl}$, and a constant multiplier for water to dry biomass in the leaf tissue $B2W$. It also assumes that the interstitial water inside the leaf tissue does not freeze and that the internal energy of the interstitial water scales linearly with temperature as a function of liquid water heat capacity, $c_{liq}$. For $n_p$ plants with $b_l$ biomass each:

$$C_{vb}(new) = n_p b_l \text{C2B}(c_{dgl} + \text{B2W}c_l)) \tag{3.6}$$

Values for the specific heat capacity of dry green leaf biomass and the biomass to water multiplier were retrieved from Gu and co-authors [Gu *et al.*, 2007]. They used a similar method as the one proposed above, incorporating the specific heat capacity of dry green leaf biomass from [Jones, 1992].

To get a sense of how the leaf heat capacity between the old method and the new

method differed, a generic tropical forest was generated with EDM and the distributions of leaf heat capacities were compared. The generic forests were generated by running the ED2.1 model over several decades of climate representative of Manaus, Brazil. The forest was started with seedlings and grew to an early successional tree canopy. In one case, the leaf heat capacities for the forest follow the legacy formulation (see Figure 3-8). In the other case, the leaf heat capacities use the mass-based approach (see Figure 3-9). The plots order the heat capacities of the vegetation cohorts and mark the 10th, 20th and 30th percentiles.

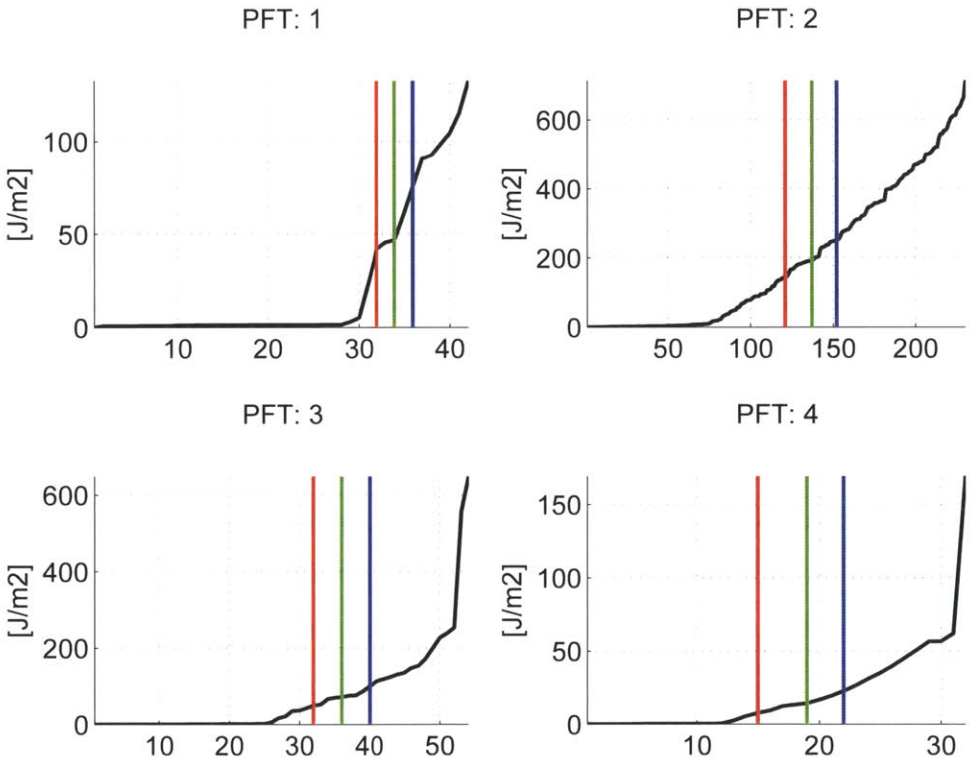


Figure 3-8: Legacy Formulation: Extensive heat capacities for the cohorts of the four tropical plant functional types (1=C4 grass, 2=early successional, 3=mid successional, 4=late successional) in a generic early successional forest. The x-axis is the ordinate of the cohorts, sorted by increasing heat capacity. The red line marks the ordinate of the cohort that is the 10th percentile for leaf biomass, the green line is the 20th percentile and the blue line is the 30th percentile.

For the same forest, the mass based heat capacities are statistically lower than the legacy formulation. Heat capacity directly affects the dynamic range of internal energy

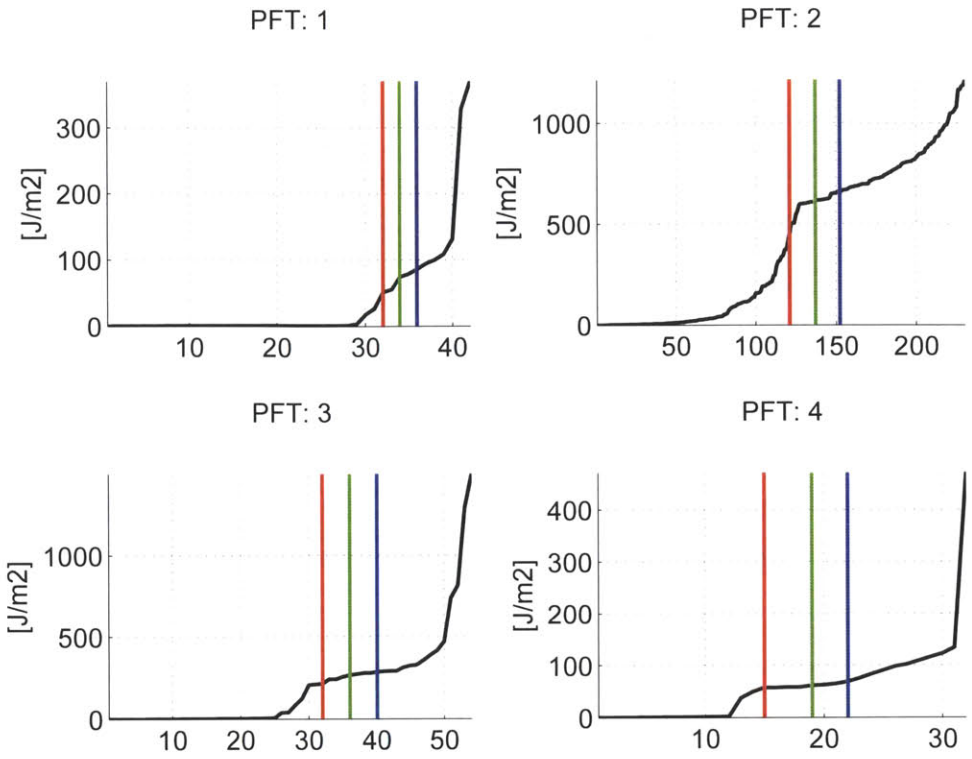


Figure 3-9: Mass Based Formulation: Extensive heat capacities for the cohorts of the four tropical plant functional types (1=C4 grass, 2=early successional, 3=mid successional, 4=late successional) in a generic early successional forest. The x-axis is the ordinate of the cohorts, sorted by increasing heat capacity. The red line marks the ordinate of the cohort that is the 10th percentile for leaf biomass, the green line is the 20th percentile and the blue line is the 30th percentile.

and vegetation temperature per unit heating. The mass based approach has indeed shown relatively greater dynamic ranges in temperature since its implementation. The modification has had a profound influence on inter-canopy heat exchange and the plant photosynthesis process. Further, when the mass based heat capacity was implemented, it was necessary to remove an arbitrary upper bound on the leaf-level bulk aerodynamic resistance. The upper bound was originally included in the model to keep the turbulent transfer of heat high in plants with disproportionately large thermal inertia. When the physically based scheme was introduced, this artificial (and indefensible) bound was removed.

### 3.5.4 Canopy Turbulence

The modeling of turbulence inside the vegetation canopy is crucial for estimating the exchange rates of sensible and latent heat between the soil, leaves and canopy air. For instance if the aerodynamic resistance estimated at the soil surface is relatively small, less of the soil moisture will exit via evaporation as opposed to runoff, inter-flow or drainage. Originally the ED model used eddy diffusivity (gradient theory) and simple linear scaling relationships to estimate the aerodynamic resistance on the leaves and soil. Ultimately, the aerodynamic resistance at the surface had a monotonic relationship with canopy height, which is a drastic over-simplification and makes little sense. According to the existing formulation, taller canopies ended up stimulating larger eddies and therefore smaller resistance at the soil surface. But in the old growth forests of the Amazon, tall forest canopies are closed (tree crowns are interwoven and have no separation), are dense with drag elements and as a result have very still winds at the surface.

A complete discussion on this topic is covered in Appendix F, including a full treatment of the mathematical relationships involved. After a period of review, a new scheme was implemented following methods of Massman and Weil [Massman and Weil, 1999] and Sauer and Norman [Sauer and Norman, 1995]. Again, this method is described in detail in Appendix F.

The purpose of adapting the methods of Massman, Weil, Norman and Sauer was to reproduce phenomenon that made sense. For a given above canopy wind-speed and vertical temperature gradient (which effects stability), there are some reasonable expectations: a closed tall canopy that is dense with drag elements is going to have very little turbulence at the forest floor, grass lands on the other hand would have more turbulence immediately at the soil surface because of the decrease in drag elements and higher surface wind-speeds, then again an open canopy with sparse tree crowns may serve to increase vertical transport at the surface due to increased shear.

The method adapting the works of Massman, Wier, Norman and Sauer is compared to the original method using a variety of typical forest structures. The canopies were

created using local climate forcing from Manaus Brazil, they represent a selection of canopy compositions likely to be found in the area. Three turbulence schemes are compared:

- (EXP) Method one assumes an exponential wind speed decay inside the canopy where surface conductance is solved by integrating the inverse diffusivity profile from the surface to the canopy top. It is assumed that diffusivity scales vertically in proportion to wind-speed. The displacement height and roughness length scale proportionally on canopy height. This is the original EDM2.0 formulation.

- (M97) Method two uses method of Massman 1997 [Massman, 1997] drag density approach of scaling in-canopy wind speed, and parameterizing the displacement height, roughness length and friction velocity. Surface conductance is estimated in the default way similar to method one, the integration of inverse diffusivity.

- (M99) Method three uses the Massman 97 drag density approach of scaling wind-speed and determining friction velocity. It also uses the Massman and Weil method of estimating surface turbulent intensity in conjunction with Sauer and Norman's approach to surface resistance/conductance.

Visualizations of the profiles are provided in Figures 3-10,3-11 and 3-12. These profiles were generated using unit wind speeds and a neutral potential temperature stratification. Three different model canopies are investigated. Canopy one has a high LAI in a relatively continuous intact canopy at 30 meters with rare emergents. Canopy two is a very diffuse canopy of tall trees with low LAI, it would resemble and open parkland. The third canopy is a grassland. It is again recommended to the reader to refer to Appendix F for background on terms. In the lower right panels of Figures 3-10, 3-11 and 3-12 are estimates of ground conductance. This term encapsulates the turbulence transport at the ground surface.

The M97/M99 methods estimate a higher displacement height than the exponential case. This is due to the center of pressure in more realistic canopies being closer to the canopy top (where all the leaves are), imposing a smaller eddy penetration into the

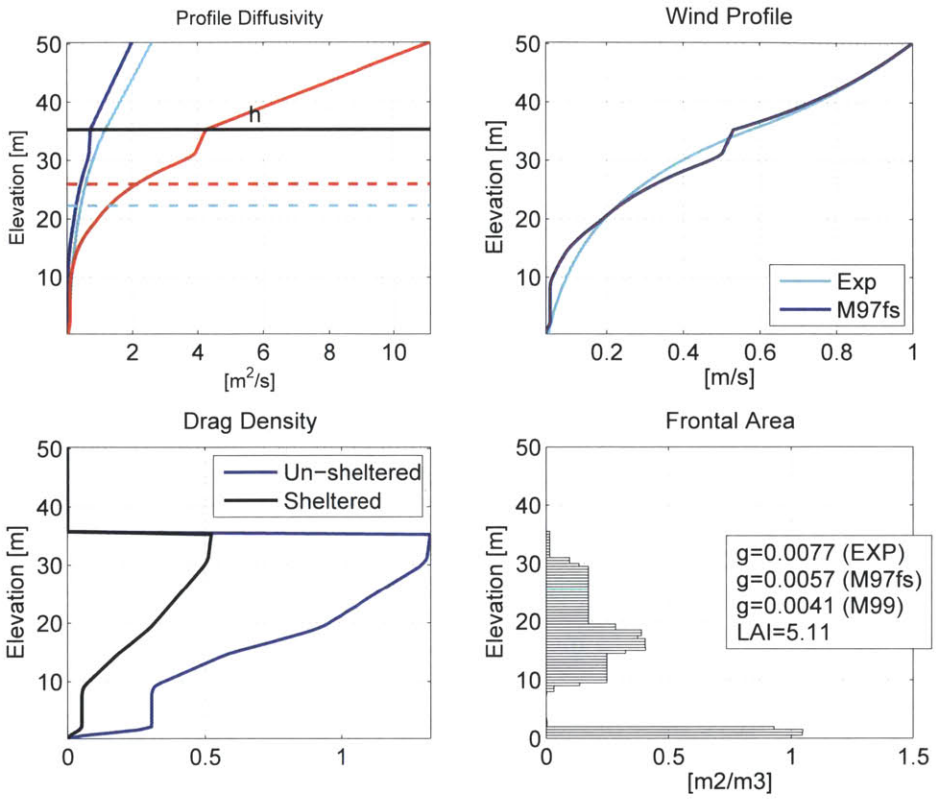


Figure 3-10: Generic ED2.1 model representation of a *CLOSED CANOPY* ecosystem. Upper left panel: Diffusivity profiles for the three methods. The red solid line (unlabeled) represents M99. The dashed horizontal lines indicate displacement height. Upper right panel: In canopy wind profiles. Lower left panel: Drag density profiles, which is frontal area times fluid drag and optional sheltering factor. Lower right panel: Profile of frontal area of the canopy drag elements, and ground conductance $g$.

canopy. This results in a smaller friction velocity (shear) in the constant shear layer above the canopy. Note that in all cases, the eddy diffusivity attenuates rapidly inside the canopy. In the M97 case, eddy diffusivity is generally less than the exponential case due to the decreased friction velocity at the canopy top. The eddy diffusivity in the M99 case is not relevant as that model uses second order model mechanics. The value that is shown is simply derived from its in-canopy wind-speed profile just for reference. For neutral thermal stratification and unit wind speeds, the exponential case conducts scalar transport from the ground surface to the canopy at the highest rate, see

$g_{EXP} = 0.0077[m/s]$, $g_{M97} = 0.0057[m/s]$ and $g_{M99} = 0.0041[m/s]$.

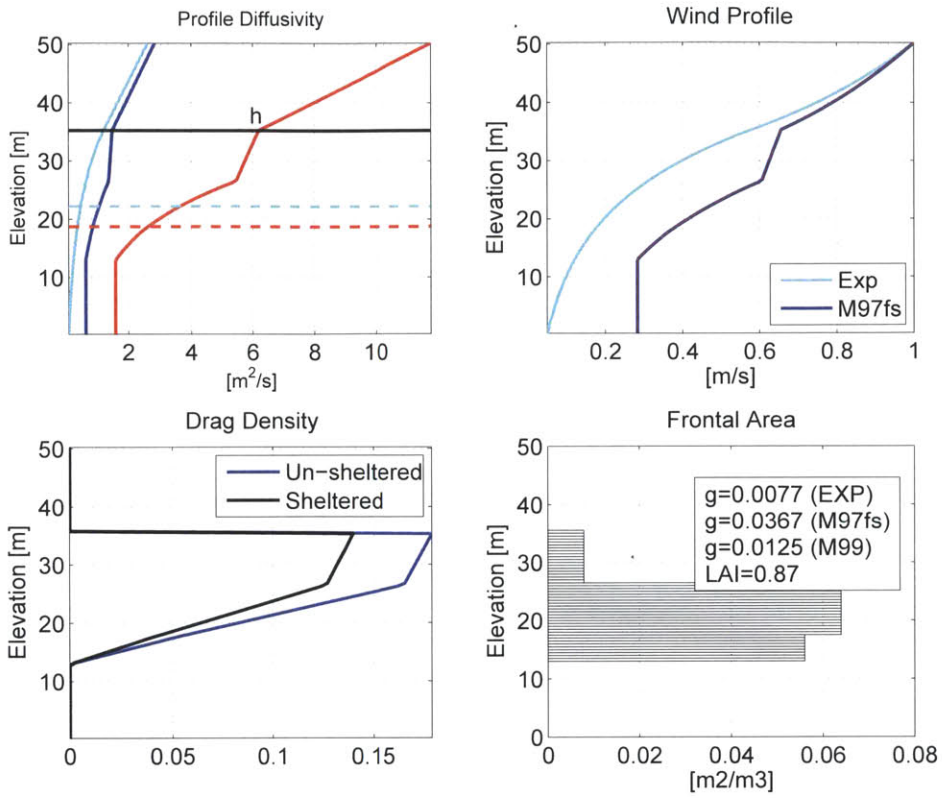


Figure 3-11: Same as 3-10, for an *OPEN DIFFUSE CANOPY*.

The diffuse canopy highlights the most distinct deficiency of the exponential scheme. Conductance, wind speed and shear are exactly the same as in the closed canopy case, because the parameterization is governed by the height of the canopy alone. Open canopies have greater variability and have more diffuse foliage elements imposing drag on the dynamic sub-layer. It would seem logical that this would promote larger penetrating eddy structures and maintain relatively high wind-speeds at the surface. This is captured in the Massman approaches, evidenced by enhanced surface conductance.

In the grassland case, wind speeds decay quickly and generate less shear in the sub-layer. The M97 method estimates a very large conductance in response to high in-canopy velocity and above canopy shear. However, it estimates that there would be

even more turbulent transport than open tree canopies (which have large and diffuse drag elements, see canopy 2). The M99 second order scheme does however estimate a slight decrease in conductance compared to the open canopy, while still estimating greater conductance than the closed canopy.

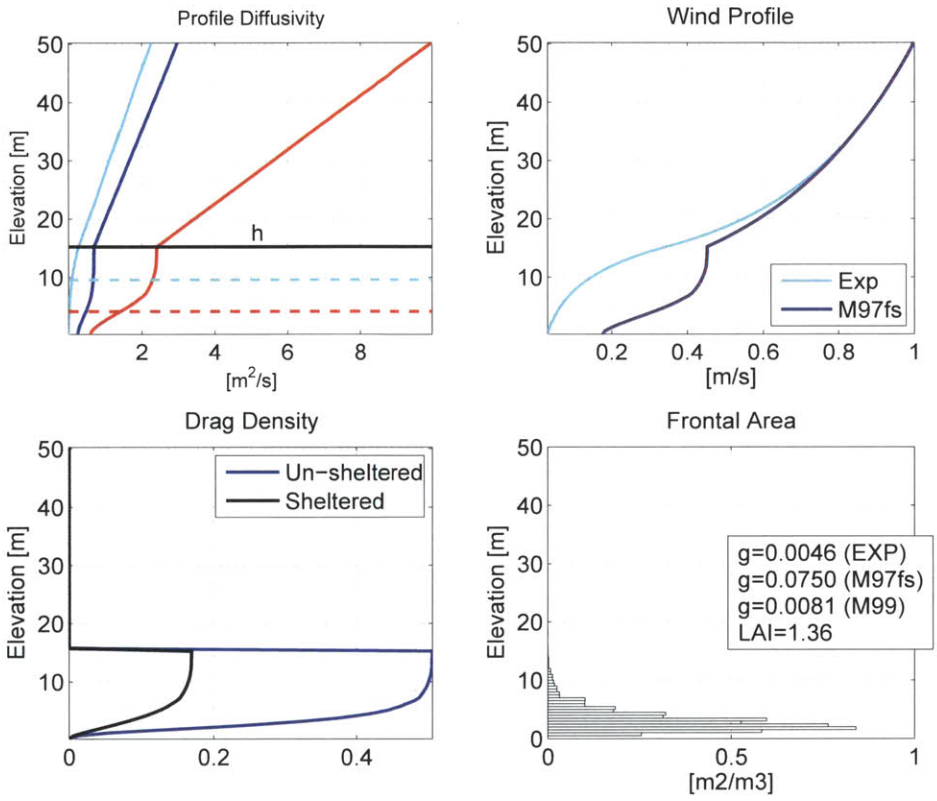


Figure 3-12: Same as 3-10 and 3-11, for a *GRASS CANOPY*.

### 3.5.5 Enthalpy Conservation and Flux

The work on re-designing enthalpy flux and conservation was motivated by a need for a more rigorous accounting. It was questioned if energy flux between different mediums was being resolved correctly. For example, the amount of energy lost by a leaf and gained by the canopy air during evaporation should be different depending on how warm the leaf and leaf water was at the time of phase change. EDM was not making this distinction. The process of water transport from liquid root uptake to canopy vapor was also inconsistent. The enthalpy in that liquid water should be removed from the soil matrix, and that sum energy should be deposited into the canopy air with some extra energy donated by the leaf tissue when the water changes phase. However, this simple addition and subtraction of energy was impossible because moist soil energy (internal energy in Joules) and moist canopy air energy used different variables (the energy of the air had been described by temperature and then virtual potential temperature at various phases of development).

The issues were addressed with a re-design of the conservative variables (enthalpy) that were consistent across across soil, vegetation, moist air and surface water (if present). The details and the derivation of this method is covered in Appendix C. The benefits of the new method are several fold. Firstly, the developers are now convinced that enthalpy is conserved across the soil-air-vegetation interfaces. In the old model it was only conserved within the land-surface model as a whole. Moreover, we are exactly aware of approximations that are made and understand the tradeoffs. For instance the specific heat capacity of liquid and vaporous water does change with temperature, but this change is inordinately small and can be safely ignored. It assured that there were no continuous biases involved in the energy of phase change. The process of liquid root water uptake transporting to the canopy air is now physically consistent. Again, the reader is referred to Appendix C for a thorough explanation of the system of enthalpy conservation.

### 3.5.6 Hybrid Forward Euler and Implicit BDF2 Numerical Integration

EDM2.1 has traditionally used the 4th Order Runga Kutta, Heun and forward Euler numerical techniques for integrating canopy biophysics. Each of these techniques has its advantages. The RK4 technique can assess step errors and adjust step length dynamically to meet an acceptable error threshold. The Euler driver is the simpler approach and therefore the quickest. Each has their draw-backs. The RK4 scheme requires multiple re-calculations of the model state derivatives at each time-step. It also has more numerically cumbersome error checking machinery which guides step size to provide accurate results. The Euler scheme is by definition unstable and has no way to assess errors or correct instabilities. The Heun style integrator makes a compromise somewhere between these two.

An implicit solution would seek to solve a forward model state by assuming that its relationship with the current state is some linear function whose slope is governed by the derivative at the future step. An implicit solution is attractive because it is inherently stable. An implicit Euler step would not guarantee small integration error, but it is very likely that numerical truncation errors associated with integration are smaller than the uncertainty already inherent in the calculation of the derivative. However, implicit numerical integration requires a linear system of equations relating the derivative of the state variables to themselves. The transport of soil moisture and heat for instance, is a second order derivative and is not readily adapted by an implicit solution. A hybrid of an implicit and explicit numerical integration bypasses this problem. It is briefly discussed here, and is explained in more detail in Appendix H.

In the hybrid method, a forward Euler step for all biophysical variables is completed first. After this, vegetation and canopy air temperatures are re-calculated using an implicit step. The implicit step uses some of the forward-time variables as boundary conditions for the implicit step on leaf and air temperature. The implicit step chosen here, the BDF2 (backwards trapezoidal), also uses the leaf and canopy temperatures of the previous time-step. The BDF2 uses the change of the state from previous time to

current time to weight its calculation of the change from current time to future time. The general form of the BDF2 step, for a vector of state variable $Y$ at current step $n$ is as follows:

$$\frac{Y_{n+1} - Y_n}{\Delta t} + \frac{1}{2}\frac{Y_{n+1} - 2Y_n + Y_{n-1}}{\Delta t} \approx \frac{\partial Y}{\partial t}, t(n+1) \tag{3.7}$$

The hybrid method has been tested and complies with mass and enthalpy conservation. Generally, when compared to the RK4 integration, the hybrid solver tends to estimate lower peak values of most biophysical variables. This was expected and is typical of inherently stable integration schemes. This may also be a result of including the previous-to-current derivative in the forward step solution. An example of these differences is provided in Figure 3-13.

The hybrid scheme also benefits from a strangely sparse matrix inversion. In this specific case, only the top row, the left column and the diagonal of the matrix are non-zero. This allows for a Gaussian elimination procedure which can be completed with only two *un-nested* loops across the vegetation cohorts. This is extremely efficient for a matrix inversion, which for general cases requires nested looping over its edge dimension. In terms of computational efficiency and model performance, the hybrid integration scheme performs faster than the RK4 scheme. Tests have shown that hybrid integration can increase the speed of model time-stepping upwards of 3-5 times as fast. In cases where the hybrid integration is taking very conservative step sizes, improvements in speed have been no less than 1.5 times faster.

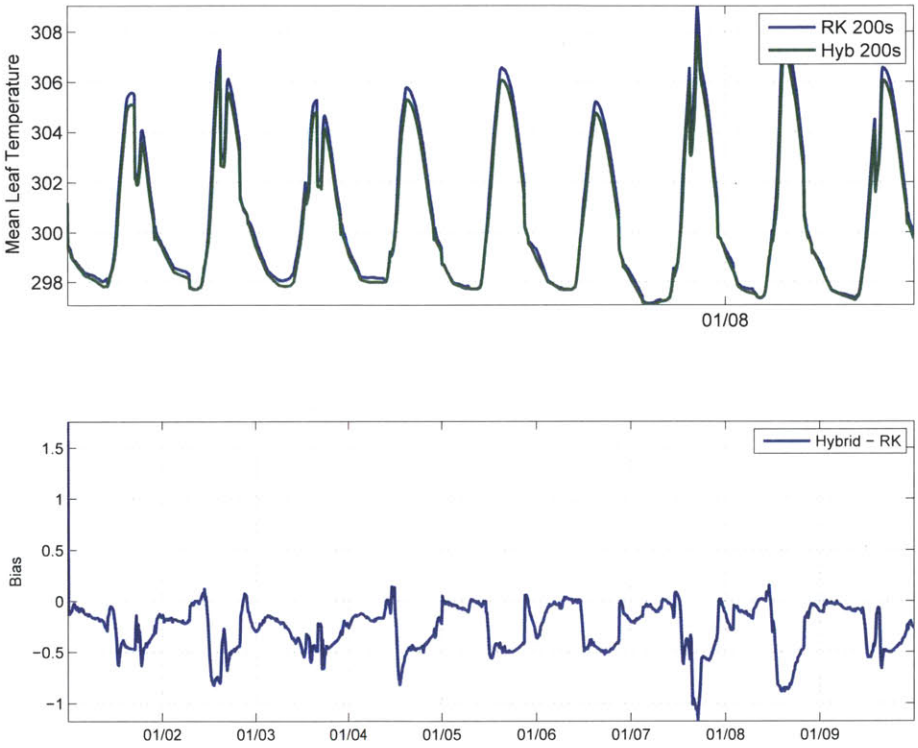


Figure 3-13: Comparison of patch average leaf temperature time series for Hybrid and RK4 solvers in a 28 year old forest site in and around Manaus.

# Chapter 4

# Model Boundary Conditions

The coupled simulations proposed in this thesis are performed on a limited area grid, utilizing numerical integration. Initial and boundary conditions are required to solve the dynamic systems of equations during run time.

The ultimate goal of this thesis research is to perform coupled simulations between the atmosphere and two different demographic conditions of the land-surface: a land-surface that reflects the actual present day ecosystem composition and one that reflects a demography where there is no human land-use in South America. The first will be referred to as the "actual" vegetation case or "AV"; the later will be referred to as the "potential" vegetation case or "PV".

The creation of both of these initial conditions is very similar, utilizing a "spin-up" process. The spin-up process is an off-line EDM simulation (no coupled atmosphere), where the vegetation demography is initialized with an equal assortment of plant seedlings. The off-line model is integrated over a period of several hundred years using a best-guess estimate of the historical regional climate. During spin-up the vegetation goes through the natural processes of growth, competition for resources, mortality and disturbance. The plant communities evolve to where their distribution of the size and type reaches a steady state.

The two initial conditions have slightly different adaptations of the spin-up process. The *Potential* condition assumes there is no human land-use, however it does assume that the vegetation evolved to the present day with a modern atmospheric carbon diox-

ide concentration. The *Actual* initial condition requires that external data on human land-use is collected and used to manually influence the fractional areas of land dedicated to crop or pasture. *The initial conditions were spun-up on the Odyssey Computer system at Harvard University by collaborators Marcos Longo and Abby Swann.* Here is the general flow of the process:

- Initialize an array of EDM polygons in South America with the "bare-ground" condition.
- Integrate the simulation for a maximum of 508 years or until steady-state is reached. Loop climate data and impose atmospheric carbon dioxide concentration of 378 ppm.
- Save the final model output as the "Potential" ecosystem condition.
- Continue the simulation using the "Potential" dataset as an initial condition, integrating over the period 1900 through 2008. Atmospheric carbon dioxide is maintained at 378 ppm. Apply human land conversion.

The land-conversion process is covered in Section 4.2. An assessment of the "AV" initial condition dataset is covered in Section 4.3. The creation and selection of the climate data are discussed in more detail below.

## 4.1 Climate Driver Data for EDM2 Spin-Up

The regional vegetation spin-up depends on the choice of model parameters, physics modules, soil textural information and the atmospheric climate data driving the model. There are some challenges in generating an accurate and spatially distributed historical record of climate. As one looks further back in time, data become more sparse, lack observations with modern instruments and lose modern standards of (accuracy) validation and uncertainty assessment. The choice was made to use modern (past several decades) climate as a proxy of historical (past several centuries) climate. It is argued

that while modern climate data will not reflect the tendencies of long-term climate variation, recycling modern data ensures that the vegetation is exposed to variables that have a more realistic covariance. Reanalysis model output can provide all of the necessary climatological information to the ED2 spin-up process and is a natural choice.

Prior to 2006, there were two high-quality and globally-distributed reanalysis products available: the European Centre for Medium Range Weather Forecasting's (ECMWF) 40 Year Re-Analysis (ERA-40) [Uppala and co authors, 2005] and the joint product by the National Center for Environmental Prediction and National Center for Atmospheric Research's NCEP/NCAR Global Reanalysis Product (NCEP-R1) [Kalnay and co authors, 1996]. Both datasets cover roughly the last several decades and assimilate similar observations such as radiosondes and the visible and infrared radiances from geostationary satellites. Aside from differences in model physics, the ERA-40 makes more use of SSM/I passive microwave observations of atmospheric water. Both datasets are available in the same 6-hour temporal resolution, time stamps fall on 0, 6, 12 and 18 UTC. The NCEP-R1 model output was available on a re-projected $2.5^o$ equal-angle grid. The ERA-40 dataset was taken from its native T106 model resolution Gaussian grid. The approximate resolution is $1.125^o$ at the equator, decreasing towards the poles.

In 2006 [Sheffield *et al.*, 2006] created a dataset for the purpose of driving long-term regional land-surface models. This product is archived under the University Corporation for Atmospheric Research dataset identification DS314. The DS314 is based on the NCEP-R1 and maintains the same global and decadal coverage period but has made bias corrections according to other composite datasets. Figure 4-1 is provided here from the original paper by Sheffield and co-authors to detail the sources they used to bias correct the NCEP-R1. Data fields concurrent with the time period of the observations are actively bias corrected; previous data fields are statistically bias corrected[1].

The DS314 assimilates those observations that are ideal for validating its accuracy.

[1]All original datasets for this study are from the Research Data Archive (RDA) which is maintained by the Computational and Information Systems Laboratory (CISL) at the National Center for Atmospheric Research (NCAR). NCAR is sponsored by the National Science Foundation (NSF). The original NCEP/NCAR R1 data are available from the RDA (http://dss.ucar.edu) in dataset number ds090.0. The original ERA-40 data are available from the RDA (http://dss.ucar.edu) in dataset number ds124.2. The original Sheffield/DS314 data are available from the RDA (http://dss.ucar.edu) in dataset number ds314.0.

TABLE 1. Summary of datasets used in the construction of the forcing dataset. The temporal resolutions given here are those used in this study but original data may be available at finer temporal resolutions. Variables are precipitation ($P$), surface air temperature ($T$), downward shortwave radiation (SW), downward longwave radiation (LW), surface air pressure (Ps), specific humidity ($q$), wind speed ($w$), and cloud cover (Cld).

| Dataset | Variables | Temporal coverage | Spatial coverage | Source |
|---|---|---|---|---|
| NCEP–NCAR reanalysis | $P$, $T$, SW, LW, $q$, Ps, $w$ | 1948–present, 6 hourly | Global, ~2.0° × 2.0° | Kalnay et al. (1996) |
| CRU TS2.0 | $P$, $T$, Cld | 1901–2000, monthly | Global land excluding Antarctica, 0.5° × 0.5° | MCJHN |
| GPCP | $P$ | 1997–present, daily | Global, 1.0° × 1.0° | Huffman et al. (2001) |
| TRMM | $P$ | Feb 2002–present, 3 hourly | 50°S–50°N, 0.25° × 0.25° | Huffman et al. (2003) |
| NASA Langley SRB | LW, SW | 1983–95, monthly | Global, 1.0° lat × 1.0°–120° lon | Stackhouse et al. (2004) |

Figure 4-1: Excerpt from Sheffield and co-authors [Sheffield *et al.*, 2006].

It is therefore implicitly understood that DS314 has a lower error bias than its native NCEP and ERA-40 products, however bias corrections can produce spurious results such as unnatural patterning and degraded covariance between datasets. It was important to evaluate the three datasets with these considerations.

### 4.1.1 Precipitation Inter-comparison

The three products generally agree on the major spatial features of annual precipitation (see Figure 4-2). The largest volumes of annual precipitation occur in the northwestern Amazon, the tropical Atlantic and pockets among the mountainous regions in Colombia and Panama. Modest yearly precipitation is found over the South American Convergence Zone (SACZ, see Chapter 1). All models also show increased rainfall in the South American Low Level Jet which borders the Andean Altiplano at the southwestern headwaters. There are striking differences in how this feature is resolved. The NCEP-R1 product shows large levels of precipitation apparently falling on the mountains themselves, but the ERA-40 precipitation adjoins but does not cover the Altiplano. NCEP-R1 estimates a strong depression in precipitation in the southwestern headwaters, whereas ERA-40 does not. The presence of dense tropical rainforests suggest that in reality this depression is not as severe as NCEP estimates. The relatively high estimate of NCEP precipitation on the Altiplano is likely due to a combination of the product's coarse resolution and perhaps the orographic lifting of moist air currents. The DS314 shows stronger agreement with the yearly rainfall patterns of the ERA-40 in the southwestern Amazon. All datasets exhibit a dry region in eastern Brazil and north of the Brazilian state of Roriama. The ERA-40 estimates that this precipitation is distinctly smaller than the other two. ERA-40 estimates a precipitation maximum in northeastern Brazil that adjoins the precipitation minimum on the eastern peninsula. This rainfall feature appears to be somewhat out of place, as evident from TRMM annual estimates in Figure 4-3.

The ERA40 data extended through August of 2002, while the TRMM satellite did not take orbit until late 1997. This period of overlap is small, so only the NCEP and DS314 are compared with the data of the TRMM 3B43. It is evident from the spatial covariance of rainfall in Figure 4-1 that DS314 obviously places high confidence in the TRMM 3B43 dataset.

The DS314 shows much smoother spatial rainfall gradients as well, placing greatest yearly precipitation roughly in the northwestern basin. It also shows less change in the

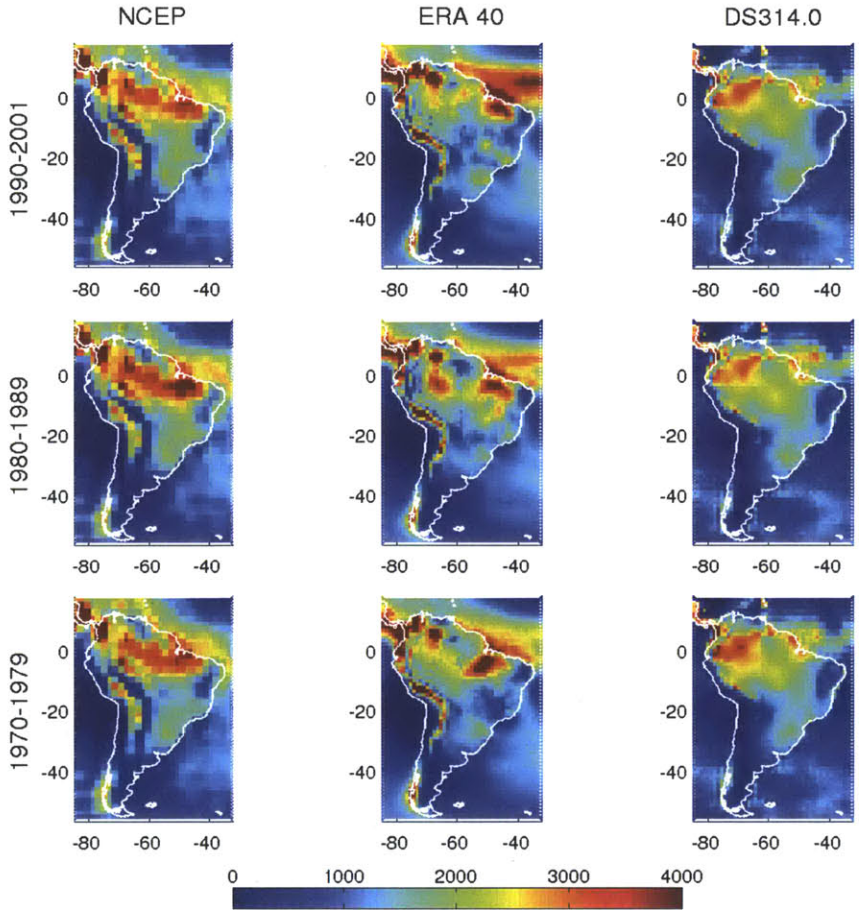


Figure 4-2: Inter-comparison of mean yearly precipitation from the three reanalysis products over three decades.

spatial patterning of decade mean rainfall compared to the two Reanalysis products. Inter-annual and inter-decadal variability in rainfall could be an important factor in the successional dynamics of the the regional ecosystems.

The three reanalysis products were also evaluated within regions of space with different climate and weather regimes. A map of these zones is provided in Figure 4-4, and a contour map of the ground surface elevation is provided to give spatial context. The agricultural belt in the southern Amazon basin and the transitional ecotones moving to the southeast is represented by zone 4. Much of the "Arc of Deforestation" can be found

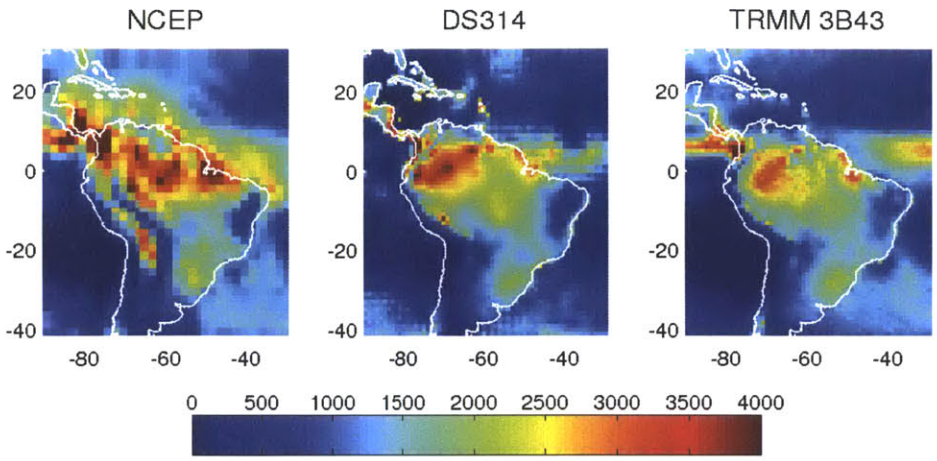


Figure 4-3: Evaluation of the NCEP and DS314 mean yearly precipitation as compared with the TRMM 3B43 product. Yearly means are calculated over the temporal intersection of the three datasets, 1997-2007. ERA40 was omitted due to weak temporal overlap at the time of this analysis (ERA40 was later extended from 2002 to 2007).

in this zone. The climate of zone 4 is strongly dependent on the circulating air masses coming in from the northern and western regions, represented by Zones 1 and 2. The fifth zone is meant to reflect locations close to the two largest Brazilian cities Sao Paulo and Rio De Janeiro. Zone 3 comprises the bulk of the central and eastern Amazon.

The inter-decadal variability of zone-mean precipitation is generally consistent across datasets (see Figure 4-5). It has been questioned whether the use of mean TRMM spatial rainfall to extrapolate bias corrections of previous years may have corrupted DS314 inter-decadal variability, but this is not the case. Modest differences in variability and a mean bias do exist between datasets. The question is: how much does inter-annual precipitation variability effect the development of forest composition and structure, and therefore what types of effects would the deficiencies of these datasets in capturing this variability (if it exists) have on modeled structure and composition? Greater variability in total daily or monthly precipitation could promote increased drought based disturbance. This would affect not only the total biomass development history but also the competition among species. Drought tolerant plant types rely on drought as a competi-

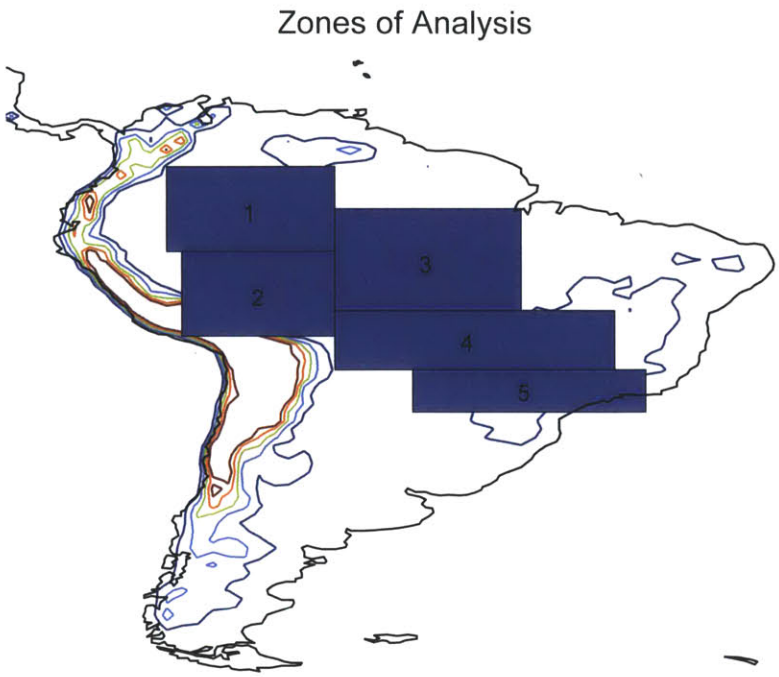


Figure 4-4: Zones of mean areal analysis.

tive advantage to emerge in significant numbers, while opportunists are equally dependant on disturbance to gain footholds. The greatest difference between the three is the relative over-estimation of the NCEP precipitation in the central-eastern and northwestern Amazon.

In all but the northwestern region, the three datasets show strong agreement in the timing of the peak wet and dry seasons (see Figure 4-6). In central-eastern Amazonia, the DS314 dataset estimates a greater total inter-seasonal variability (while agreeing on timing). In the northwest, the NCEP product diverges from the other two regarding the timing of peak rainfall. The three datasets show the strongest similarities over the region covering the South American Convergence Zone which features the transition between tropical evergreen forests and mixed-grasslands. Ecosystem structure and composition in transition regions is sensitive to the inter-seasonal timing and magnitude of precipitation, hence the similarities between the three regarding seasonal timing is

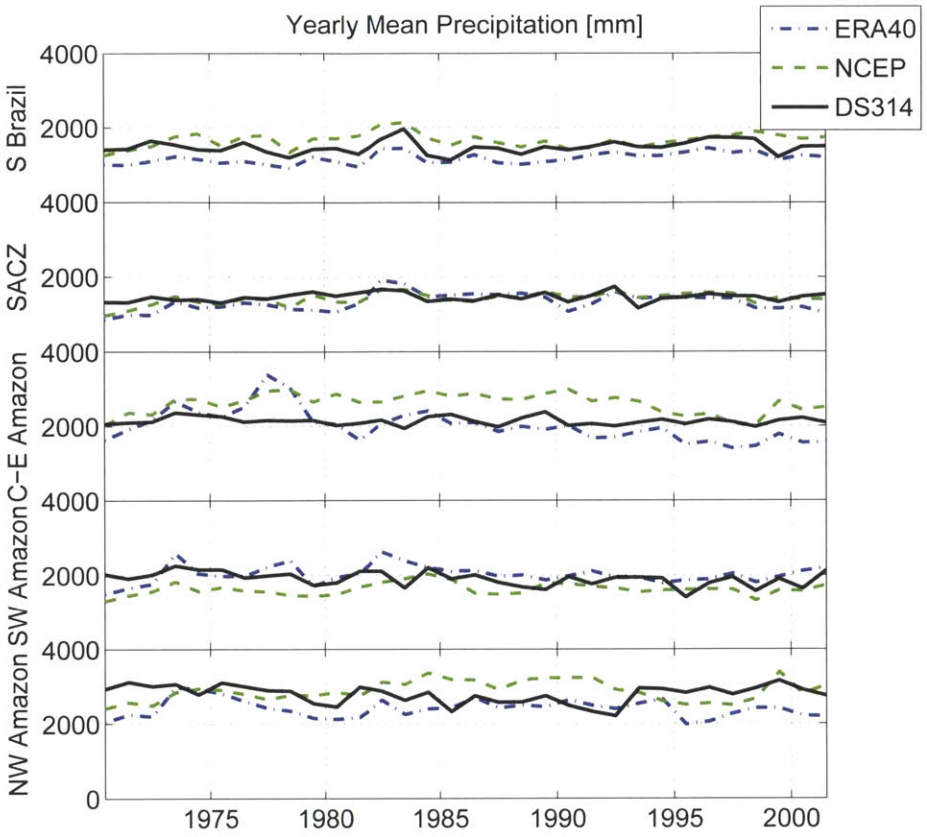


Figure 4-5: Spatial mean yearly precipitation for the five zones.

reassuring.

The monthly mean precipitation collected at a group of gauging stations is provided in Figure 4-8. This can be compared with the seasonal means of the datasets referenced in Figure 4-6. A map of their locations, and the time of peak seasonal rainfall is shown in the accompanying panel. Their data availability is provided (see Figure 4-7). The stations at Manaus and Santarem suggest that peak rainfall in the Central Amazon occurs later, toward March and April. The DS314 estimates a peak near February while the other datasets estimate a flatter peak with equal precipitation from December through March. The stations at Jaru and Fazenda show stronger agreement with the analysis, confirming that precipitation does indeed tend to peak at the turn of the year in southern Amazonia.

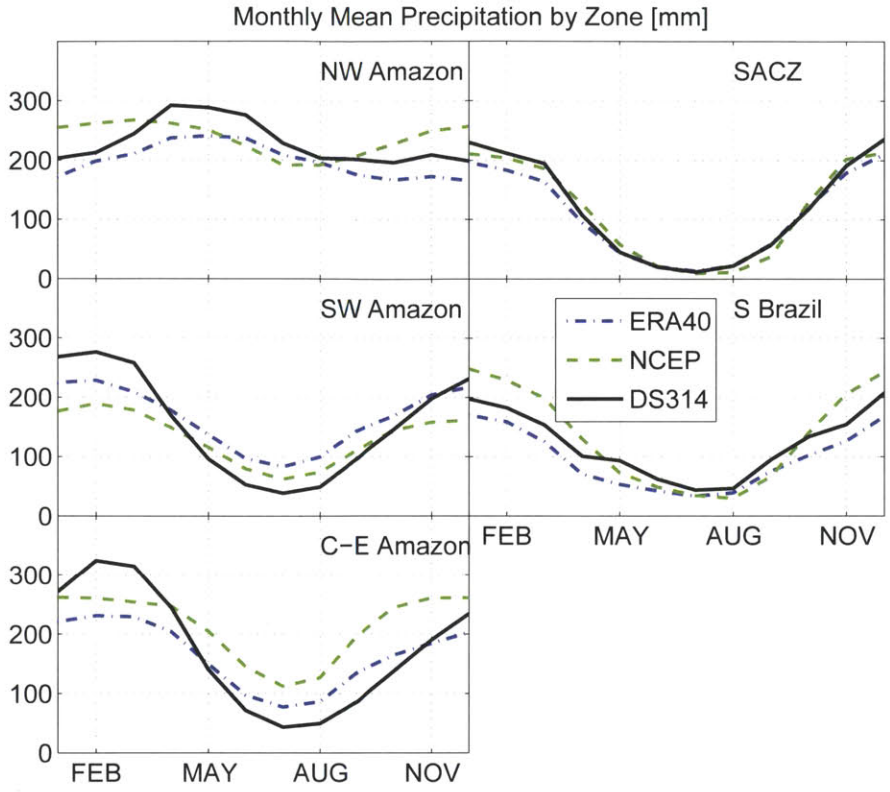


Figure 4-6: Spatial mean monthly precipitation for the five zones. Monthly precipitation is averaged from 1970 through 1999.

The spatial, annual and seasonal comparisons of the three precipitation datasets suggested that DS314 did not show any spurious results or data abnormalities. Further, it generated spatial and seasonal characteristics comparable to observations while not sacrificing inter-decadal variability. Moreover, the spatial features of rainfall, in context of the geography and the climate regime, is very reasonable. In summary, the DS314 rainfall provides a compelling option to drive a regional ecosystem spin-up process.

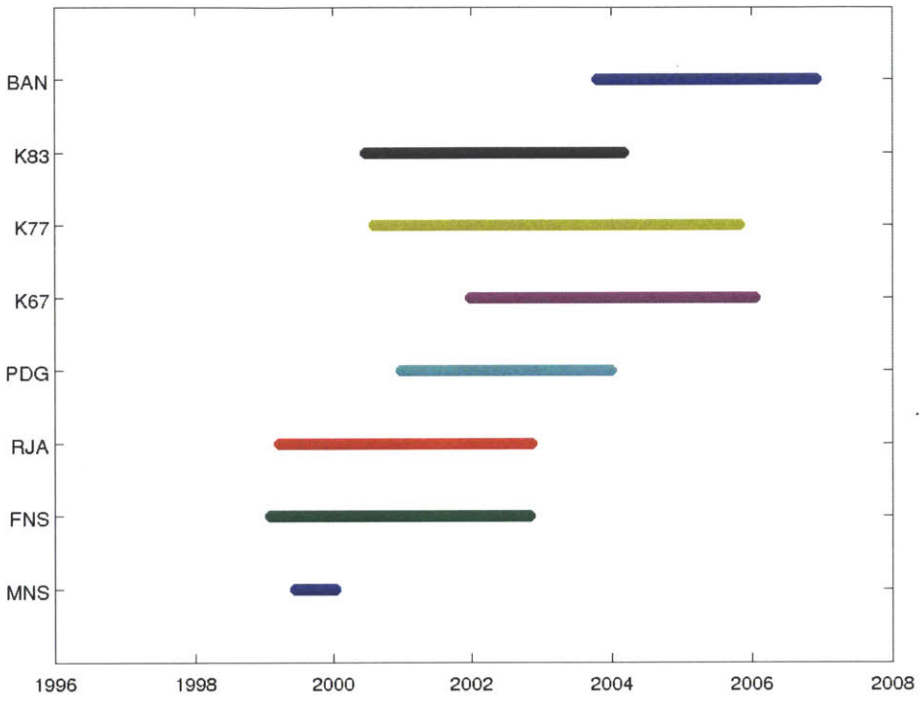


Figure 4-7: Periods of data availability for various tipping bucket rain gauging stations.

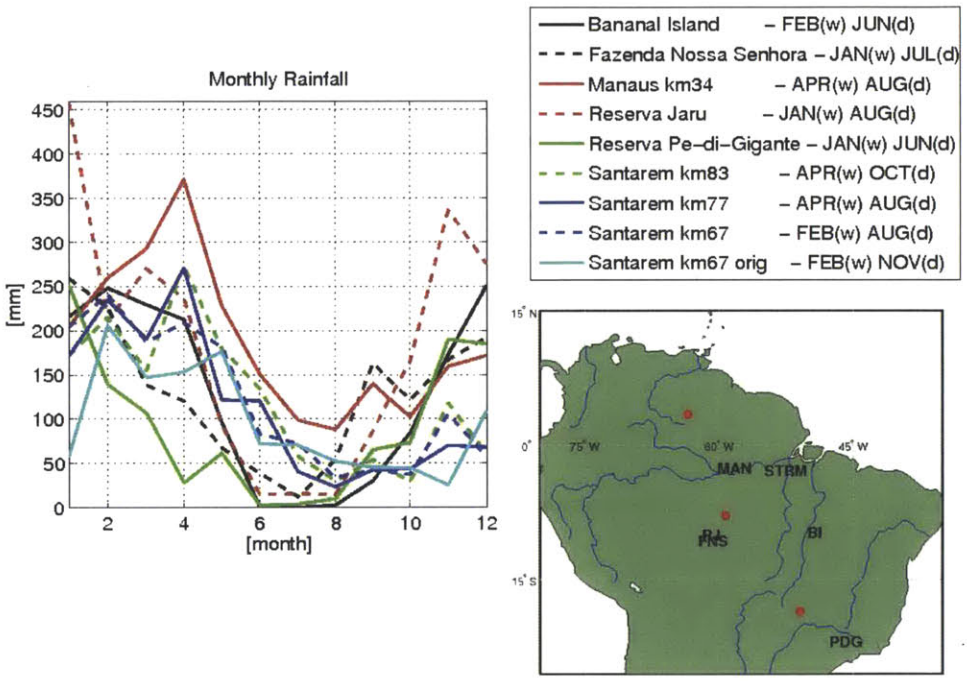


Figure 4-8: Monthly mean precipitation accumulations at measurement stations. Measurement stations were active over variable time periods between 1998 and 2005. A regional maps shows the locations of the stations, using abbreviations.

### 4.1.2 A Simple Precipitation Downscaling Technique

Precipitation in the Amazon is dominated by convective processes. The areal footprint of convective precipitation events is controlled by the scale of the cloud, which can have length scales of a few kilometers or less in the case of isolated convective events. Reanalysis models operate at resolutions far too large to capture this spatial variability or the dynamical processes of convective updrafts and downdrafts. Large scale models use techniques such as moisture convergence analysis and microwave radiance assimilation to improve their estimate of spatial mean integrated precipitation, however spatial and temporal averages over a large pixel reduces the intensity of rainfall over time and space.

The physical processes that govern the distribution of mass and flux at the land-surface are highly rainfall rate dependent. For instance, high intensity rainfall is more likely to overflow leaf holding surfaces and reach the canopy under-story. This is the danger of using grid scale precipitation on physically based ecological models: the lack of high rainfall rates influences canopy throughfall. The same argument applies to soil surface infiltration. This problem was encountered in the EDM2 model during the spin-up process as most of the Amazon basin appeared to over-estimate total latent heat flux and underestimate the amount of throughfall available to the root-zone.

Naturally, rainfall statistics vary in time and space. Key rainfall statistics are 1) distributions of rainfall intensity, 2) time between storms, 3) storm duration and 4) the fraction of time in which rainfall is occurring at a location of interest, i.e., precipitation fraction ($\mu$). Eltahir and Bras [1993] suggest that precipitation fraction can be derived from rain gauges, where the fraction $\mu$ of precipitation $P_l$ can be approximated by dividing the expectancy of precipitation by the density of precipitation $\rho$. In this case, precipitation $P_l$ is the local (point) precipitation reported by a rain gauge.

$$\mu = \frac{E[P_l]}{\rho} \tag{4.1}$$

The density of precipitation is the integrated precipitation intensity occurring only during times when rain is falling, whereas the precipitation expectancy includes times

of no rain. Density is calculated by summing all precipitation and dividing through by the sum of times rain was falling $t$ over all $N$ instances of time $i$.

$$\rho = \frac{\sum_{i=1}^{N} P_l(i)}{\sum_{i=1}^{N} a(i)}, \text{ where } a(i) = \begin{cases} 1 & \text{if } P_l(i) > 0, \\ 0 & \text{if } P_l(i) = 0 \end{cases} \tag{4.2}$$

This indicates the fraction of time that rain is falling at a point. Making the assumption that that the rainfall characteristics are uniform in space, this fraction can also be interpreted as the mean fractional area of the rainfall footprint over the window of time the fraction was calculated.

Gridded models can only resolve part of the total rainfall fraction; this portion is denoted $\mu_G$. The remainder, which is a physical manifestation of sub-grid processed and thus un-resolved, is denoted $\mu_{SG}$. Their product describes the whole:

$$\mu = \mu_G \cdot \mu_{SG} \tag{4.3}$$

Lammering and I.Dwyer [2000] suggest that the distribution of local precipitation $P_l$ rates within an area represented by averaged rainfall $P_A$ is exponentially dependent on the rainfall fraction $\mu$.

$$f(P_l) = (\mu/P_A)exp(-\mu P_l/P_A) \tag{4.4}$$

If we are only interested in assessing this probability distribution during times when grid rainfall is non-zero, then we must first remove the grid component of the rainfall fraction from the total. We can rearrange Lammering and Dwyer's equation to utilize our gridded data:

$$f(P_l) = (\mu_{SG}/P_G)exp(-\mu_{SG} P_l/P_G) \tag{4.5}$$

With the estimated grid rainfall provided by the reanalysis model, a realization of rainfall with point-like statistical qualities can be formed by pseudo-randomly drawing rainfall rates from this distribution. This technique was applied to the rainfall volumes

of the re-analysis products at hourly sub-steps. The basic pseudo-code of the process goes as follows:

- A vector of one month of six-hourly gridded rainfall is selected from the reanalysis product. Each of these six-hourly estimates can alternately be called "blocks".
- The native gridded rainfall fraction $\mu_G$ is calculated for this vector. The total rainfall fraction $\mu$ is selected from a table based on the season, time of day and geo-position. The sub-grid rainfall fraction $\mu_{SG}$ is now readily calculated.
- The cumulative density function of point-like local rain rates $f(P_l)$ is calculated independently for each six hourly block of grid rainfall using the grid rainfall and its precipitation fraction.
- Depending on the temporal resolution on which point-like rainfall is desired, a series of sub-steps is iterated within the six-hour gridded rainfall block.
- For each sub-step: If the six-hour gridded rainfall integration of the block is zero, then the point-rainfall sub-step is zero. If the six-hour gridded rainfall integration of the block is non-zero, then local rainfall is selected from the CDF via a uniformly random process.
- At the end of the month, the total point scale rainfall is uniformly scaled so that the total rainfall depth is equivalent to the original grid scale rainfall.
- This process is inherently stochastic, therefore several realizations of the datasets must be made. Repeat this procedure for each realization.

To get a sense of the variability in rainfall fraction, point statistics were assessed at meteorological stations used in the LBA-ECO CD-32 LBA Model Inter-comparison Project (LBA-MIP) [de Goncalves *et al.*, NA]. There are two datasets for kilometer 67 at the Tapajos National Forest in Para. The first, denoted km67, comes from the LBA-MIP dataset and spans 2002-2004. The second, denoted km67+, spans 2002-2006 and was procured directly from Lucy Hutyra of Harvard University who, in collaboration

with her colleagues in the Wofsy Research group, compiled and measured the data at this station. Precipitation fractions for these stations, partitioned by season and time of day, are shown in Figure 4-9. A time of 13-18 GMT roughly corresponds with midday rainfall in the Amazon, while 0:6 GMT roughly corresponds with late evening rainfall. The results indicate that late afternoon rainfall has the highest detection fraction, with the exception of the Manaus tower, where early morning has the highest detection fraction. There is also confirmation that the dry season has lower rainfall fractions.

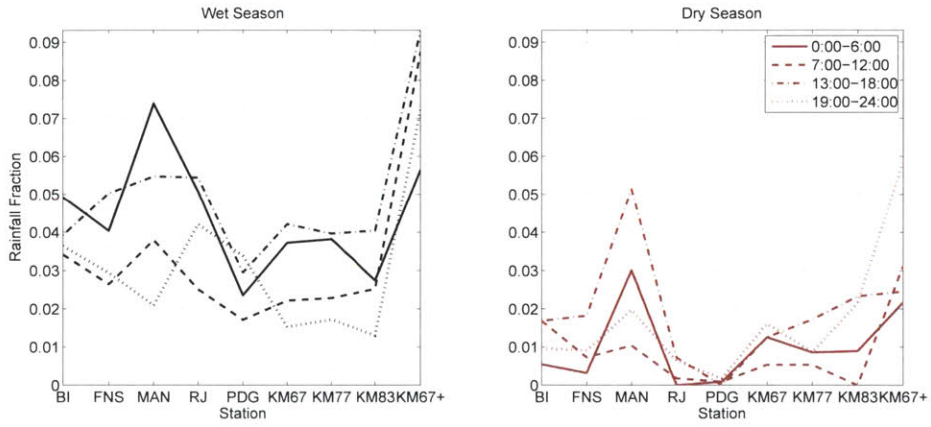


Figure 4-9: The precipitation fractions calculated at each station. The left panel is for wet season months while the right panel is for dry season months.

All stations had significant periods of missing data. Without convincing evidence that the missing data periods had no correlation with precipitation, the data was questioned as a good source for generating regional precipitation fractions. The task of spatially distributing the point data is no simple task either. While kriging is a viable methodology, synoptic and geographic structures have huge influences on spatial rainfall statistics and would be a significant undertaking. Therefore the precipitation fractions drawn from the Santarem kilometer 67 station, which benefited from the most continuous rainfall record, were used for the whole region.

A test of the downscaling procedure was conducted on the ERA40 gridded rainfall data over the km67 site near Santarem. The resulting distributions of rainfall intensity, inter-storm period and storm duration of the downscaled data were compared with the

gauge data and are shown in Figure 4-10. Note that the ERA40 is only available through the summer of 2002, yet the gauge data is available from 2002 through 2005, so they do not temporally overlap.

The distributions of intensity and inter-storm period show good agreement with the gauge data and the downscaled gridded precipitation data. It is clear from the distributions of intensities that the native gridded rainfall does not capture the dynamic range and variability associated with point rainfall. The downscaling significantly improves the distribution of rainfall intensities. The distribution of storm duration leaves the most to be desired. Because the downscaling procedure only utilizes information on the mean rain/no-rain time fraction, it contains no information regarding the distribution of the time between storms or storm length.

Alternative downscaling techniques that preserve spatial correlations of storms would have limited benefit to a land-surface model that is distributed only in the vertical direction. Despite the simplicity in the chosen method, the energy balance in the EDM2 model shows improved results when driven with downscaled precipitation. To test this, EDM2 biophysics were integrated through September of 1999 at a primary forest near Manaus Brazil. Two scenarios were compared: one simulation using the original grid precipitation and one using the downscaled precipitation. The model ecosystem was initialized using a spin-up procedure based on ERA40 data. The hourly flux variables of short wave radiation, net radiation, sensible heat flux and latent heat flux for both scenarios are compared with measurements made at an eddy flux tower over a primary forest (see Figure 4-11).

The downscaling procedure improves the Bowen ratio of the model and more closely matches observation. The latent heat flux associated with downscaled precipitation decreases, suggesting that a greater portion of rainfall was partitioned into throughfall and ultimately into runoff. The downscaling appears to have created the anticipated increase in canopy throughfall.

To get a better sense of how the downscaling affects the flux variables and moisture storage in and out of the soil column, a time series of model estimates is evaluated at two sites in the Brazilian Amazon at the approximate coordinates $20^oS$,$50^oW$ and

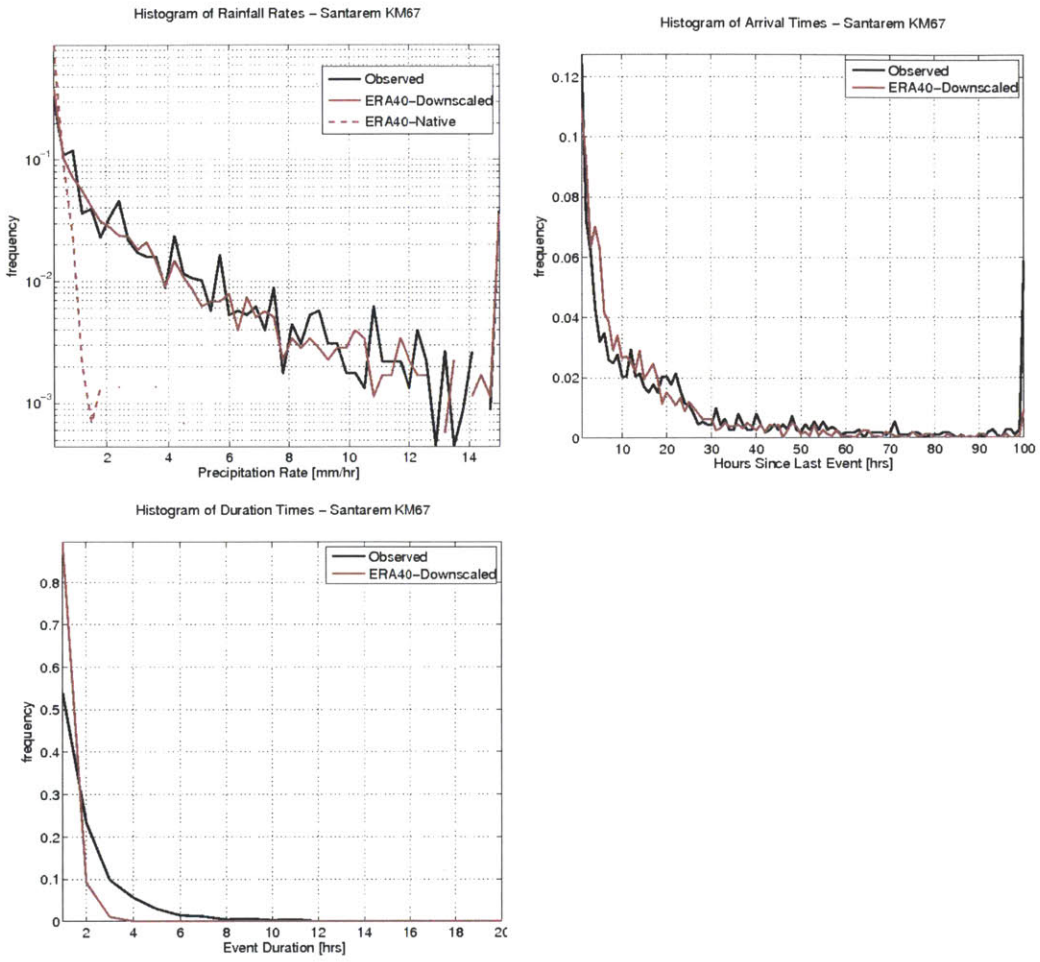


Figure 4-10: The distributions of precipitation intensity, inter-storm period (arrival time), precipitation duration and precipitation fraction. Statistics are calculated at km67 in the Tapajos National Forest Brazil. The ERA40 gridded rainfall is abstracted at the closest grid-cell to the station, of which is downscaled according to the gage statistics.

$3^oS$,$66^oW$ (see Figures 4-12 and 4-13).

The results suggest biophysical response is somewhat more complex than originally anticipated. In the southeastern Amazon (Figure 4-12), yearly precipitation at this site reached roughly 1500mm and flux was dominated by soil evaporation. Downscaling precipitation promoted the expected increase in soil evaporation and transpiration. It also promoted a decrease in base-flow (flux through the bottom of the soil column). It

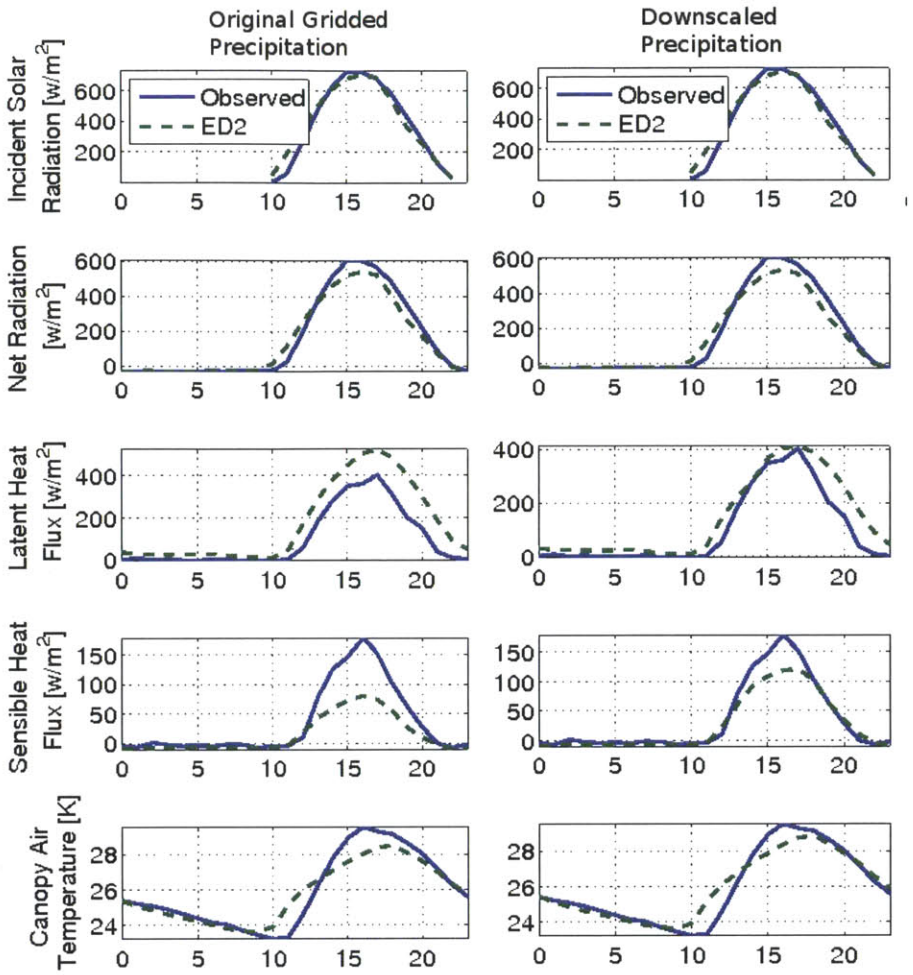


Figure 4-11: Site level surface fluxes at Manaus using gridded and downscaled precipitation drivers. Model data is compared with flux data from the km34 tower during September 1999.

is hypothesized that the leaf and soil surfaces experience less time at saturation with downscaling, promoting a dryer canopy air-space and enhancing transpiration via increased vapor pressure deficit. While more water infiltrates the soil column, proportionally more water is extracted from the root zone, thus decreasing base-flow.

At the northern site, leaf evaporation decreases while transpiration increases, but this time there is a decrease in soil evaporation. The high intensity pulse rain events moved larger quantities of water quickly through the column in the downscaled case,

thus increasing base flow. Although throughfall was still greater in the downscaled, the it appears that the timing of the pulses enabled a greater fraction of the water to percolate through the soil column, ultimately rendering dryer conditions in the top soil layers. This resulted in decreased soil evaporation rates.

A comparison of the regional yearly water balance for the two methods (downscaled vs. grid rainfall) tells a more comprehensive story. A prototype regional spin-up over 109 years was created using ERA40 downscaled data. At the 109th year, the regional model was integrated for one more year using both scenarios (downscaled and gridded precipitation). An increase in transpiration and a decrease in leaf evaporation is nearly ubiquitous for downscaled rainfall (see Figures 4-14 and 4-15). Downscaling promoted both increases and decreases in yearly soil evaporation. While the evidence suggests increased throughfall is ubiquitous with downscaling, this phenomena is likely a result of intense rainfall "pulsing". It appears that the decrease in soil evaporation at $19.64^{o}S$,$50.33^{o}W$ is not an isolated case. The rain pulsing leads to greater incidence of surface runoff and possibly greater vertical gradients in total moisture head.

A long-term comparison of the effect on vegetation indicated that downscaled precipitation promotes increased EDM 2.1 estimated biomass in the southern Amazon and the Cerrado/grassland transition regions on the Amazon's southern border (see Figure 4-16). It is premature to use these differences in biomass to motivate an argument that downscaled precipitation is better, but it does highlight its significance. The downscaling procedure undoubtedly improved the statistical nature of the point-rainfall statistics, as well as the energy and mass balance of the model.

The downscaling procedure demonstrated improvements to the statistical qualities of the precipitation, most significantly the distribution of precipitation intensity. The downscaling also showed significant effects on the partitioning of moisture in modeled vegetation canopies. Therefore, this downscaling technique was applied to the climate driver datasets used to fulfill the objectives of this thesis.

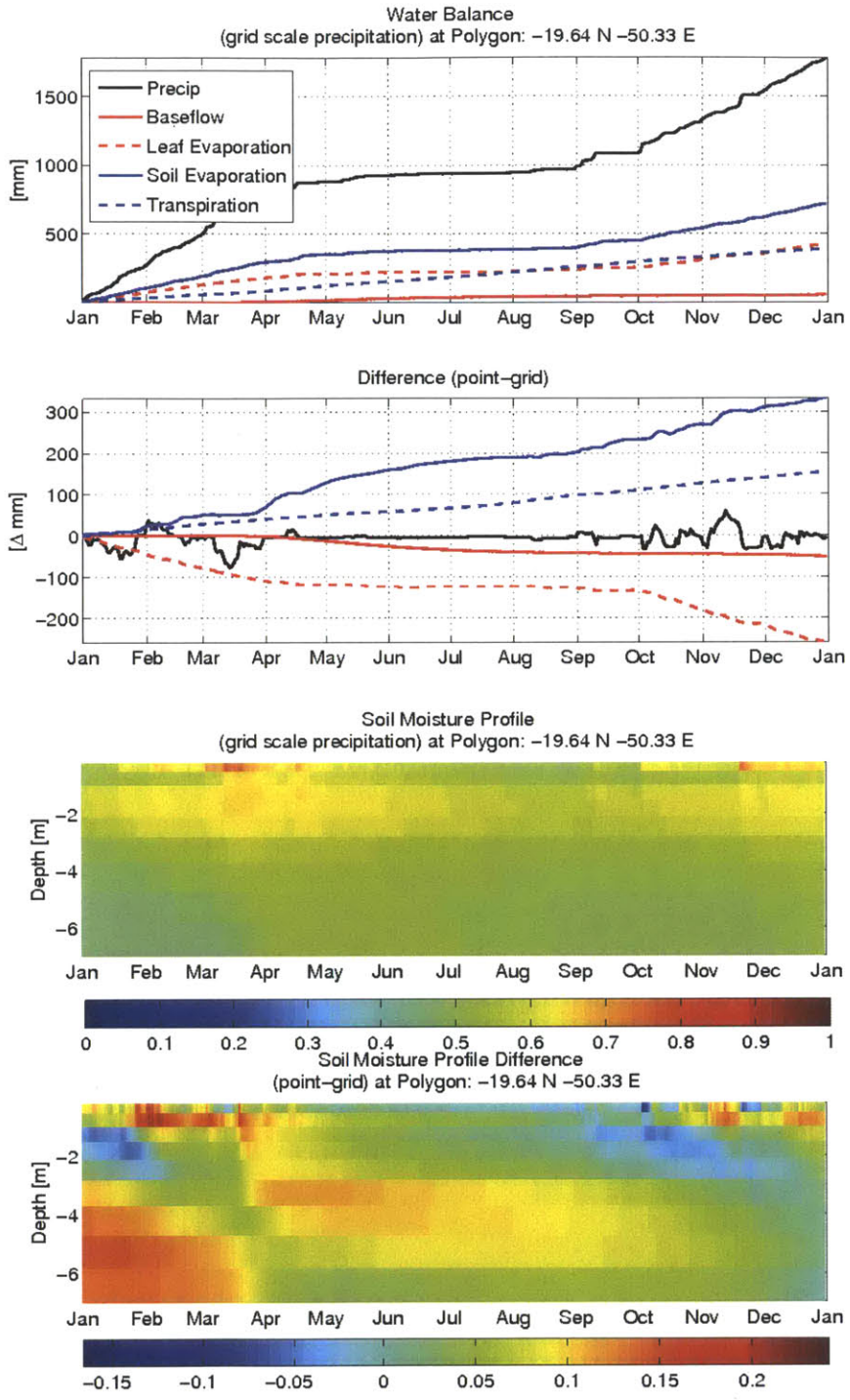


Figure 4-12: Comparison of EDM2 estimated yearly integrated water balance for down-scaled and grid precipitation in southeastern Amazonia, $19.64^oS$,$50.33^oW$.

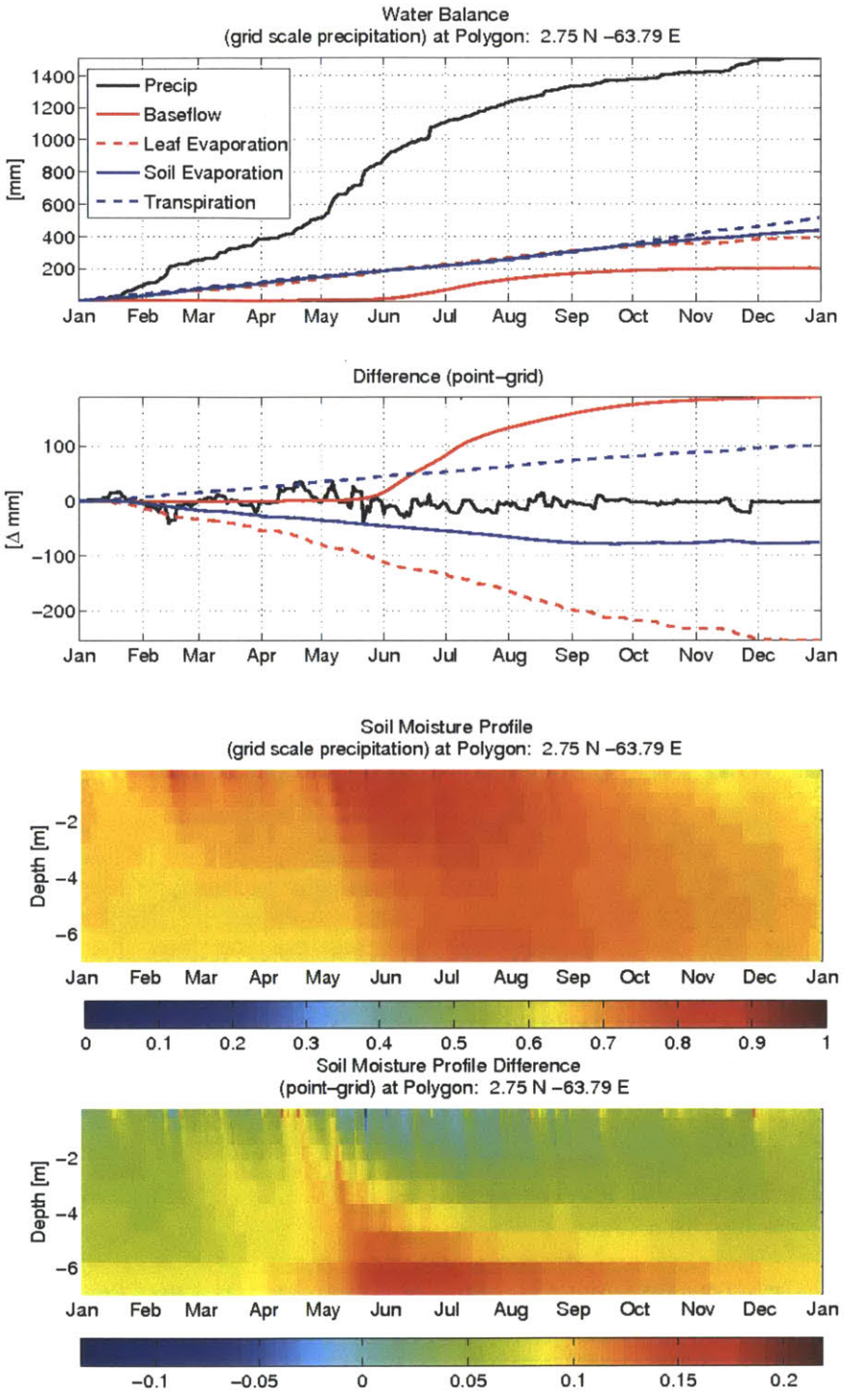


Figure 4-13: Comparison of EDM2 estimated yearly integrated water balance for downscaled and grid precipitation in northwestern Amazonia, $2.75^oS$,$65.79^oW$.

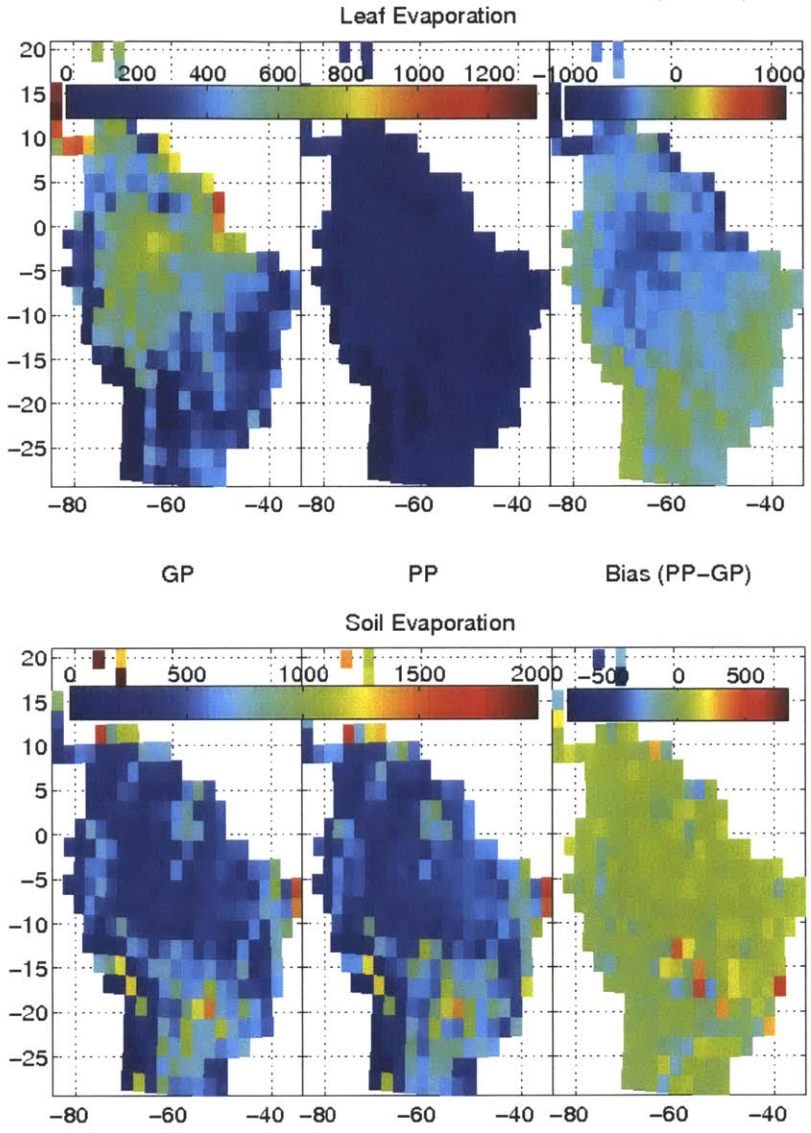


Figure 4-14: Regional maps of total annual leaf evaporation and soil surface evaporation for simulations driven with Grid Precipitation (GP) and downscaled Point-like Precipitation (PP). The total bias between the cases is provided.

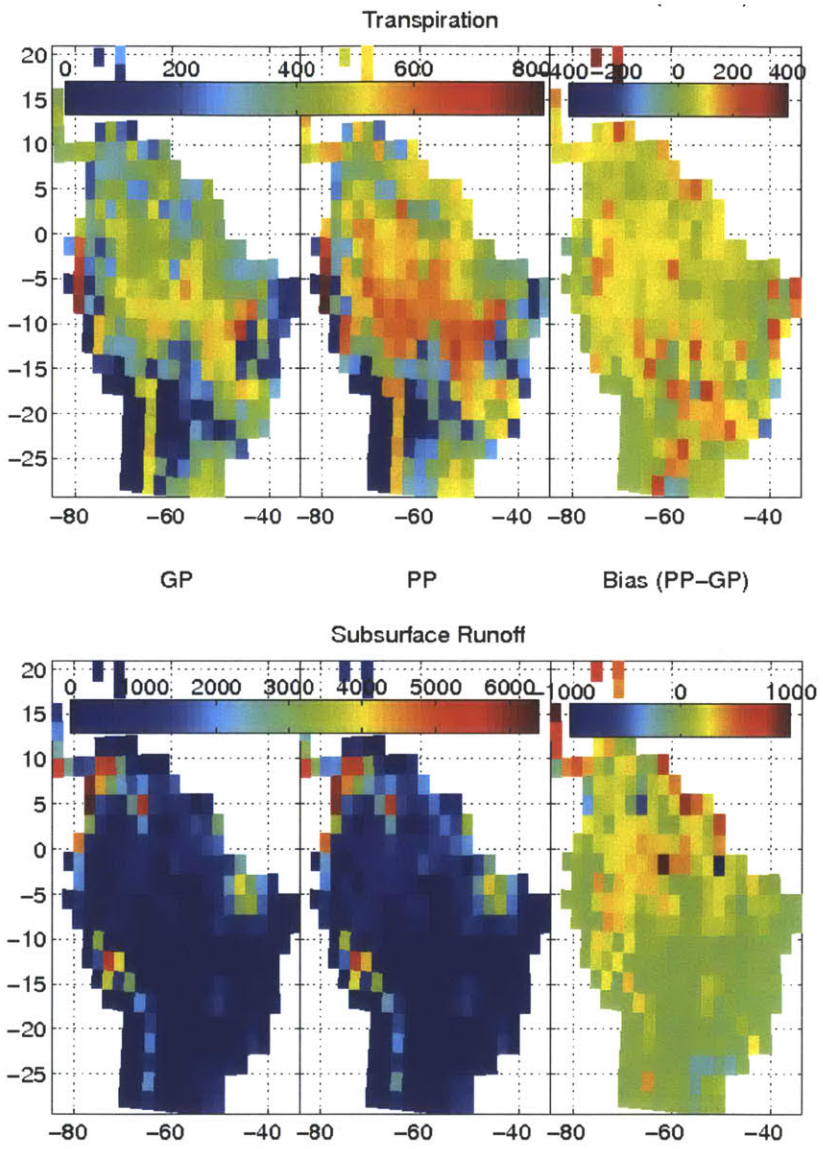


Figure 4-15: Regional maps of total annual transpiration and subsurface runoff for simulations driven with Grid Precipitation (GP) and downscaled Point-like Precipitation (PP). The total bias between the cases is provided.

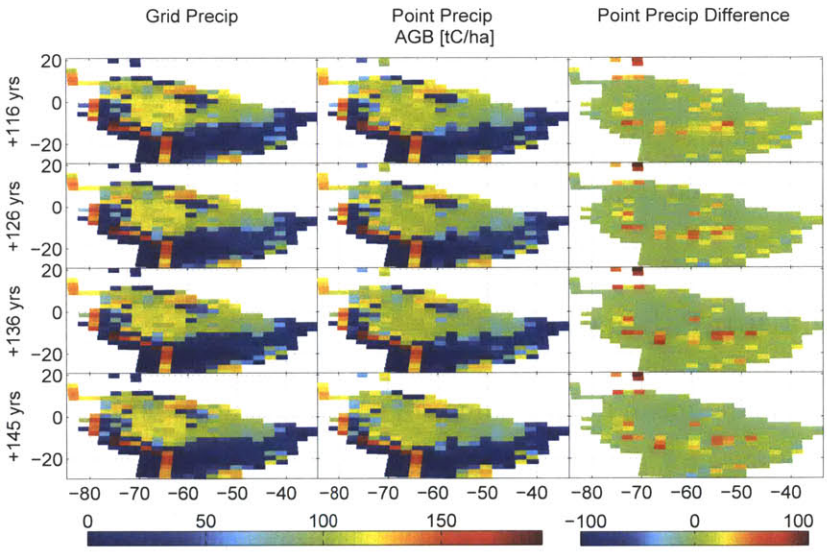


Figure 4-16: Regional map of EDM2 simulated total above ground biomass at different times. The vegetation in the left column was driven with ERA-40 climate data using native gridded rainfall, the center column vegetation was driven using ERA-40 climate data with downscaled precipitation. The right column shows the positive bias of agove ground biomass using the downscaled precipitation.

### 4.1.3 Radiation Inter-comparison

Ecosystem response, and consequently the vegetation initial conditions used in the coupled model experiments, are sensitive to the patterning of downwelling shortwave radiation. This is especially true in the Brazilian Amazon where pervasive overcast conditions (especially during the wet season) have been thought to promote a light limited growth condition [Hutyra *et al.*, 2007]. The ERA-40 and NCEP-R1 both utilize assimilation of ground and ocean synoptic observation data which includes measurements of surface solar radiation. Oldest records rely heavily on military and airport data. Of the three candidate reanalysis datasets, only the Sheffield product (DS314) actively assimilated a spatial radiation product, the NASA/GEWEX Surface Radiation Budget (SRB[2]) product (see [Pinker and Laszlo, 1992] and [Fu *et al.*, 1997]).

### 4.1.4 Radiation Patterning

Figure 4-17 shows the mean downwelling shortwave radiation for each product during the month of January for the years 1990-1999. The DS314 follows the spatial patterning of the SRB product very closely. While NCEP typically estimated a wetter climate than the ERA-40, it also estimates brighter conditions during the wet season month of January. There is agreement that each dataset features maximum radiation at roughly 30 south. The depression associated with the Amazon basin and the persistent cloud albedo generally shows a similar shape in each dataset. The greatest depression is on the basin's western headwaters.

Significant discrepancy in light conditions exist on the Amazonian foothills of the Altiplano, where the low level jet forms. The NCEP over-predicts shortwave radiation in these locations, while the ERA40 shows a distinctly cloudier picture. Note that the ERA40 shows a strange block patterned depression of radiation at $30^{o}S$. This is mostly likely an artifact of the model assimilating validation information that apparently disagreed strongly with the native model estimates.

[2]These data were obtained from the NASA Langley Research Center Atmospheric Sciences Data Center NASA/GEWEX SRB Project.

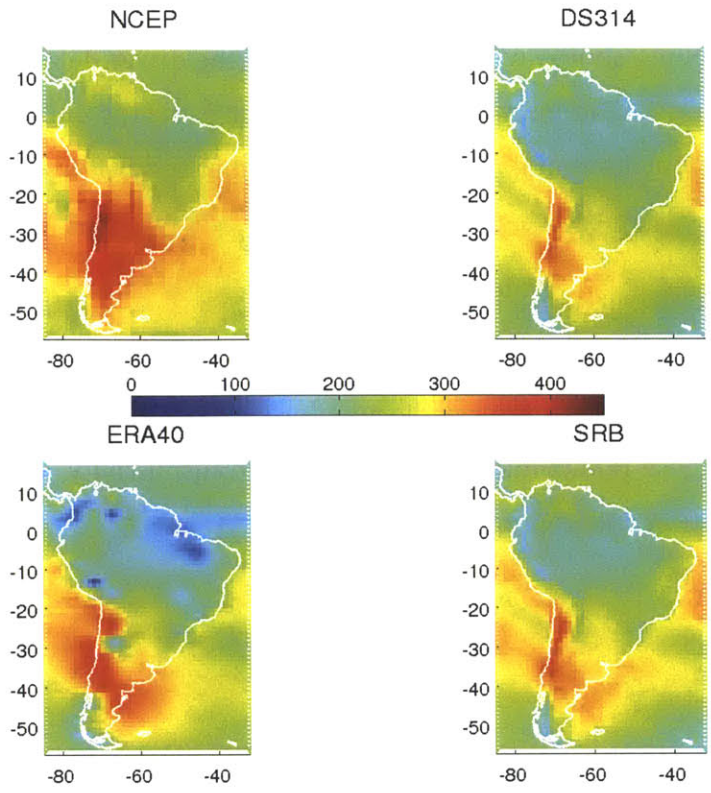


Figure 4-17: Evaluation of the mean monthly downwelling shortwave radiation for the month of January. Means are calculated over the twenty four hour daily cycle, from 1990-1999.

### 4.1.5 Radiation Interpolation

The data products report radiation information at relatively coarse temporal frequencies of 3-6 hours, barely capturing diurnal variability (6-hourly for NCEP/ERA40 and 3-hourly for DS314). As discussed in Chapter 3, the EDM2 model explicitly integrates leaf and soil energy based on heat and radiation fluxes. Likewise, shortwave radiation drives the leaf photosynthesis model. In the interest of model accuracy and providing smooth gradients to the numerical solvers, it is advantageous if downwelling solar radiation is provided at temporal resolutions close to the model time step. To achieve this, a simple zenith weighted interpolation of transmissivity is performed.

First the optical transmissivity $T_r$ is calculated at a known time step $i$. This is the ratio of actual downwelling shortwave radiation $R_s$ from the driver dataset to the estimated "no-sky" short-wave radiation, where no sky radiation is the top of the atmosphere solar radiation $S_o$ scaled by its zenith angle $cos(\alpha_{z(i)})$ for that time of day.

$$T_{r(i)} = R_{s(i)} / \left(S_o \cdot cos(\alpha_{z(i)})\right) \tag{4.6}$$

The transmissivity between the first point $i$ and the next known point at $i + N$ is linearly interpolated to an intermediary point $i + n$. The estimated solar radiation $R_{s(i+n)}$ between these points multiplies the optical transmissivity $T_{r(i+n)}$ by the top-of-atmosphere radiation and appropriate zenith angle.

$$T_{r(i+n)} = T_{r(i)} \left(1 - \frac{n-i}{N-i}\right) + T_{r(i+N)} \frac{n-i}{N-i} \tag{4.7}$$

$$R_{s(i+n)} = T_{r(i+n)} S_o cos(\alpha_{z(i+n)}) \tag{4.8}$$

### 4.1.6 Point Validation of Diurnal Mean Downwelling Shortwave Radiation

The products' ability to capture the diurnal mean cycle of downwelling radiation is validated against measurements from station data (see Figure 4-18). The NCEP data was the first reanalysis dataset used by the EDM2 development team, and therefore solar radiation was interpolated using a legacy formulation not discussed in detail here. Briefly, the legacy formulation used a zenith cosine forward extrapolation, assuming a constant transmissivity at intermediary points that were equal to the previous known point. The ERA40 and DS314 were adopted later in development, and therefore the optical transmissivity method of interpolation described above was used. The means were calculated at Manaus, Fazenda Nossa Senhora and Santarem during select dry and wet season months.

Step-like inconsistencies associated with the legacy interpolation are apparent in

the late mornings. The transmissivity interpolation described above does not have this issue. The timing of sunrise and sunset is consistent across each model (expected since each dataset was interpolated using the same zenith cosine function). The station data at Manaus and Fazenda show a distinct phase lag with the reanalysis datasets (on the order of one hour or less). For three out of four cases, the lag is only associated with sunrise whereas the Fazenda station in January shows lag at sunrise and sunset. It is possible that vegetation or local topography occludes the actual sunrise.

There is no consistent pattern of over or under-predicting peak solar between the datasets: each dataset shows cases of over and under-predicting peak solar radiation. By a small margin, the NCEP dataset does have greater mean peak solar radiation than the other two, however outside the problems with the legacy interpolation method, there is no consistent outlier among these datasets in estimating peak radiation or the timing of the solar cycle.

The regional patterns of mean downwelling radiation for September 1990-1999 were fairly similar across datasets (see Figure 4-19). A thin atmosphere promoted a reduction of longwave radiation over the mountains. Cloud activity over the equatorial Atlantic and Amazonian head-waters promoted an increase in long-wave radiation.

All three products compare well with the Fazenda station's longwave radiation at 0, 6 and 12 UTC (see Figure 4-20). However, they all fail to capture the true minima due to lack of temporal granularity. Likewise, they all significantly underestimate the magnitude of peak long-wave radiation in the early afternoon (18 UTC).

The ERA-40 and NCEP-R1 were successful in matching peak solar radiation at Fazenda in September. The fact that they underestimate downwelling longwave at the same time and location suggests several possibilities. Perhaps model estimates of cloud water were accurate and radiative transfer models were less so. Perhaps the cloud model was incorrect and the solar radiation showed low bias for the wrong reason. Again, no dataset significantly out-performed the others. While this is only one sample point among the region, underestimates in downwelling long-wave radiation will contribute to reduced net radiation and decreased equilibrium canopy temperatures. The significance of this is difficult to estimate.

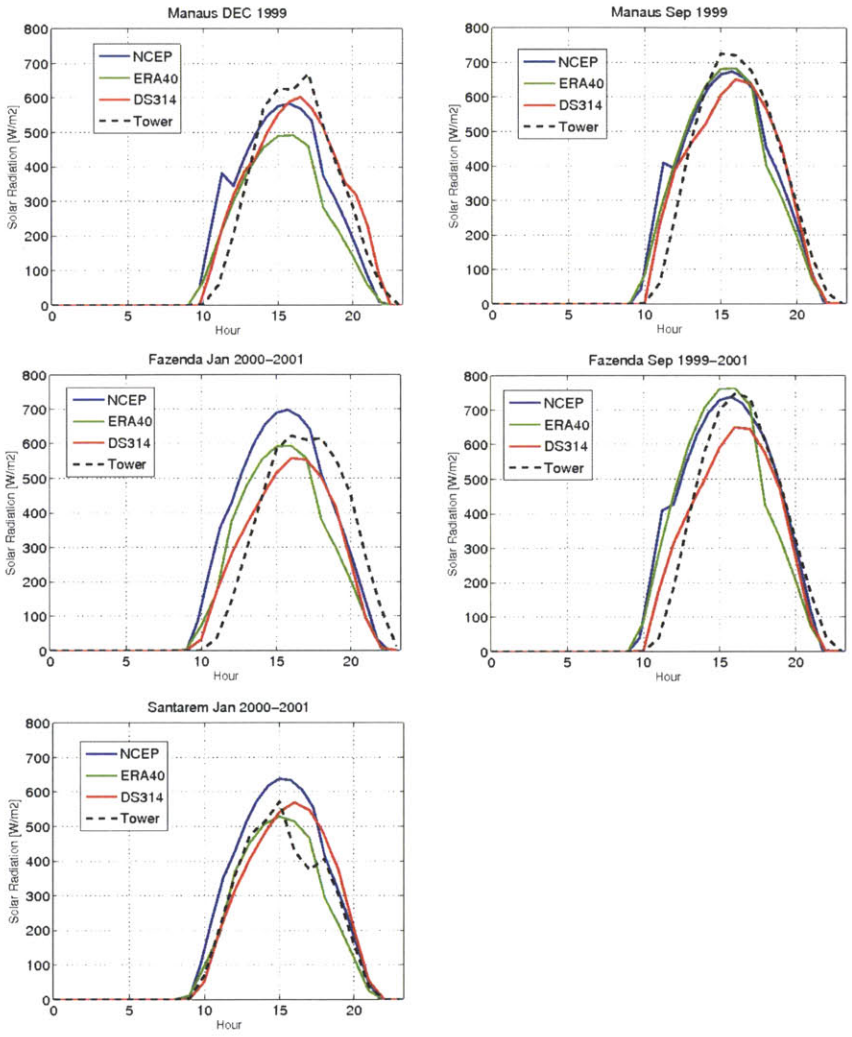


Figure 4-18: Diurnal mean downward total solar radiation: model estimates and flux tower validation at 3 sites.

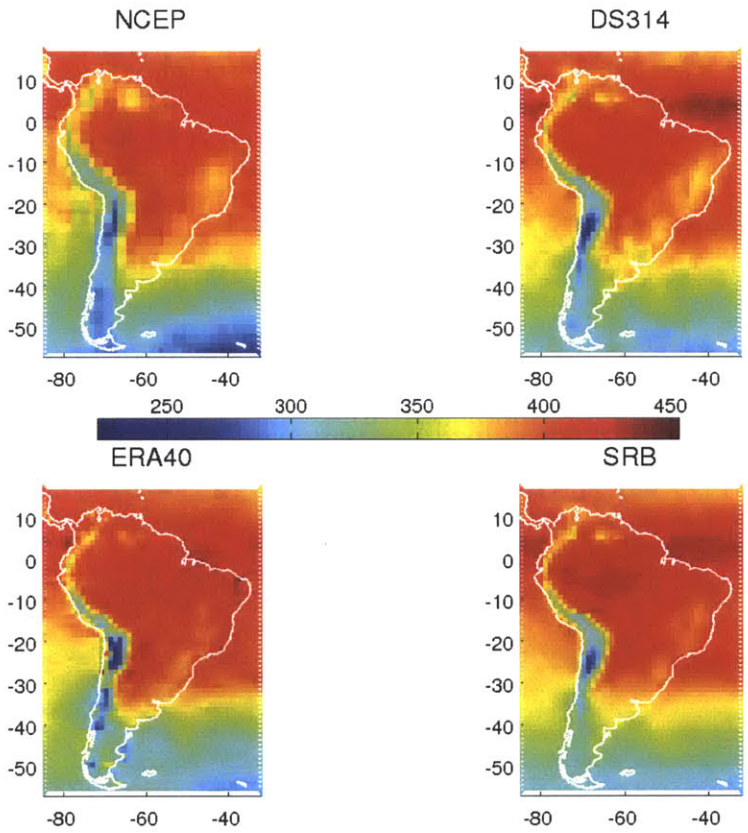


Figure 4-19: Mean downwelling longwave radiation [W/m2] at the surface for September 1990-1999.

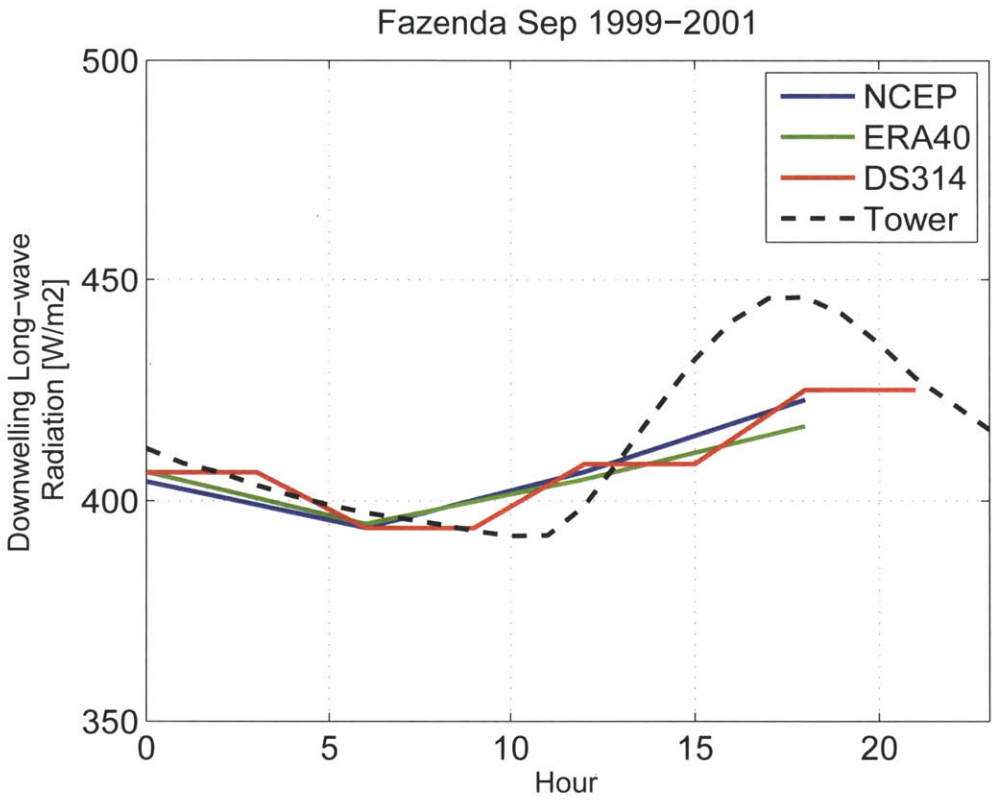


Figure 4-20: Diurnal mean downward long-wave radiation: model estimates and flux tower validation at Fazenda Nossa Senhora.

## 4.2 Incorporating Data from Human Land-Use

Recall that the coupled model simulations require two initial conditions: a land-surface that reflects the actual present day ecosystem composition (Actual Vegetation), and a land-surface that reflects a vegetation demography where there is no human land-use in South America (Potential Vegetation).

The ED2.1 model applies human land-use by reading in an externally compiled dataset of *land-use transition matrices* $\lambda$. A land-use transition defines the fraction of area of one type of land-cover that will change to another type of land-cover over the course of the year, with units $[1/year]$. There are three types of land-cover that transition from one to the other: Primary Forests, Secondary Forests and Pastures. Pastures are used to describe all areas of agricultural development. ED2 model Patches classified as pasture are fixed to be populated only by C4 grasses. Primary and Secondary forests can transition into pastures. Pastures can be abandoned to become secondary forests. Primary forests can become secondary forests through harvesting cohorts and decreasing number density.

The transition matrix data was compiled by Ke Zhang and Marcos Longo at Harvard University as a hybrid of two base datasets. The first dataset is the Global Land-use Dataset by Hurtt *et al.* [2006] using the SAGE-HYDE 3.3.1 method[3]. This is a global 1-degree yearly dataset compiled from 1700-1999. The SAGE-HYDE data are natively available as land-use transitions. The second dataset is the SIMAMAZONIA SA1 product (see [Soares-Filho *et al.*, 2006]). The SIMAMAZONIA product is a yearly series of 1 kilometer gridded maps covering only the Amazon basin; for reference the map for 2008 is provided in Figure 4-21. The SIMAMAZONIA data categorize pixels on their land-cover status: forested, deforested and Cerrado type non-forests. The SIMAMAZONIA 1 estimates that in 2008, $11\%$ of the basin had been deforested, $69\%$ was forested and $20\%$ was designated savanna/Cerrado. Transition rates are calculated by taking the difference in counts for the three land-cover types from year to year.

The SAGE-HYDE transition data only cover the period through 1999. In areas where

[3]The use of the SAGE-HYDE 3.3.1 Global Land-use Dataset acknowledges the University of New Hampshire, EOS-WEBSTER Earth Science Information Partner (ESIP) as the data distributor for this dataset.

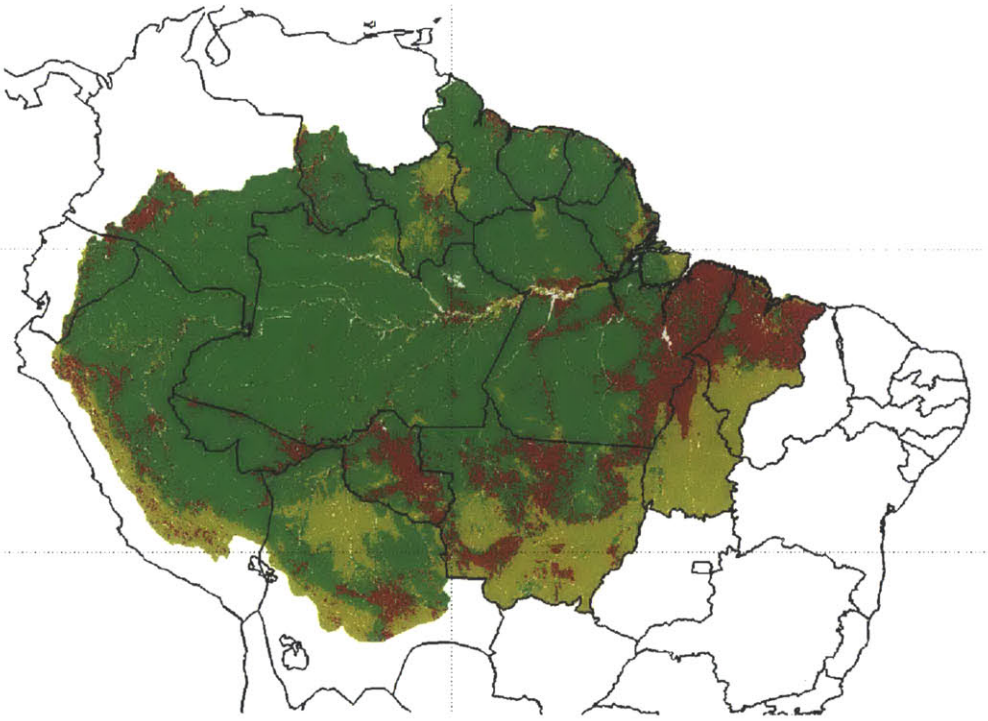

Figure 4-21: Regional deforestion and land-cover estimate from SIMAMAZONIA 1, year 2008.

there was no spatial overlap, the SAGE-HYDE transitions from 1999 were maintained until 2008. For regions where there was spatial overlap with SIMAMAZONIA, the SAGE-HYDR transitions from 1999 were maintained until 2001 (prior to the first year of SIMAMAZONIA data). In areas with dataset overlap, the SAGE-HYDE transitions from 1978 through 2001 were also scaled by a correction factor via least squares regression, such that the total amount of converted land matched the SIMAMAZONIA product in 2002.

Much of the SIMAMAZONIA product designates land-cover as a savanna/Cerrado but does not distinguish if it is natural or converted. In areas that had some forest cover, the primary-to-pasture transition was based purely on the decrease in forested pixels. For example if the forest decreased by $2\%$ in one year, it would be assumed that the all-land conversion rate was $2\%$. This is undoubtedly a conservative estimate on land conversion rates, as conversion from natural grasslands would undoubtedly be

higher on average than the conversion from forests because it requires so much less work. In areas where there were no SIMAMAZONIA forest pixels, the transition rates were maintained from the SAGE-HYDE 1999 data (as if the SIMAMAZONIA data were not there).

The end result (2008) converted fraction of land for the Actual Vegetation EDM initial condition is presented in Figure 4-22.

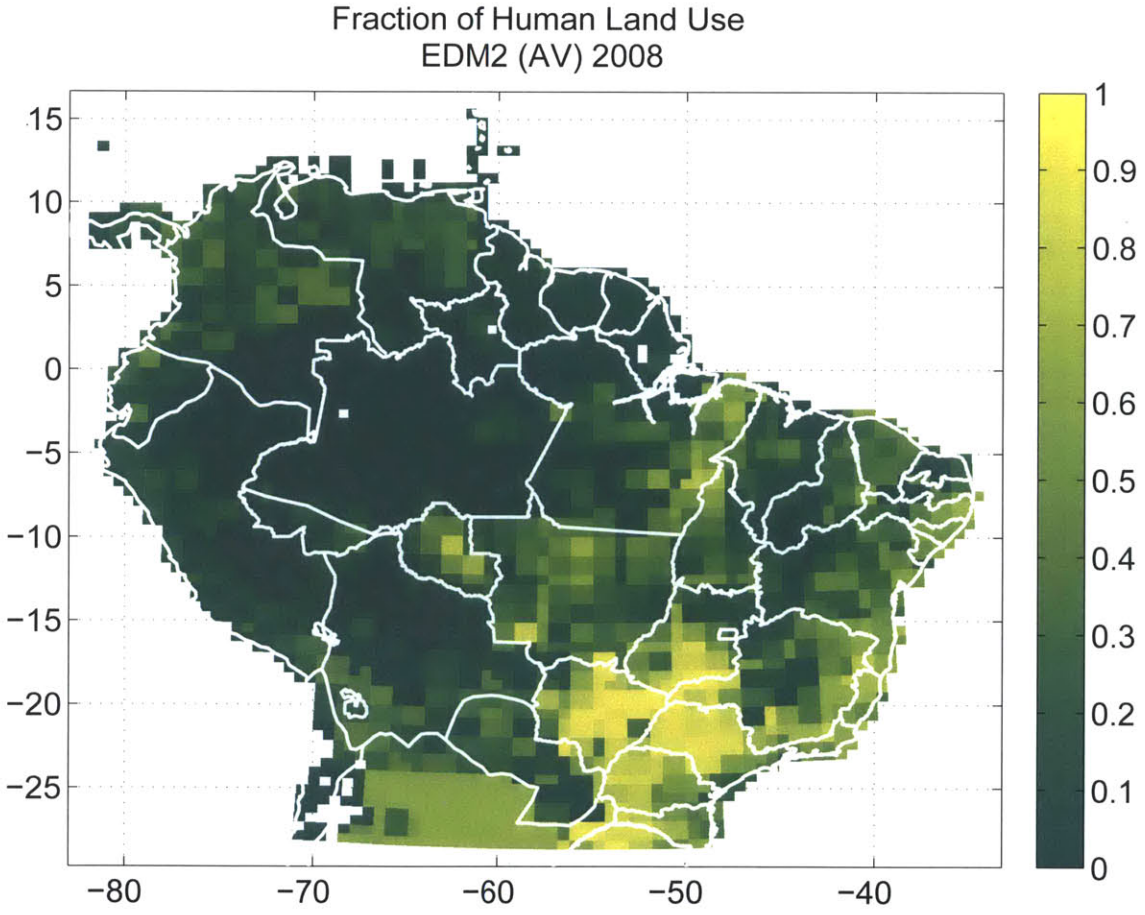


Figure 4-22: The fraction of the land-surface with coverage type pasture for the Actual Vegetation (AV) condition, estimated by the ED2 initial condition for January 2008. Pastures are used in the ecosystem model to represent all human land-use classes.

## 4.3 Evaluation of Ecosystem Structure and Composition - Initial Condition

The model estimated Leaf Area Index, Basal Area and total Above Ground Biomass are compared to estimates from the Moore campaign ecosystem monitoring stations. These are all year averages, and the data collected at the measurement station is taken from un-managed, non-degraded and un-converted ecosystems. The EDM2 output is averaged over all patches that are designated primary forests at the polygon nearest to the measurement station. A map of the Moore station locations is provided in Figure 4-23.

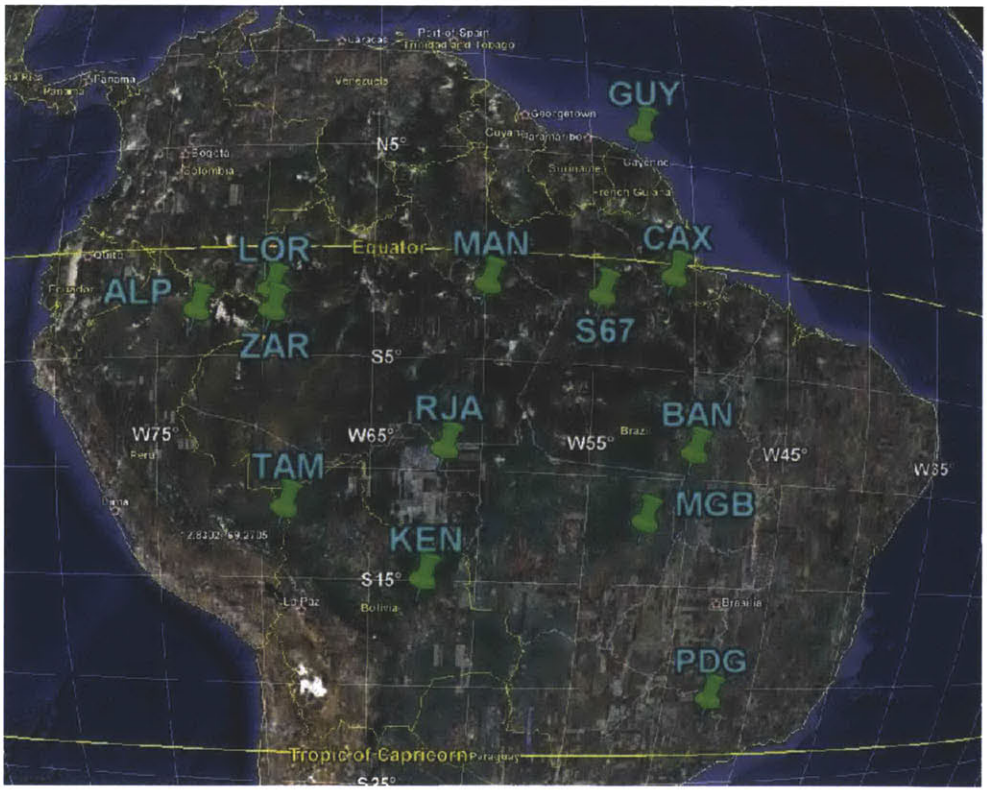


Figure 4-23: Regional map showing the location of the Moore project validation sites. Thirteen sites were selected in total. Mapping rendered with Google Earth Software. Copyright Google 2006.

The mean model estimated total above ground biomass [kg/m2] is 4.3% higher than

| | EDM | Station | MODIS |
|---|---|---|---|
| RMS | 1.89 | 1.43 | 2.15 |
| Bias | -0.329 | 0.007 | 0.322 |

Table 4.1: Three way comparative statistics on estimates of mean yearly Leaf Area Index. All statistics are the average of the individual comparisons against the other two datasets.

estimates from the Moore stations, with a mean error of 7.4. The estimates at each station are shown in Figure 4-24. A site by site comparison of Basal Area is provided in Figure 4-25. The model significantly under-predicts the Kenia site and over-predicts the Jaru and Zar sites. The Kenia site is located in northwestern Bolivia, which is roughly in the path of the moist northwesterly winds in the South American circulation, near where the low level jet forms. It is likely that either there is a discrepancy in the soils textural dataset between the site and the mean characteristics of that model pixel, or that the climate driver dataset (DS314-Sheffield *et al.* [2006]) could not resolve the exact position or boundary of the moist northwesterly air mass. The data from Kenia reports that it is classified as a lowland dry forest but does not provide information soils information. The sites Reserva Jaru (RJA) and El Zafire (ZAR) are both found in areas that can be characterized as closed canopy forests, however the soil conditions at both stations are very sandy. The El Zafire has a 78% sand content and the Jaru site has an 80% sand content. The water holding capacity of sandy soils is decreased, promoting increased soil moisture stress compared to clay-loam soils. This could explain why the model over-predicts biomass and stem area compared to the sites.

The site by site comparison of Leaf Area Index includes a third estimate from the MODIS C5 product (see [Samanta *et al.*, 2011]). The mean LAI estimates are compared in Figure 4-26. The root mean squared error and mean normalized bias was calculated between each method. Each method therefore had an error and a bias associated with the two other methods, of which the means are reported in Table 4.3. The comparison indicates that the the error and bias associated with the ED estimates are comparable to the average error of the other two estimates.

Regional patterns of leaf area and above ground biomass are provided in Figures

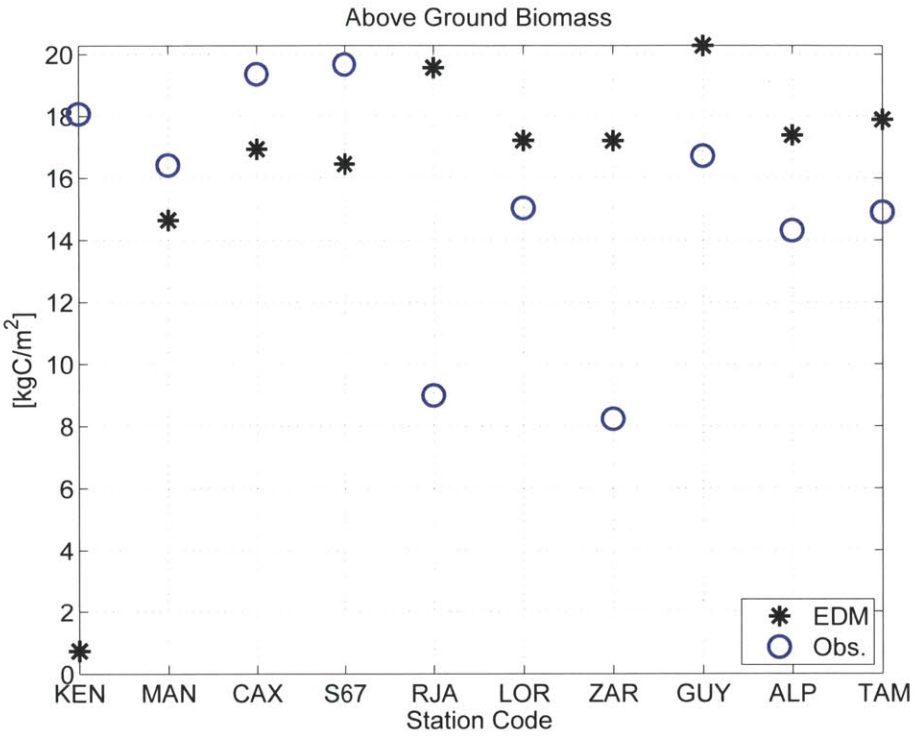


Figure 4-24: Yearly mean total Above Ground Biomass (AGB) $[kg/m2]$ at Moore validation sites and the EDM2 Actual Vegetation Initial Condition (2008).

4-27 and 4-28. These maps are instantaneous estimates for January 1st 2008 and provide spatial analysis and comparison of the potential and actual vegetation estimates of the model. The left columns show the estimates from the potential vegetation initial condition. The right column shows the difference between the two conditions $(LAI_{AV} - LAI_{PV})$.

Several features in the potential vegetation are noted in Figure 4-28. The Amazon basin is dominated by old growth closed canopy forests. Early successional species are ubiquitous but dominate the savanna regions as low LAI open canopy systems. However, their presence in this realization of a potential vegetation equilibrium is strong enough to completely out-compete tropical (C4) and sub-tropical grasses parameterized by the model. The general patterns of total biomass and leaf coverage are reflective of the yearly root zone soil moisture availability.

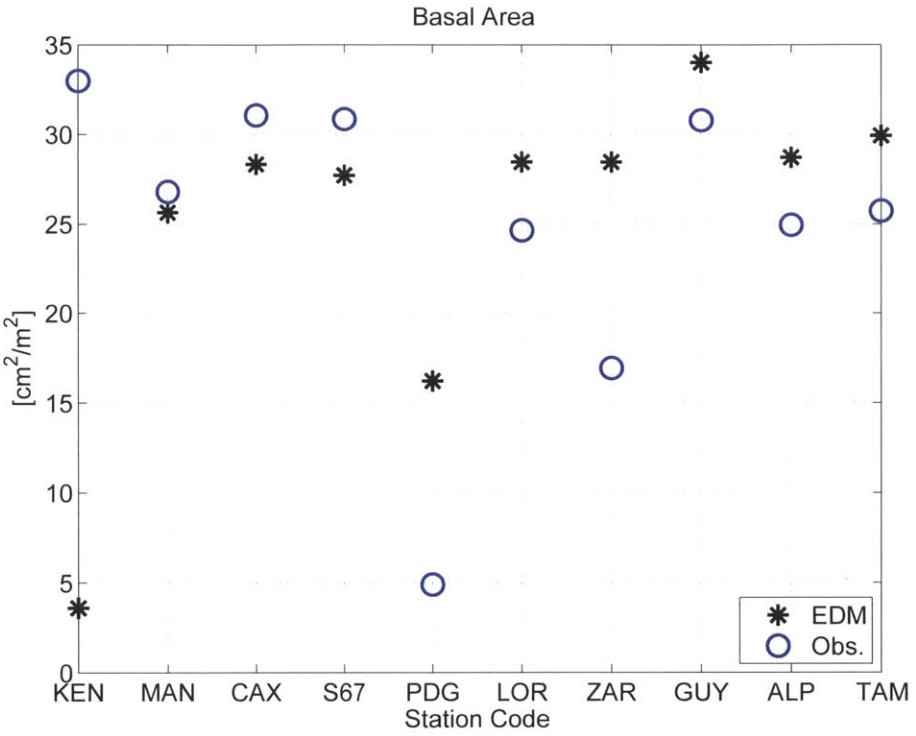


Figure 4-25: Yearly mean basal area (BA) $[m2/m2]$ of plant stems at Moore validation sites and the EDM2 Actual Vegetation Initial Condition (2008).

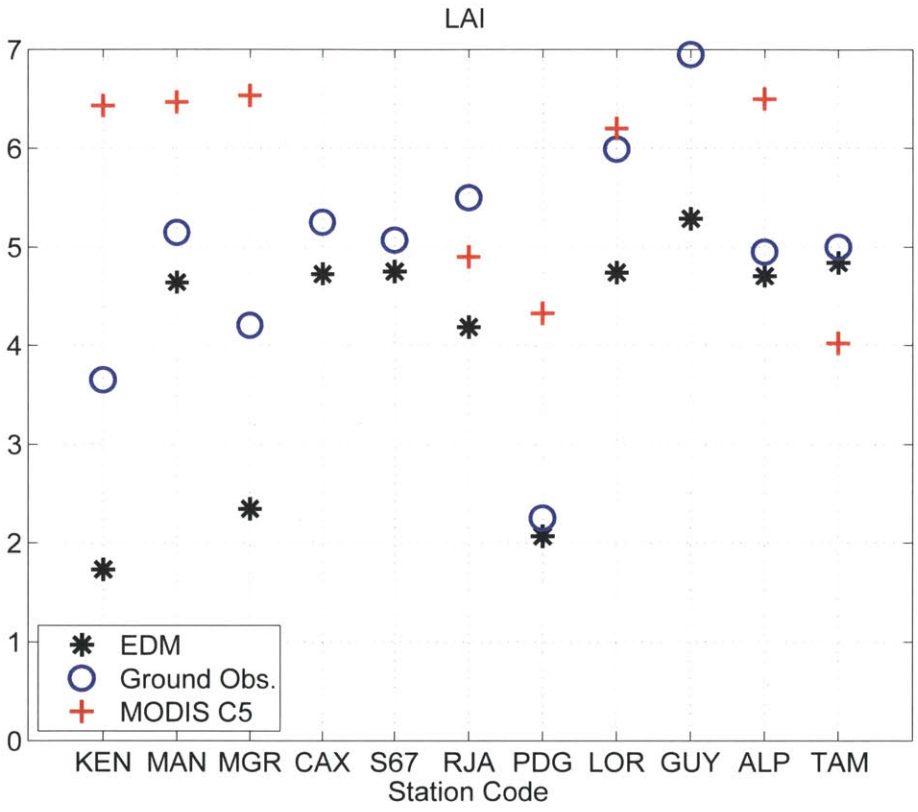


Figure 4-26: Yearly mean Leaf Area Index (LAI) $[m2/m2]$ at Moore validation sites, as estimated from MODIS MCD15A2 (C5) and the EDM2 Actual Vegetation Initial Condition (2008).

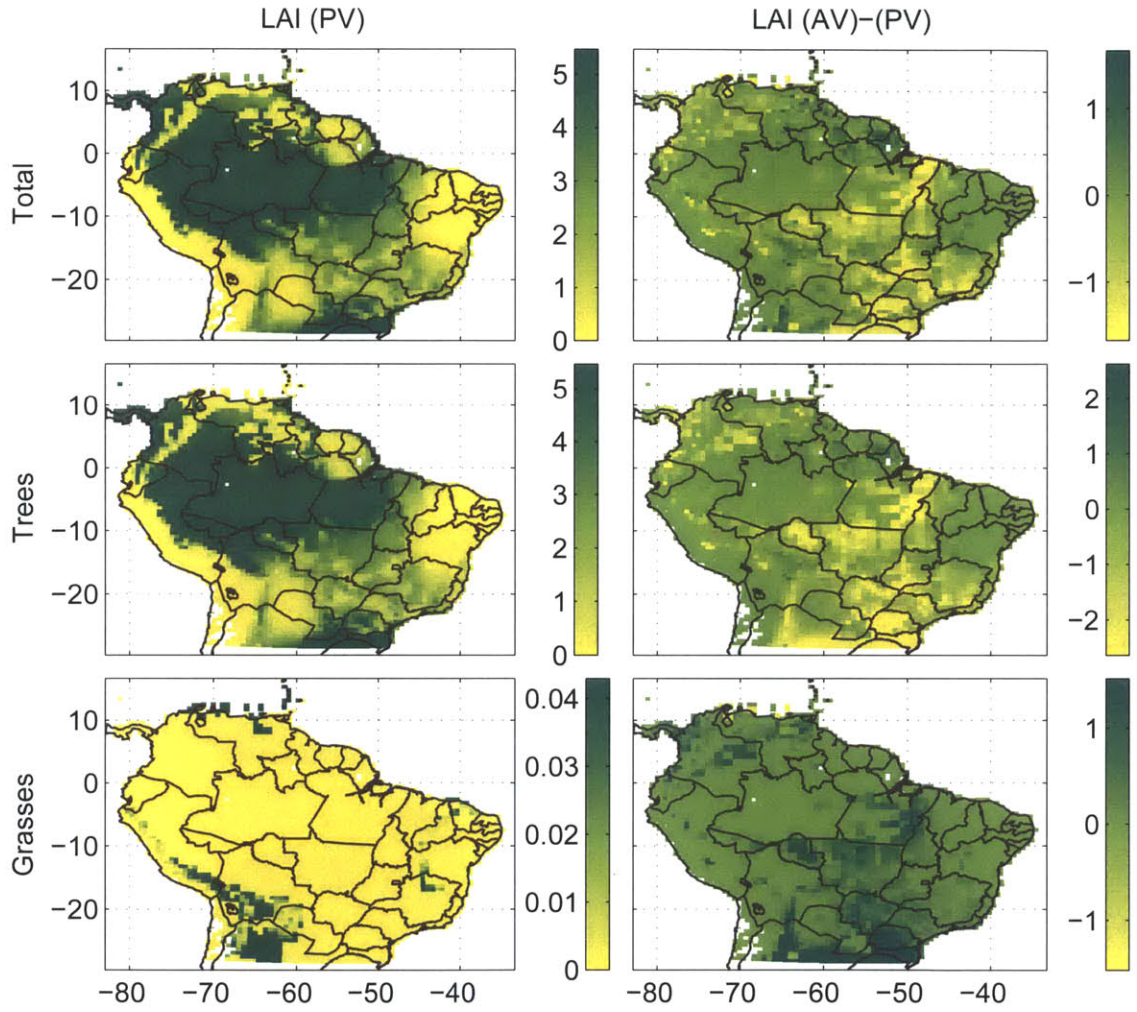


Figure 4-27: Regional maps of Leaf Area Indices $[m2/m2]$ from the EDM2 initial condition. The left column indicates results are from the Potential Vegetation condition, the right column is the relative difference in the Actual Vegetation condition.

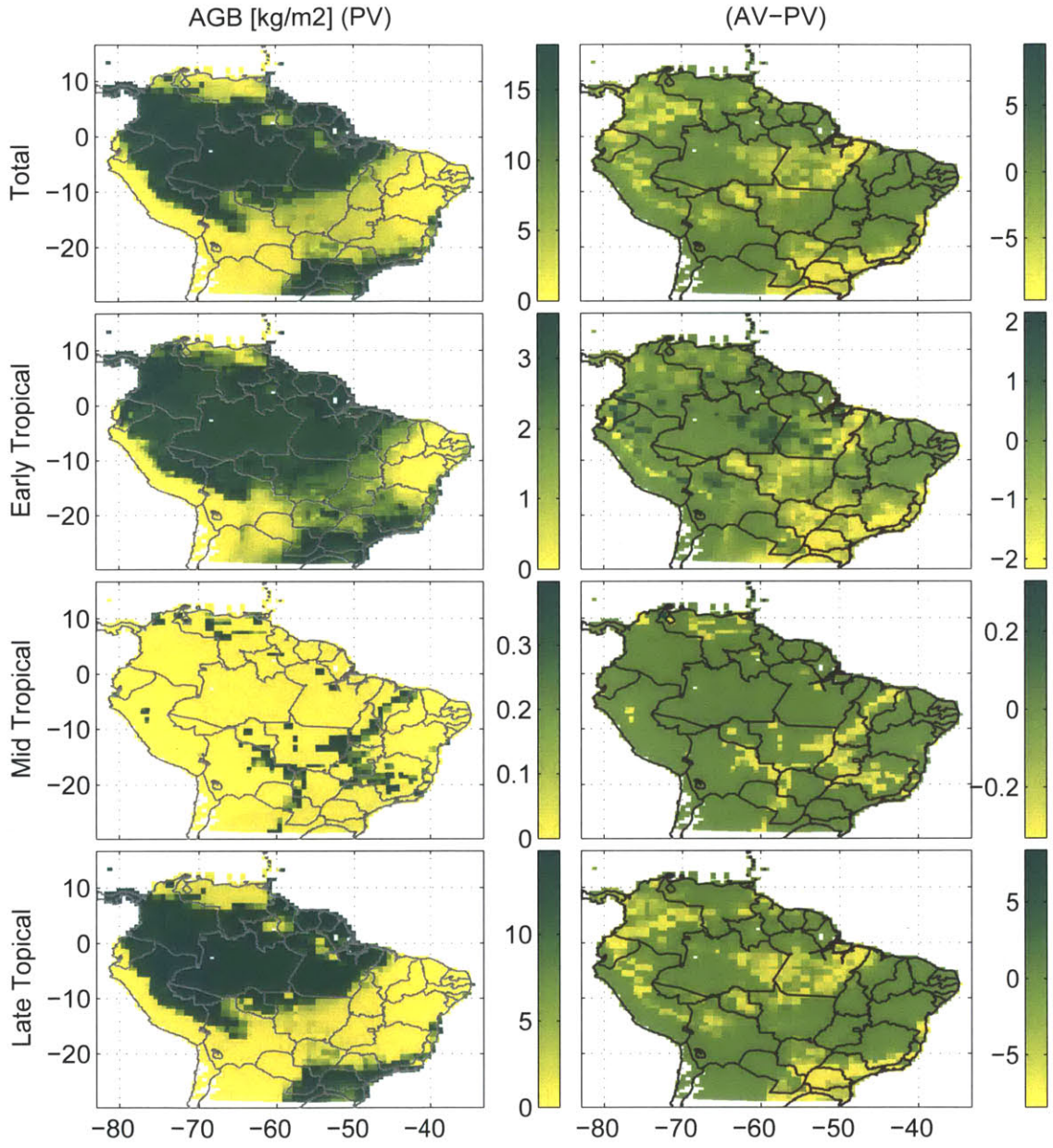


Figure 4-28: Regional maps of total Above Ground Biomass $[kg/m2]$ from the EDM2 initial condition. The left column indicates results are from the Potential Vegetation condition, the right column is the relative difference $(AGB_{AV} - AGB_{PV})$ in the Actual Vegetation condition. Columns partition results by plant functional groups, including Total, Grasses, Early, Mid and Late Successional trees.

## 4.4 Lateral Boundary Conditions - An Argument For Reanalysis Datasets

One of the objectives of this thesis is to perform limited area atmospheric model simulations. These simulations are used to test the response of regional patterns of hydrology to land-conversion. Originally there was interest in not only looking at how land-conversion currently influences regional hydrology, there was interest also in making predictions of vegetation response to the changes in regional hydrology of future climates. This would require forecasted boundary conditions, most likely generated by model output from a General Circulation Model. The Community Climate Modeling System (CCSM) is one of the premier climate models used operationally and offers arguably the largest scientific and developer user-base. The alternative to using forecasted lateral boundaries is using conditions derived from reanalysis datasets such as ERA-40 or NCEP-R1.

From an ecological perspective, it is imperative that model simulations (be they global or limited area in nature) resolve statistically realistic quantities of precipitation and surface radiation. Precipitation controls the availability of root-zone soil moisture, and radiation drives the surface energy balance and photosynthesis. The patterning of precipitation and clouds in South America is largely controlled by the convergence of moisture through the synoptic scale circulations of air.

The ability of the boundary conditions to adequately represent moisture flux will influence the internal dynamics of the limited area coupled model system. Mean moisture flux is computed as the product of wind velocity and specific humidity (see Figure 4-29). The vectors represent the direction and magnitude of the flux, while the shaded background corresponds to the total magnitude of the flux. Units are in $[kg/m^2/s]$. The moisture flux along the main arc of the South American circulation is significantly lower in CCSM3 than in ERA40. CCSM3 generates easterly momentum fields as strong as those generated by ERA40 in the coastal Inter-Tropical Convergence Zone regions north of the equator and south of $5^oS$, however the CCSM3 moisture flux in these regions is relatively low. It appears the difference in moisture is symptomatic of the humidity lev-

els in the equatorial Atlantic, and the vertical transport of moisture from the equatorial Atlantic and tropical forests. Examine the band of air currents between the equator and $5^oS$: while the circulation patterns of ERA40 are driving large amounts of moisture in a wide arc across the basin, the advection of moisture in CCSM3 follows a tighter and shallower arc. There is clear difference in moisture flux arriving to the headwaters of the Amazon basin.

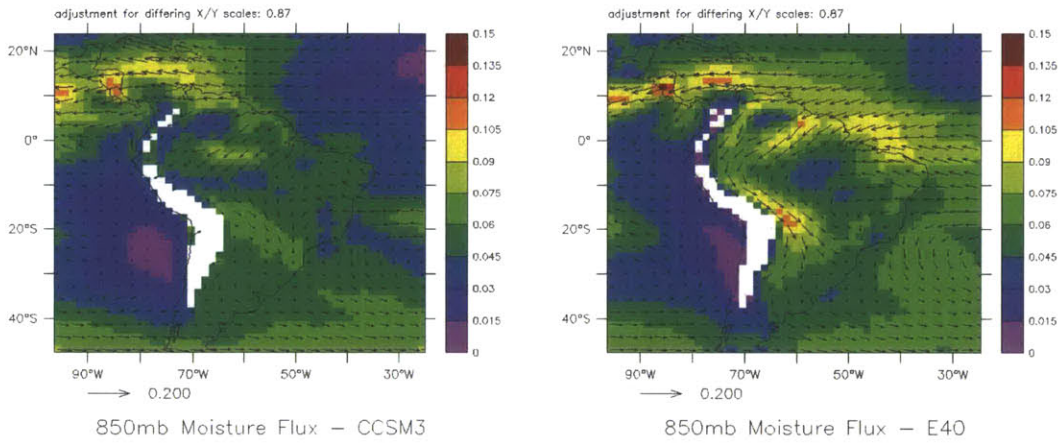


Figure 4-29: Advective moisture flux at 850 mb and 18Z [$kg\ m^{-}2\ s^{-1}$]. Mean values of the analysis period. Regions devoid of vector bars and shading indicate the presence of surface terrain and have therefore been masked out.

From the perspective of the regional model, the boundary conditions provided by GCM output over the equatorial Atlantic will be the driving force of the regional counter-clockwise moisture circulation. While there is an acceptable level of agreement regarding the momentum and vorticity fields at 850mb, there is a significant under-estimation of moisture convergence in the CCSM3 model. It is concluded that the ensemble E CCSM3 model output for the A2 scenario did not provide suitably realistic synoptic patterns of moisture and momentum to drive a comparative analysis on land-atmosphere interaction. It was therefore elected to utilize the more trusted product, ERA40, as the lateral boundary condition for the coupled model runs.

# Chapter 5

# Validation and Calibration of ED2-BRAMS

The EDM2 has been designed to simulate ecosystem dynamics as a stand-alone modeling framework. It has undergone a history of model testing in the Amazon and surrounding areas. The model is validated in terms of its ability to arrive at a comparable structure and composition to that of observations after a time of spin-up (covered in the previous chapter). Its ability to accurately model carbon fluxes have been reported and validated in other studies and will not be discussed here (see [Medvigy *et al.*, 2009], [Kim *et al.*, 2012] and [Levine and co authors, 2012] (in press)). This chapter will cover the coupled model's calibration process and ability to reproduce mean land-surface energy fluxes, precipitation, mean cloud profiles, radiative fluxes and mean thermodynamic profiles.

## 5.1 Numerical Grid Mesh

The experimental design projects the coupled model on a polar-stereographic grid: 96 points in the East-West direction, 80 points in the North-South direction, 54 points in the vertical direction and 16 soil layers. The grid center and pole point is situated at geographic coordinate $6.5^oS$ $55.5^oW$. The horizontal resolution at the pole point is 64 kilometers in each direction. The atmospheric spacing in the vertical dimension

stretches with increasing geopotential. The rate of stretching was designed to enable a high resolution among the band ofelevations where cumulus convection is triggered. This was done by using a layer depth of 110 meters at the surface and increasing layer thickness at a rate of 3% until ˜3000 meters, where stretching was increased to a rate of 8% to the top of the model. The horizonal mesh is shown in Figure 5-1.

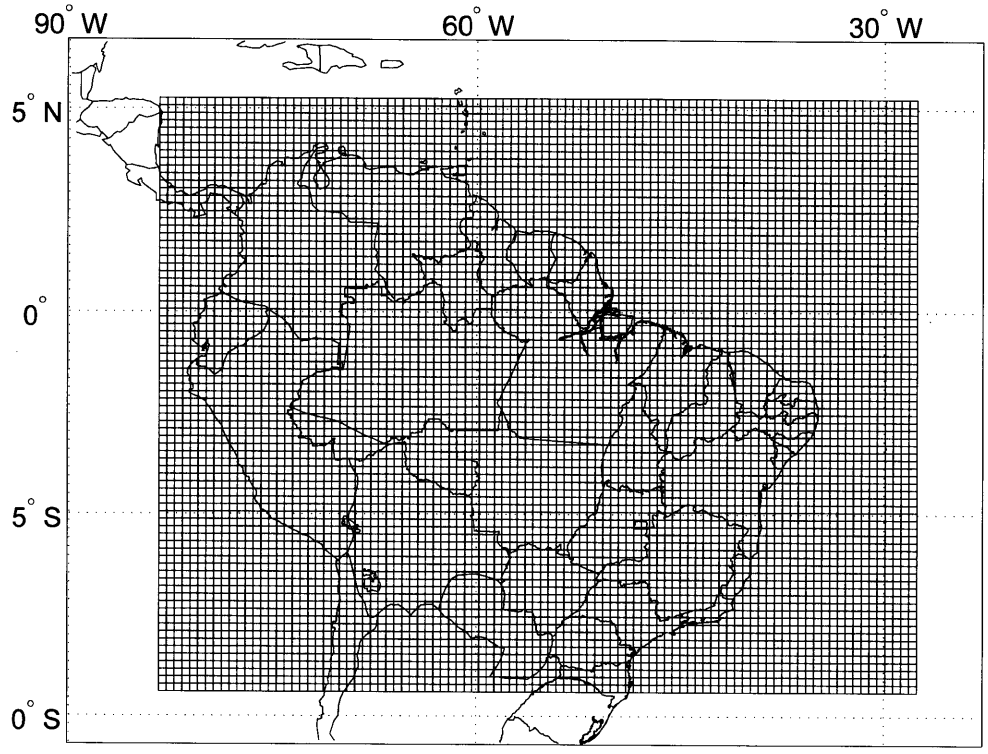


Figure 5-1: Horizontal view of the Coupled Simulation Mesh, 98 centerpoints in the zonal direction, 80 centerpoints in the meridional direction. The grid resolution is 64 kilometers in both horizontal directions.

## 5.2 Cumulus cloud Fraction Parameterization

During the process of tuning the cumulus parameterization, it was observed that ED2-BRAMS consistently underestimated total cloud optical depth and overestimated surface shortwave radiation. It was unclear if the lack of optical depth was due to underestimation of cirrus, stratus or cumulus clouds. The precipitation regime of the testing period

(February) is dominated by convective precipitation in the central and southern basin. It was natural to investigate how the model incorporates cumulus cloud water into the radiation scattering process.

Most cumulus parameterizations focus on the estimation of vertical mass flux in cumulus convection. However, the horizontal area through which the mass passes is not necessarily dictated by the cumulus parameterization. Cloud fraction must be known to calculate in-cloud mixing ratios from grid total cloud water.

The radiation scattering parameterization is sensitive to the estimate of cloud fraction and in-cloud mixing ratios. Radiation scattering is a non-linear process, and is estimated over atmospheric columns in the cloudy and clear sky portions separately. Surface radiation is the area weighted mean of these estimates.

The legacy method of estimating cloud fraction holds that the fraction of sky covered by clouds updrafts $f_{up}$ is equal to the fraction of eddies in the atmospheric boundary layer that have enough velocity to raise parcels above the cloud base. A normal distribution of wind-speeds populate the boundary layer at the level of cloud updraft, defined by mean $\overline{w}_z$ and variance $\sigma_{w_z}$. A parameterization of drag and bouyancy (not covered here) estimates a minimum vertical velocity $w_{up,z}$ needed at the level of updraft to penetrate the cloud base.

$$f_{up} = 1 - \text{cdf}(w_{up,z}|\overline{w}_z, \sigma_{w_z}) \tag{5.1}$$

In theory this method was intended to give consistent cloud fractions, but in practice it almost always yielded cloud fractions near 0.5 because the variance of the vertical wind-speed is relatively large compared to the difference between the mean vertical wind velocity and the updraft velocity.

A second approach followed the method proposed by [Fritsch and Chappell, 1980]. The updraft area is governed by the conservation of the mass flux $m_{up}$ assuming a mean air density $\rho$ and expected updraft velocity:

$$f_{up} = \frac{m_{up}}{\rho E(w_{up,z})} \tag{5.2}$$

The method of [Fritsch and Chappell, 1980] provided a broader distribution of cloud fractions and in-cloud mixing ratios which were more in line with those found in the literature [Rogers and Yau, 1989]. After migrating to the Fritsch Chappel method, surface estimated short-wave radiation showed greater sensitivity to modifications to the cumulus convective parameters. Examples of the distributions of cloud fractions and in-cloud mixing ratios estimated by the two competing methods are are compared in Figure 5-2.

## 5.3 Manual Optimization of Cloud and Radiation Parameters

The majority of the model options and parameters were selected based on their relative merits, wisdom drawn from the model user-base (such as parameters used by by operational forecasters at Centro de Previsao de Tempo e Estudos Climaticos (CPTEC)) and published results [Medvigy *et al.*, 2010]. There remained a group of parameters related to convection and the choice of radiation scattering method that required calibration. These are explained in Table 5.1.

The calibration procedure was performed manually. The process first isolate modules that provided better results (such as radiation scheme or convective triggers), and then focus on parameter groups with continuous ranges (such as cloud radius or precipitation efficiency). Computing resources roughly allowed for two test simulations to be conducted simultaneously, which encouraged binary search behavior. The calibration procedure first made use of the LEAF3 land-surface model [Walko *et al.*, 2000]. The LEAF3 is a big-leaf land-surface model which uses similiar biophysics methods as the ED2 model but is computationaly inexpensive and good for rapid testing. The calibration procedure was conducted in three stages:

- Stage 1: Run rapid manual calibrations using a scaled down domain and the LEAF3 land surface scheme which has low computational burden. Evaluate maps of model estimated accumulated rainfall and mean radiation with TRMM 3B43

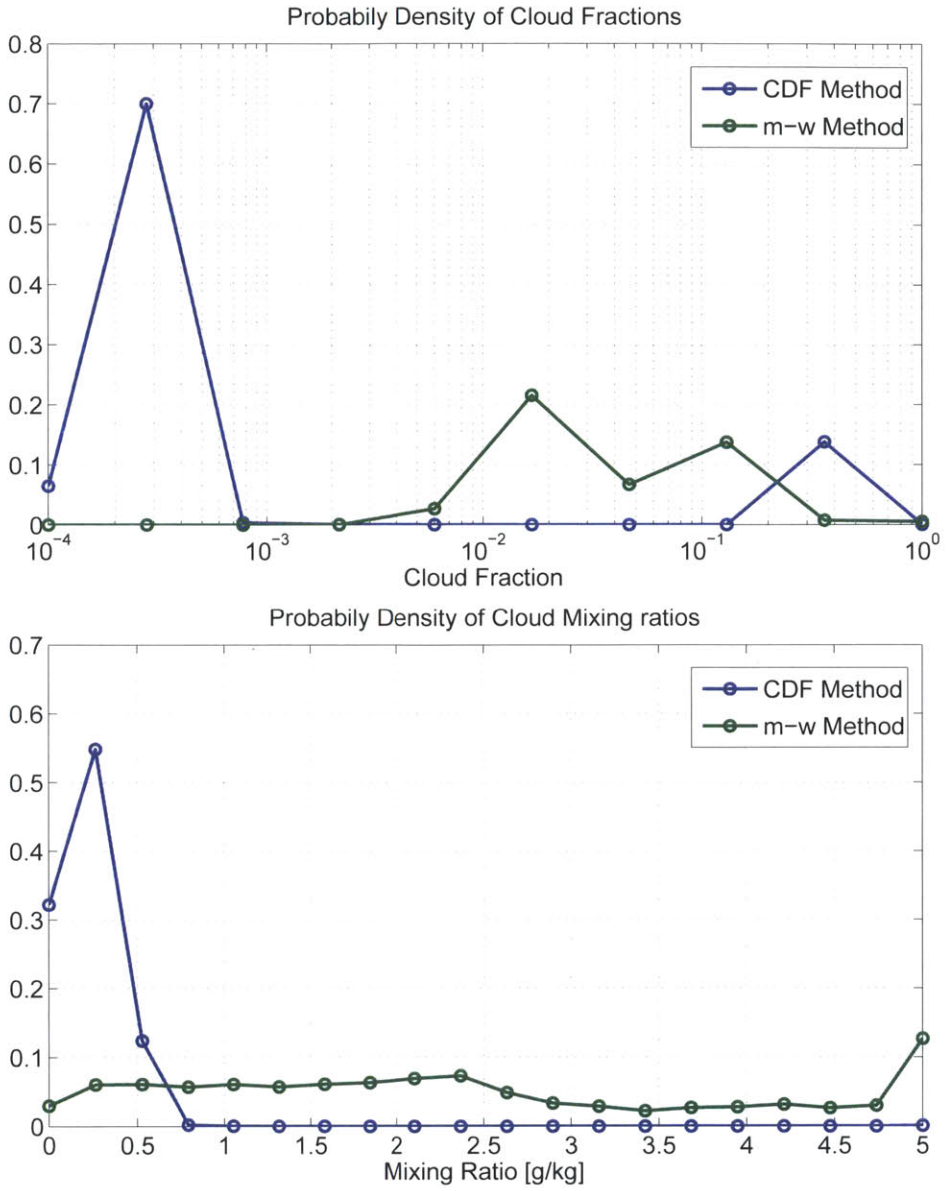


Figure 5-2: Histograms of cumulus cloud area fractions and in-cloud mixing ratios for the legacy (CDF) and mass-based approaches to calculating cumulus cloud area.

rainfall and GEWEX-SRB downwelling radiation for February 2002 (the second month of simulation).

- Stage 2: Keep the same testing protocol as Stage 1 while expanding the simulation domain to roughly the full extent of that used in the main experiment. Incorporate

comparisons of mean cloud profile data with CloudSat estimates.

- Stage 3: Run the full model domain with the ED2 land-surface "Actual-Vegetation" condition. Perform calibrations based on second month (February 2002) results. As desired parameter set converges, test long-term hydrology. Compare surface fluxes with flux tower measurements.

The calibration procedure focused on four efficiency metrics: the normalized difference bias $bd$ and root mean squared error $rmse$ of the monthly mean downwelling short-wave radiation $\overline{R}_s$ and the monthly sum total precipitation $\overline{P}$. Statistics were calculated over all $M$ points on the grid. The variance ratio $vr$ was observed as well, but provided similar information as the $rmse$. Shortwave radiation was validated against the GEWEX-SRB product. Precipitation was validated against the TRMM 3B43 product. Parameter set "CL" was ultimately chosen to be used in the main experiment.

| option | meaning | result |
|---|---|---|
| iupmethod | method of calculating updraft base | z@max(w+sig(w)) |
| nclouds | number of different cloud scales | 2 |
| R1 | mean radius of cloud 1 | 20,000 m |
| D1 | minimum depth of cloud 1 | 4000 m |
| R2 | mean radius of cloud 2 | 800 m |
| D2 | minimum depth of cloud 2 | 80 m |
| capmax | convective trigger | $p_{LFC} - p_{up,base} < 100$ hpa |
| dc | dynamic control | Kain-Fritsch (Kain and Fritsch [1990]Kain [2004]) |
| cld2prec | condensate to precipitation conversion efficiency | 3% |
| rshort | short-wave radiation scattering | Harrington (Harrington and Olsson [2001]) |
| rlong | long-wave radiation scattering | Chen-Cotton (Chen and Cotton [1983]) |
| feedback | cumulus feedback on radiation? | Yes |

Table 5.1: Parameters and modules adjusted during the manual calibration procedure. The final results correspond with iteration "CL" in Figure 5-3.

$$bd = \frac{\sum_1^M \overline{R}_s^{EDBRAMS} - \sum_1^M \overline{R}_s^{SRB}}{\sum_1^M \overline{R}_s^{SRB}} \tag{5.3}$$

$$\text{rmse} = \sqrt{\frac{1}{M}\sum_1^M \left(\overline{R}_s^{EDBRAMS} - \overline{R}_s^{SRB}\right)^2} \tag{5.4}$$

| TEST ID | IUPMETHOD | NCLOUDS | R1 | DMIN1 | R2 | DMIN2 | R3 | DMIN3 | CAP_MAX | Dyn Cont | CLD2PREC | Rshort | Rlong | Feeback? | Grid | RSD NB | RSD RMSE | RSD VR | RLD NB | RLD RMSE | RLD VR | PCP NB | PCP RMSE | PCP VR | NOTES |
|---|---|---|---|---|---|---|---|---|---|---|---|---|---|---|---|---|---|---|---|---|---|---|---|---|---|
| BASE | 4 | 2 | 12000 | 6000 | 900 | 300 | | | 50 | GR | 0.002 | CC | CC | N | 50x40 | -.780 | | 6.000 | -.040 | | 4.850 | .040 | | 3.320 | |
| A | | | | | | | | | | | | Harr | Carma | Y | 50x40 | .520 | | 1.000 | -.060 | | 1.690 | -.590 | | .230 | |
| B | | | | | | | | | | | | CC | CC | N | 98x76 | -.550 | | 4.840 | -.020 | | 2.790 | -.120 | | 1.610 | |
| C | | | | | | | | | | | | Harr | CC | Y | 50x40 | .530 | | .740 | .030 | | 1.800 | 1.240 | | 3.250 | |
| D | | | | | | | | | | KF | | Harr | CC | Y | 50x40 | .530 | | .740 | .030 | | 1.800 | 1.240 | | 3.250 | |
| E | 2 | | | | | | | | | | | Harr | CC | Y | 50x40 | .560 | | .880 | .040 | | 1.520 | .010 | | 1.920 | good stats |
| F | | | | | | | | | 100 | | | Harr | CC | Y | 50x40 | .470 | | .950 | .040 | | 1.510 | -.160 | | .570 | |
| G | | | | | | | | | | | | Harr | CC | Y | 50x40 | x | | x | x | | x | x | | x | weirdness |
| H | | | | | | | | | | | 0.001 | Harr | CC | Y | 50x40 | .370 | | 1.650 | .010 | | 2.160 | 1.380 | | 2.960 | |
| I | | | | | | | | | 75 | | 0.001 | Harr | CC | Y | 50x40 | .240 | | 2.870 | .020 | | 2.940 | -.690 | | .250 | |
| J | | | | | | | | | -15 | | | Harr- | CC | Y | 50x40 | .240 | | 2.870 | .020 | | 2.940 | -.690 | | .250 | |
| K | | | | | | | | | -15 | | 0.002 | Harr- | CC | Y | 50x40 | .260 | | 2.480 | .020 | | 2.930 | -.660 | | .320 | |
| L | | | | | | | | | -10 | | | | | | | .259 | | 2.471 | .020 | | 2.956 | -.650 | | .339 | |
| M | | | | | | | | | -5 | | 0.003 | | | | | .267 | | 2.311 | .020 | | 2.958 | -.636 | | .372 | |
| N | | 1 | 12000 | 6000 | | | | | -10 | | 0.002 | | | | | .240 | | 2.532 | .021 | | 2.690 | -.635 | | .368 | |
| O | | 1 | 12000 | 6000 | | | | | -10 | | 0.002 | | | | | .174 | | 2.139 | .333 | | 2.892 | -.645 | | .338 | WEAKENING CENTRAL NUDGING 43200, NO HIGH NUDGING |
| P | | | | | | | | | | | | | | | | .176 | | 2.156 | .033 | | 2.690 | -.639 | | .353 | 3x3 Ensemble Members |
| Q | | | | | | | | | | | | | | | | | | | | | | | | | STRONG BOUNDARY FORCING |
| R | | | 12000 | 3000 | | | | | -10 | | 0.002 | | | | | .239 | | 2.400 | .020 | | 2.712 | -.625 | | .388 | SHORTER CLOUDS, MORE RAIN BUT LESS OPTICAL DEPTH |
| S | | | 6000 | 6000 | | | | | -10 | | 0.002 | | | | | | | | | | | | | | |
| T | | 1 | | | | | | | -10 | AS | 0.002 | | | | | .282 | | 2.849 | .026 | | 2.753 | -.840 | | .088 | |
| U | | 1 | | | | | | | -10 | KF | 0.002 | | | | | .320 | | 1.880 | .014 | | 2.550 | .349 | | 1.636 | |
| V | | 3 | 8000 | 6000 | 4000 | 3000 | 800 | 400 | -7 | KF | 0.002 | | | | | .330 | | 2.131 | .014 | | 2.811 | .175 | | 1.510 | |
| W | | 2 | 8000 | 8000 | 800 | 400 | | | -7 | KF | 0.002 | | | | | .338 | | 1.781 | .015 | | 2.819 | .080 | | 1.688 | |
| X | | 2 | 12000 | 8000 | 800 | 800 | | | -10 | KF | 0.002 | | | | | .335 | | 1.652 | .014 | | 2.766 | .245 | | 1.870 | RADIUS EFFECTING ENTRAINMENT IS SENSITIVE |
| Y | | 2 | 12000 | 8000 | 800 | 800 | | | -10 | KF | -0.020 | | | | | .240 | | 2.663 | .019 | | 2.914 | -.714 | | .073 | PRECIP EFFICIENCY IS SENSITIVE ALSO |
| Z | | 2 | 12000 | 8000 | 800 | 800 | | | -10 | KF | -0.100 | | | | | | | | | | | | | | |
| AA | | 2 | 12000 | 8000 | 800 | 800 | | | -10 | KF | -0.200 | | | | | .300 | | 2.004 | .014 | | 2.751 | .084 | | 1.286 | |
| AB | | 2 | 12000 | 8000 | 800 | 800 | | | -10 | KF | -0.100 | | | | | .292 | | 2.076 | .016 | | 2.781 | -.170 | | .706 | NO MASS SCALING ON CLOUD AREA |
| AC | | 2 | 12000 | 8000 | 800 | 800 | | | -10 | KF | -0.100 | | | | | .234 | | 3.200 | .015 | | 2.738 | -.215 | | .623 | FORCED UNITY ON CLOUD AREA |
| AD | | 2 | 12000 | 8000 | 800 | 800 | | | -1 | KF | -0.100 | | | | | .227 | | 3.523 | .015 | | 2.742 | -.201 | | .656 | |
| AE | | 2 | 12000 | 2000 | 800 | 400 | | | -1 | KF | -0.050 | | | | | .263 | | 2.747 | .017 | | 2.833 | -.447 | | .288 | FORCED UNITY AGAIN, BUT NOW SHALLOWER CLOUDS A |
| AF | | 2 | 12000 | 2000 | 800 | 800 | | | 5 | KF | -0.050 | | | | | -.094 | | 8.077 | .007 | | 3.084 | .038 | | .896 | VERTICAL WINDS SCALE DEP, REVERT TO CIN DEPTH |
| AG | | 2 | 12000 | 8000 | 800 | 800 | | | 5 | KF | -0.050 | | | | | .100 | | 4.065 | .012 | | 3.103 | .163 | | 1.160 | |
| AH | | 2 | 12000 | 8000 | 800 | 800 | | | 10 | KF | -0.050 | | | | | .100 | | 4.065 | .012 | | 3.103 | .163 | | 1.160 | REVERTING TO NORMAL CLOUD FRACTIONS |
| AI | | 2 | 12000 | 8000 | 800 | 800 | | | 10 | KF | -0.040 | | | | | .027 | | 5.501 | .013 | | 3.000 | .124 | | 1.032 | BEST CASE |
| AJ | | 2 | 12000 | 8000 | 800 | 800 | | | 50 | KF | -0.040 | | | | | .027 | | 5.501 | .013 | | 3.000 | .125 | | 1.032 | |
| AK | | 2 | 12000 | 4000 | 800 | 800 | | | 10 | KF | -0.040 | | | | | .026 | | 5.428 | .012 | | 3.007 | .126 | | 1.036 | |
| AL | | 2 | 8000 | 8000 | 800 | 800 | | | 10 | KF | -0.040 | | | | | .034 | | 4.656 | .015 | | 2.883 | .072 | | .780 | |
| AM | | 2 | 12000 | 8000 | 800 | 800 | | | 10 | KF | -0.030 | | | | | -.440 | | 6.618 | .014 | | 2.899 | .088 | | .912 | |
| AN | | 2 | 12000 | 8000 | 800 | 800 | | | 10 | KF | -0.030 | | | | | -.046 | | 6.486 | .014 | | 2.898 | .088 | | .920 | DEFAULT SCATTERING PARAMETER |
| AO | | 2 | 12000 | 8000 | 800 | 800 | | | 10 | KF | -0.040 | | | | | | | | | | | | | | TNUDTOP = 7200 |
| AP | | 2 | 6000 | 8000 | 800 | 800 | | | 10 | KF | -0.030 | | | | | -.002 | | 4.731 | .018 | | 2.713 | -.098 | | .464 | TNUDTOP=0 |
| AQ | | 2 | 6000 | 8000 | 800 | 800 | | | 10 | KF | -0.030 | | | | | -.003 | | 4.718 | .018 | | 2.717 | -.099 | | .461 | TNUDTOP = 21600 |
| AR | | 2 | 8000 | 8000 | 800 | 800 | | | 10 | KF | -0.030 | | | | 98x76 | | | | | | | | | | |
| AS | 2 | 2 | 8000 | 8000 | 800 | 800 | | | 10 | KF | -0.025 | | | | | .070 | | 5.192 | .024 | | 2.896 | .032 | | .824 | "PEAKY" |
| AT | 4 | 2 | 8000 | 8000 | 800 | 800 | | | 10 | KF | -0.025 | | | | | -.057 | | 5.685 | .018 | | 2.765 | .010 | | .067 | |
| AU | 4 | 2 | 8000 | 8000 | 800 | 800 | | | 10 | KF | -0.025 | | | | | -.580 | | 5.911 | .018 | | 2.750 | .016 | | .066 | SOIL AND LAI |
| AV | 2 | 2 | 8000 | 8000 | 800 | 800 | | | 10 | KF | -0.025 | | | | | .071 | | 5.303 | .025 | | 2.872 | .033 | | .827 | SOIL AND LAI |
| AW | 2 | 2 | | | | | | | 10 | KF | -0.025 | | | | | .058 | | 5.714 | .024 | | 2.910 | -.027 | | | NEW VERTICAL LAYERING |
| AX | 4 | 2 | 8000 | 8000 | 800 | 800 | | | 10 | KF | -0.025 | | | | | -.062 | | 6.041 | .018 | | 2.757 | -.042 | | .551 | |
| AY | 4 | 2 | 8000 | 8000 | 800 | 800 | | | 50 | KF | -0.025 | | | | | -.062 | | 6.041 | .018 | | 2.757 | -.042 | | .551 | |
| AZ | 2 | 2 | 12000 | 8000 | 800 | 800 | | | 10 | KF | -0.025 | | | | 98x76ed | .112 | | 2.137 | -.001 | | 3.222 | .076 | | 1.044 | |
| BA | 2 | 2 | 10000 | 8000 | 800 | 800 | | | 10 | KF | -0.020 | | | | 98x76ed | | | | | | | | | | |
| BB | 4 | 2 | 8000 | 8000 | 800 | 800 | | | 10 | KF | -0.030 | | | | 98x76ed | | | | | | | | | | |
| BE | 4 | 2 | 8000 | 8000 | 800 | 800 | | | 10 | KF | -0.030 | | | | 98x76ed | .091 | | 2.150 | .005 | | 3.161 | -.050 | | .681 | USES IGRASS 0, IBRANCH 2, PVE VEGETATION |
| BG | 4 | 2 | 8000 | 8000 | 800 | 800 | | | 10 | KF | -0.030 | | Carma | | 98x76ed | .099 | 46.212 | 2.036 | -.049 | 28.687 | 2.413 | -.046 | 97.063 | .752 | |
| BH | 4 | 2 | 8000 | 8000 | 800 | 800 | | | 10 | KF | -0.030 | | Carma | | 98x76ed | | | | | | | | | | MODIFIED Z 45 layer, MEDVIGY RADIATION PARAMETERS |
| BI | 4 | 2 | 8000 | 2000 | 800 | 800 | | | 10 | KF | -0.030 | | Carma | | 98x76ed | .158 | 55.166 | 1.506 | -.056 | 27.800 | 2.682 | -.056 | 93.192 | .750 | |
| BJ | 4 | 2 | 8000 | 2000 | 800 | 800 | | | 10 | KF | -0.025 | | | | 98x76ed | .115 | 50.798 | 1.976 | .003 | 23.367 | 3.198 | -.145 | 97.870 | .527 | New Cloud Distributions? |
| BK | 4 | | 8000 | 8000 | 800 | 800 | | | 10 | KF | -0.030 | | | | 98x76ed | | | | | | | | | | No Rescaling direct CDF approach |
| BL | | | 8000 | 2000 | 800 | 800 | | | 50 | KF | | | | | 98x76ed | .104 | 59.856 | 2.091 | -.009 | 26.825 | 3.860 | -.143 | 117.035 | .365 | m/mow |
| BM | 4 | 2 | 8000 | 8000 | 800 | 800 | | | 50 | KF | -0.030 | | | | 98x76ed | .089 | 47.164 | 2.272 | .004 | 21.987 | 2.966 | -.091 | 100.530 | .582 | LEAF_MAXWHC= 0.07 |
| BN | 4 | 2 | 8000 | 8000 | 800 | 800 | | | 50 | KF | -0.030 | | | | 98x76ed | | | | | | | | | | LEAF_MAXWHC= 0.07, RK4 |
| BO | 4 | 2 | 8000 | 8000 | 800 | 800 | | | 50 | KF | -0.030 | | Carma | | 98x76ed | | | | | | | | | | |
| BQ | 4 | 2 | 8000 | 4000 | 800 | 800 | | | -15 | KF | -0.100 | | | | 98x76ed | .248 | 67.135 | .766 | .007 | 23.410 | 3.192 | -.118 | 87.547 | .703 | New mass based area calculation |
| BR | 4 | 2 | 8000 | 4000 | 800 | 800 | | | -15 | KF | -0.100 | | | | 98x76ed | .289 | 76.548 | .507 | .008 | 23.489 | 3.200 | -.089 | 88.747 | | Mass based area calculation without max scaling |
| BS | | | | | | | | | -7 | KF | -0.080 | | | | 98x76ed | .270 | 72.171 | .659 | .008 | 23.267 | 3.160 | -.178 | 90.302 | .615 | Rescale turned off |
| BT | | | | | | | | | 100 | KF | -0.080 | | | | 98x76ed | .220 | 61.452 | 1.068 | -.002 | 23.637 | 3.224 | .212 | 104.931 | 1.177 | Rescale turned off |
| BU | | | | | | | | | 75 | KF | -0.070 | | | | 98x76ed | .199 | 57.927 | 1.254 | -.001 | 23.354 | 3.183 | .151 | 101.393 | 1.029 | |
| BV | | | 4000 | 2000 | 800 | 800 | | | 75 | KF | -0.070 | | | | 98x76ed | .218 | 61.070 | 1.070 | -.055 | 22.682 | 3.089 | -.055 | 95.154 | .627 | |
| BX | | | | | | | | | 75 | KF | -0.050 | | | | 98x76ed | .148 | 51.394 | 1.717 | .001 | 22.617 | 3.107 | .037 | 97.920 | .769 | |
| BZ | 4 | 2 | 15000 | 4000 | | | | | -5 | KF | -0.050 | | | | 98x76ed | .253 | 68.102 | .786 | .008 | 23.108 | 3.128 | -.305 | 98.803 | .433 | |
| CA | 4 | 2 | 15000 | 4000 | | | | | -20 | KF | -0.050 | | | | 98x80ed | .252 | 67.824 | .790 | .009 | 23.046 | 3.118 | -.309 | 98.739 | .428 | |
| CB | 4 | 2 | 15000 | 4000 | | | | | 75 | KF | -0.020 | | | | 98x80ed | .049 | 52.624 | 3.135 | .001 | 23.187 | 3.169 | -.141 | 100.318 | | |
| CC | 4 | 2 | 15000 | 4000 | | | | | 75 | KF | -0.010 | | | | 98x80ed | | | | | | | | | | |
| CD | 4 | 2 | 8000 | 4000 | | | | | 100 | KF | -0.050 | | | | 98x80ed | .148 | 51.407 | 1.734 | .000 | 51.407 | 3.117 | .048 | 97.198 | .760 | |
| CE | 2 | 2 | 8000 | 4000 | | | | | 75 | KF | -0.050 | | | | 98x80ed | | | | | | | | | | |
| CF | 4 | 2 | 8000 | 4000 | 800 | 80 | | | 75 | KF | -0.050 | | | | 98x80ed | .156 | 52.976 | 1.756 | -.002 | 23.454 | 3.216 | -.008 | 96.603 | .744 | |
| CG | 4 | 2 | 8000 | 4000 | 800 | 80 | | | 75 | KF | -0.050 | | | | 98x80ed | .156 | 53.010 | 1.970 | .000 | 3.390 | 23.580 | -.014 | 74.460 | 1.400 | |
| CH | | | 8000 | 4000 | 800 | 80 | | | 75 | KF | -0.050 | | | | 98x80ed | | | | | | | | | | |
| CI | 4 | 2 | 8000 | 4000 | 800 | 80 | | | 75 | KF | -0.050 | | Carma | | 98x80ed | .258 | 72.889 | 1.186 | -.113 | 57.220 | 2.220 | -.391 | 135.150 | .580 | Feb 2003 |
| CK | 4 | 2 | 20000 | 4000 | 800 | 80 | | | 100 | KF | -0.050 | | | | 98x80ed | .271 | 76.700 | 1.460 | .009 | 30.120 | 5.200 | -.140 | 90.848 | 1.689 | More clouds and more rain. |
| CL | 4 | 2 | 20000 | 4000 | 800 | 80 | - | - | 100 | KF | -0.030 | Harr | CC | Y | 98x80ed | | | | | | | | | | |

Figure 5-3: Table showing the iterations of the manual calibration procedure.

## 5.4 Evaluation of the Calibrated Model

The final validation makes a comparison with observed data for the second year of simulation. The second year of simulation uses lateral boundary conditions from the ERA-INTERIM 2003 dataset. The southern portion of the basin experiences wet-season conditions in February and dry-season conditions in June. These two months were evaluated for their spatial patterning, mean atmospheric profiles and surface fluxes.

### 5.4.1 ED2-BRAMS Rawinsonde Comparison - Feb 2003

Mean monthly profiles of model estimated windspeed, air temperature, specific humidity and moist static energy are compared with mean rawinsonde data over Manaus (see Figures 5-4 through 5-7). Comparisons are made at 00:00Z UTC (8pm local time) and 12:00Z UTC (8am local time). Note that windspeed from rawinsondes reflect point-scale measurements (which include energy at the turbulent scale), while the model output reflects only the mean advective velocities. Even so, the model estimates relatively high wind-speeds in the lower troposphere and atmospheric boundary layer, while estimating relatively lower wind-speeds in the mid to upper troposphere. Underestimation of wind-speeds in the upper atmosphere could be attributed to the fact that eddies at scales smaller than the atmospheric grid are contributing significantly to the point-scale wind-magnitudes. It is also possible that the turbulent component of the total wind-speed scales on advective wind-speed, which increases at high altitudes.

The model estimates a consistently warmer atmosphere, in the range of about two degrees both morning and evening. Model estimated specific humidity in the lower troposphere is lower than the rawinsondes. The cool mid troposphere and its low water vapor content decrease the possible variability in specific humidity, which is likely why there is little difference between model and measurement.

Moist static energy, the combined energy of geopotential, moisture and temperature, is slightly underestimated by the model in the lower troposphere and then overestimated in the mid to upper troposphere. Assuming that the model total albedo and lateral boundary conditions are unbiased, this may suggest that the model is convecting

relatively large quantities of warm moist air at the surface and entraining it to the upper atmosphere.

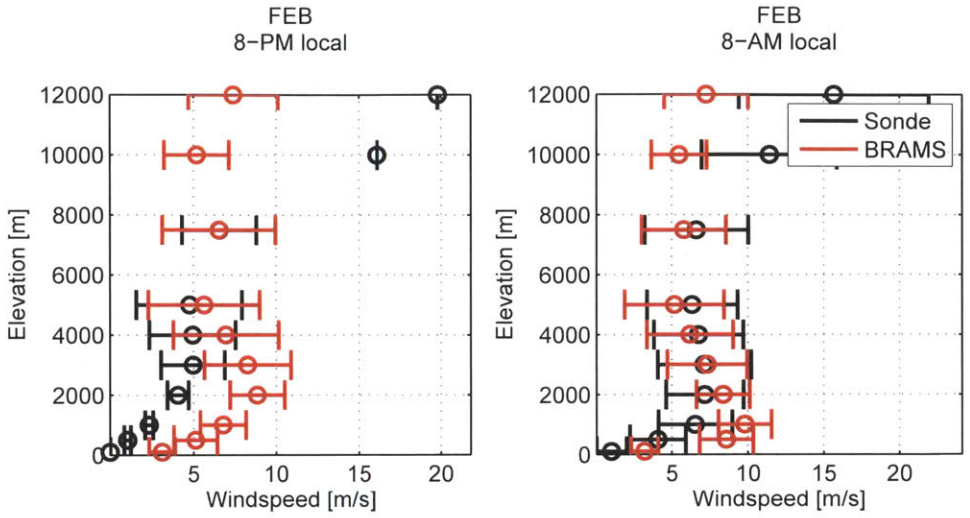


Figure 5-4: Comparison of model estimates with rawinsonde data, mean wind magnitude. Manaus, February 2003.

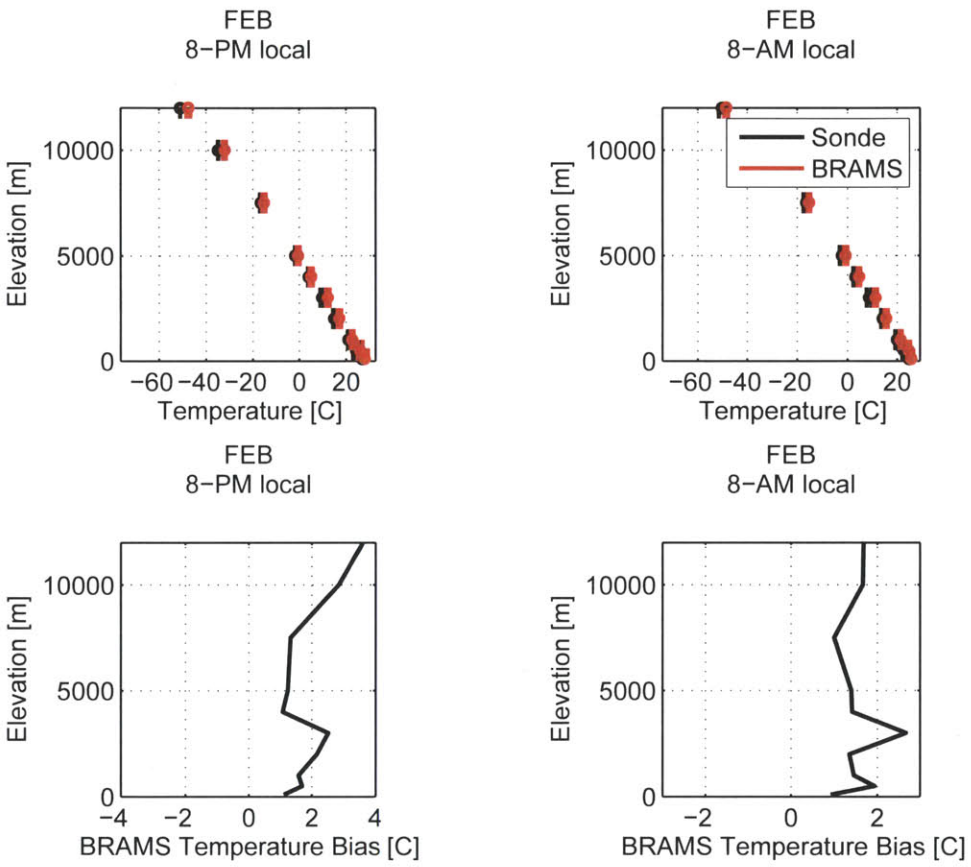


Figure 5-5: Comparison of model estimates with rawinsonde data, mean air temperature. Manaus, February 2003.

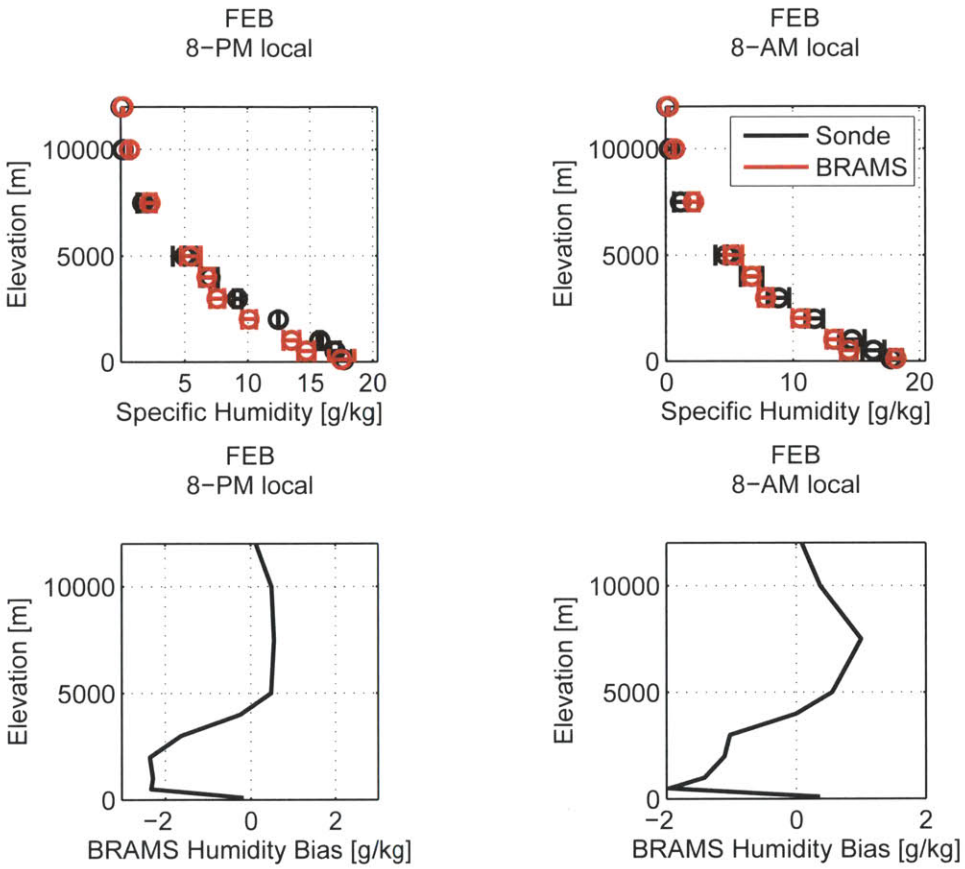


Figure 5-6: Comparison of model estimates with rawinsonde data, mean specific humidity. Manaus, February 2003.

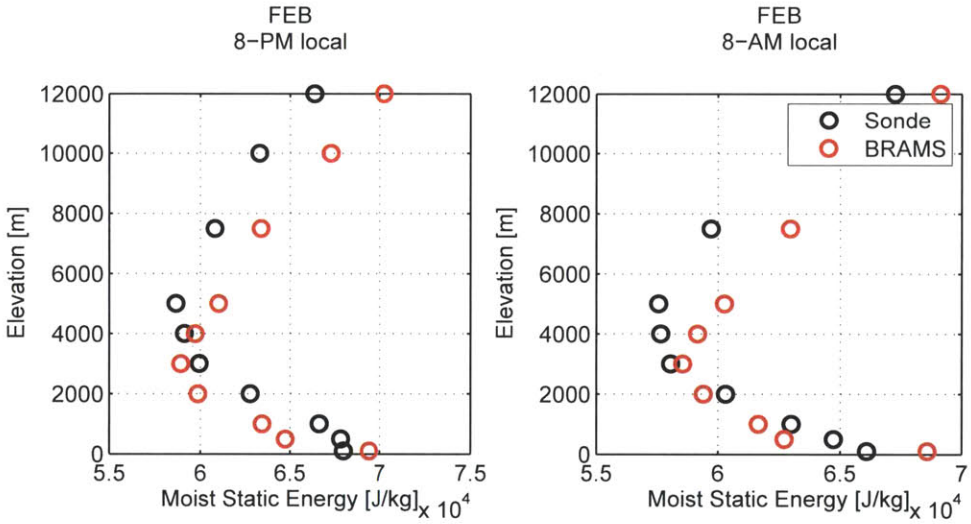


Figure 5-7: Comparison of model estimates with rawinsonde data, mean moist static energy. Manaus February 2003.

### 5.4.2 ED2-BRAMS Radiation and Precipitation Comparison

The model shows a fair amount of agreement with the TRMM 3B43 in terms of the distribution of rain volumes over the study area (Figures 5-10 and 5-13), and good agreement on the spatial patterning and locations of precipitation maxima (Figures 5-8 and 5-11). The greatest discrepancies in February are found north of the equator (its dry season) and in far eastern Brazil. The TRMM data validates that strong depressions in monthly precipitation exist in these areas but does not suppose that zero monthly precipitation occurs. Significant differences exist over the Andes mountains and over the equatorial Atlantic, however these may be attributed to measurement or algorithmic uncertainties in the TRMM system. There is generally good agreement between the model and the measurments regarding interseasonal variability (see Figure 5-14). Here monthly means are partitioned into the five zones of analysis shown in Figure 4-4. The seasonal variability in both datasets is significantly greater than their differences. There is some difference in the peakiness of the wet-season onset in the South American Convergence Zone, but the time of peak wet and dry season shows good agreement.

The model estimated patterns of downwelling shortwave radiation at the surface have a high correlation with precipitation patterns, which are associated with the optical depth of precipitating clouds. In regions of heavy monthly precipitation, the model is fairly successful at matching downwelling shortwave radiation with SRB estimates (see Figures 5-9 and 5-12). The model seems to overpredict surface shortwave radiation in regions of low-precipitation, which appears to be due to under-estimation of non-cumulus clouds, perhaps stratus or cirrus ice clouds. The relatively higher estimate of dry-region short-wave radiation is consistent with the zone-by-zone inter-seasonal trends shown in Figure 5-15. The three Amzonian analysis zones with higher monthly precipitation showed less overall bias, whereas the Southern Brazil region showed the largest positive bias.

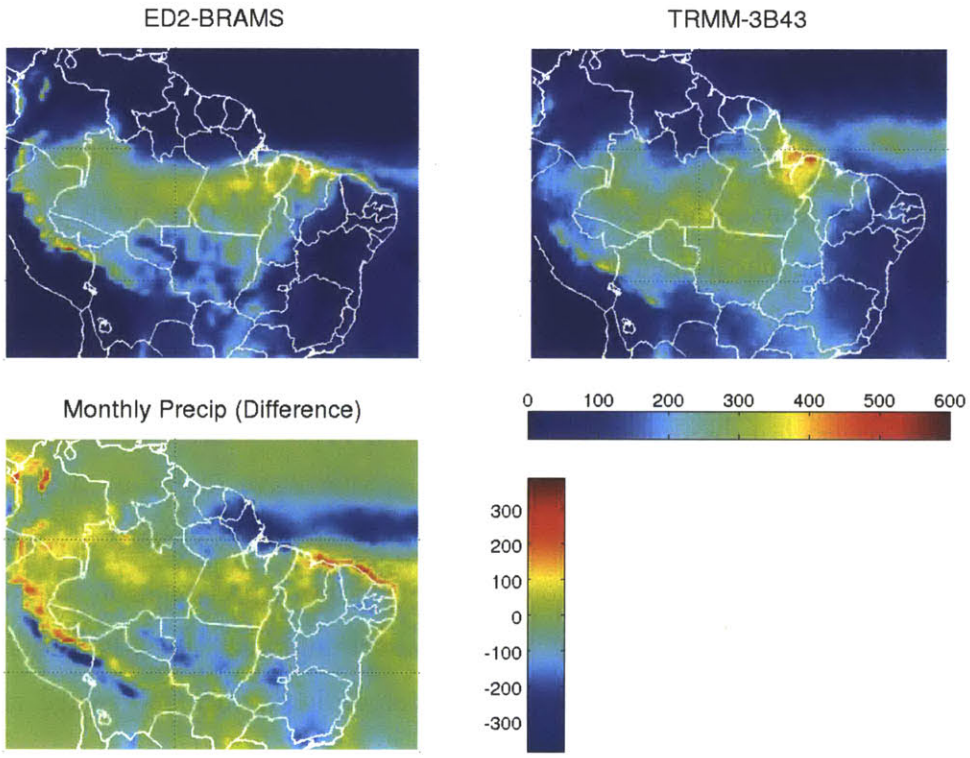


Figure 5-8: Model estimated and TRMM 3B43 observed precipitation, February 2003. The arithmetic bias difference for the model estimate is provided in the lower left panel.

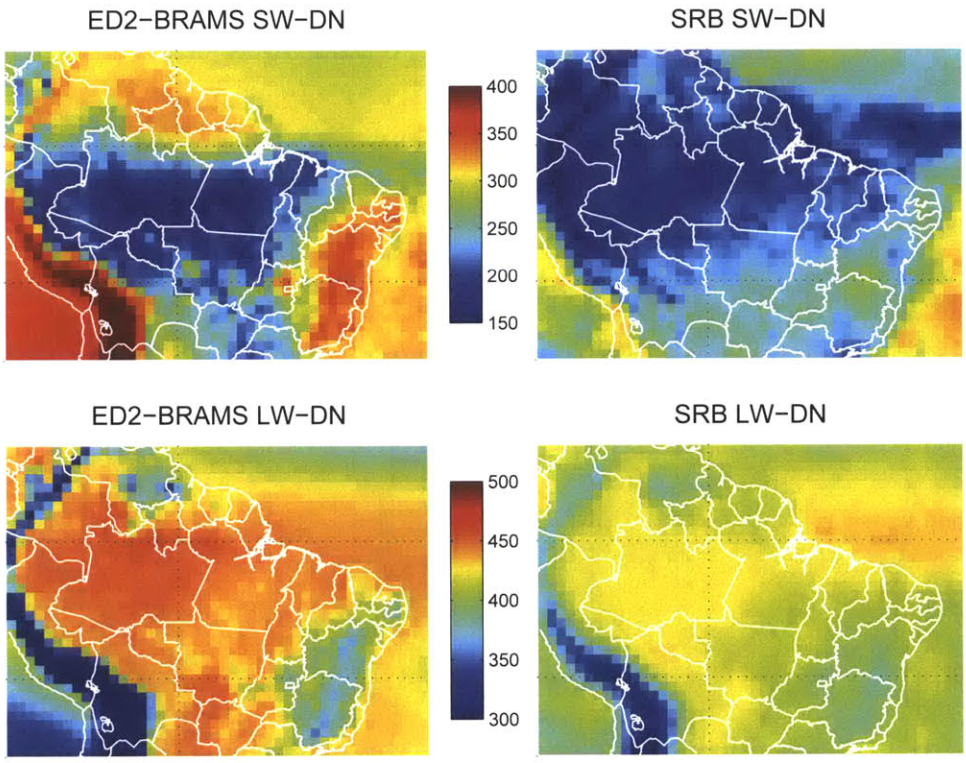


Figure 5-9: Model estimated and GEWEX-SRB observed short and longwave radiation, February 2003.

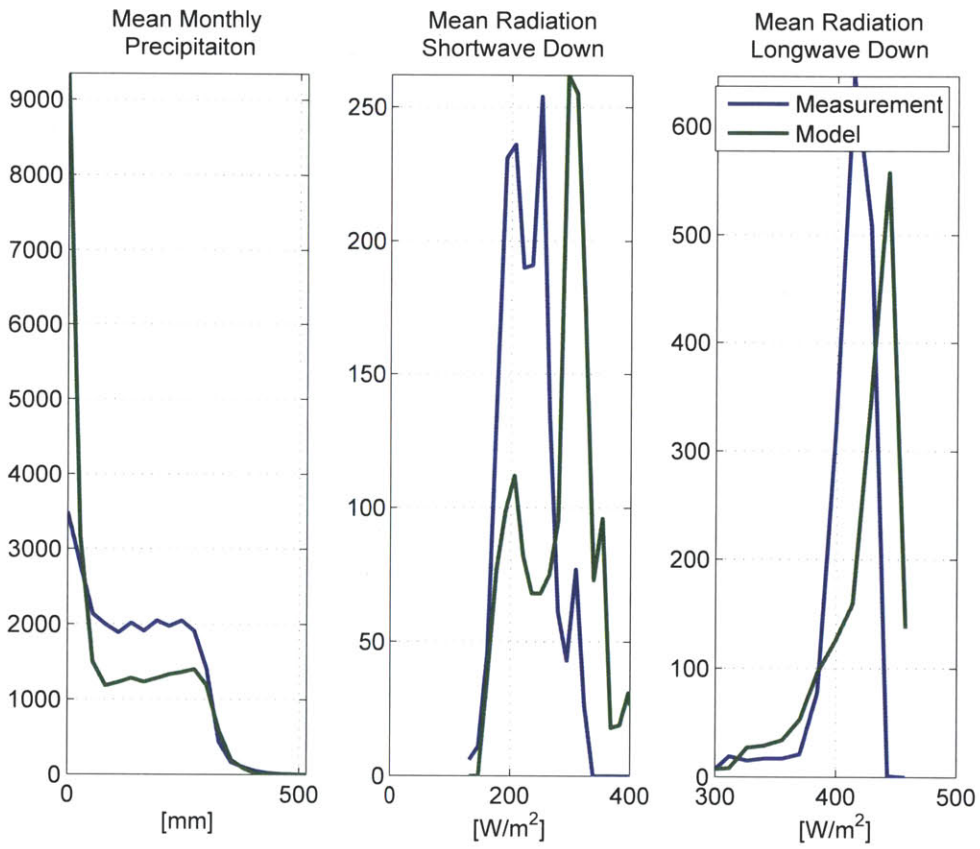


Figure 5-10: Histograms of the spatial field of observed and model estimated monthly precipitation and radiation, February 2003.

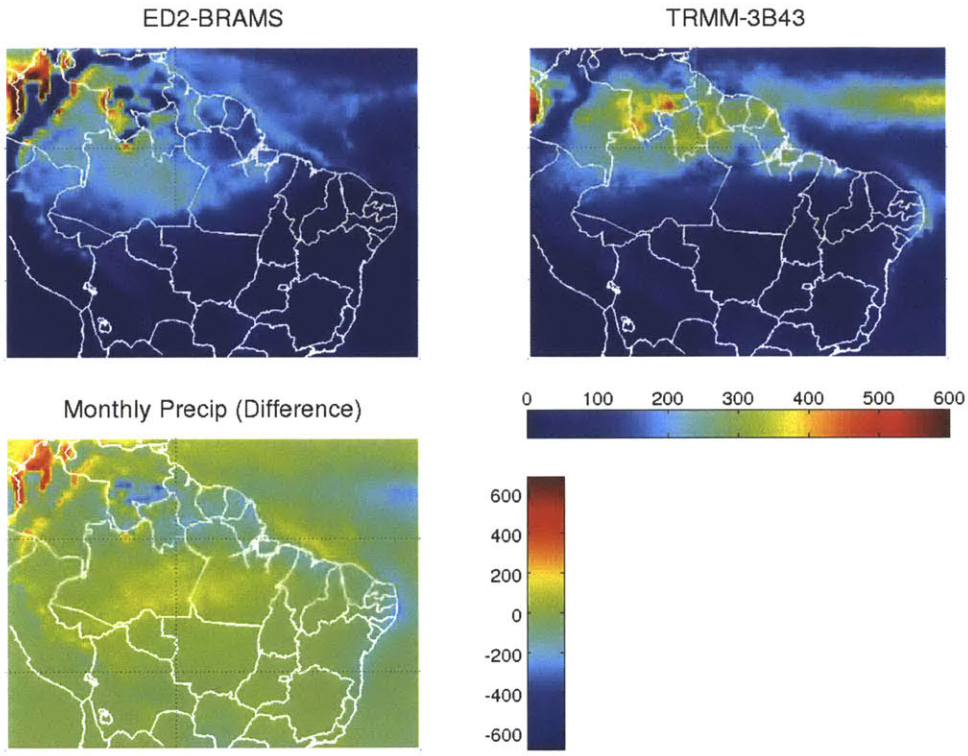


Figure 5-11: Model estimated and TRMM 3B43 observed precipitation, June 2003. The arithmetic bias difference for the model estimate is provided in the lower left panel.

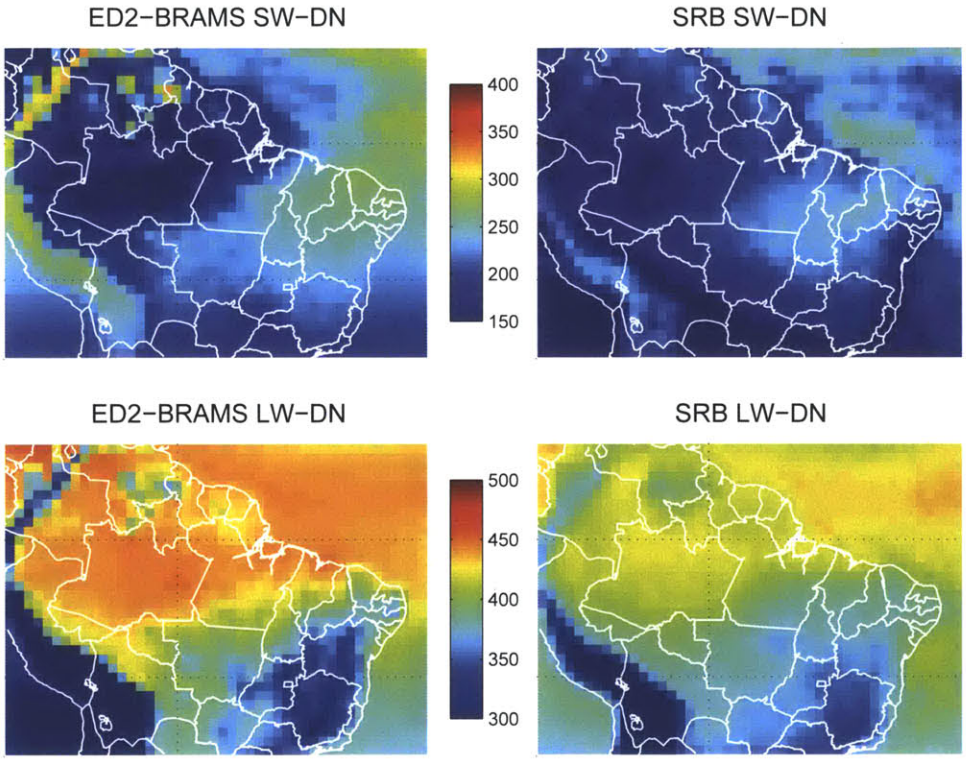


Figure 5-12: Model estimated and GEWEX-SRB observed short and longwave radiation, June 2003.

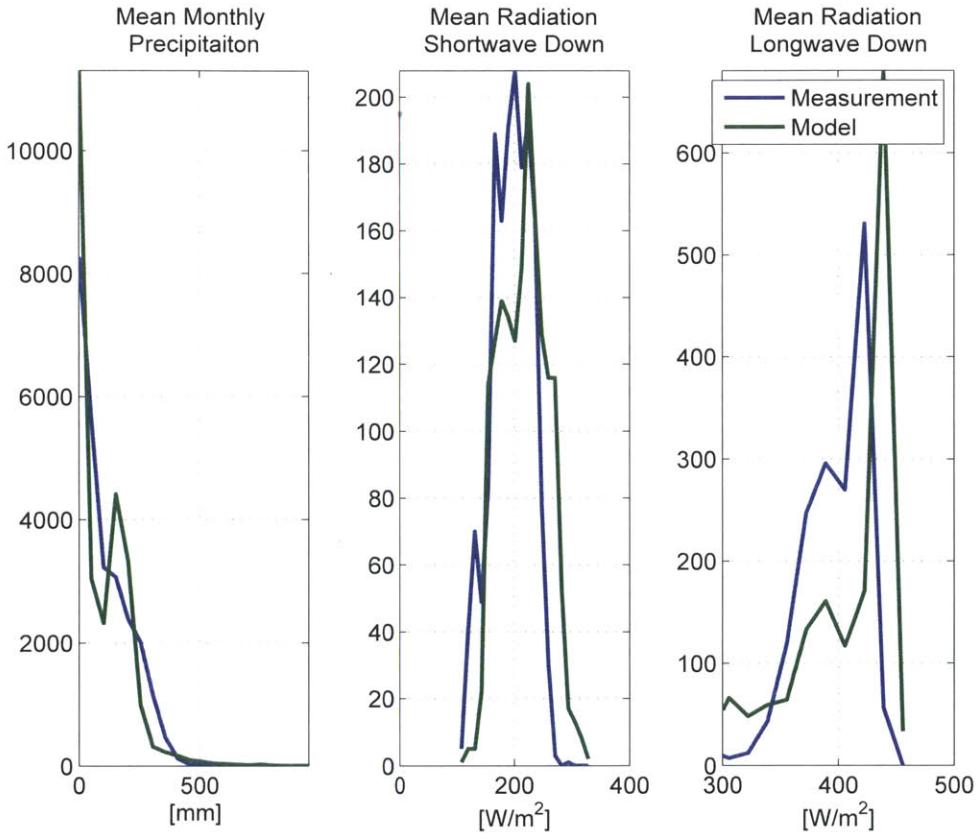


Figure 5-13: Histograms of the spatial field of observed and model estimated monthly precipitation and radiation, June 2003.

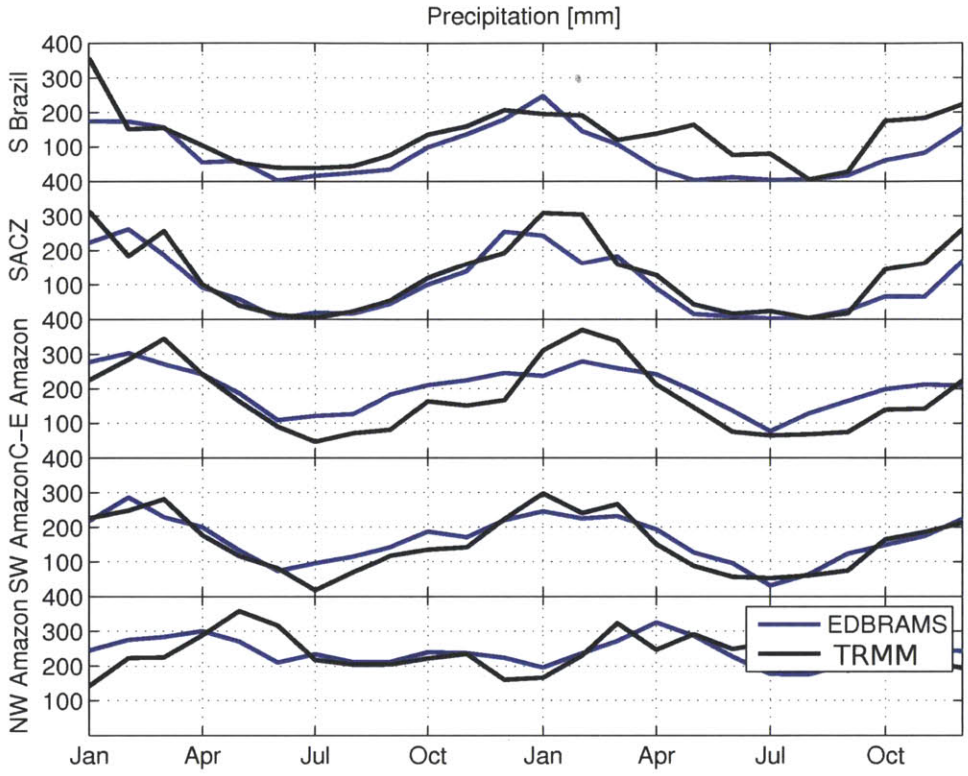


Figure 5-14: Mean monthly precipitation from ED-BRAMS and the SRB product. Spatial means are taken within zones according to Figure 4-4.

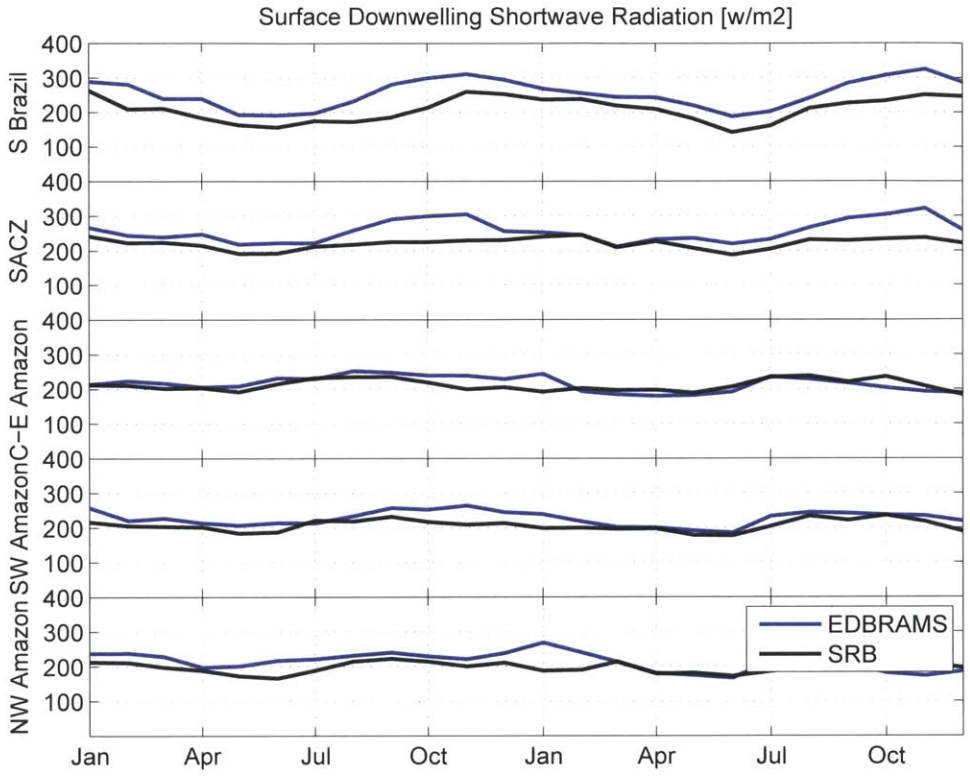


Figure 5-15: Mean monthly downwelling short-wave radiation from ED-BRAMS and the SRB product. Spatial means are taken within zones according to Figure 4-4.

### 5.4.3 Cloud Mean Profile Data

Cloud profile validation datasets were constructed from CloudSat 2B-CWC-RO (Cloud Water Content (Radar-Visible Optical Depth) and 2B-CLDCLASS-LIDAR (Radar-Lidar Cloud Classification)[1]). The combination of these datasets allowed for an assessment of the vertical mean profile of liquid water content, ice water content and also classification as cumulus or non-cumulus. Overpasses during February 2007-2011 that intersected the geographic region $3^oN - 12^oS$ and $70^oW - 55^oW$ were collected and interpolated to a constant vertical datum above the surface. Profile mean quanitities were calculated over all day-time overpasses; these overpasses all occured at approximately 17hrs UTC. ED2-BRAMS grid pixels located within the CloudSat intersection domain and time were selected. The cumulus and non-cumulus mean cloud liquid water, ice water, and cloud fractions were calculated for comparison with CloudSat.

The purpose of the comparison was to get a sense of whether the simulations were within reasonable ranges of water contents and cloud fractions, and also if the transitions (liquid to ice) were occuring at reasonable elevations. The comparison was not expected to have low differencing errors. CloudSat measurements are known to have issues returning signals during moderate to intense rainfall and therfore do not reflect profiles of precipitating clouds. This cannot be filtered from the model mean profiles. It must also be assumed that the cloud classification algorithm is not without error. Finally, EDBRAMS model output is returned every 3 hours to save space. The closest model output time to the CloudSat overpass is 18 UTC (2 pm local), which is one hour later than the 1 pm CloudSat overpass.

Nonetheless, the mean profile data gives the sense that the model can roughly approximate the vertical profile of mean cloud liquid and water content (see Figure 5-16). Note this is the all-sky mean water content, not the in-cloud water content (all-sky includes non-cloud zeros). The upper left panel in Figure 5-17 suggests that the model is somewhat successful at estimating the average cumulus cloud base. There is more disagreement regarding the water content associated with the liquid to ice transition

[1]Cloudsat datasets were provided online by CloudSat Data Processing Center, courtesy of NASA, Colorado State University and their partners.

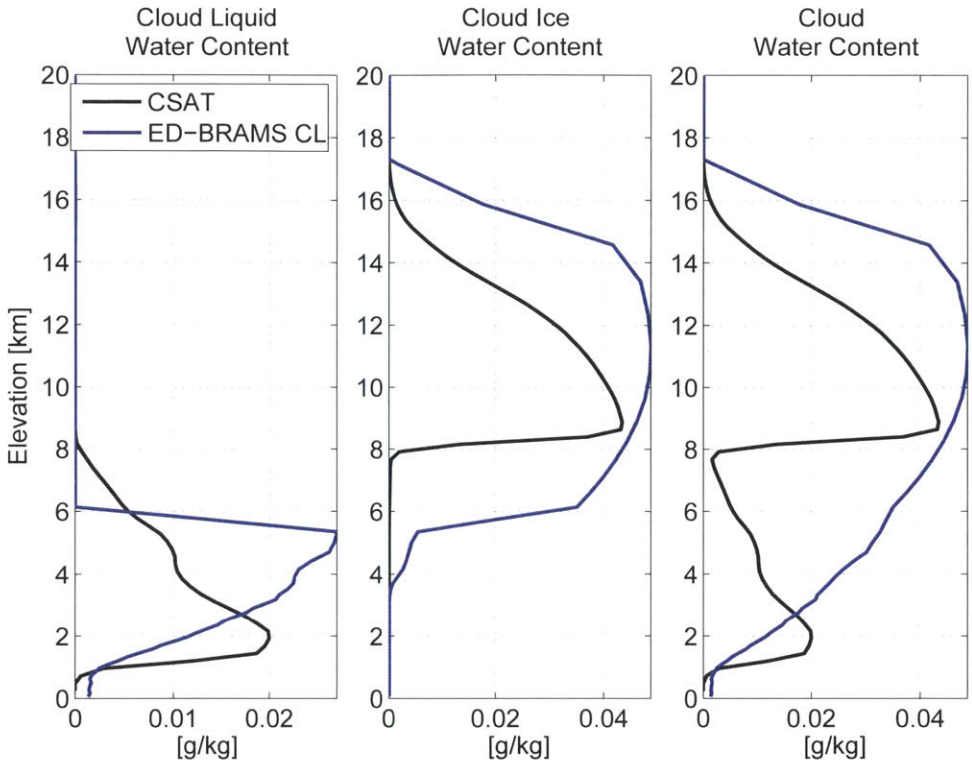


Figure 5-16: Mean profiles of CloudSat and model estimated total water content for $3^oN - 12^oS$ and $70^oW - 55^oW$.

region in cumulus clouds. CloudSat suggests this zone is located at approximately $7500$ meters, at which virtually no cloud water can be found. Interestingly enough, it does find that non-cumulus clouds have the same freezing point, at which both phases are detected. The vertical separation of the CloudSat liquid and ice cumulus cloud water is questionable.

Cloud fraction is a two dimensional variable in ED2-BRAMS and appears as a vertical line in the mean profiles (see the lower panels of Figures 5-17 and 5-18). It could be argued that, compared to CloudSat, the model tends to generate fewer cumulus clouds or perhaps clouds that take up a smaller mean footprint (at peak elevations of water content), yet it estimates clouds more laden with water.

EDBRAMS estimates a larger mean non-cumulus cloud fraction with comparable mean water content. A signficant difference between the two is also observed in the

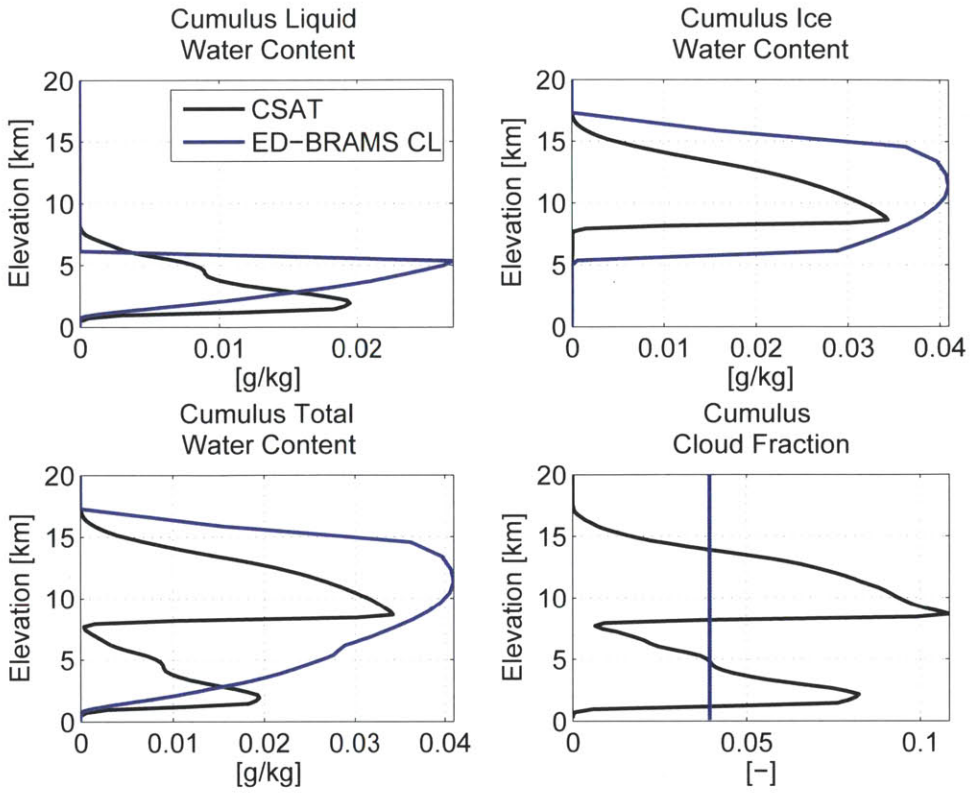


Figure 5-17: CloudSat and model estimated cumulus cloud profile data, $3^oN - 12^oS$ and $70^oW - 55^oW$.

profile of non-cumulus liquid water content. The model estimates non-cumulus liquid water inside the planetary boundary layer to the earth's surface.

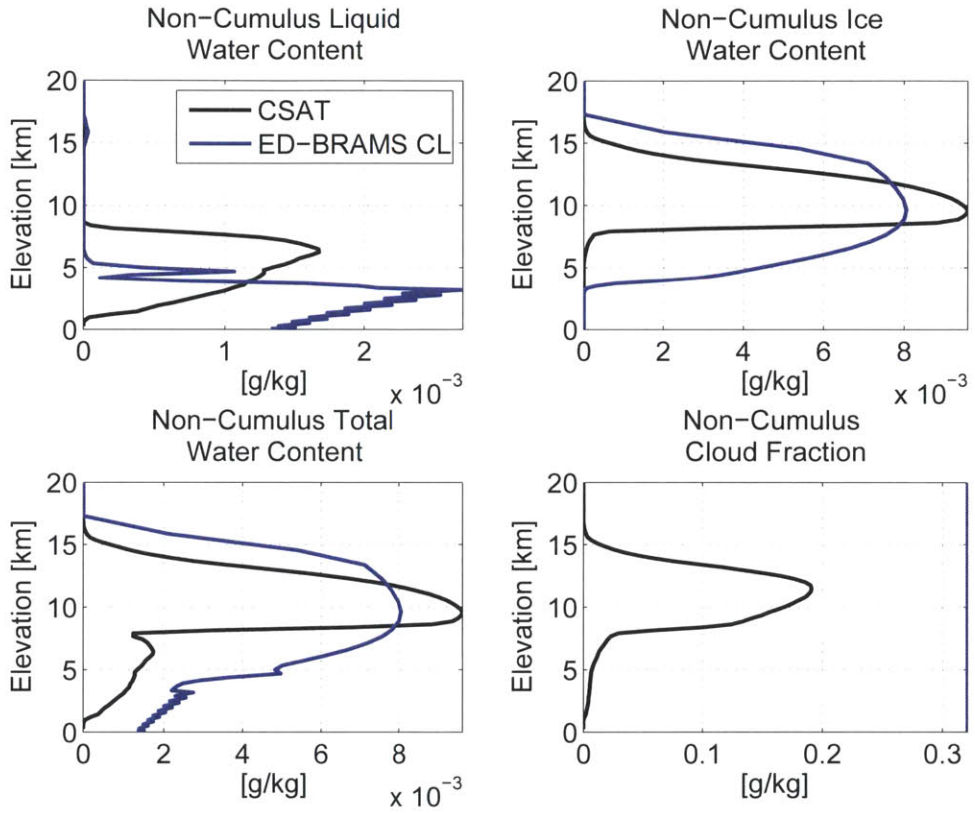


Figure 5-18: CloudSat and model estimated non-cumulus cloud profile data, $3^o N - 12^o S$ and $70^o W - 55^o W$.

### 5.4.4 Validation of Surface Energ Fluxes

Monthly mean land surface energy fluxes of net radiation, sensible and latent heat fluxes are validated against flux tower measurements at the validation sites. A comparison for February of 2003 is provided in Figure 5-19. (Recall that Figure 4-23 shows the locations of the various stations.) The kilometer 67 site at Santarem was excluded from this analysis because of questionable solar radiation data. The mean of kilometer 77 and 83 are compared with the model. The comparison with the tower data in February shows that model estimated net-radiation is within the daily variability range for four out of five sites. Estimates of latent heat show some positive bias, but three of the sites have overlapping standard deviations. The model typically unerestimated sensible heat flux compared to the station observations.

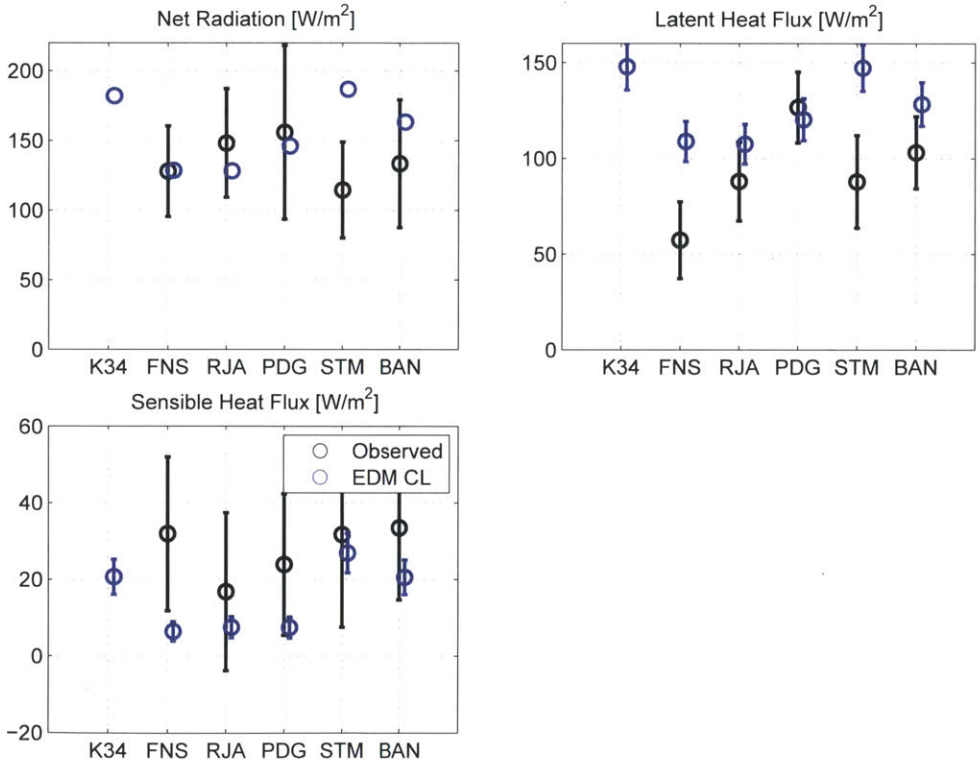


Figure 5-19: Mean surface energy budget comparison with measurement stations, February 2003.

## 5.5 Summary of Model Behavior

Monthly mean maps of precipitation for the period are provided, see Figure 5-20. These 12 maps show the meridional oscillation of the Intertropical Convergence Zone (ITCZ) which coincides with precipitation.

The ED2-BRAMS system is ultimately going to be used to test hydrologic feedback to land-conversion. In esssence this is a sensitivity analysis. As such, there is less concern that the model can reproduce weather that matches day-to-day or hour-to-hour observations. The objectives of this experiment require that the modeling system is adequate at estimating mean tendencies. It requires that over seasonal time-scales the distributions of mass and energy match observations to such a degree that there is trust in the physical processes. While both the model and the validating observations are by no means perfect, there is evidence that the modeling system can capture the seasonal variability of precipitation and radiation, and climate that is consistent with the terrestrial biomes.

The sensitivity experiment is going to be observed mostly through a lens that concerns changes in rainfall. There are many model processes and conditions relevant to the estimation of rainfall; such as boundary layer turbulence, profiles of moist static energy, profiles of temperature and humidity. As well there are indirect processes that lead to these conditions such as the convergece, divergence and advection of moisture and energy. And there are atmospheric diagnostics that correlate with the presence of rainfall, and serve to acknowledge that it was generated with some consistency (such as the presence of cumulonimbus clouds during intense rainfall). This validation has shown that the model can provide reasonable estimates of these supporting variables as well. Again, it is stressed that physical land-atmospheric models have limitations, but this validation suggests that the physical system is operating in such a way that a sensitivity analysis can be conducted with confidence that the results are modestly unbiased.

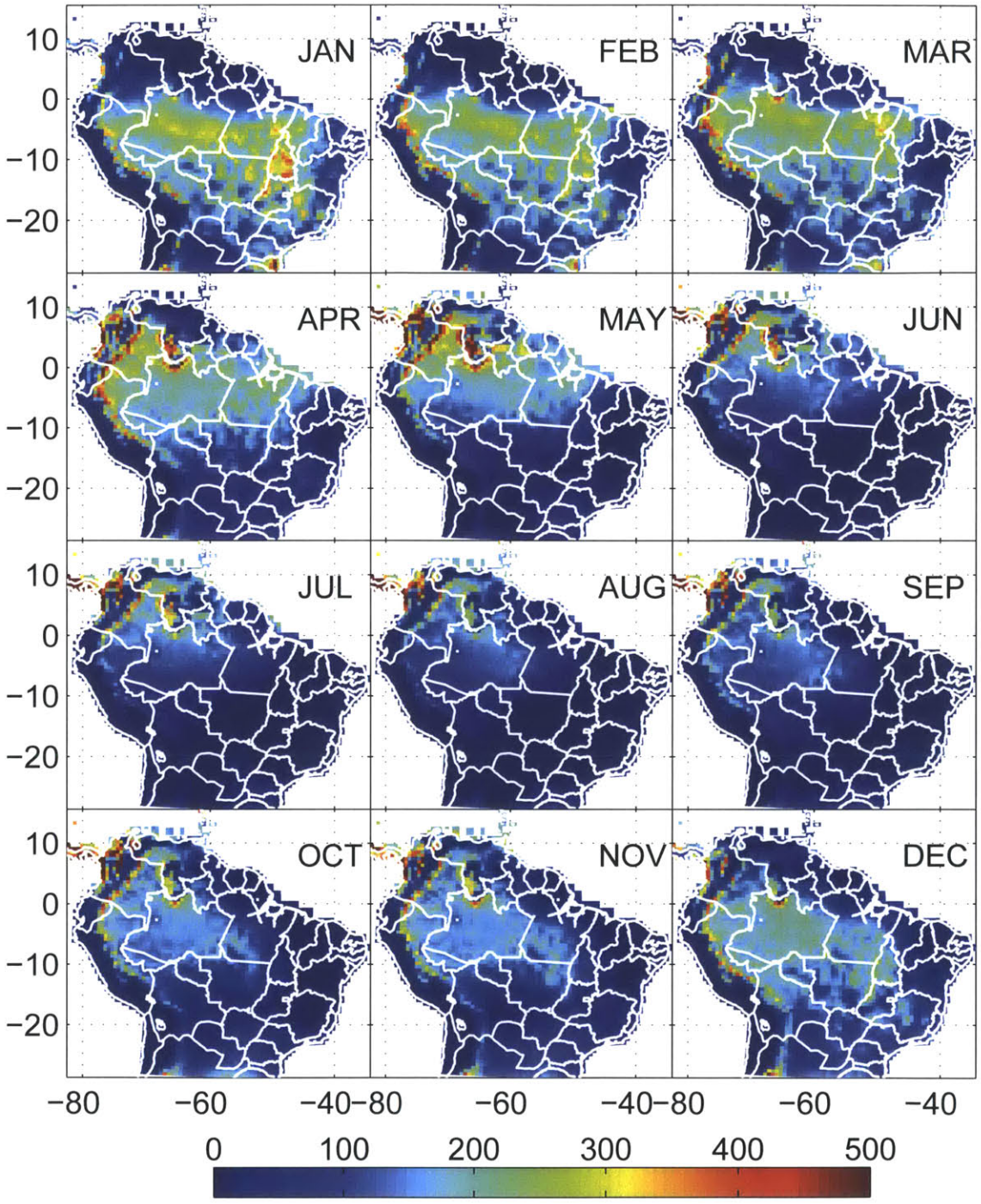


Figure 5-20: Maps of ED2-BRAMS estimated monthly mean precipitation for the "Actual" vegetation boundary condition, 2002-2005.

# Chapter 6

# Hydrologic Response to Human Land-Conversion

This chapter will discuss hydrologic response from the coupled model simulations that use Potential and Actual vegetation surface conditions. Mean differences in key hydrologic variables are mapped out and compared. Focus areas are chosen where hydrologic response between the two simulations shows significance, and ecosystems show they are susceptible to change.

## 6.1 Regional Assessment of Hydrologic Differences

Maps of the differences in mean monthly simulated precipitation are shown in Figure 6-1. Differences are calculated by subtracting Potential Vegetation (PV) simulation results from the Actual Vegetation (AV) simulation results. Recall that monthly mean precipitation accumulations for the (PV) condition are provided in Figure 5-20. Precipitation accumulation totals for the potential case can be visually extrapolated by adding the differences from Figure 6-1 to the totals in Figure 5-20. The difference in annual mean precipitation for each year are provided in Figure 6-2.

*Unless otherwise noted, differences and differentials indicate the subtraction of variables of the Potential Vegetation (PV) case from the Actual Vegetation (AV) Case, i.e. (AV-PV).*

There are certain features in the (AV-PV) differential precipitation that are consistent

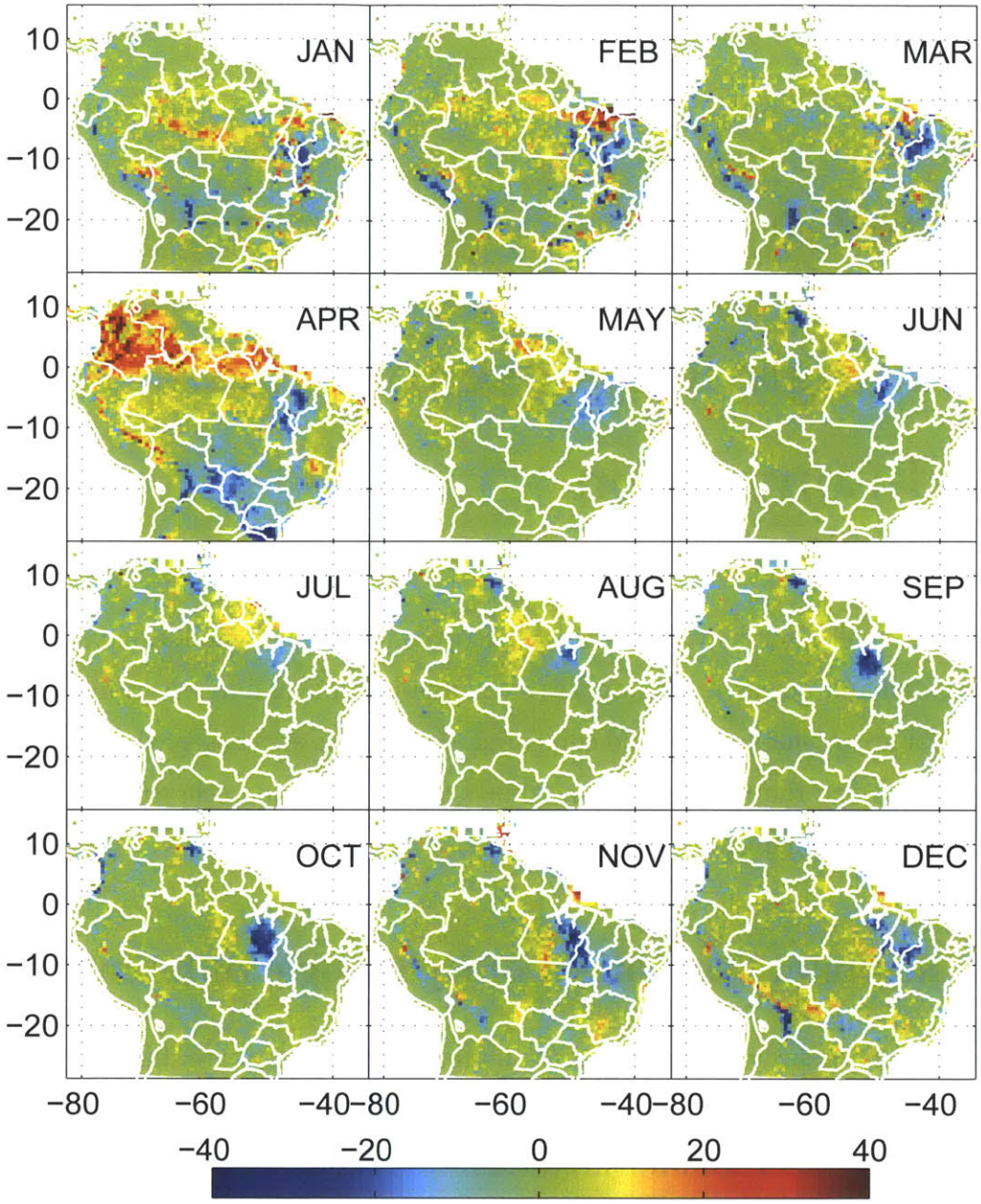


Figure 6-1: Maps of the differences in mean monthly precipitation accumulations estimated by ED2-BRAMS. Differences are in mean accumulations using the "Potential" minus the "Actual" vegetation boundary conditions, 2002-2005.

across inter-seasonal and inter-annual time scales. One prominent feature is a dipole of decreased precipitation southeast of the Amazon river delta and an area of increased precipitation northwest of the delta. The (AV) condition generates a modest *increase*

over most of the Amazon basin in general, although this difference does not appear to be very large and has considerable spatial variability. The increased precipitation over the basin is highest January through April. The month of April shows a particularly strong difference compared to the other months, featuring a strong positive differential precipitation in the northern regions and Amazon basin, while a strong negative differential exists in the southern regions below $10^oS$ and above the deforested areas near $5^oS$ $50^oW$. Another consistent feature in differential precipitation is a prominent decrease east of the Andes mountains at $20^oS$. This depression is seasonal, only appearing in the wet-season. The annual maps of differential precipitation each confirm these three features.

The differential yearly mean down-welling shortwave radiation shows a strong negative correlation with annual precipitation, see Figure 6-3. The 95th percentile differences peak at about $10W/m2$, and are strongest over the dipole associated with the precipitation differential, as well as over the eastern Brazilian dry lands ($41^oW$).

From a biological perspective, the significance of the mean annual precipitation and radiation differential is dependant on how consistent the changes are (inter-annual variance), when the changes occur (seasonality) and how large the differences are compared to the total. Along with the total differences in precipitation and radiation, Figure 6-4 shows normalized differences (the differential divided by the average of the two cases), as well as a standard difference. In this case the standard difference is the normalized difference divided by the standard deviation of the normalized difference (across years). A standard difference of 1, suggests that the normalized difference is equal to its inter-annual standard deviation.

Normalized precipitation differentials in the bulk of the Amazon basin are weak compared to other areas of the continent. A relatively strong normalized bias is apparent on the negative lobe of the differential precipitation dipole. Another area of significant normalized differential precipitation is in southern Bolivia. There is significant differential precipitation over the eastern Brazil dry-lands. However, upon inspection of the standard differences (see lower left panel of Figure 6-4) at these locations, precipitation differences in eastern Brazil do not appear to be consistent from year to year.

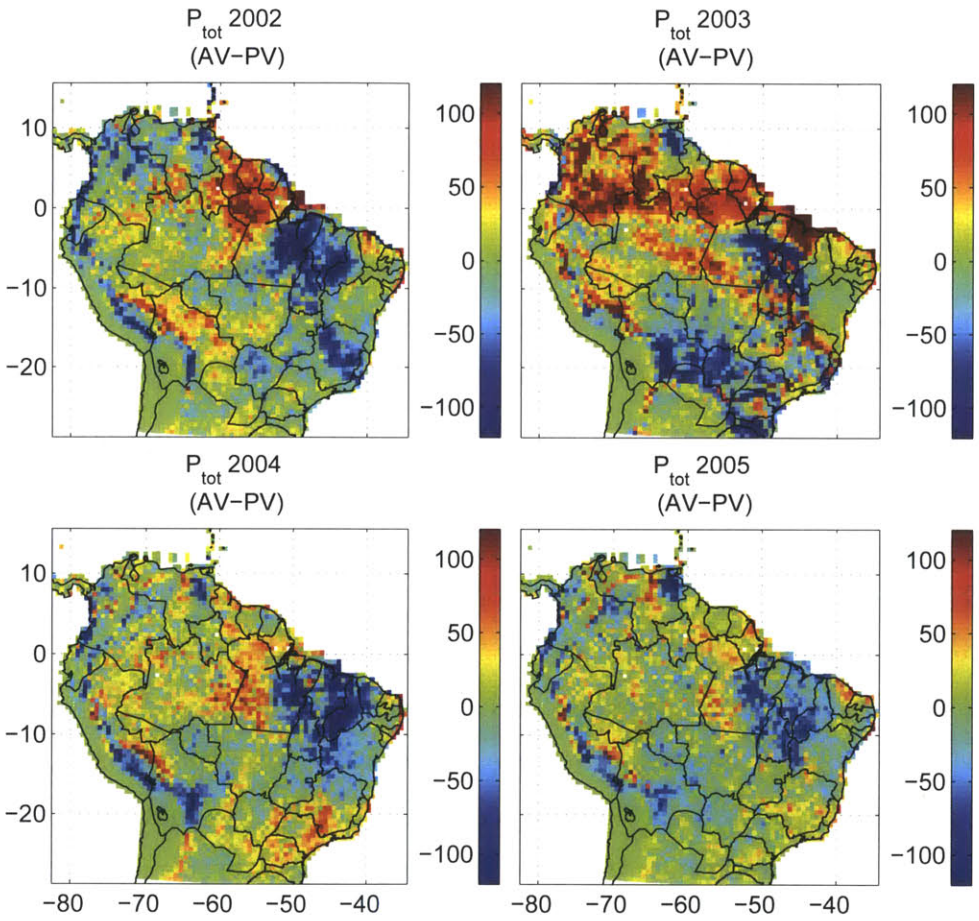


Figure 6-2: Differences in total annual precipitation [mm], 2002-2005. Potential Vegetation Condition is subtracted from the Actual Vegetation condition.

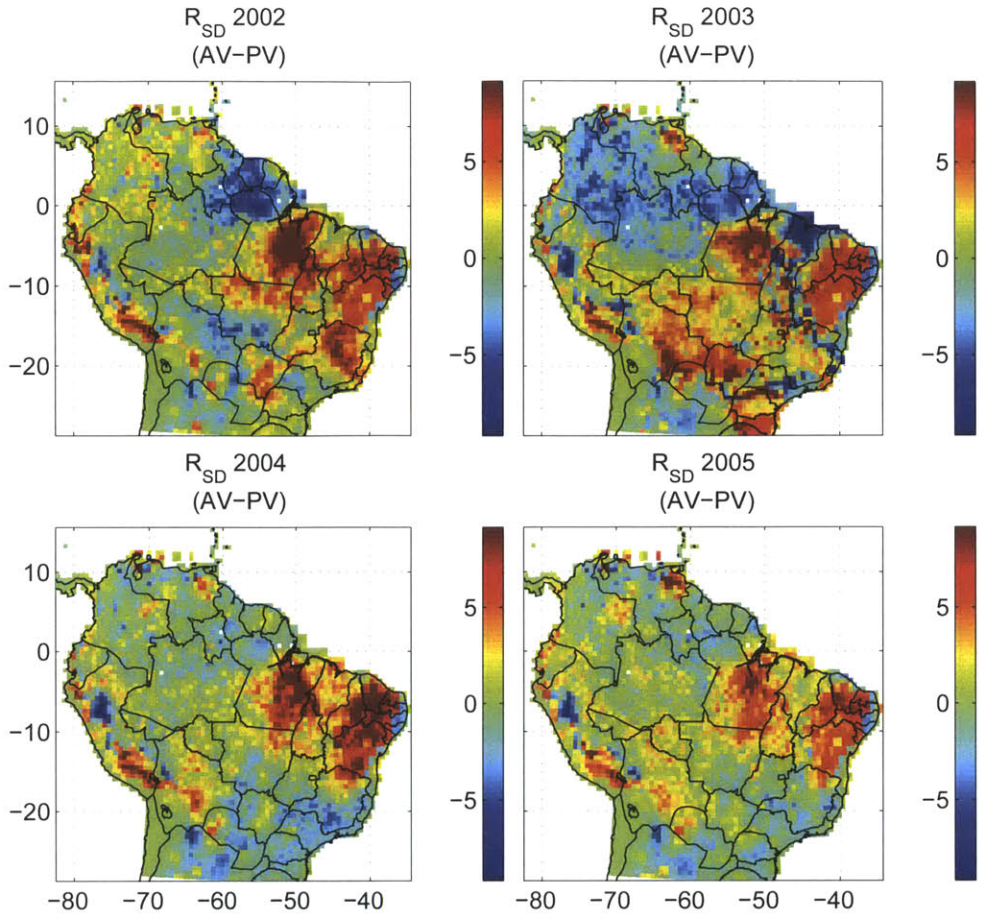


Figure 6-3: Differences in mean annual down-welling surface shortwave radiation [W/m2], 2002-2005. Potential Vegetation Condition is subtracted from the Actual Vegetation condition.

Land conversion decreased continental evapotranspiration all four years and showed slightly decreased precipitation for 3 out of 4 years, see Figure 6-5. The positive differential in continental precipitation in 2003 is associated with the ubiquitous positive differential in northern Amazonian precipitation. In summary, differences in annual continental precipitation are insignificant. However, land conversion decreased simulated continental evapotranspiration significantly across all four years.

Latitudinal monthly precipitation is often used as a metric to assess the seasonal oscillation of the Inter-Tropical Convergence Zone. The solid lines in Figure 6-7 show the Meridional profile of mean monthly precipitation for the (PV) case, dashed lines

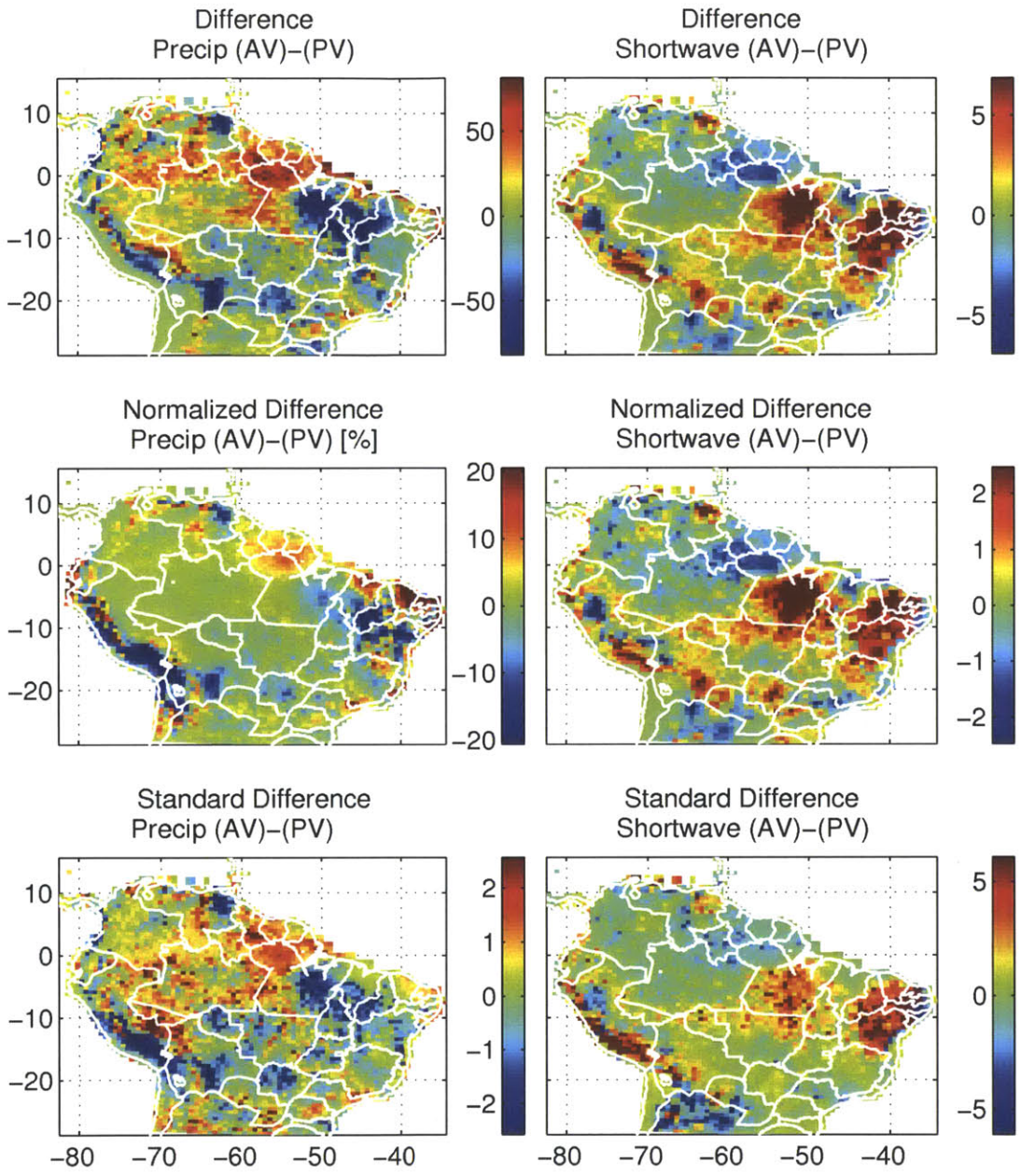


Figure 6-4: Annual mean differences in precipitation $[mm]$ and down-welling radiation at the surface $[W/m2]$

show the (AV) case. Precipitation in February and December show peaks below the equator, while June through October the convergence is in the Northern Hemisphere. It is clear that land-conversion has not influenced the timing or location of the Inter-

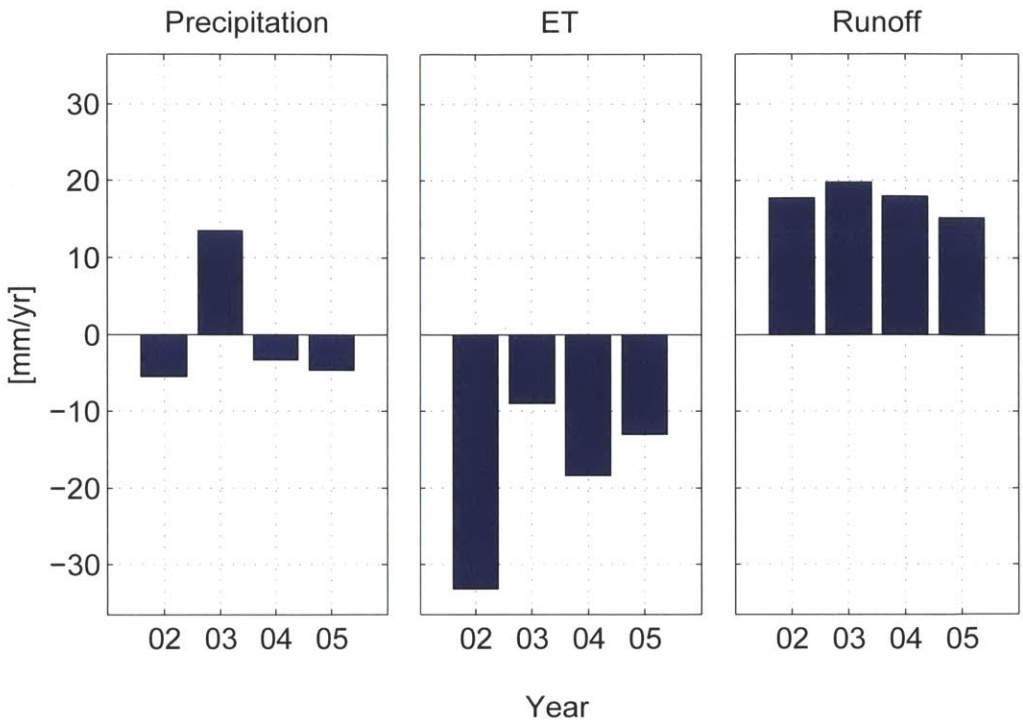


Figure 6-5: Difference in annual mean precipitation, evaporation and total runoff, between the Actual Vegetation case and Potential Vegetation case.

tropical convergence zone in South America.

Accumulations and differences in mean annual transpiration and total evapotranspiration are provided in Figure 6-8. Similar maps for the sensible heat flux and mean wind-speed at 100 meters are provided in Figure 6-9. There is a negative bias in both transpiration and total evapotranspiration associated with the "arc of deforestation" (starting at $48W2S$ going clockwise to $62W10S$). Deforestation has a direct impact on transpiration by decreasing unit area stomatal density. The deforestation of tropical rain forests in the eastern and southern Amazon also decreases leaf surface area, which reduces leaf evaporation and increases through-fall. The increase in through-fall, coupled with the decrease in root water uptake is a likely reason for increased continental equilibrium soil moisture of the AV condition, shown in Figure 6-6. While increased through-fall also supports increased soil surface evaporation, the total latent heat flux from deforested canopies is most strongly correlated with decreased leaf and stomatal

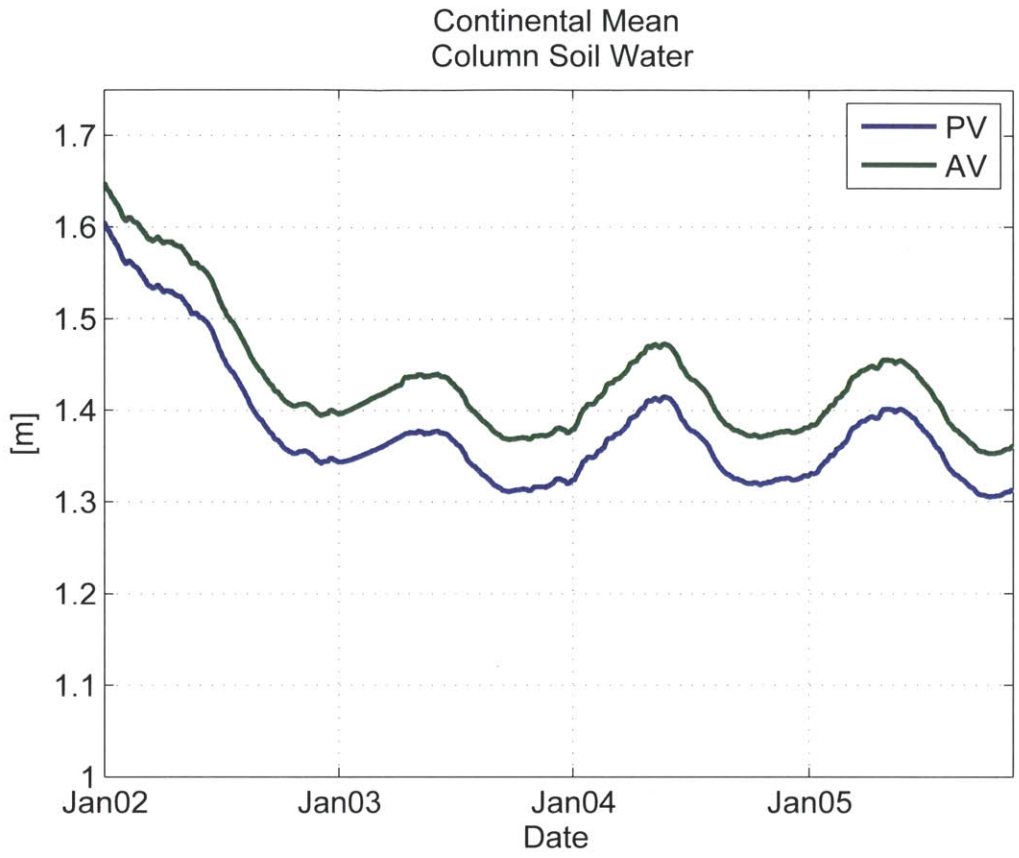


Figure 6-6: Time series of mean continental soil water for each coupled simulation case. Total soil water is the depth integrated volume of water over the soil column.

vapor flux.

The spatial correlations for the differentials of several variables are calculated, see Figure 6-10. Variables in the table use the following identifiers: Above Ground Biomass (agb), Precipitation (pcp), Shortwave Radiation Down-welling (rsd), Transpiration (tr), Evapotranspiration (et), Sensible Heat Flux (shf), Wind Speed (wind), Soil Evaporation (sevap), Moist Static Energy (mse) and Vegetation Stress Index (vsi).

The strongest positive correlations (in-order), are:

1. precipitation and evapotranspiration

2. evapotranspiration and transpiration

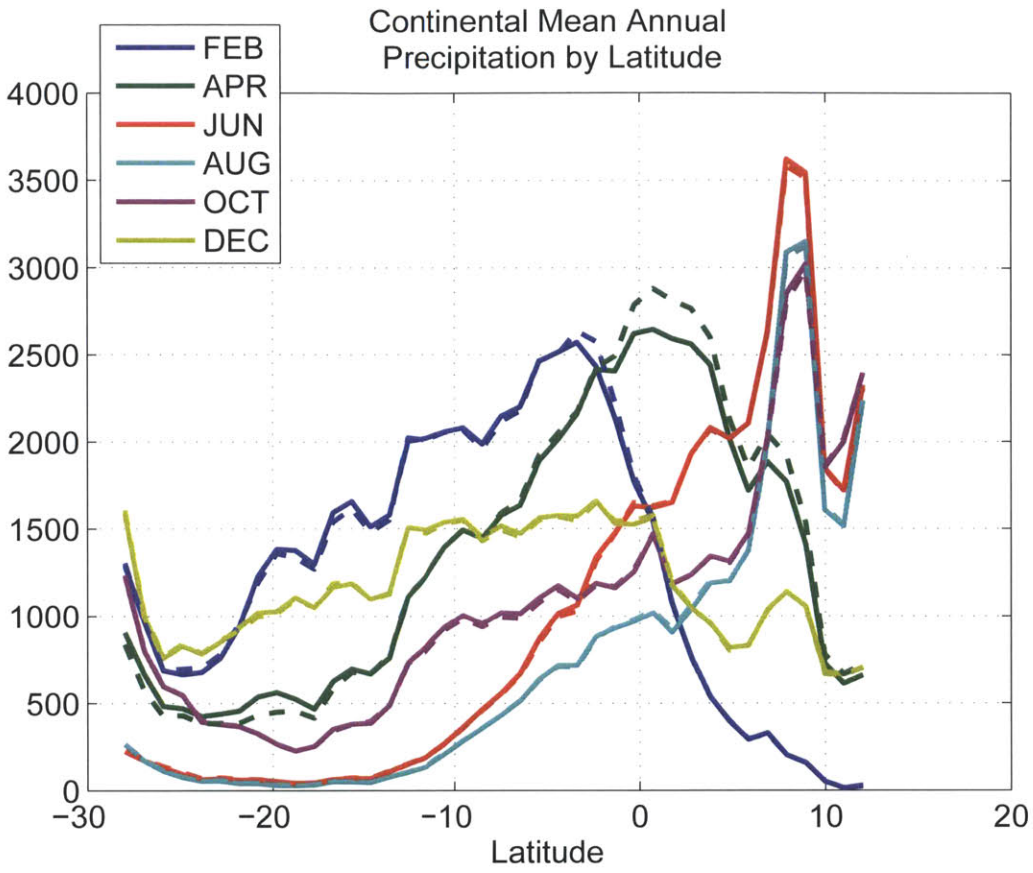


Figure 6-7: Mean monthly continental precipitation for (PV-solid) and (AV-dashed), as a function of latitude, 2002-2005.

3. sensible heat flux and short-wave radiation

4. vegetation stress index and sensible heat flux

5. soil evaporation sensible heat flux

6. evapotranspiration and above ground biomass

The strongest negative correlations (in-order), are:

- soil evaporation and transpiration
- moist static energy and sensible heat flux
- shortwave radiation and precipitation

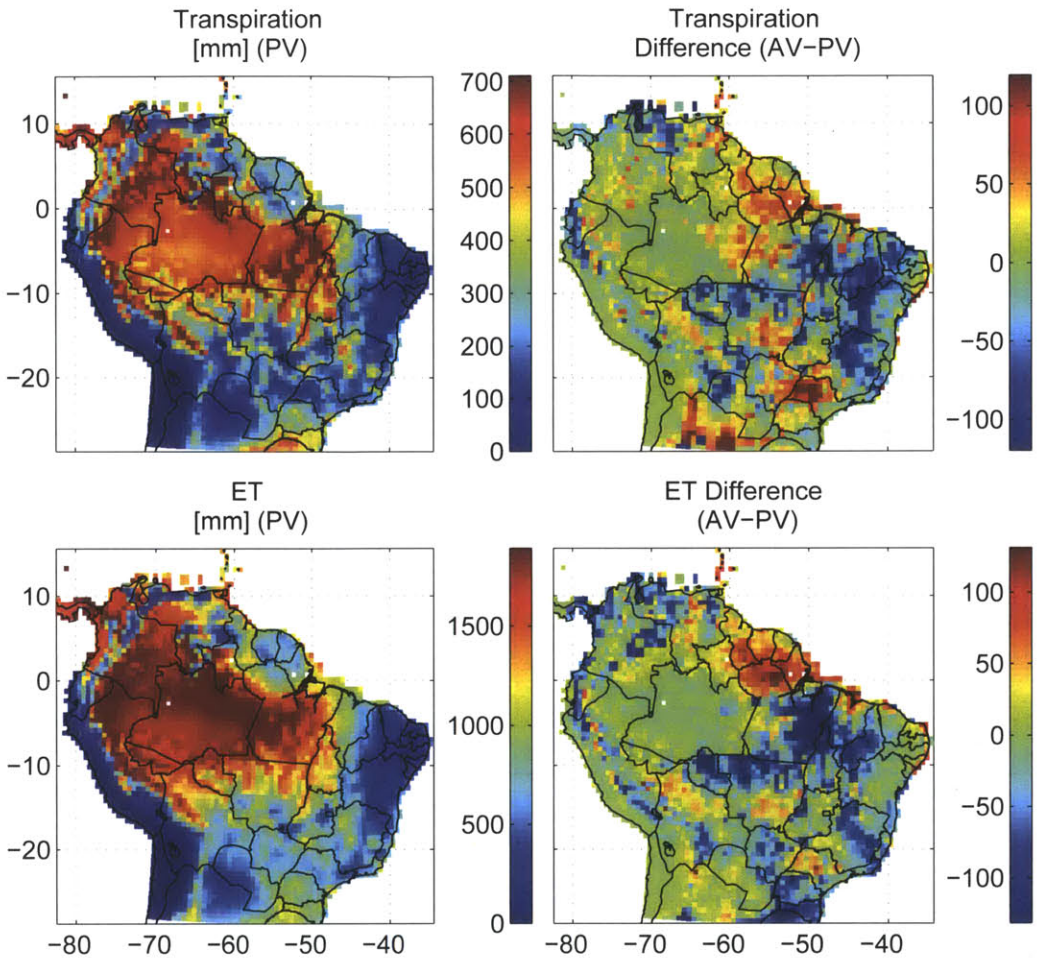


Figure 6-8: Annual transpiration and evapotranspiration [mm]. Totals for the Potential Vegetation condition and differences, 2002-2005.

- wind speed and above ground biomass
- vegetation stress index and above ground biomass
- shortwave radiation and evapotranspiration
- shortwave radiation and transpiration

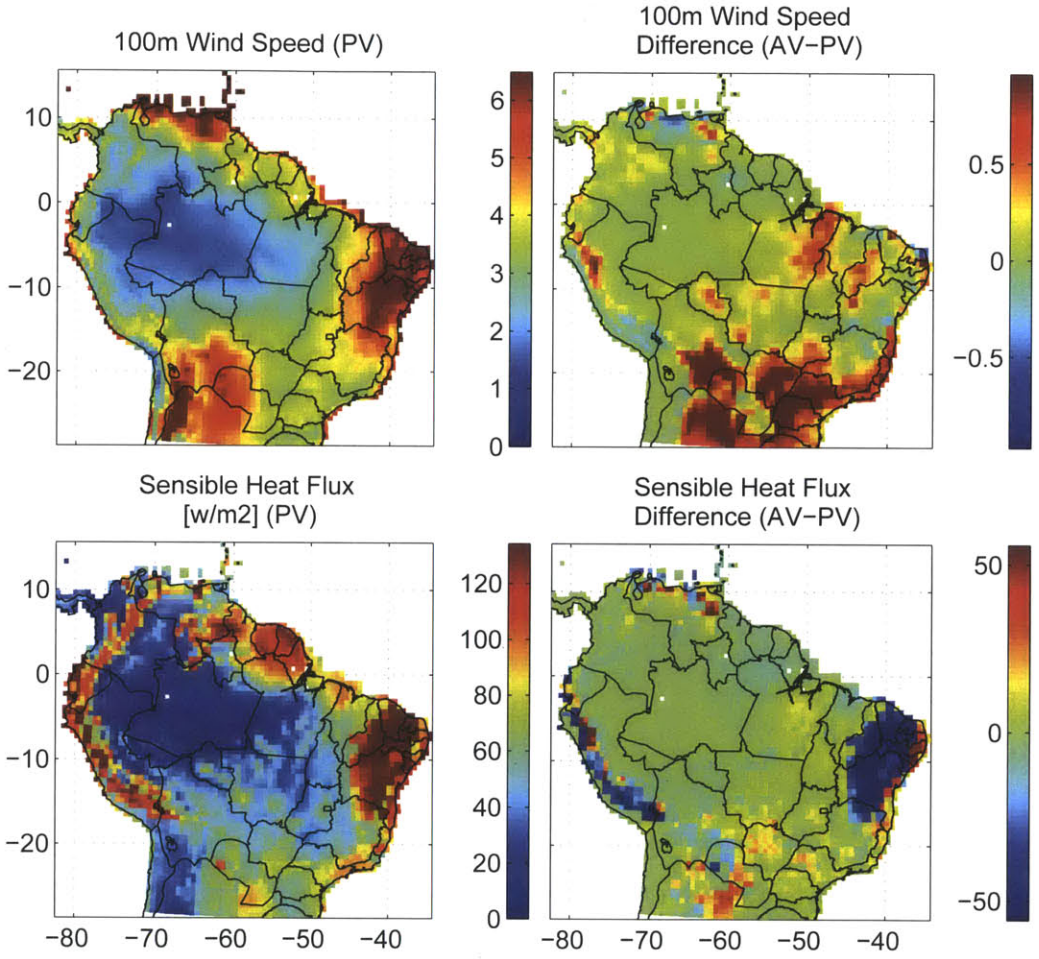


Figure 6-9: Mean wind-speed $[m/s]$ and sensible heat-flux $[w/m^2]$. Totals for the Potential Vegetation condition and differences, 2002-2005.

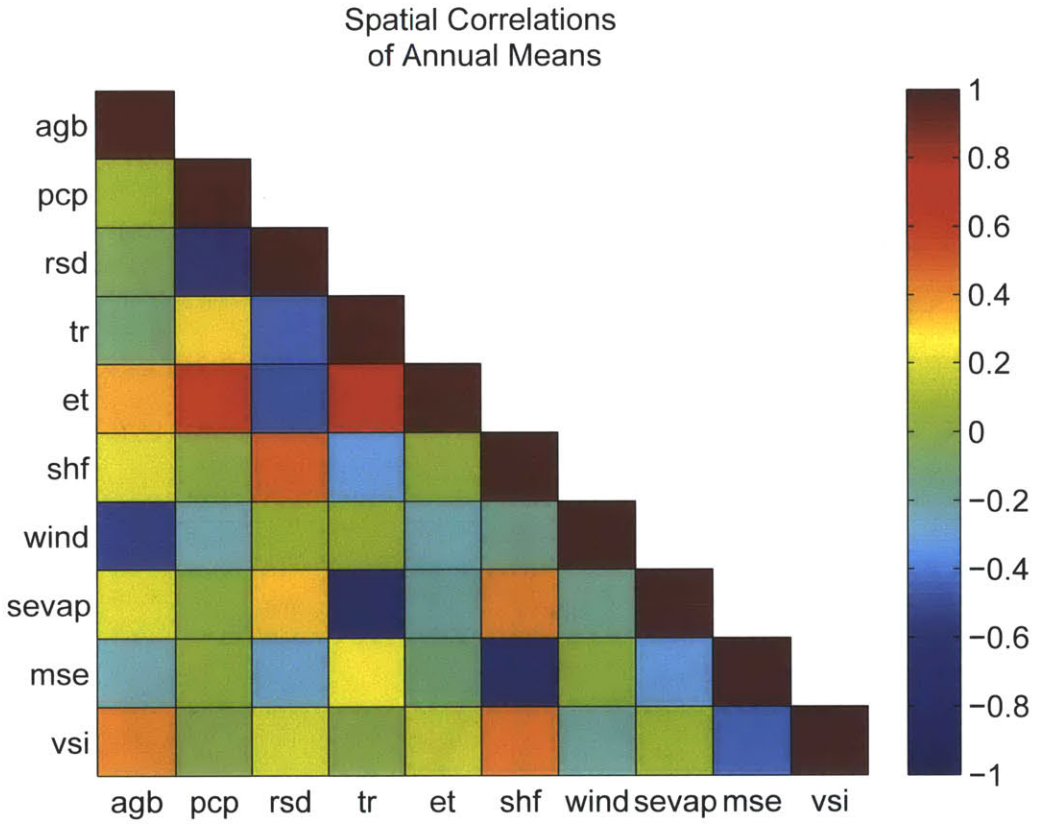


Figure 6-10: Correlation table for the mean *differences* (AV-PV) in various hydrologically relevant variables: Above Ground Biomass (agb), Precipitation (pcp), Shortwave Radiation Down-welling (rsd), Transpiration (tr), Evapotranspiration (et), Sensible Heat Flux (shf), Wind Speed (wind), Soil Evaporation (sevap), Moist Static Energy (mse) and Vegetation Stress Index (vsi).

## 6.2 Ecological and Hydrologic Susceptibility to Change

This thesis questions if "the changes in regional hydrology are significant enough to produce an ecological response". In order to answer this question, it is necessary to first identify ecosystems that may or may not be susceptible to change. There are typically three major resource limitation modes that govern ecosystem response: light limitation, water limitation and nutrient limitation. Nutrient limitations were turned off in the ED model, understanding and comparing nutrient limitation were not part of the experimental design. It is hypothesized that if changes in regional hydrology are significant enough to produce an ecological response, then it would likely be in:

- water limited ecosystems where changes in precipitation are significant or
- light limited ecosystems where changes in photosynthetically active radiation (PAR) are significant

The vegetation stress index $vsi$ can give an idea of the resource limitation regime of an ecosystem. Each EDM cohort has an open stomata transpiration rate and a cuticular (closed) stomata transpiration rate. The actual transpiration rate is a linear combination of the open and closed states, weighting the open state by the "stomata open fraction" $f'_o$. The vegetation stress index $vsi$ is unity minus the leaf area weighted and time averaged mean of $f'_o$. For an ecosystem with $N$ cohorts indexed $i$, using general notation implying time and space averaging:

$$vsi = 1 - \langle\langle \frac{\sum_{i=1}^{M} LAI_{(i)} f'_{o(i)}}{\sum_{i=1}^{M} LAI_{(i)}} \rangle_{area} \rangle_{time} \tag{6.1}$$

The ED model uses the stress function to scale the fraction of time a plant has stomata in the open or closed state. It calculates this based on the ratio of the plant's $demand$ for root zone soil moisture to satisfy its transpiration requirement (given ample water), and the $supply$ of root zone water the roots are capable of extracting at that time.

$$f'_{o(i)} = \frac{1}{1 + \frac{Demand}{Supply}} \tag{6.2}$$

Water *demand* and transpiration is calculated by the EDM photosynthesis solver. This is coupled to the plant carbon assimilation rate and becomes a complex function of light availability, ambient carbon concentration, vapor pressure deficit across the leaf surface boundary layer and various plant parameters. The *supply* of water available to the plant is essentially the vertical integration of root zone liquid water above the wilting point. The stomata open fraction $f_o'$ approaches 1 when supply is infinitely greater than demand, and approaches zero when demand is infinitely greater than supply or if the supply of water approaches zero. The biophysics are covered in greater detail in Appendix D.

The simulation mean vegetation stress index $vsi$ for the Actual Vegetation case is shown in the lower left panel of Figure 6-11. The mean water stress function is strongly correlated with precipitation and above ground biomass. It is zero in the parts of the Amazon rainforest where annual precipitation is high. The stress function approaches an annual mean of 1 in various parts of the Andean Altiplano and eastern Brazil. These are locations where water is scarce, and plants are almost in a perpetual state of closed stomata. In the absence of a metric that directly assess light limitation, ecosystems with high water stress functions are considered water limited, and otherwise are considered light limited.

Ecosystems that have high water stress indices are probably more likely to show a shift in equilibrium structure and composition given a strong shift in mean precipitation. This comparison can be evaluated in Figure 6-11, the upper panels show the mean differences in standard precipitation and standard down-welling shortwave radiation (note: recall that standard refers to differences normalized by the totals, and then normalized by the standard deviation). Differential down-welling shortwave radiation were consistent and showed a clear signal, but the magnitude of the signal is small compared to the precipitation signal. Two sites are chosen where precipitation differentials are large, in ecosystems that show some degree of water stress. These sites are indicated by circles on the maps of Figure 6-11, and numbered inside the circles in the lower right panel.

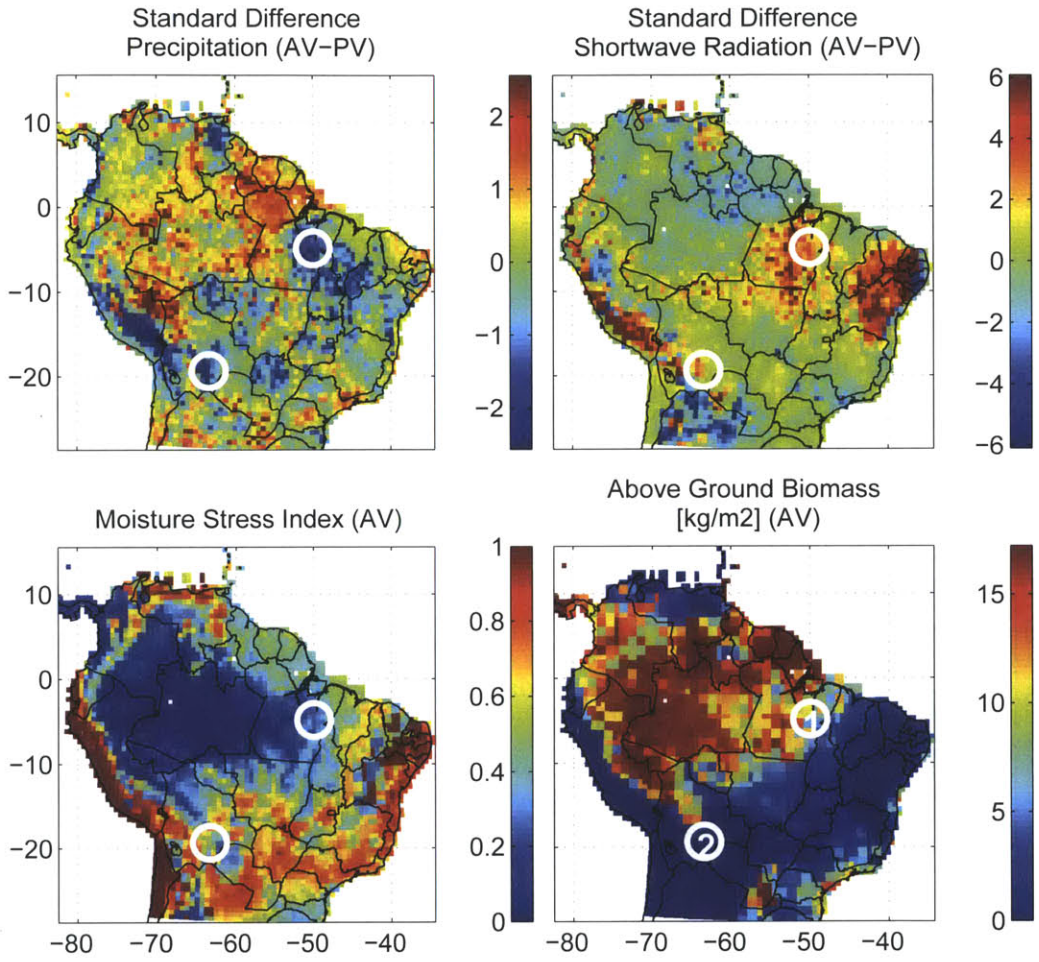


Figure 6-11: Combined assessment of ecosystem susceptibility to regional land-conversion. White circles on each map show the locations of the focus sites. Upper panels give standard differences for precipitation and short-wave radiation. The lower panels show the simulation mean Vegetation Stress Index (VSI) (0-stomata unregulated, 1-stomata closed), and the Above Ground Biomass from the Actual Vegetation scenario.

Site 1 is located within the boundaries of the Amazon basin at $4.5^oS50.5^oW$. Located on the southeastern lobe of the differential precipitation dipole where AV precipitation was depressed, this area experiences somewhere between 1-2 meters of precipitation per year, with a relatively pronounced dry season. The natural vegetation landscapes are dominated by tropical forests. The area borders the ecotone transition between tropical forests and Cerrado. Significant land-conversion exists, pastures account for approximately $1/3$ of the land-cover. Roughly $10\%$ of the landscape contains old-growth forests over 200 years old. See Figure 6-12 for a profile on the site's structure and composition.

Site 2 is located in Bolivia, at $19.5^oS63.5^oW$ in the foothills of the Andes mountains. This site is unique in that is is located in a region influenced by the outlet of the South American Low Level Jet. The continental precipitation recycling ratios in this area are generally very high (meaning that most of the precipitation can be traced back to the continental land mass as opposed to the ocean). In the coupled simulation using the Actual Vegetation (AV) boundary condition, precipitation in the area ranged from less than 500 millimeters to just less than 1 meter. Annual precipitation increased significantly when using the Potential Vegetation boundary condition, upwards of 200 millimeters per year. The vegetation profile, see Figure 6-13, shows natural landscapes are grasslands. It also indicates that $25\%$ of the landscape is actively converted to pasture and roughly $20\%$ is abandoned and degraded lands. However, the vegetation profile before humans land-conversion showed and open tree canopy (small amounts of woody biomass).

Sections 6.3 and 6.3.3 take a closer look at the hydrology of the area. One intention is to get a better understanding of how the hydrology of these locations differ between simulations of differing land-cover. The other interest, is to determine why these two sites are experiencing a persistent precipitation decrease in the AV scenario simulation.

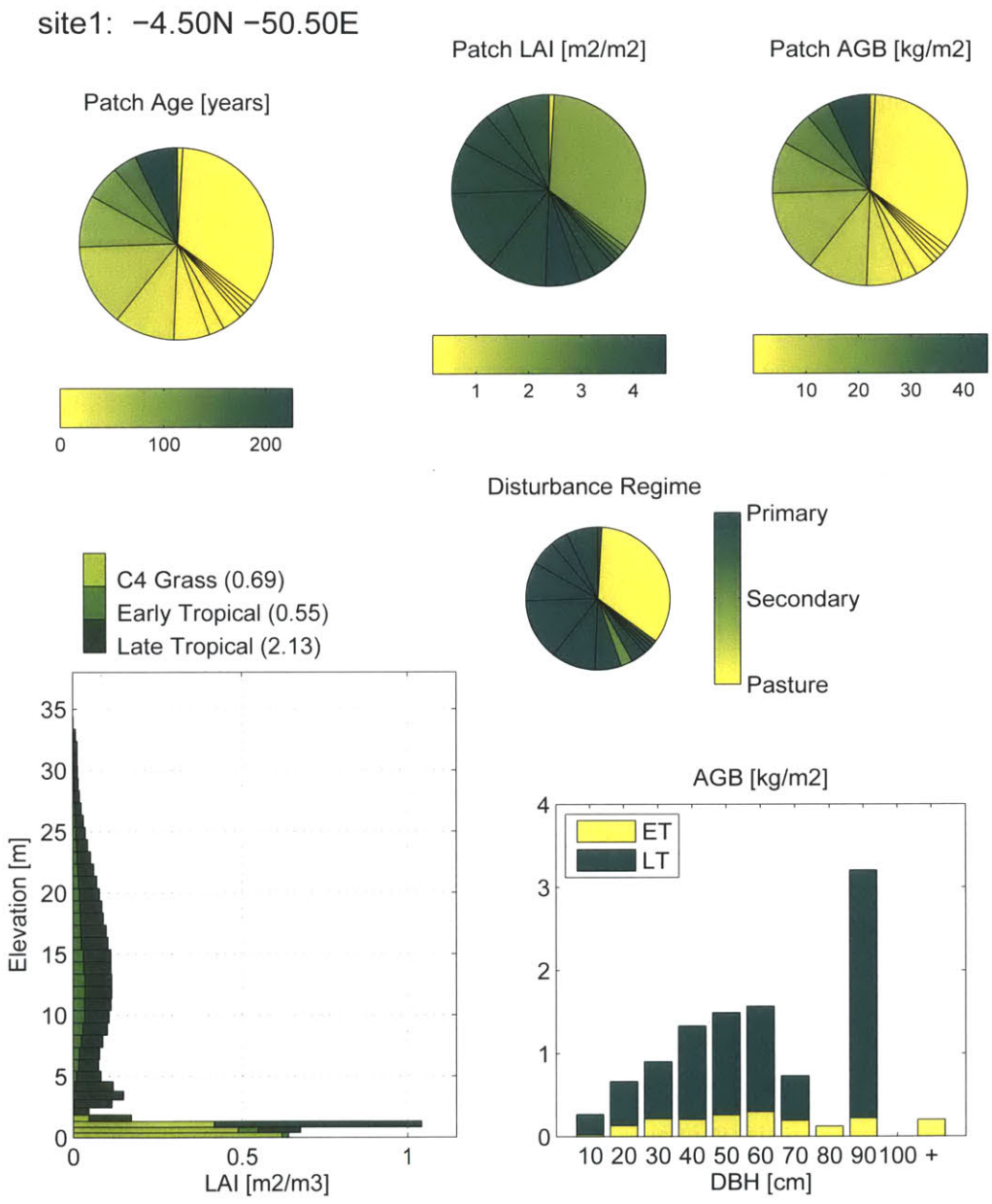


Figure 6-12: Vegetation profile at focus site 1.

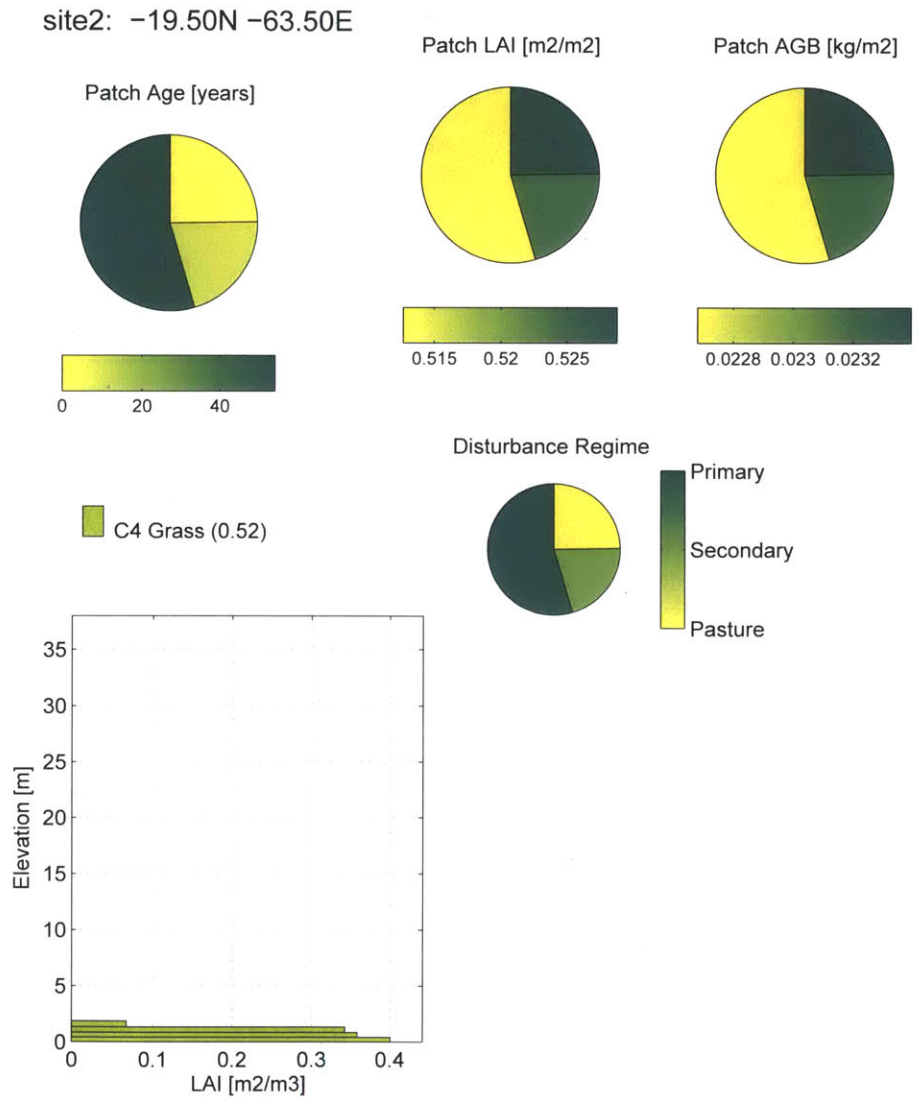


Figure 6-13: Vegetation profile at focus site 2.

## 6.3 Focus: Site 1

### 6.3.1 Site 1: Differential Hydrology in the Soil and Canopy System

The accumulated water flux at site one is captured in Figure 6-14. This site received a little more than 1.5 meters of rainfall per year in the PV scenario, and approximately $10\%$ less rainfall in the AV scenario. There were sites in the area that had stronger relative differential in precipitation, but this site still represents a differential in the upper percentile of those sites. Leaf evaporation and transpiration constitute the majority of water losses from the soil-canopy system, each removing roughly $40 - 40\%$ of the precipitated water, soil evaporation and drainage/runoff contributed roughly $10\%$ of the losses each.

Leaf evaporation and transpiration predictably decrease with the Actual Vegetation (AV) condition, this is due to the drop in stomatal and leaf surface density that comes with converting forests to pastures. Despite decreased precipitation, soil evaporation in the AV case is greater than the PV case. One possible explanation is that the per unit through-fall of precipitation increases as forests are cleared and leaf interception surfaces are removed. It is also possible that converted lands have drier hotter surface air which promotes increased evaporation rates. Deforestation also reduces the mean forest drag density and promotes greater turbulent transfer at the ground surface. Recall that this site is in a region where the AV scenario also had greater differential mean wind-speed in the Atmospheric Boundary Layer, see Figure 6-9.

The surface energy balance tells a similar story. Higher transpiration and leaf interception in the PV scenario promote a higher mean evaporative fraction, see Figure 6-15. The actual vegetation condition receives more total shortwave and longwave radiation $(R_{SD} + R_{LD})$, which is undoubtedly related to a decrease in convective cloud albedo associated with the decrease in convective rainfall at the site. Although the site receives more total incoming radiation in the AV scenario, the surface albedo decreases with the conversion of forests to pasture. This results in more reflected radiation and a decrease in combined sensible and latent heat flux $(H + L)$, see the right panel of Figure 6-15.

The forest canopies in both cases show similar daily mean temperature and humidity

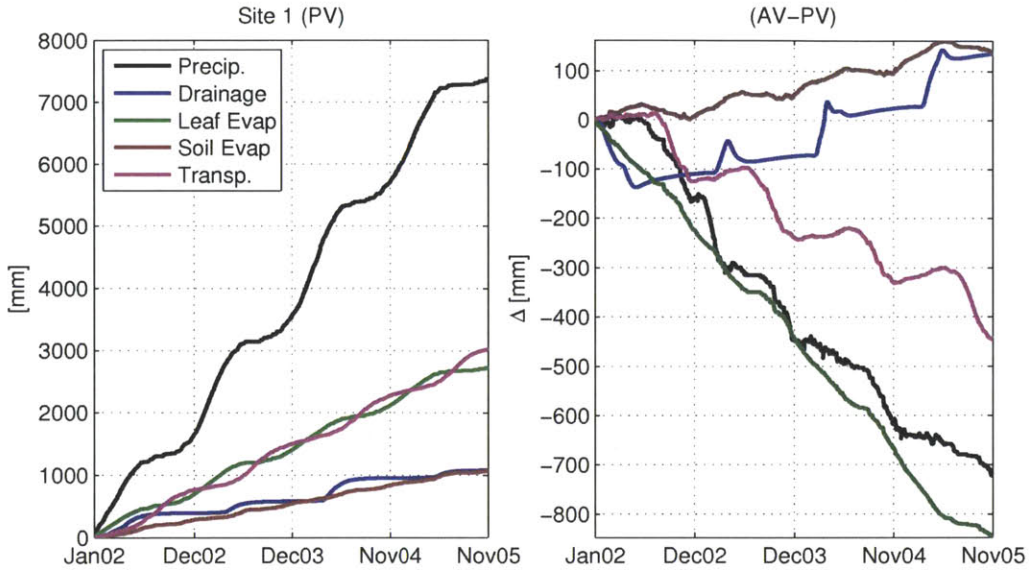


Figure 6-14: Time series accumulations of water mass flux through the vegetation canopy at site 1 during the coupled model experiment, 2002-2005. The left panel shows accumulated fluxes in the PV case. Differences are shown in the right panel.

during the wet season, November through April, see Figure 6-16. In the dry season the AV canopy diverges, peaking two degrees warmer and two grams per kilograms dryer than the primary forests of the PV condition. Again, this is a potential contributing factor to increased soil evaporation. Referring back to Figure 6-14, one can see that differential leaf water flux is linear, but differential transpiration shows much stronger seasonality. Precipitation differentials in the early dry season are modest, suggesting that the canopy and moisture differentials are influenced primarily through the differential in transpiration cooling.

Dry season draw-down of root zone soil moisture is shown in Figure 6-17. This location shows a full re-saturation of the soil column in both cases peaking around February. The Potential Vegetation shows greater root zone extraction. Both simulations show the same timing in seasonality. Figure 6-18 shows the rate of change in total column soil moisture for each condition. Both simulations show the same timing of flipping to sources and sinks of moisture, as evidenced by the location of the time axis

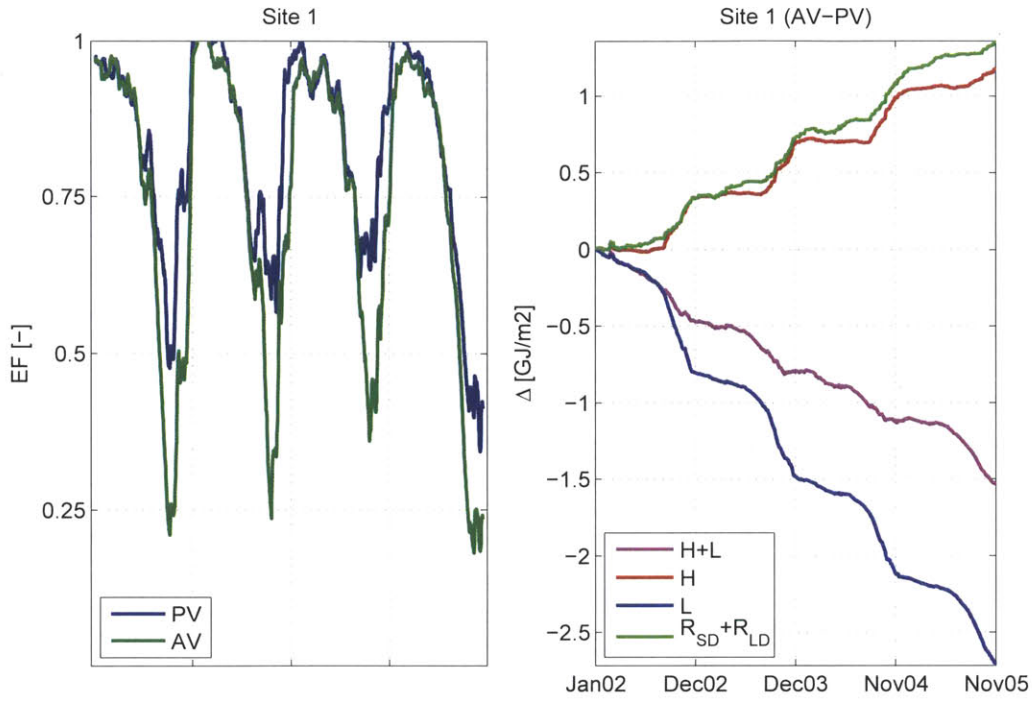


Figure 6-15: Left Panel: Time series of evaporative fraction (latent/(latent+sensible)) at site 1. Right Panel: Time series of the differential in accumulated energy fluxes at site 1.

intercepts.

Differences in the hydrology between the two scenarios has been established at the canopy scale. The differences attributed to the Actual Vegetation scenario can be summarized as follows:

- AV: mean annual precipitation deficit on the order of $10\%$
- AV: decreased evaporative and transpiration cooling, particularly in the dry season
- AV: dry season canopies are hotter and dryer
- AV: increased soil evaporation driven by increases in through-fall, turbulent transport and dry-season vapor-pressure deficit
- AV: decreased total sensible and latent heat fluxes driven by decreased albedo

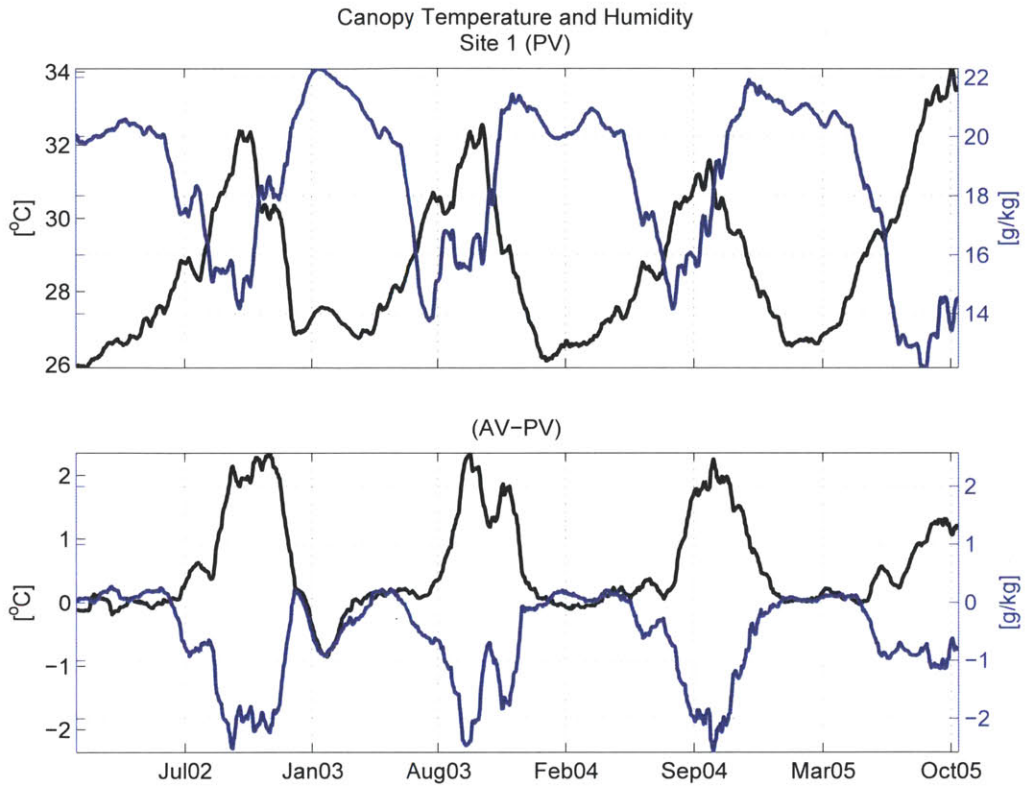


Figure 6-16: Upper panel: Time series of mean daily canopy temperature and humidity at site 1 during the coupled model experiment. Lower Panel: Differential canopy temperature and humidity.

- AV: decreased dry season evaporative fraction

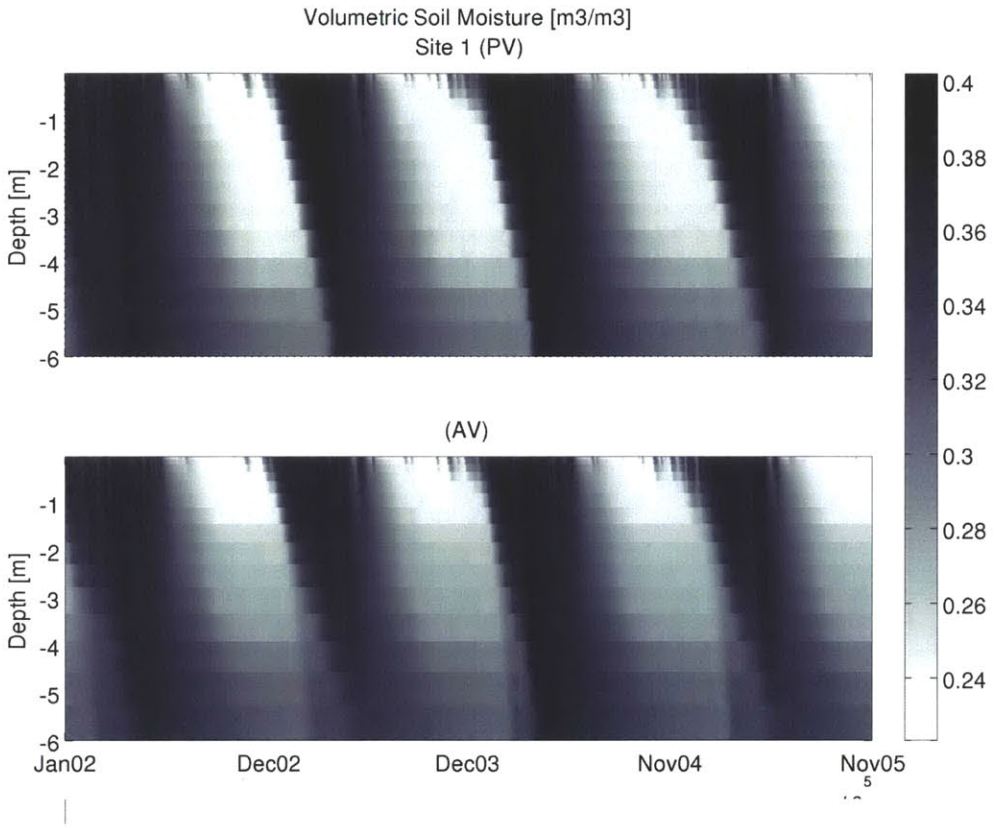


Figure 6-17: Time series profile of volumetric soil water at site 1.

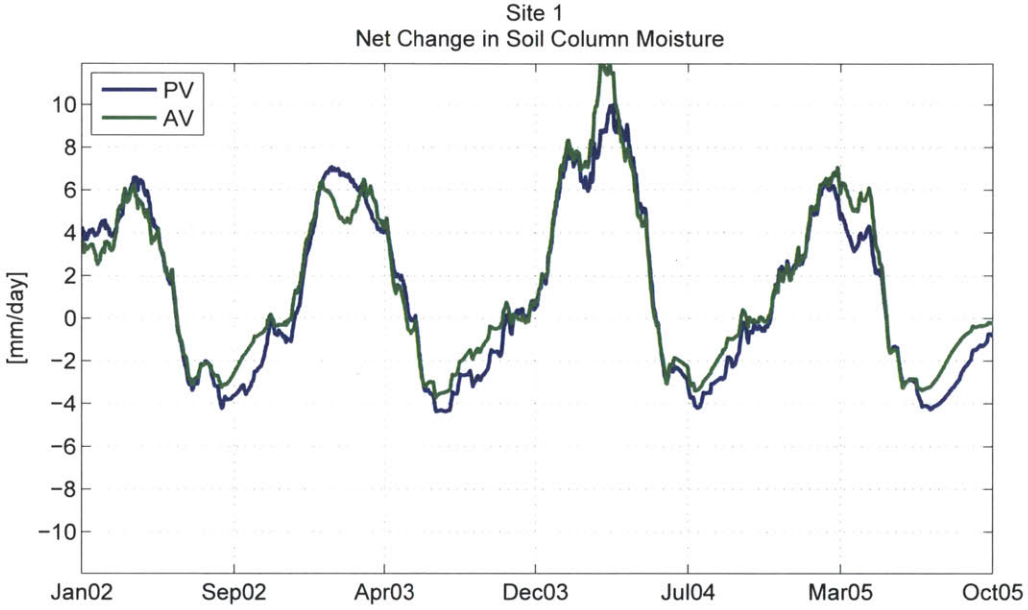


Figure 6-18: Net rate of change in soil moisture at focus site 1 during the coupled experiment. Positive values indicate the soil column is gaining water, negative values indicate the column is losing water. The intersection points of the time axis are good proxies as to the starts and stops of the dry season and wet season.

### 6.3.2 Site 1: Differential Hydrometeorology of the Area, September 2003

The monthly mean differential precipitation described in Figure 6-1 indicates that the precipitation depression associated with AV surface conditions is strong in September. A bounding box is constructed around the depression in differential precipitation associated with the AV simulation. Within this bounded region, spatial mean hydrometeorological tendencies for September 2003 are evaluated. The bounding box is shown in Figure 6-19, which also provides maps of total and differential accumulations of precipitation and evapotranspiration.

The vast majority of rainfall in the focus region is convectively driven and peaks at noon (local time, 15Z); Figure 6-20 shows the proportion of simulation mean total and resolved (stratiform) precipitation distributed by time of day.

The domain mean quantities for change in precipitable water $\Delta M_{pw}$, accumulated evapotranspiration $ET$, precipitation $P$ and resolved moisture convergence $Mc$ are provided in Table 6.1. Moisture convergence is calculated by doing a simple mass balance on the other three terms. It is clear that the bounded domain experiences dry season conditions in September. Most of domain is experiencing less than 100 millimeters of precipitation for the month.

| Case | $\Delta M_{pw}$ | $ET$ | $P$ | $Mc$ | $T$ | $r$ |
|---|---|---|---|---|---|---|
| Units | $kg/m^2$ | $kg/m^2$ | $kg/m^2$ | $kg/m^2$ | $^oC$ | $g/kg$ |
| AV | -3.457 | 63.1 | 29.8 | -37.14 | 32.83 | 12.18 |
| PV | -3.515 | 94.7 | 47.3 | -51.32 | 32.35 | 12.93 |

| Case | $\theta_e$ | $\alpha$ | $R_{SD}$ | $R_{net}$ | $H$ |
|---|---|---|---|---|---|
| Units | $K$ | - | $w/m2$ | $w/m2$ | $w/m2$ |
| AV | 334.95 | 0.26 | 300.2 | 180.89 | 44.03 |
| PV | 336.27 | 0.25 | 285.55 | 187.75 | 43.91 |

Table 6.1: Hydrologic monthly means within the bounded area above case study 1, September 2003. Total change in column precipitable water $\Delta M_{pw}$, evapotranspiration $ET$, precipitation $P$ and resolved moisture convergence $Mc$, air temperature (55m) $T$, mixing ration (55m) $r$, equivalent potential temperature $\theta_e$, surface albedo to shortwave radiation $\alpha$, downwelling shortwave radiation $R_{SD}$, net surface radiation $R_{net}$ and sensible heat flux $H$.

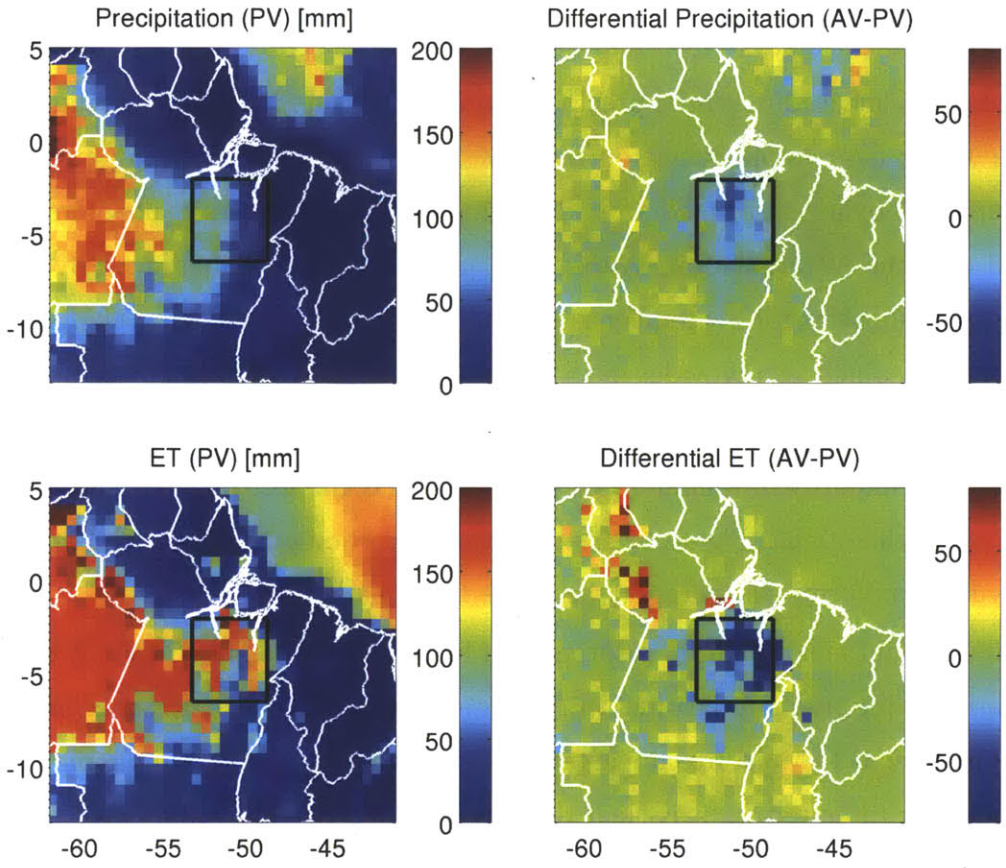


Figure 6-19: Upper left panel: map of integrated monthly precipitation, case AV. Upper right panel: map of the integrated difference in monthly precipitation, case PV minus case AV. Lower right panel: map of integrated monthly evapotranspiration, case AV. Lower left panel: map of the integrated difference in monthly evapotranspiration, case PV minus case AV. The boundaries of the focus region are provided. September 2003.

The Potential Vegetation condition produces significantly more precipitation and total evapotranspiration during this period. Both cases net a negative moisture convergence budget for the month. The PV scenario loses more precipitable water through its lateral boundaries.

One way to conceptually model this system is to approximate the dynamics of the bounded region as fully and instantaneously mixed. With this assumption, the fraction of precipitation derived from water coming from surface evaporation is simply the ratio

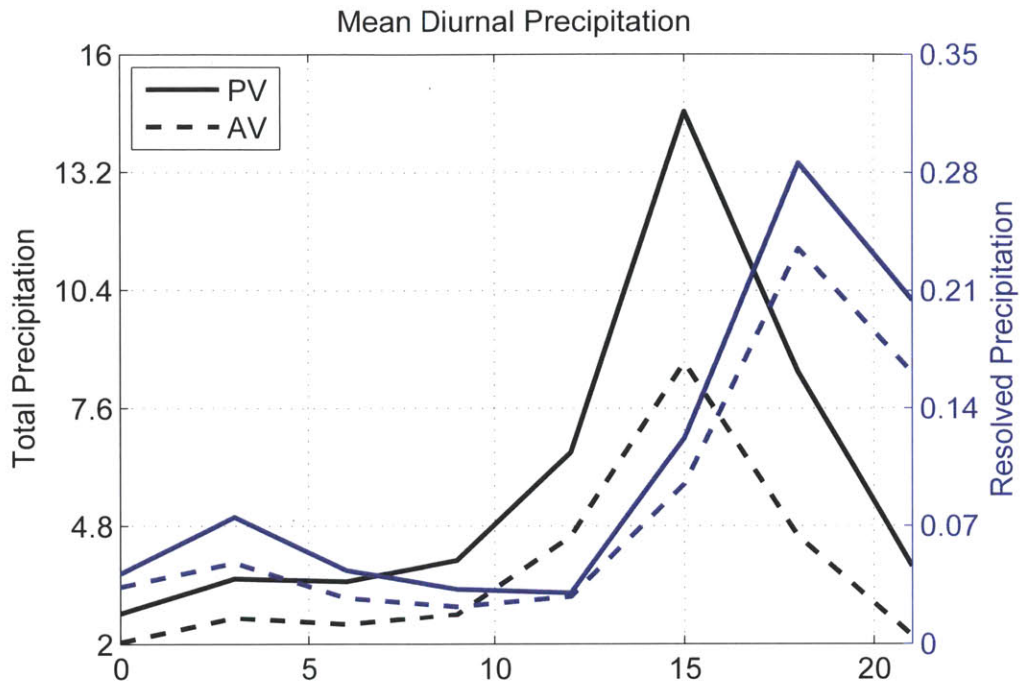


Figure 6-20: Monthly domain averages of diurnal precipitation for the focus region above site 1. Both vegetation cases are covered, black lines use the left axis and indicate total precipitation (resolved+convective) and blue lines use the right axis and indicate only resolved (stratiform) precipitation. September 2003.

of evaporation over the combination of evaporation and lateral moisture convergence. With the fully and instantaneously mixed assumption, a region that is experiencing negative moisture convergence would therefore trace all precipitated water back to surface evaporation. In a divergent system, a perturbation in precipitation would be a proportional to the perturbation in surface evaporation. Of course, a fully and instantaneously mixed model is a crude representation of reality. But it can be argued that if a fully mixed model is biased, it is such that too much of the precipitable water is traced back to lateral moisture convergence. The reasoning is that evaporation feeds directly into the atmospheric boundary layer. Convective rainfall comes from updrafts of moist parcels originating in the boundary layer, and therefore the more influential of the five flux boundaries is the surface (not the four lateral boundaries).

The moisture flux at this location is divergent, the rainfall is convectively driven and

the even though the potential vegetation simulation produces more precipitation it also experiences increased divergence. This combination of factors supports the conclusion that differences in the surface energy flux is driving the differences in precipitation.

The advective moisture flux around the focus region is a strong easterly flow, see Figure 6-21. The right panel in Figure 6-21 shows the differential flux vectors of precipitable water (AV-PV). Even though this site is located near the coast, virtually none of the advecting moisture comes from the ocean. The flow vectors run parallel to the coast. The moisture entering the focus region has traveled over land, particularly from areas with relatively lower mean precipitable water. It is also visible by looking at the moisture flux vectors that they flow *up-gradient* along total column precipitable water. This is logical, given that the bounded focus region is divergent (i.e. a source of moisture).

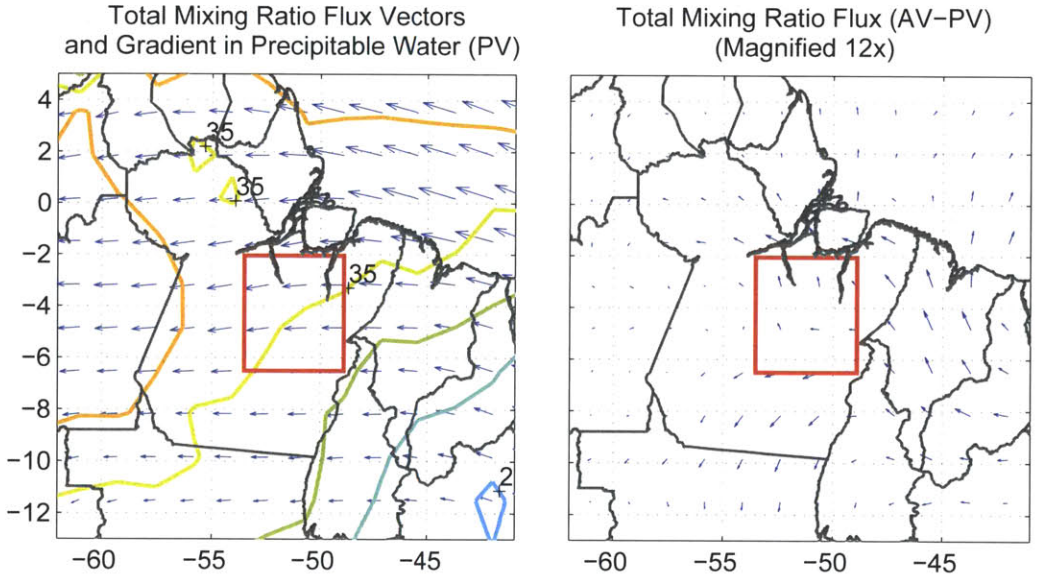


Figure 6-21: Left Panel: Map of vertically integrated total water advective flux vectors (quivers) and vertically integrated precipitable water (contours) for the Actual Vegetation case (PV). September 2003. Quivers are scaled and convey only directionality and relative magnitude. Contours of precipitable water are labeled, units are $[kg/m2]$. Right Panel: The differential in vertically integrated advection of total precipitable water, Potential Vegetation minus Actual Vegetation (AV-PV). Quivers are scaled to 12 times relative to the left panel.

A large fraction of the total surface energy flux is contained in sensible heat, see

Figure 6-22. Note also that differentially, the AV condition releases more sensible heat flux. Increased sensible heat flux is consistent with rapid boundary layer growth. Likewise, the AV scenario has higher surface wind-speeds particularly over this area. Subsequently, the mean turbulent kinetic energy in the AV scenario atmospheric boundary layer is greater than that of the PV scenario, see Figure 6-23.

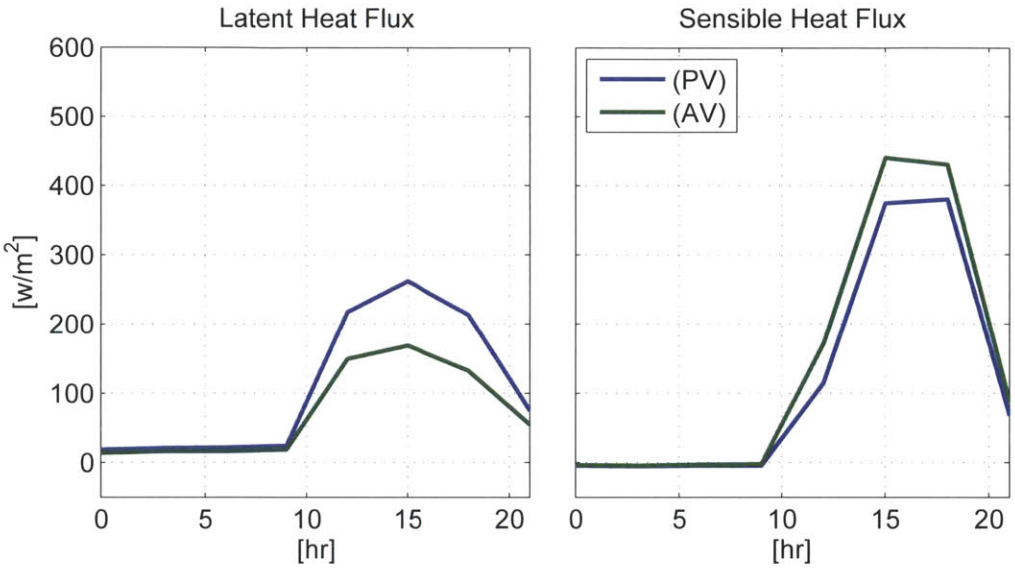


Figure 6-22: Spatially averaged diurnal mean sensible and latent heat fluxes for focus region 1.

There is evidence that suggests boundary layer turbulent kinetic energy is essential in forming convective updrafts. In situations where there is a layer of negative buoyancy between the top of the mixed layer and the level of free convection (where a surface parcel attains positive buoyancy with the environment), turbulent eddies provide the mechanical energy necessary for lifting the moist surface parcels through negative buoyancy. If differential kinetic energy was indeed having an influence on on convective tendencies in this region, it is likely that the increased boundary layer turbulence associated with the AV case would lead to more rainfall events. Given that the AV case experienced less total accumulated rainfall, this would translate into a greater number of weaker precipitation events.

However, this was not the case. Histograms were constructed of actively raining

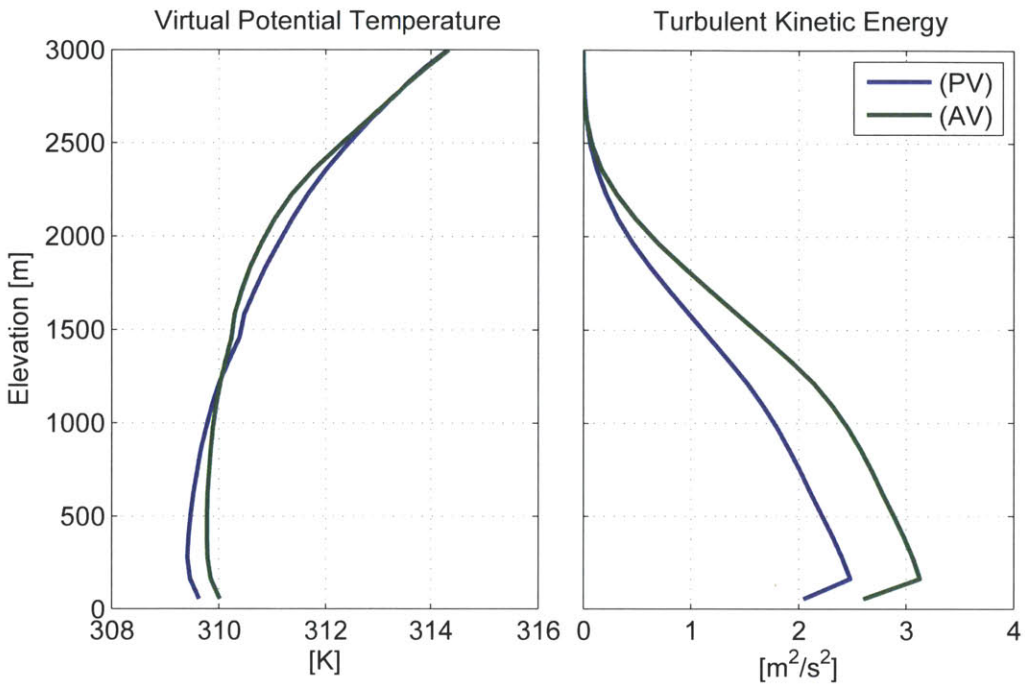


Figure 6-23: Profiles of monthly mean virtual potential temperature and turbulent kinetic energy within focus Regiona 1 at 15:00 UTC (noon local).

convective events for the level where updrafts originate (LOU), the lifting condensation level (LCL), level of free convection (LFC) and the level of neutral buoyancy (LNB), see Figure 6-24. Note that there were more total events for the Potential Vegetation scenario. So increased turbulent kinetic energy has had little impact on the triggering of convective events. From the perspective of model mechanics, convective triggering was based only on a minimum depth between the updraft origin and the level of free convection. Perhaps models that place more emphasis on vertical velocities of boundary layer eddies for triggering convection would generate different results.

More total events occur in the PV scenario, but the distributions of the key elevations associated with the updrafts are very similar. The distributions of negative buoyancy for the the two simulations are also very similar, see Figure 6-25. This is not surprising seeing how this is essentially a proxy of the distance between the updraft base and the level of free convection. The distribution of work performed in cloud updrafts for active convection show a subtle difference. Updrafts in the PV scenario have updrafts which

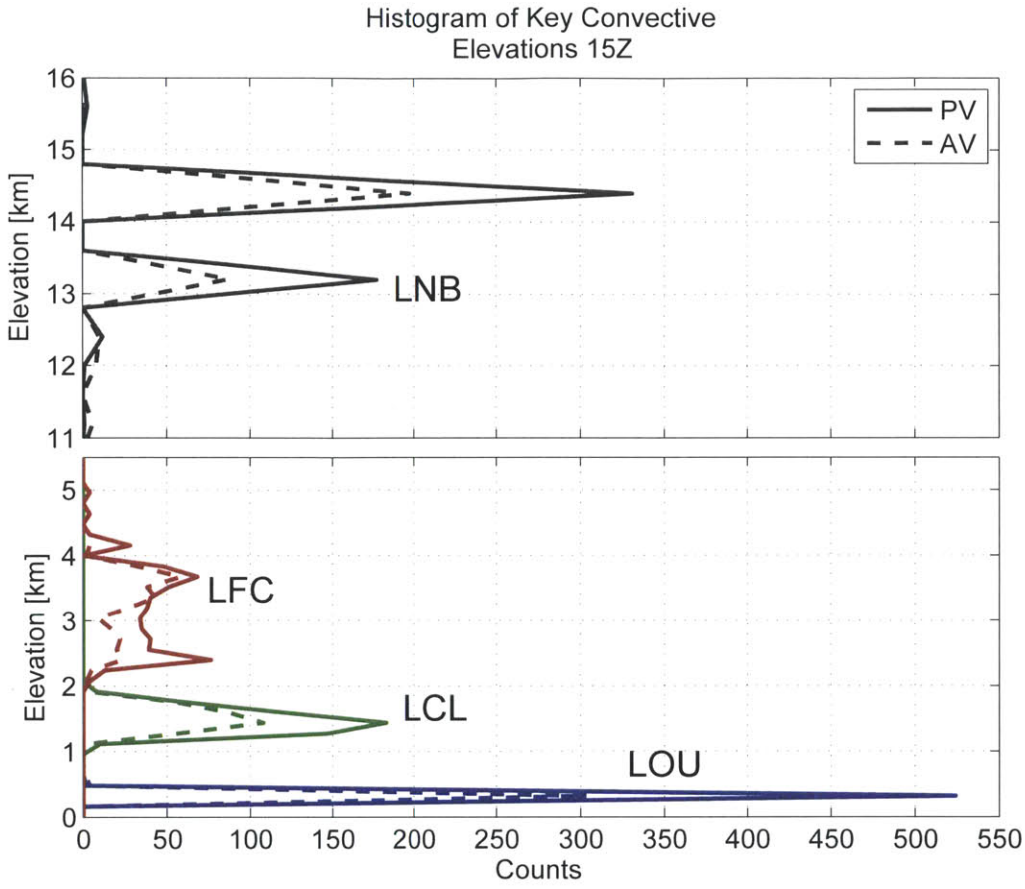


Figure 6-24: Histograms for the elevations of key convective elevations at focus area 1 for successful convective events (ones that performed work and precipitation). LOU: Level of Updraft. LCL: Lifting Condensation Level. LFC: Level of Free Convection. LNB: Level of Neutral Buoyancy.

release more energy, see Figure 6-25.

An inquiry into the error flags of failed convective events was very telling of why the AV simulation generated fewer events. Figure 6-26 shows a histogram of the differential error flag counts between the two scenarios. The AV simulation generated far more events with condition 6. These were instances where moist parcels were successfully lifted to positive buoyancy, but the the resulting cloud was too shallow to be significant and produce appreciable rainfall. This condition occurs when the parcels lifted from the surface lack appreciable moist static energy to achieve deep convection. The AV

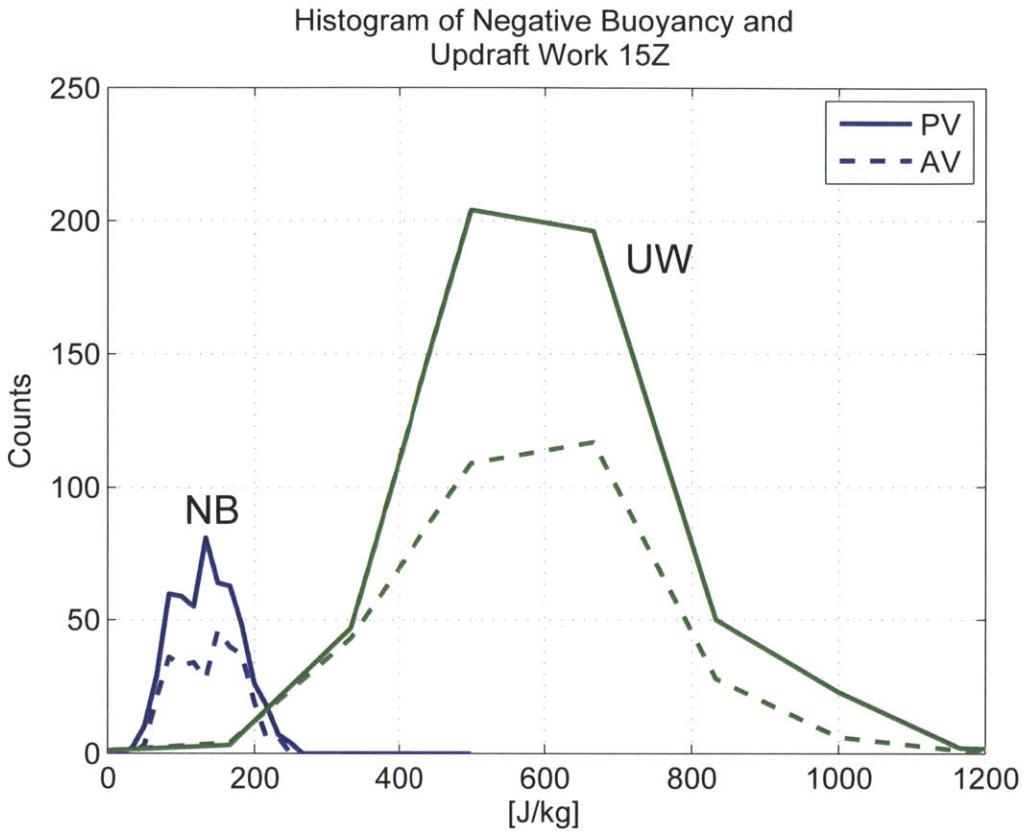


Figure 6-25: Histograms of negative buoyancy and work performed in the convective updraft at focus area 1 for successful convective events (ones that performed work and precipitation).

scenario had less total energy flux and lower evaporative fraction in the dry season, this is consistent with a condition of decreased moist static energy and convective events that release less energy.

In summary, the the land-surface condition with deforestation (AV) had higher levels of sensible heat flux and more turbulent kinetic energy. Although, the difference was not strong enough to generate more convective events. Alternatively, a significant number of the updrafts from the (AV) simulation had overcome negative buoyancy but then lacked the moist static energy necessary generate significant work and precipitation.

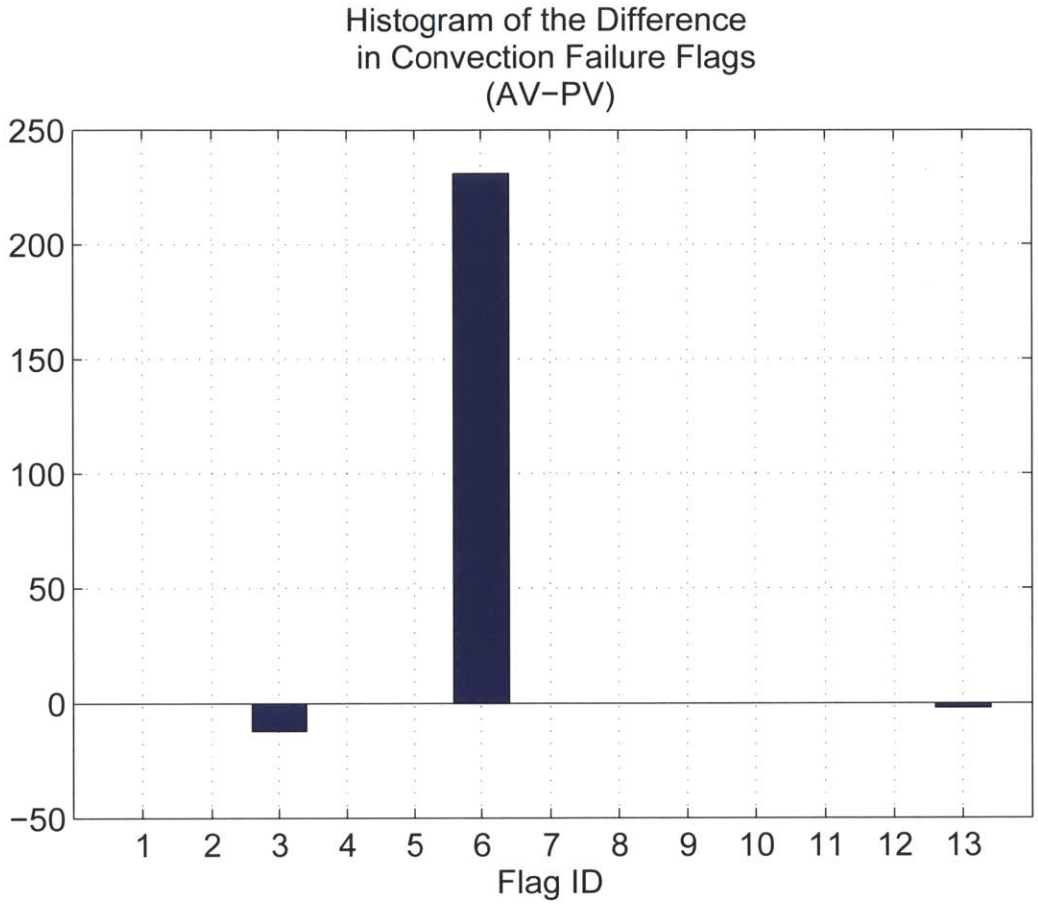


Figure 6-26: Differential convective failure flags at focus area 1, September 2003. Key: Flag 3: The level of free convection is too far from the level where updrafts originate, so it is out of reach. Flag 6: This cloud would be too thin to fall in this spectral type. Flag 13: Dynamic control didn't leave any positive member of reference mass flux, so this cloud can't exist.

### 6.3.3 Focus: Site 2

### 6.3.4 Site 2: Differential Hydrology in the Soil and Canopy System

Cumulative water flux at Site 2 for the PV scenario, and the differential water mass flux (AV-PV) are provided in Figure 6-27. Annual precipitation in the PV scenario was approximately 750 millimeters per year. The AV scenario received roughly 15% less precipitation. Losses at this site are dominated by soil evaporation, which contributes to half of total losses. Leaf evaporation and transpiration contribute about 25% of the total losses each, drainage is negligible in both cases.

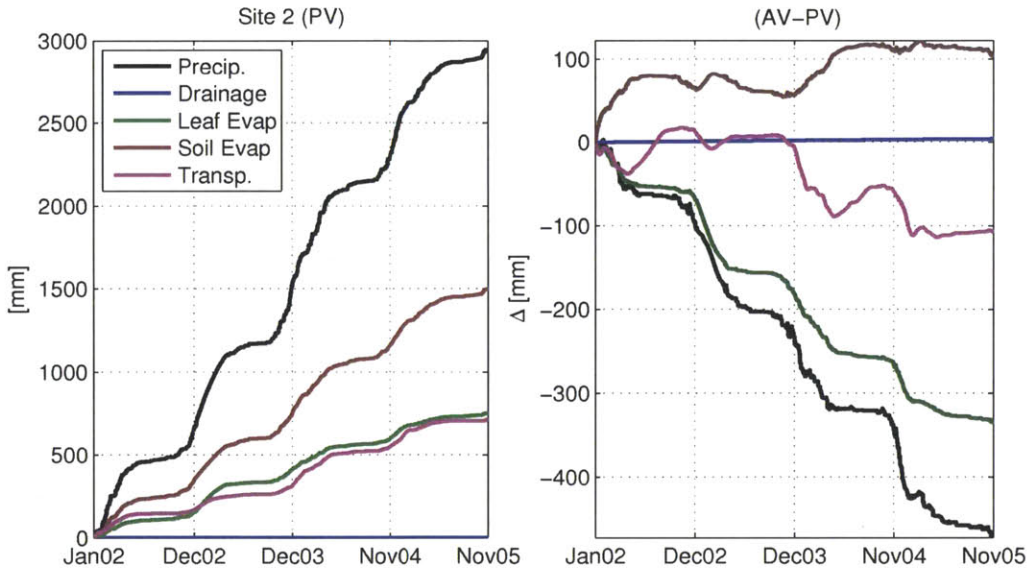


Figure 6-27: Time series accumulations of water mass flux through the vegetation canopy at focus site 2 during the coupled model experiment, 2002-2005. The left panel shows accumulated fluxes in the PV case. Differences are shown in the right panel.

As with Site 1, differential leaf evaporation shows a continuous negative bias associated with land conversion. This is likely attributed to a combined decrease in precipitation and leaf interception surfaces. Differences in soil evaporation and transpiration are not consistent from year to year. The AV scenario has increased soil evaporation only after the two stronger wet seasons, which peaked January-February of 2002 and

2004. The time series soil moisture profiles in Figure 6-28 give an idea of soil wetting during these periods. There is a distinct difference in the moisture profiles between the two simulations. Above 1.5 meters depth in the AV profile, there is a strong wetting and drying cycle occurring. The top 1.5 meters of the AV scenario are dryer than the PV scenario, distinguished by lower minimum soil moisture in the dry season. The AV scenario vegetation is completely grass and has a shallower rooting system, below 1.5 meters there is no root uptake which promotes increased soil moisture in the lower column. The vegetation condition in the PV scenario is an open canopy dry forest, which extracts moisture through its roots to a depth of several meters.

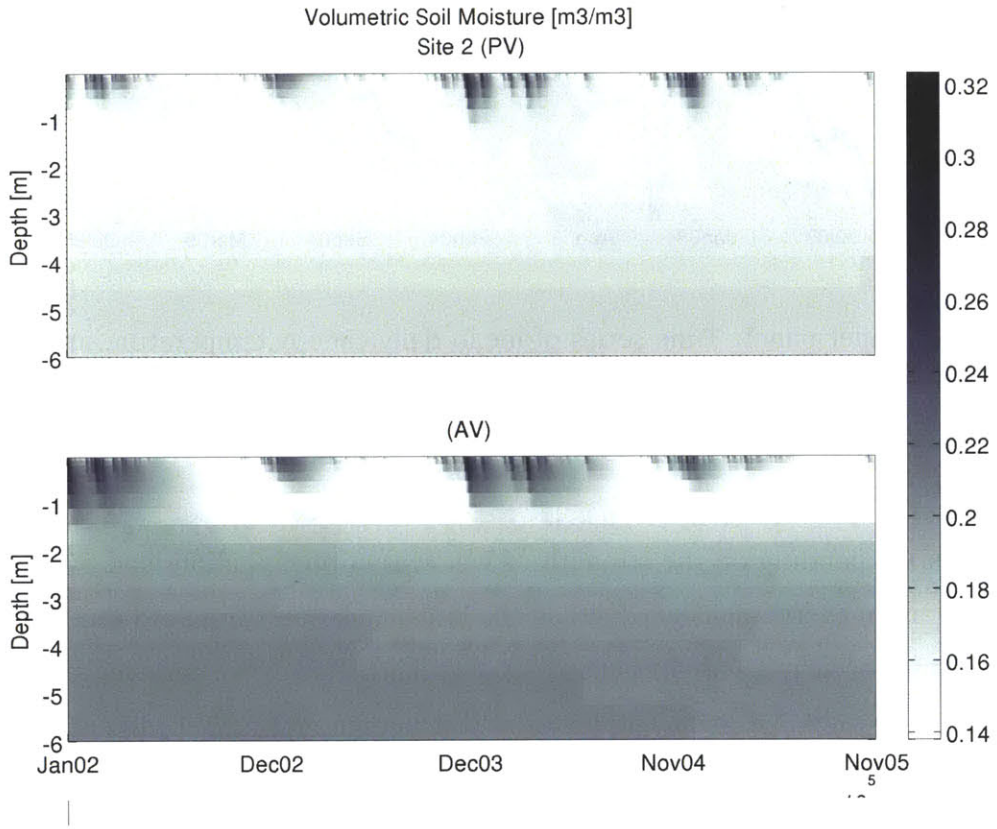


Figure 6-28: Time series profile of volumetric soil water at focus site 2 during the coupled experiment. Both cases are shown.

The soil moisture system does not hold a large store of water that is released to the atmosphere continuously over the dry season. The time series soil moisture profile

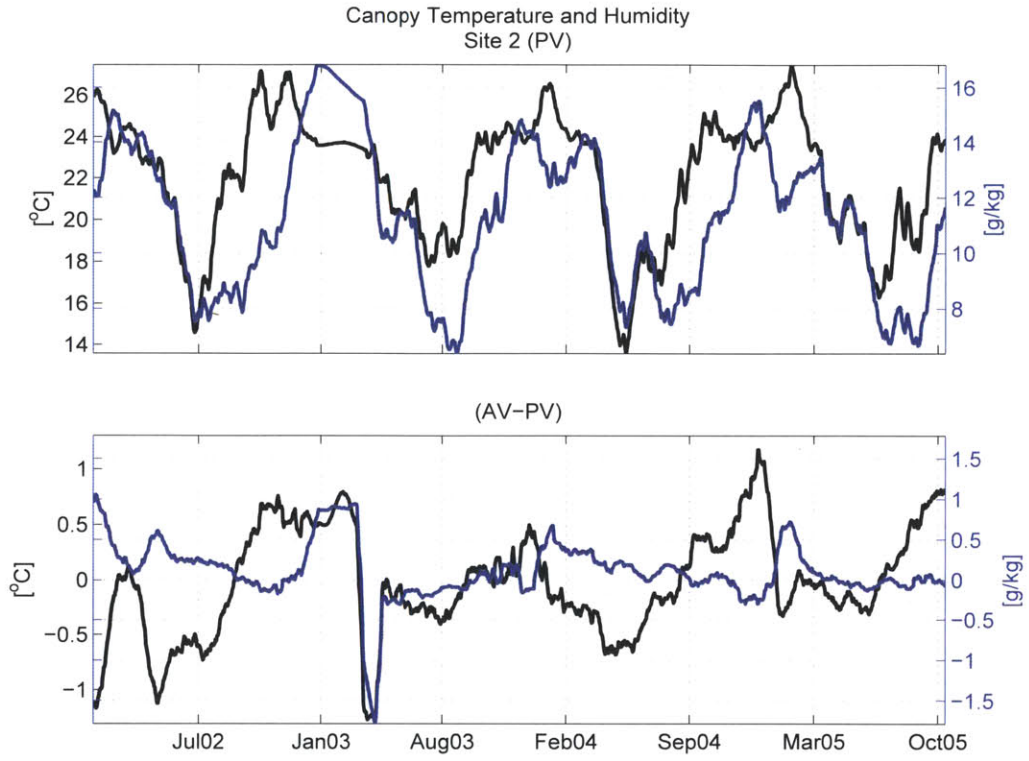


Figure 6-29: Upper panel: Time series of mean daily canopy temperature and humidity at site 2 during the coupled model experiment. Lower Panel: Differential canopy temperature and humidity.

showed this. Depending on the strength of wet season precipitation, soil evaporation and transpiration eventually shut down in the late dry season (Aug,Sep) and very little water exchange occurred with the canopy air over this period. This is conveyed in Figure 6-30 which shows the net gains and losses of soil column moisture. Unlike the tropical environment of site 1, this system shows a stronger event by event response, and not a continuous seasonal oscillation. One difference between the two scenarios emerged. The AV scenario showed longer drawn out soil column losses in the early to mid dry season that followed appreciable wet-season precipitation (2002 and 2004). This was counter intuitive at first, as this is symptomatic of deeper rooted vegetation accessing lower soil moisture stores that sustain throughout the dry season. This is more in-line with the what would be expected of the open dry forest of the PV scenario.

Referring to Figure 6-27, sustained soil column moisture loss in the AV scenario's early to mid dry season is coincident with increased AV scenario transpiration. A differential response in transpiration can come from several sources. Differential photosynthesis rates are unlikely, as atmospheric carbon concentrations were held constant and differential radiation in the early to mid dry season was minor (see Figure 6-31). Increased plant root biomass and leaf area were actually higher in the PV scenario so this is not the reason. The vapor pressure deficit between the canopy air and the leaf stoma also showed minor differences,see Figure 6-29. The result must be due to increased through-fall. Figure 6-27 shows that early dry season differential precipitation is relatively insignificant, but looking closely at the wetting in the top soil layers in Figure 6-28 more precipitation in the AV case is penetrating the canopy. The increased leaf area in the PV vegetation canopy is actually having a negative feedback, in that it intercepts a greater proportion of the weak precipitation events in the early dry season preventing wetting of the soil column.

The differential in total energy balance shows that the land-surface in the AV scenario receives more down-welling short and longwave radiation (Figure 6-31). The decreased albedo of the AV scenario again has an effect to decrease total surface energy flux even when incident radiation has increased due to cloud albedo effects. The decrease in AV scenario latent heat flux is consistent with overall decrease in mean annual precipitation. Surprisingly, sensible heat flux in the AV case shows a very weak decrease as well.

A general idea of the differences in the hydrologic phenomenon between the two scenarios has been established at the canopy scale. In summary, the differences in the Actual Vegetation scenario can be summarized as follows:

- AV: mean annual precipitation deficit on the order of $15\%$
- AV: decrease in total latent heat flux and total energy flux
- AV: greater dynamic variability in upper column soil moisture
- AV: lower leaf area promotes more early dry season through-fall

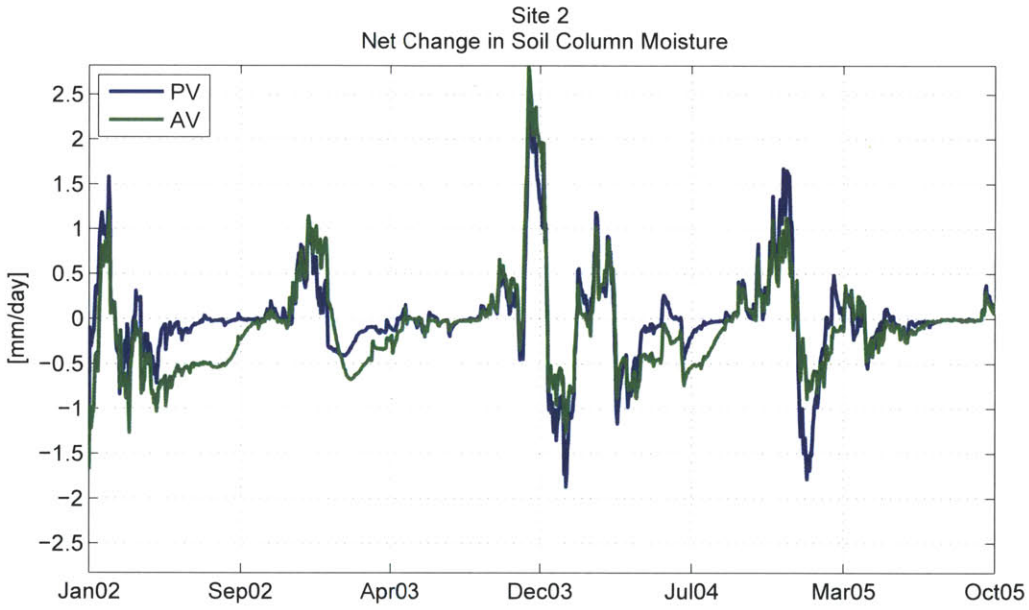


Figure 6-30: Net rate of change in soil moisture at focus site 2, both conditions are shown. Positive values indicate the soil column is gaining water, negative values indicate the column is losing water. The intersection points of the time axis are good proxies as to the starts and stops of the dry season and wet season.

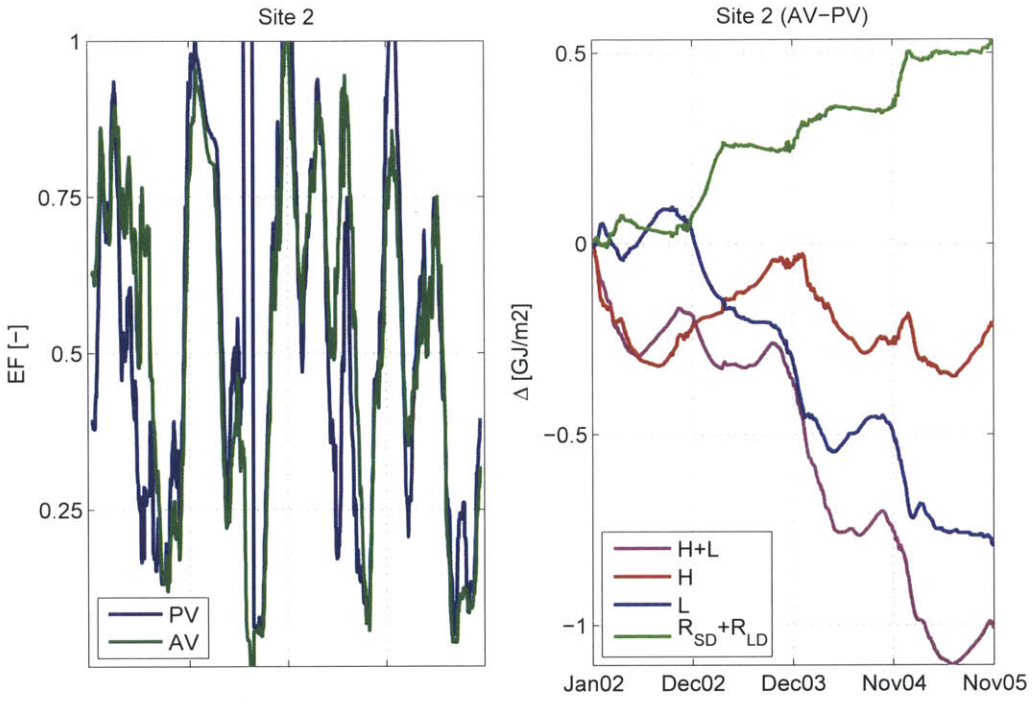


Figure 6-31: Left Panels: Time series of evaporative fraction (latent/(latent+sensible)). Right Panel: Time series of the differential in accumulated energy fluxes. Site 2.

### 6.3.5 Site 2: Differential Hydrometeorology of the Area, April 2003

At site 2, there is a strong depression in precipitation associated with the AV scenario for the month of April, see Figure 6-1. April of 2003 is selected as a case study to examine some of the features of the local hydrometeorology. A bounding box is constructed around the depression in differential precipitation at Site 2, it is shown by a red line in Figure 6-32.

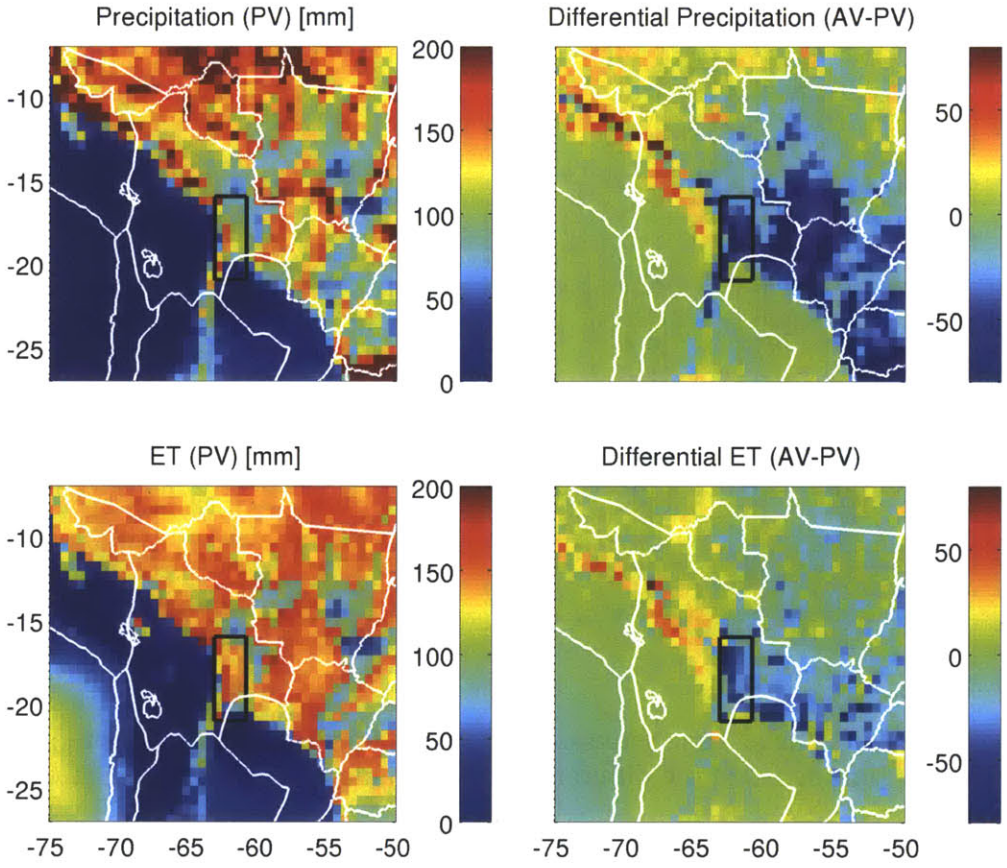


Figure 6-32: Upper left panel: map of integrated monthly precipitation, case AV. Upper right panel: map of the integrated difference in monthly precipitation, case PV minus case AV. Lower right panel: map of integrated monthly evapotranspiration, case AV. Lower left panel: map of the integrated difference in monthly evapotranspiration, case PV minus case AV. The boundaries of the focus region are provided. April 2003.

The precipitation here is dominated by convection, the diurnal average total and

resolved precipitation for the area is provided in Figure 6-33. There are differences in the timing of peak diurnal precipitation between the two scenarios. Both scenarios estimate maximum precipitation at 18 UTC which is 2pm local time, although the peak in PV scenario precipitation is more exaggerated. The PV scenario also shows a second mode in the evening at 11pm local time. The peak in evening precipitation is due mostly to its stratiform component. There is significantly less precipitation over all times of day in the AV case. The AV scenario does not have a distinguished evening peak.

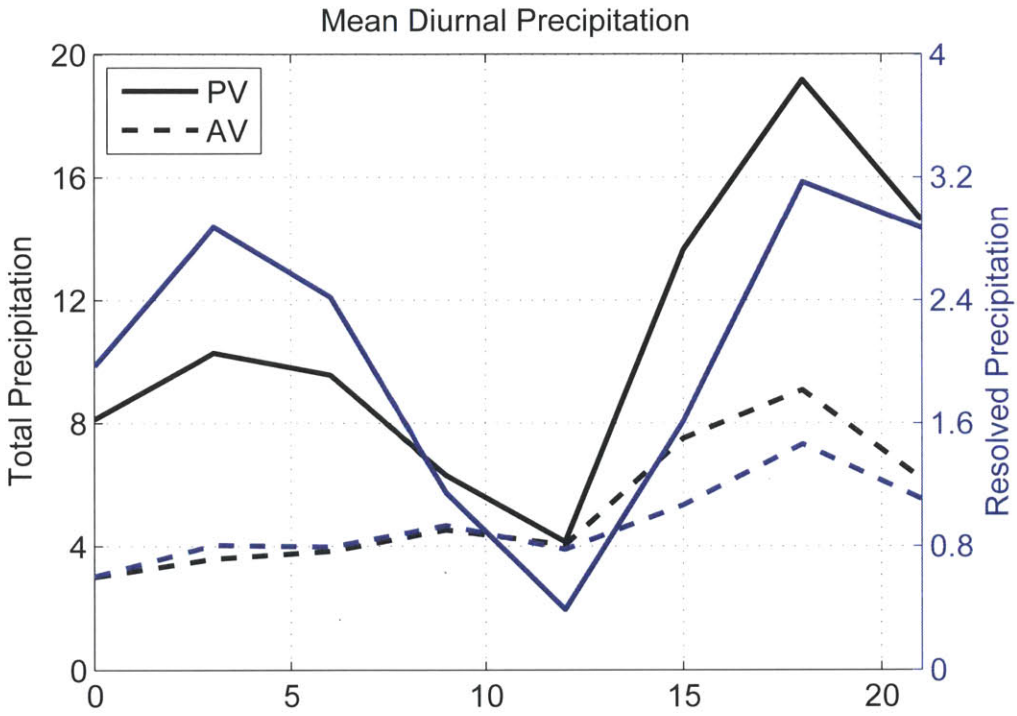


Figure 6-33: Spatial average of diurnal precipitation for the focus region above site 2. Both vegetation cases are covered, black lines use the left axis and indicate total precipitation (resolved+convective) and blue lines use the right axis and indicate only resolved (stratiform) precipitation. April 2003.

The mean totals for the domain averaged change in precipitable water $\Delta M_{pw}$, accumulated evapotranspiration $ET$, precipitation $P$ and resolved moisture convergence $Mc$ for the month of April are provided in Table 6.2. The PV scenario experiences over twice as much precipitation than the AV scenario ($85[kg/m2]$ compared to $41[kg/m2]$). Differential evaporation between the two scenarios is not as extreme ($111[kg/m2]$ in the

PV scenario compared to $83[kg/m2]$ for AV). Along with a decrease in total precipitable water $\Delta M_{pw}$, the domain showed negative moisture convergence in both cases which is typical as April is the onset of the dry season in this region. The PV scenario showed significantly less moisture divergence ($-37[kg/m2]$) than the AV scenario ($-52[kg/m2]$).

| Case | $\Delta M_{pw}$ | $ET$ | $P$ | $Mc$ | $T$ | $r$ |
|---|---|---|---|---|---|---|
| Units | $kg/m^2$ | $kg/m^2$ | $kg/m^2$ | $kg/m^2$ | $^oC$ | $g/kg$ |
| AV | -11.42 | 82.95 | 41.89 | -52.49 | 25.36 | 12.73 |
| PV | -11.02 | 111.89 | 85.91 | -36.99 | 27.36 | 15.15 |

| Case | $\theta_e$ | $\alpha$ | $R_{SD}$ | $R_{net}$ | $H$ |
|---|---|---|---|---|---|
| Units | $K$ | - | $w/m2$ | $w/m2$ | $w/m2$ |
| AV | 329.14 | 252.6 | 111.74 | 0.33 | 32.57 |
| PV | 336.2 | 218.7 | 130.2 | 0.297 | 35.81 |

Table 6.2: Hydrologic monthly means within the bounded area above case study 2, April 2003. Total change in column precipitable water $\Delta M_{pw}$, evapotranspiration $ET$, precipitation $P$ and resolved moisture convergence $Mc$, air temperature (55m) $T$, mixing ration (55m) $r$, equivalent potential temperature $\theta_e$, surface albedo to shortwave radiation $\alpha$, downwelling shortwave radiation $R_{SD}$, net surface radiation $R_{net}$ and sensible heat flux $H$.

x

The advective flux vectors of precipitable water are provided in Figure 6-34. Moisture flux comes from the north out of the moist Amazonian air mass. The differential flux vectors show significantly less northerly advective moisture flux in the AV scenario. The AV scenario also shows a greater amount of domain average moisture divergence.

The mean atmospheric profile of the virtual potential temperature (left panel Figure 6-35) shows that the AV scenario is symptomatic of a depression in the southward flowing advective moisture flux. As a whole the AV scenario shows a stark contrast to the PV scenario in terms of the moist energy in the lower troposphere. Although, this is not necessarily indicative of how stable the atmosphere is or how prone to convective redistribution of energy.

The higher monthly precipitation in the PV scenario is mostly attributed to to triggering of more convective events, Figure 6-36 indicates that PV convective events at 11 am were more frequent and shared similar modes of energy release in the convective updrafts. Surprisingly, the AV scenario convective updrafts showed a slight skew

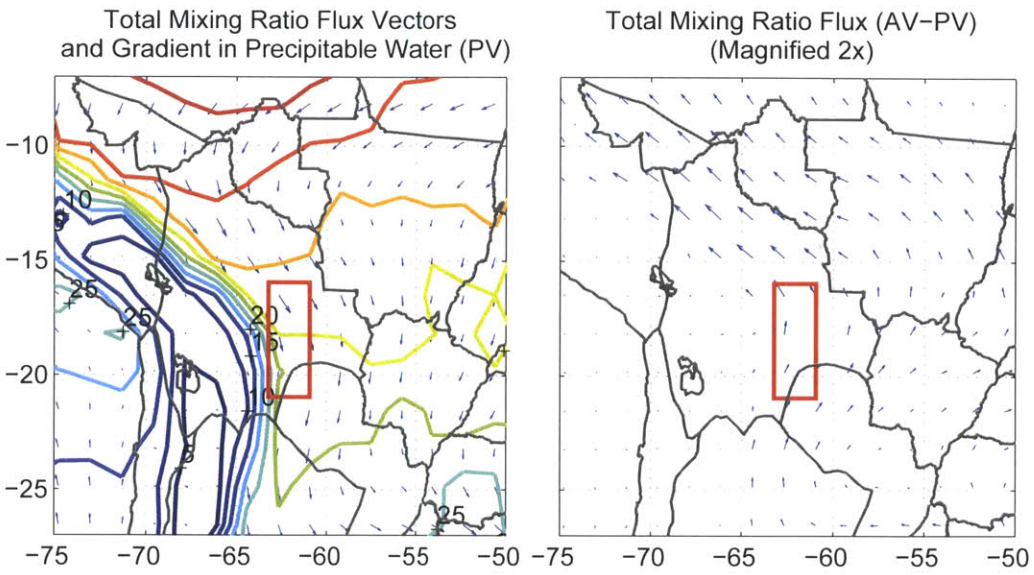


Figure 6-34: Upper left panel: Vertically integrated total water advective flux vectors for the Actual Vegetation case. Upper right panel: The differential in vertically integrated total water advective case, Potential Vegetation minus Actual Vegetation (PV-AV). Quivers are scaled to 20 times relative to the left panel. Lower left panel: Vertically integrated advective dry mass vectors for the Actual Vegetation (AV) case. Lower right panel: The differential in vertically integrated dry air mass advective fluxes, Potential Vegetation minus Actual Vegetation (PV-AV). Quivers are scaled to 2 times, relative to the left panel.

towards deep convection as compared to PV convective events. The distribution of negative buoyancy associated with PV convective events showed a strong peak in the low energy portion of the spectrum that was not evident in the AV scenario. Another way to look at this, is there were a number of events in the PV scenario that had a lower energy barrier to overcome to trigger convection, that was not present in the AV scenario.

The record of the convective failure flag differential in Figure 6-37 confirms that a number of AV scenario events failed due to overcome negative buoyancy in instances where PV scenario convection did not fail (flag 3). The record also indicates even more AV scenario updrafts that had achieved positive buoyancy were too shallow to generate any significant convection.

This case study showed a significant negative bias in early dry season precipitation in the case with human land-use. It is likely that the significant weakening of the advec-

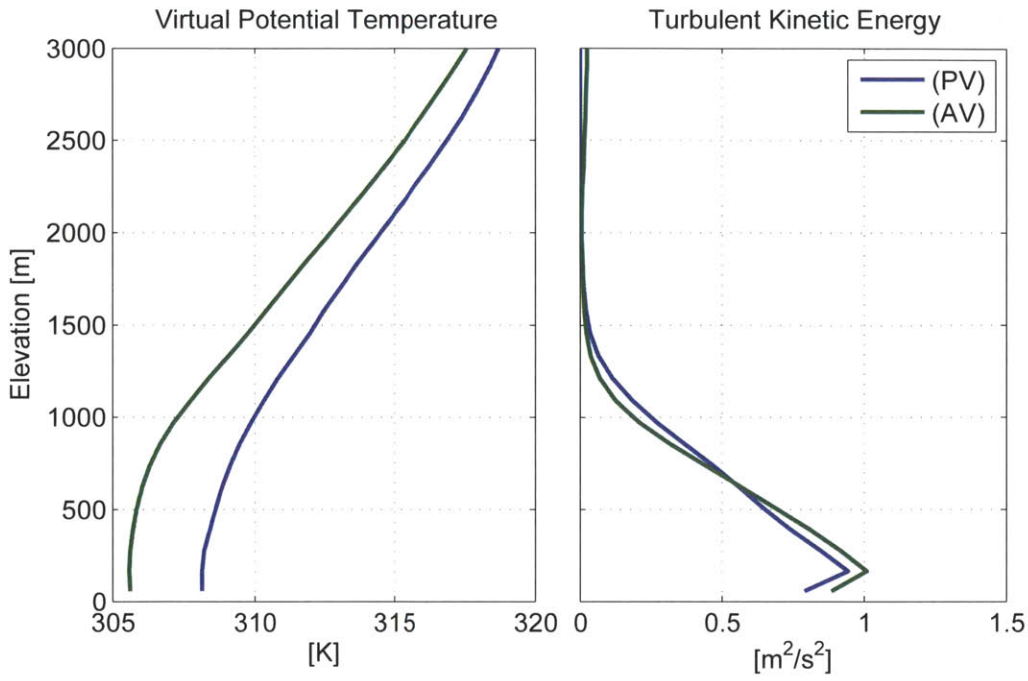


Figure 6-35: Profiles of monthly mean virtual potential temperature and turbulent kinetic energy. Focus region 2, April 2003 at 15Z (11:00 AM local).

tive flux of precipitable water was influencing convective precipitation. The atmosphere in this case showed a weakened profile of overall moist energy, although this was also likely to have been influenced significantly by a negative bias in both total surface energy flux and surface latent heat flux. Domain average latent heat flux rates peaked at $50\%$ lower in the AV scenario, see Figure 6-38.

In summary, this region showed reduced convective precipitation in the AV scenario due to both decreased ability to overcome negative buoyancy, and instances of weak convection upon achieving buoyancy. The inability to achieve buoyancy was apparently not due to weakened boundary layer turbulence, as the turbulent kinetic energy of the AV simulation was larger than that of the PV simulation at within the elevation window of the level of updraft. The majority of non-convecting events in the AV scenario were due to decreased moist static energy in the surface parcels. This is likely symptomatic of the decrease in total and latent heat flux at the surface, and to a lesser extent an overall decrease in advected precipitable water.

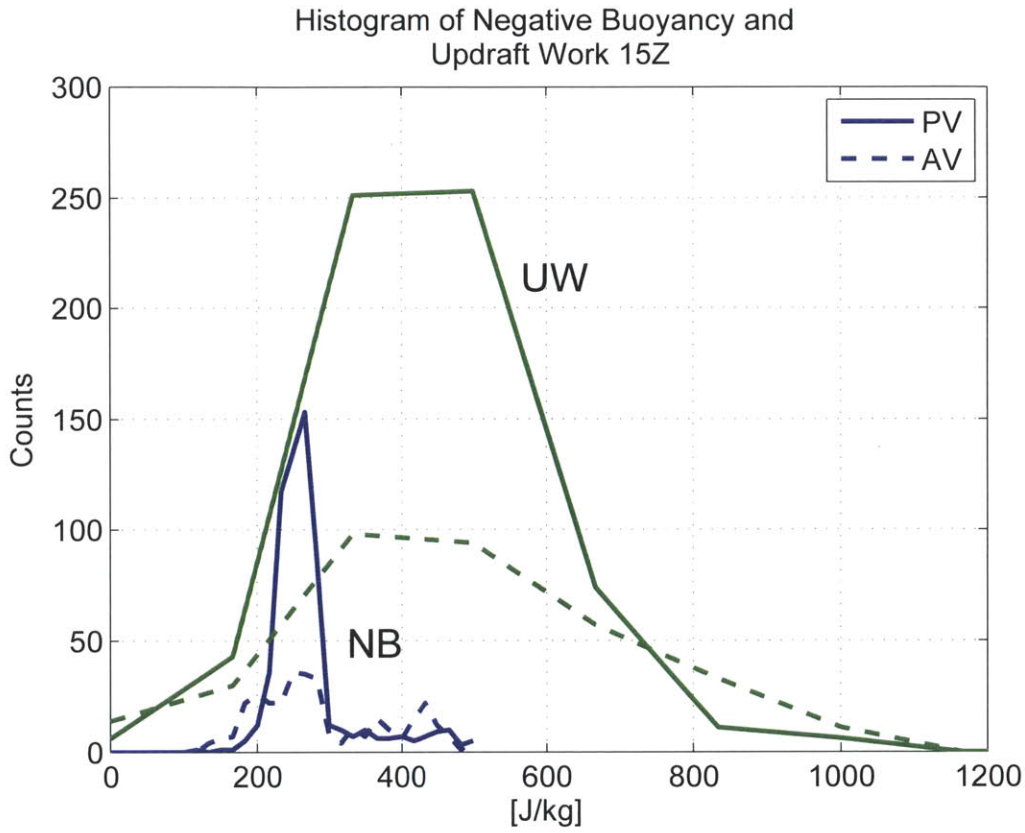
Histogram of Negative Buoyancy and
Updraft Work 15Z
PV
AV
UW
NB
Counts
[J/kg]
0
50
100
150
200
250
300
0
200
400
600
800
1000
1200

Figure 6-36:

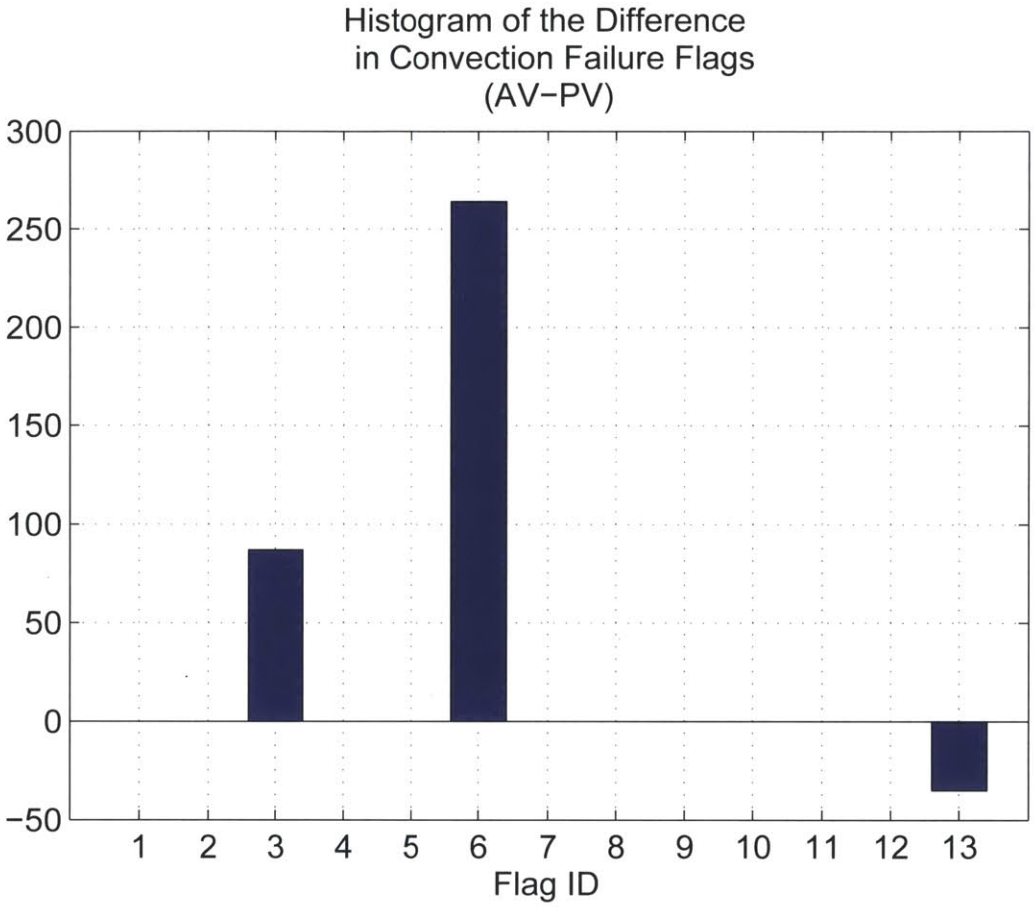


Figure 6-37: Key: Flag 3: The level of free convection is too far from the level where updrafts originate, so it is out of reach. Flag 6: This cloud would be too thin to fall in this spectral type. Flag 13: Dynamic control didn't leave any positive member of reference mass flux, so this cloud can't exist.

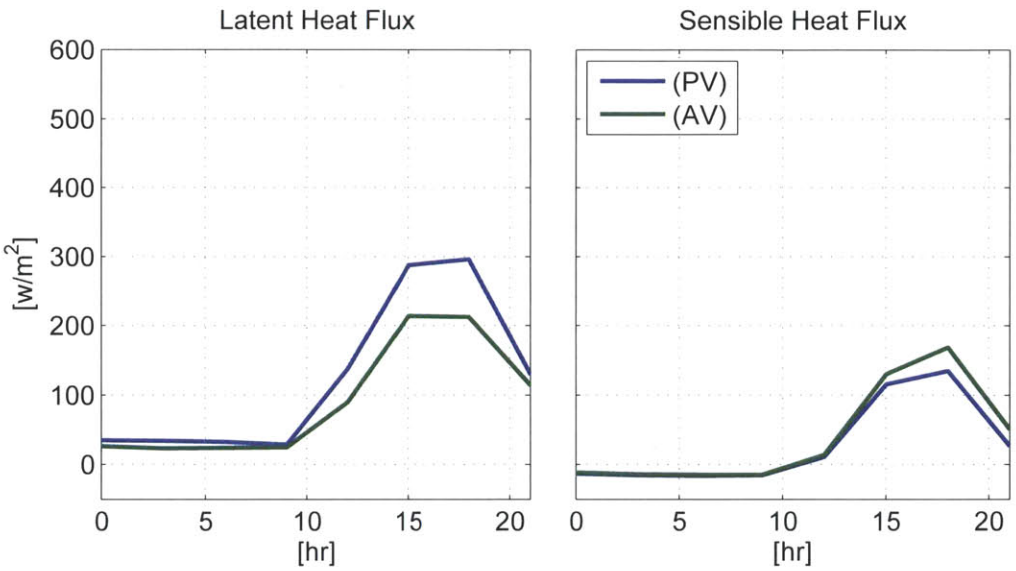


Figure 6-38: Spatially averaged diurnal mean sensible and latent heat fluxes for the focus region at 62W 18S. Both vegetation cases are covered. April 2003.

# Chapter 7

# Ecosystem Response to Climate Perturbations

The mean monthly precipitation volumes and number of days with precipitation generated in the coupled simulations were recorded at the two sites of interest. With this information a bias ratio of the Potential Vegetation scenario over precipitation generated in the Actual Vegetation scenario is calculated for both number of rainy days per month, and depth of precipitation per month. The objective is to create a perturbation that is applied to the climate driver dataset originally used to create the initial condition vegetation used in the coupled simulations.

While the previous hydrologic analysis focused on the differential effects of the AV scenario, the perturbation will reflect the differential effect of the PV scenario. This is because the existing climate driver dataset, the DS314, is a real world record based on observations associated with Actual Vegetation. A perturbation therefore has to be relative to the AV case. The monthly perturbations are applied to the existing climate dataset, such that it generates a realization of what climate would had been like if the continent had no human land-use. This potential perturbation climate is then applied over multiple decades to the sites to see if the vegetation shows any response.

## 7.1 The Re-sampling Process

The perturbation climates were generated via a re-sampling process. The (PV/AV) bias ratio $R_V$ for monthly precipitation volume $R_V$ is multiplied by the climate datasets accumulated monthly precipitation volume $V$ to get a perturbation volume $V'$. The bias ratio in the number of precipitating days $R_N$ is multiplied by the original number of days with precipitation $N$ to get a perturbation number $N'$.

The climate driver data is parsed by day, and days with rain are flagged. The set of precipitating days is re-sampled through all the possible combinations of those days that could be used to populate the new perturbation number of precipitating days. For instance, if the original dataset had $N = 2$ raining days, and the perturbation set calls for $N' = 3$ raining days, the perturbation set could be populated by using the first rainy day in the original dataset 3 times, or perhaps the second rainy day 3 times, or various combinations of the two. The ideal combination of rainy days minimizes the difference between the volume of the re-sampled days with the desired perturbation volume $V'$. A diagram of this process is provided in Figure 7-1.

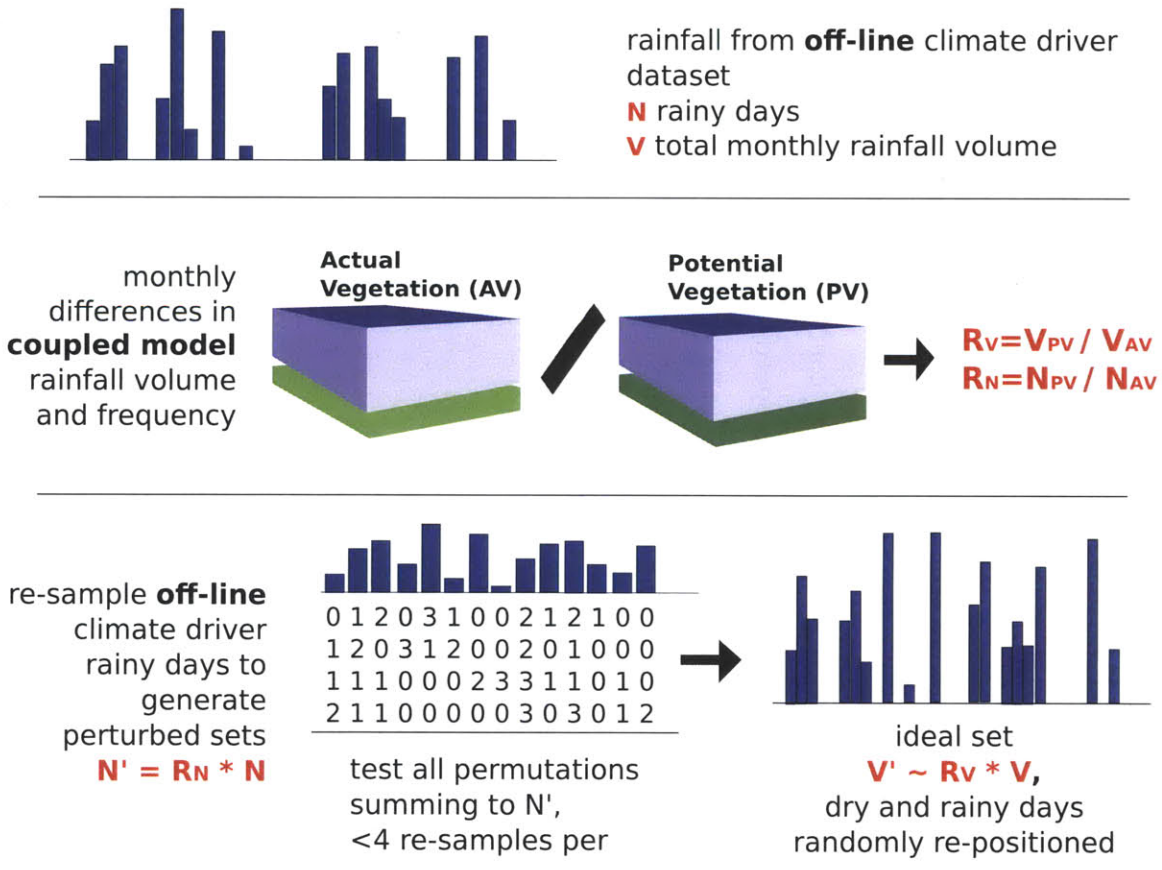


Figure 7-1: Diagram showing the process of creating perturbed climate forcing datasets for off-line ED2 simulations.

As the number of precipitating days in the original and output dataset get larger, a greater number of combinations become possible. The benefit of this is that the difference between the re-sampled total rainfall volume and the desired rainfall volume gets smaller. Searching all of the permutations can also get extremely cumbersome. To bring the computational cost of searching to a reasonable level, a cap was placed on how many precipitating days from the original sample could be used. Also, a cap was placed on how many times each day could be sampled. Testing found that beyond searching permutations of 16 sampled days and maximum re-sample rate of 3 was unfeasible.

The set of sampled rain days are re-distributed randomly throughout the month in the perturbation dataset. Each of these days contain variables that remain unchanged (pressure, air temperature, humidity, wind-speed, down-welling radiation and precipitation) and have a sub-daily granularity. The days with no precipitation in the original dataset are then randomly selected and randomly injected into the perturbation dataset. In the final step, the precipitation rates are adjusted so the actual monthly precipitation volume in the perturbation dataset matches the exact value that is desired, $V'$.

## 7.2 Vegetation Response

### 7.2.1 Site 1

Four un-coupled EDM simulations were initialized with the vegetation structure and composition from site 1. The simulations differ only in the climate data driving them. Each of the climate records is based off of the DS314 data from 1980 through 2005. Climate that drives the model is looped when it hits the end of the record. This is a valid approach because the climate record is intended not to simulate individual years with accuracy, but to provide a record that is representative of recent climate of no particular order. The specific differences in the four simulations are as follows:

**Control** This simulation uses the original climate dataset, with no perturbations

**Re-sample 0** This simulation is used to test the effect of re-sampling climate with no

bias. The number of precipitating days is held the same as the original dataset, and the volume is preserved, but days are still randomly selected and reassigned.

**PV/AV** This simulation uses the climate data that is perturbed based on the volume and frequency ratios calculated in the PV/AV coupled model simulations.

$+20\%$ This simulation uses a perturbation on the original dataset that assumes the the number of precipitating days is unchanged, but the volume of precipitation is increased by $20\%$ each month.

The off-line perturbation experiment at Site 1 lasted for 100 years, a comparison of the accumulated and monthly mean precipitation for the four test cases are provided in Figure 7-2. There is no difference in the precipitation accumulated in the control and Re-sample 0 runs. This is expected and confirms the integrity of the re-sampling process. Notice also that the $PV/AV$ perturbation precipitation has roughly the same or greater accumulation as the $20\%$ constant bias case. In the coupled simulations, annual differences at this site did not exceed $15\%$. The largest bias ratios were calculated in the dry season. The climate dataset estimated greater dry season precipitation than that of the coupled simulations, which in effect increased the effective annual bias applied during the offline equilibrium simulations discussed here.

A time series trajectory of above ground biomass $AGB$ for the four cases is plotted in Figure 7-3. The biomass represents the average over each patch of land, which includes areas of different disturbance histories and land-use classes. There are three major modes of variability evident in the time series. Each simulation shows the seasonal oscillation of leaf flushing evident at the highest frequency. There is also inter-annual variability that reflects the periodicity of the climate record. For instance there are several droughts that reoccur on the 25 year time-scale of the climate record. The third mode of variability is the steady increase in biomass over the first 65 years, and its plateau through the last 35 years. The differences between the control and the $Resample0$ simulations show evidence that the differences in the estimated biomass can be explained not only by the biases in seasonal precipitation, but also from differences

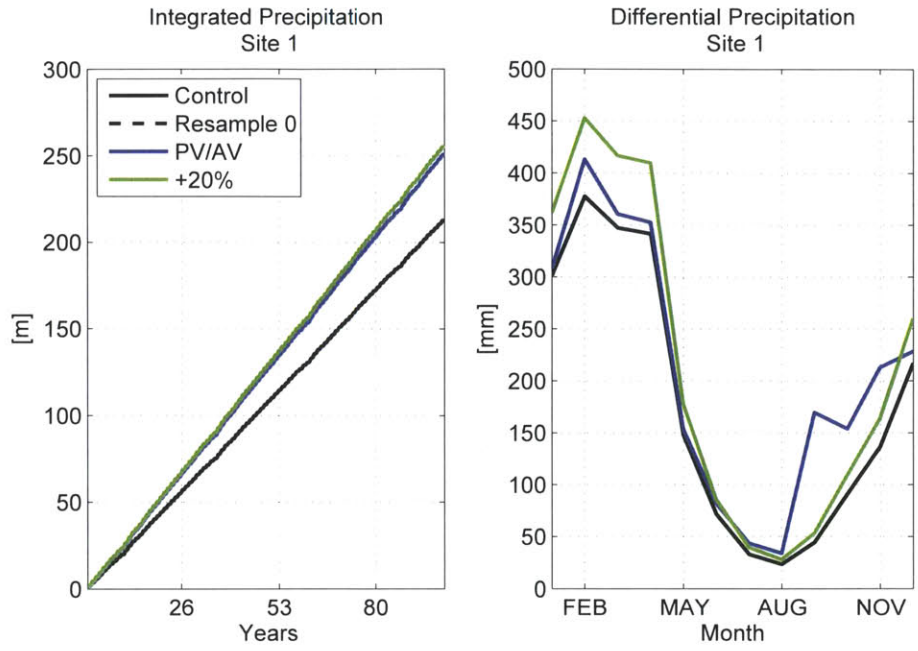


Figure 7-2: Integrated precipitation from control and perturbation climates. Monthly mean precipitation from control and perturbation climates.

in the daily variability of the climate record. The $Resample0$ climate is virtually identical to the $Control$ as monthly averages are concerned.

The four simulations show clearly different trajectories of above ground biomass. The $PV/AV$ simulation shows the greatest separation from the control simulation. Most of the change in biomass is associated with the growth of early successional plant functional types. Figure 7-5 shows that differences in Early Successional biomass in the $PV/AV$ simulation and the control simulation peak at $6\%$.

There were differences between the $PV/AV$ and control simulations regarding the conditions of growth, stress and disturbance. The moisture stress experienced by the plants is not severe, yet not insignificant. The vegetation stress index averaged below $20\%$, indicating that plants were not frequently closing their stomata to conserve water. The smoothed monthly mean vegetation stress index is shown in Figure 7-4. Notice that the inter-annual variability of the vegetation stress index is lower in the $PV/AV$ simulation compared to the control simulation. The control simulation shares a similar

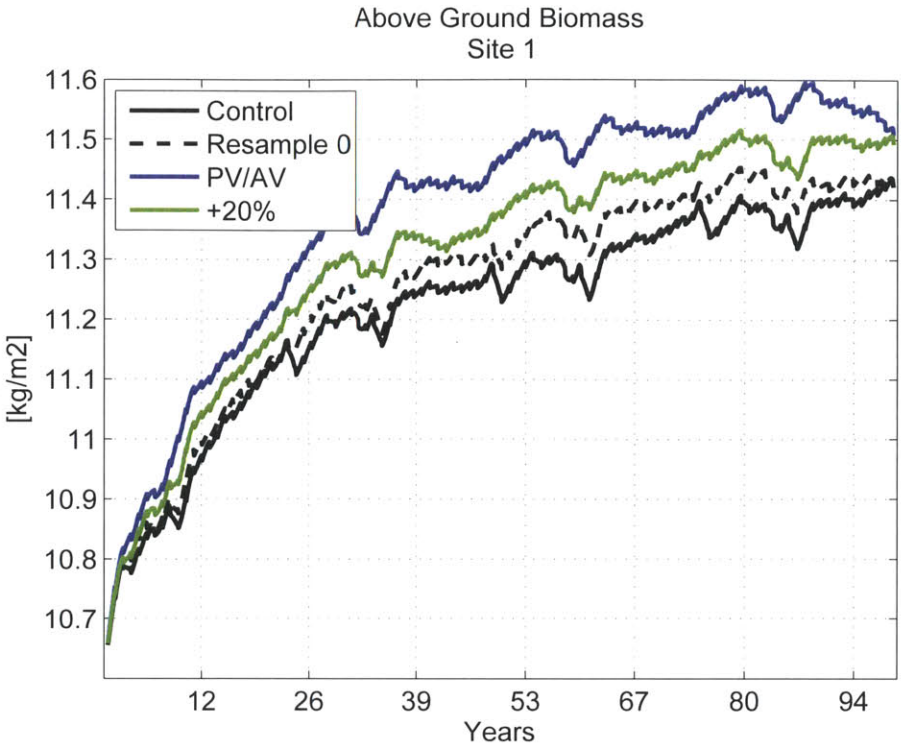


Figure 7-3: Time series of above ground biomass at site 1. Original climate (control) and perturbations.

mean, but also experiences years with more significant moisture stress, as well as years with less. The control simulation showed periodic episodes of drought induced leaf drop every few decades as well, but the magnitudes were insignificant. The evidence suggests that the increased biomass in the PV/AV simulation is attributed to increases in net primary production due to the marginal decreases in water stress function.

Tree fall was the more significant natural disturbance regime. No natural fires occurred at this site over the duration of the simulation.

The vegetation canopy in each perturbation is dominated by late successionals, which at the initialization of the simulation accounted for $8.6kg/m2$ of the total $10.5kg/m2$ mean above ground biomass. The late successionals show very little reaction to the increased precipitation in the perturbation case. Late successional functional types can be generally described as having slower growth and slower turnover. Althrough differ-

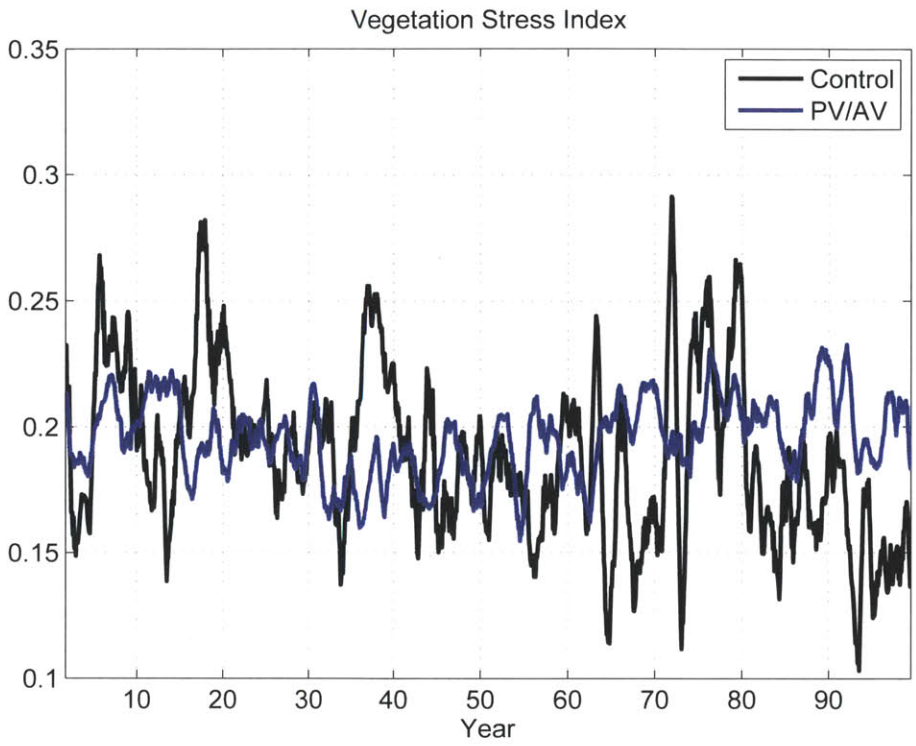


Figure 7-4: Time series of the Vegetation Stress Index for early successional plant functional types in the $PV/AV$ and control simulations. The vegetation stress index is averaged over all early successional cohorts monthly, and is smoothed over a 12 month window.

ential total above ground biomass in the late successionals was minimal, there were observed differences in the biomass distribution across the stem diameter size classes, see Figure 7-6.

By the end of the simulation, there are subtle differences between the vertical profiles of the PV/AV canopy and the control canopy. The left panel in Figure 7-7 gives a binned vertical profile of the average leaf area index for the control simulation canopy.

Near the end of the 100 yeas, the four simulations show some evidence of converging towards a similar equilibrium. It is possible that prior to the vegetation reaching equilibrium, there was less competitive stress on resources. In other words, before the biomass reached the equilibrium value, there was still room in the resource niche for the vegetation to grow into. Vegetation in the $PV/AV$ perturbation climate, and the

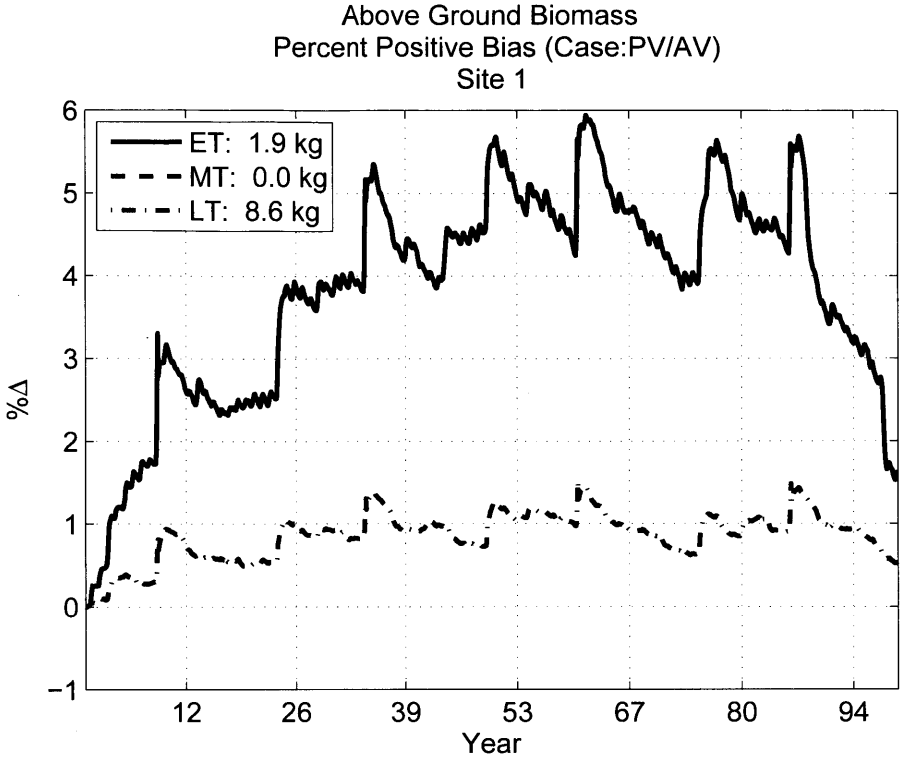


Figure 7-5: Time series of the percent difference in the differential above ground biomass bias in the (PV/AV) perturbation, relative to control simulation biomass for each plant functional type. ET: Early Tropical. MT: Mid Tropical. LT: Late Tropical. The legend indicates the starting biomass of each class per $m^2$.

$+20\%$ perturbation climate showed increase production and reached the equilibrium condition through a steeper trajectory.

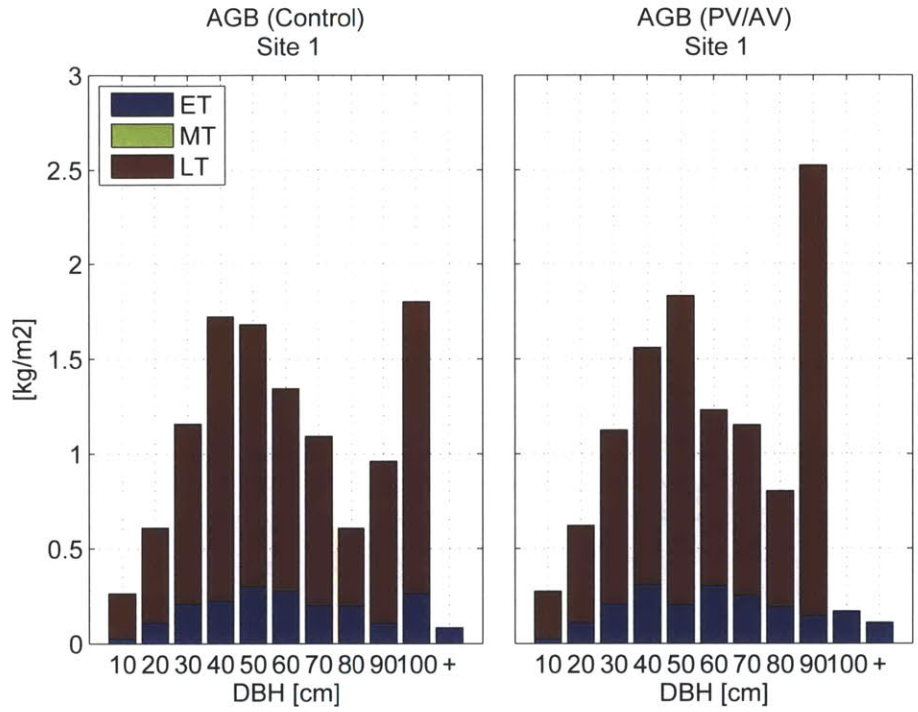


Figure 7-6: Distributions of Above Ground Biomass binned by stem diameter at breast height, generated via original (control) and perturbation (PV/AV) climates. Distributions are observed in the 100th year of simulation.

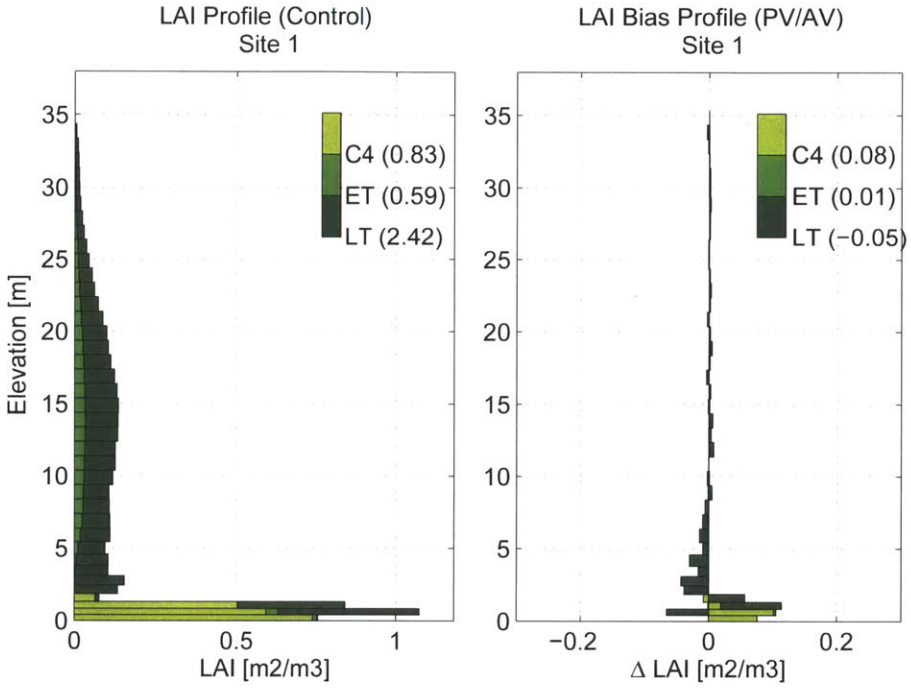


Figure 7-7: Profile of leaf area from control climate and the differential leaf area profile generated by the potential (PV/AV) perturbation climate. Profiles are yearly leaf area means observed on the 100th year of simulation.

### 7.2.2 Site 2b

The Actual Vegetation condition at site 2b that served as the initial condition for the coupled experiment was a grassland. This site had no biomass from trees. In contrast, the Potential Vegetation scenario could be described as an open canopy dry forest or Cerrado, composed of grasses and sparse trees. The difference in these two initial conditions is hypothesized. The percentage of primary landscapes that were converted to pasture in the spin-up simulation was not 100 percent, yet the primary lands that were left still collapsed to grasslands. Note that these simulations used the same climate record as well. The only explanation for the collapse in terms of the model construct was a decrease in total seed biomass pool that generated recruits of early successional tree species. With land-conversion, the ability of newly recruited early successional tree species may had been compromised, and had trouble competing with grasses in a region with significant fire disturbance rates.

Subsequently, the Actual Vegetation scenario at Site 2 cannot be used to test a change in equilibrium because it lacks the seed pool that is necessary to recruit new trees. As an alternative, the test of climate-vegetation equilibrium at site 2 instead uses a near-bare ground condition as a starting point for all four climate perturbation scenarios. A near bare ground condition, gives a small amount of biomass to each of the viable plant functional types to start with. This site is now called "2b" to indicate the use of the near-bare ground initial condition.

This simulation was conducted over several hundred years. However, the forest dynamics showed quasi steady-state behavior early on and therefore analysis will be restricted to the first 120 years. The integrated and monthly mean precipitation of the original and the three climate perturbations are provided in Figure 7-8. In this case, the $+20\%$ perturbation is is comparable to the $PV/AV$ simulation in both seasonality and magnitude.

In this experiment, there is clearly a significant difference between the forest biomass in the $PV/AV$ and $+20\%$ simulations compared to the two controls. The forest biomass in the control simulations nearly collapsed in the 15th year of simulation, and then com-

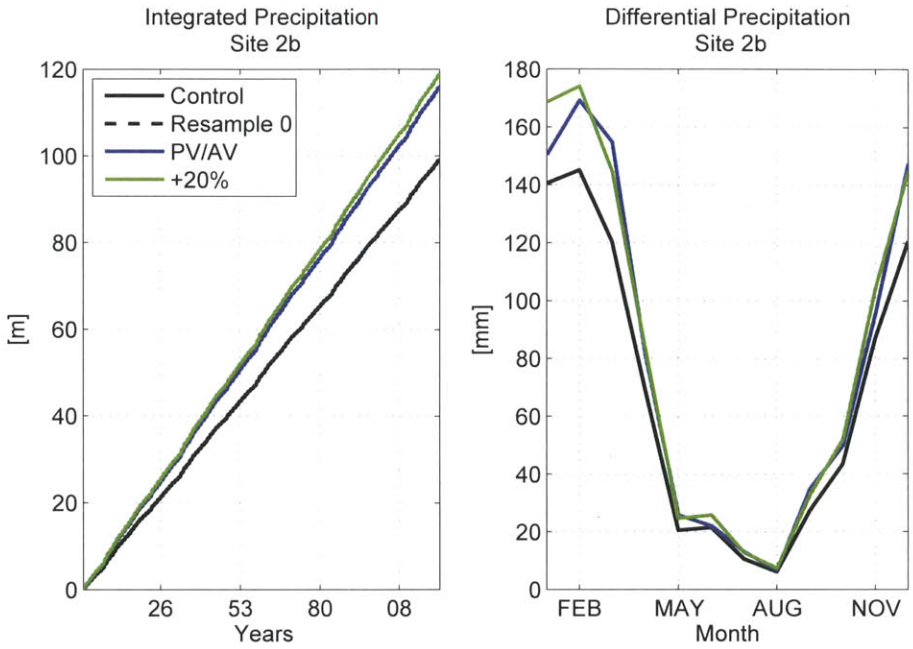


Figure 7-8: Integrated precipitation from control and perturbation climates. Monthly mean precipitation from control and perturbation climates.

pletely disappears after 60 years. The time series projection of above ground biomass is provided in Figure 7-9.

The collapse of the forest in the control climate case is inspected in greater detail. In the first several years of the simulation, both the $PV/AV$ perturbed climate and the control climate start out by accumulating biomass in early successional functional types. The time series of leaf and seed biomass for early successional plant functional types is provided in Figure 7-10. The control simulation accumulates less biomass in leaves and seeds. Leaf biomass is necessary for the plants be productive, seeds are necessary to recruit new members. In a sense, the size of these two pools have some influence on the stability or survival of the group.

Prior to the collapse of the early successional trees, the seed and leaf biomass decreases, with the decrease there is less production dedicated to adding biomass to these pools. The net primary production directed towards these two pools are provided in Figure 7-11. The decreases in leaf and seed producation and biomassed are clearly cou-

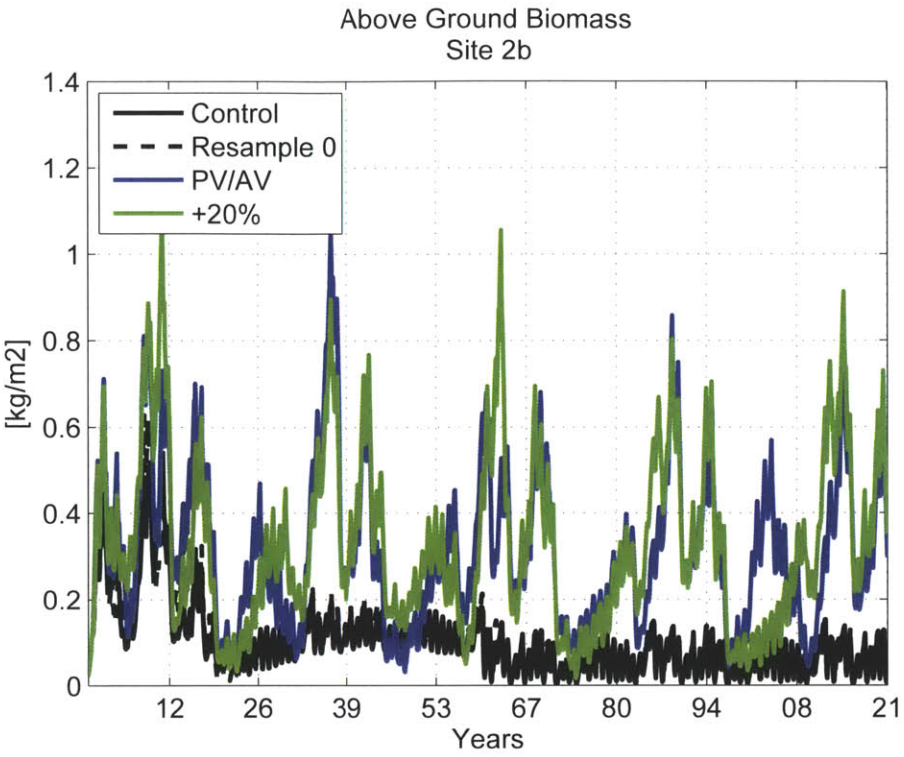


Figure 7-9: Time series of above ground biomass at site 2b. Original climate (control) and perturbations.

pled together, and indicate the early successional tree species can not succeed in the control climate.

As the control simulations enter the decline before the collapse of the early successionals, it is clear that the plants are losing the ability to produce and are suffering negative consequences for it. It is still unclear why exactly this is the case. One potential explanation could be increased disturbance rates associated with the control precipitation. Figure 7-12 shows the time series of natural disturbance at the site. The natural rate of treefall disturbance is 0.014, disturbance rates greater than 0.014 signal that the primary disturbance mode is fire. The EDM2 model only applies the maximum of the two natural disturbance rates, in this case the natural disturbance regime is completely dominated by fire. The rates describe the fraction of the land-surface that will be disturbed by fire each year. Fires peak in the dry season, and in in the first 50 years of

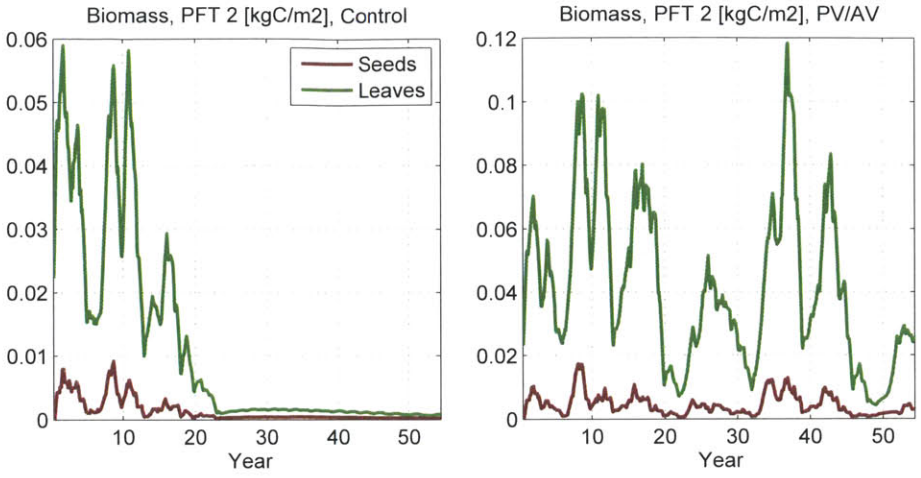


Figure 7-10: Time series of the seed and leaf biomass pools for the early successional tree types at Site 2b. Values for the control simulation are in the left panel, the $PV/AV$ simulation is on the right panel. Values are monthly means, smoothed uniformly with a 12 month mean.

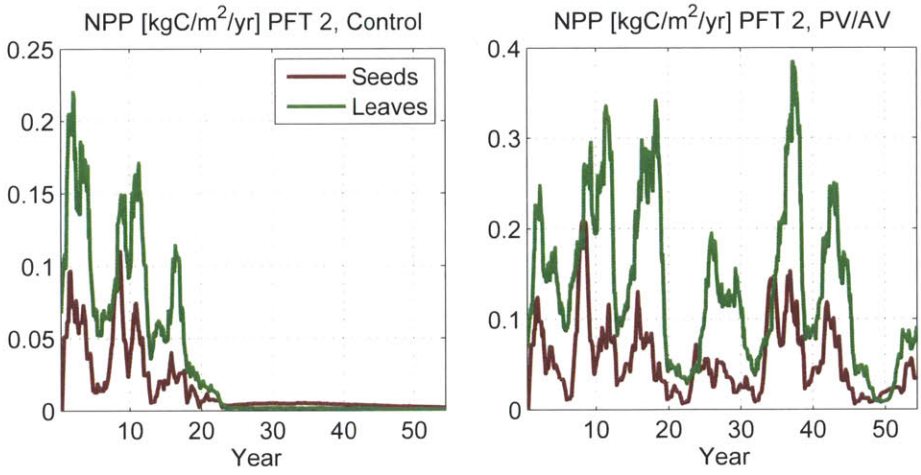


Figure 7-11: Time series of the net primary production diverted to seed and leaf biomass pools for the early successional tree types at Site 2b. Values for the control simulation are in the left panel, the $PV/AV$ simulation is on the right panel. Values are monthly means, smoothed uniformly with a 12 month mean.

the $PV/AV$ simulation they range from 0.03 to 0.08. The fire disturbance rate in the $PV/AV$ simulation is relatively higher. The fire ignition rates are dependant on biomass as a fuel source, so the more successful tree community ultimately has the higher distur-

bance rates. It can be safely concluded that increased fire disturbance is not the driving force behind the collapse of the early successional trees in the control simulation

The failure of early successional trees in the control simulation is attributed primarily to drought induced leaf drop, see the right panel of Figure 7-12. leaf drop has a catastrophic effect on this community, essentially robbing the trees of hard earned biomass and removing their ability to produce and build biomass pools for potential new recruits. Drought induced leaf drop is a direct indication that soil moisture levels in the control simulation reach sustained mimumum values close to the wilting point.

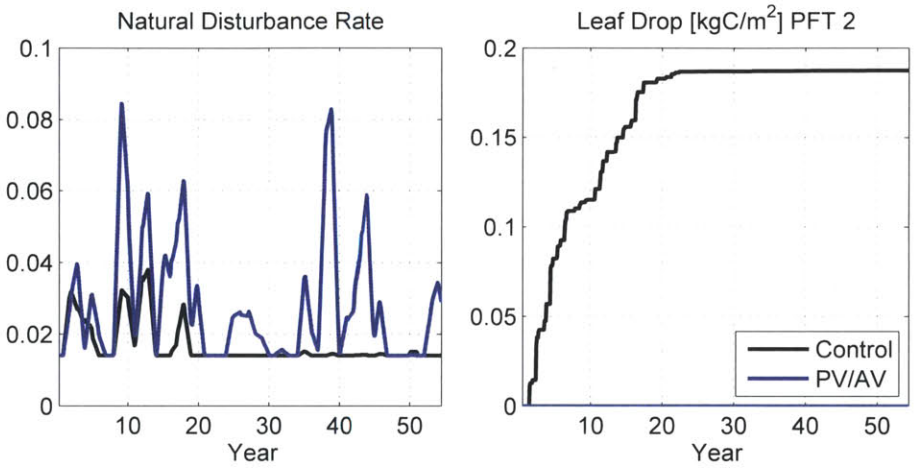


Figure 7-12: The natural disturbance rate (left panel) and the leaf drop rate (right panel) for early successional tree types (PFT=2) in the control and $PV/AV$ simulations at Site 2. The disturbance rate is the yearly areal fraction of lands that are burned through fires.

The ecosystem driven by the enhanced climate ($PV/AV$ and $+20\%$) suffers from marginal and near drought induced ollapse of the early successional tree species as well. However, the $PV/AV$ perturbation simulations do not undergo catastrophic leaf drop. They do however suffer effects of high fire disturbance rates and water stress reductions in primary production. A conservative mean annual fire disturbance rate of $3\%$ has an approximate ecosystem turnover rate of 33 years, this of course assumes that fires only pick locations that have not burned yet. But it gives an idea of how significant the effect of fire is on this ecosystem. It is also clear that this ecosystem is fragile.

There is evidence to this, in that perturbed climate simulations have a continuous cycle of collapse and re-emergence; and that the non perturbed climate transitioned to a complete grass-land.

The final vertical profile of leaf area and the distributions of biomass after 125 years are provided in Figures 7-13 and 7-14. The early successional trees that emerge in the $PV/AV$ simulation are very short compared to tropical canopies, peaking typically under 10 meters with some rare exceptions over 15 meters.

The $PV/AV$ simulated ecosystem has structure and composition that approximates an open canopy dry forest. Naturally, the canopy height is much shorter than that of tropical rainforests which typically exceed 30 meters in central and western Amazonia. Dry forests in the Bolivian lowlands are shorter on average than the tropical rainforests of Brazil. Closed canopy dry forests in the Northern Bolivian lowlands have canopy heights as low as 20 meters [Toledo *et al.*, 2011b], [Murphy and Lugo, 1986]. The canopy heights of southern open dry forests of the Gran Chaco where site 2 is located can be lower still. This will be conveyed in photographic depictions in the conclusion.

The early successional trees are indeed having a competitive suppression on grasses, most certainly through a moisture stress feedback. The total leaf area cover for the perturbed simulation increases almost undetected over the control simulation. The success of the early species can be likened to their ability to fill the role of the opportunist. The high disturbance rates creates a continuity of landscapes that are open for the competitive process. Early successional trees are successful in these environments because they can grow quickly and have large seed pools.

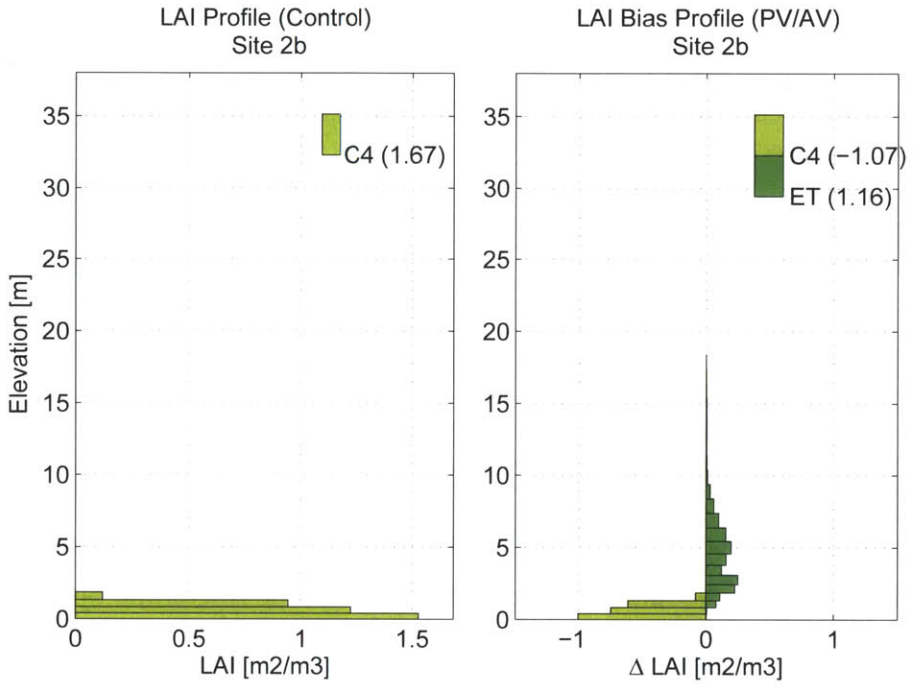


Figure 7-13: Profile of leaf area from control climate and the differential leaf area profile generated by the potential (PV/AV) perturbation climate. Profiles are yearly leaf area means observed on the 125th year of simulation.

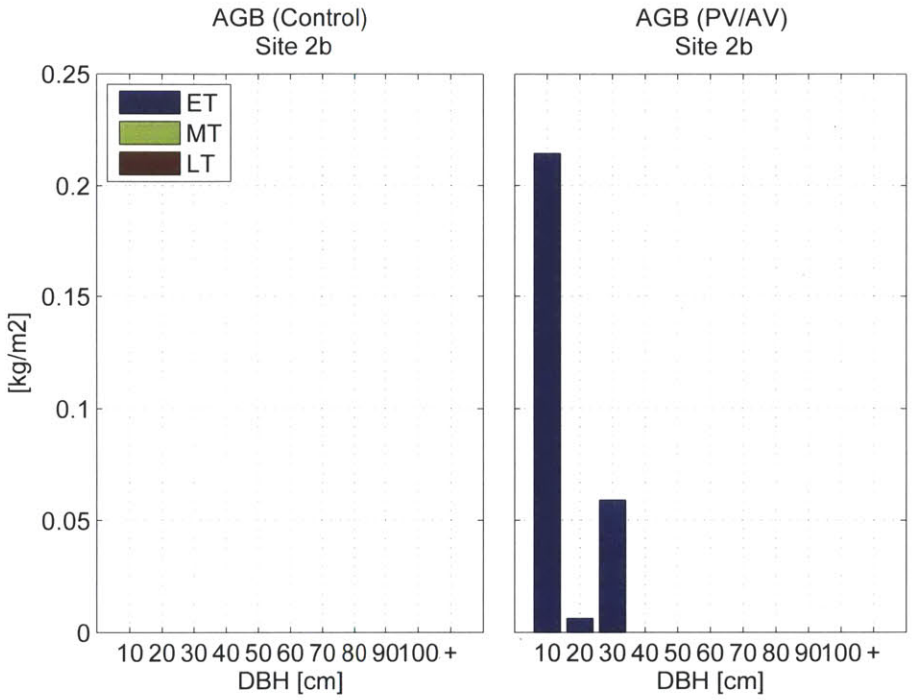


Figure 7-14: Distributions of Above Ground Biomass binned by stem diameter at breast height, generated via original (control) and perturbation (PV/AV) climates. Distributions are observed in the 125 year of simulation.

# Chapter 8

# Conclusions

This thesis used a numerical model of the terrestrial biosphere and atmosphere (EDM2-BRAMS) to investigate how land conversion in the Amazon and the surrounding regions have changed regional hydrology, and to see if those changes are significant enough to produce an ecological response. The following chapter offers some discussion and concluding remarks regarding the major findings of this thesis research.

## 8.1 Regional Patterns in Precipitation Differences

The coupled simulation results have shown that land conversion, as it defines the regional structure of vegetation in 2008, has influenced the patterning of South American precipitation. In select locations such as the dipole pattern over the Amazon delta and the depression in Bolivia, precipitation patterns have had modest but persistent inter-annual biases on the order of 5 to 15%.

### 8.1.1 Observations of Historical Climate

A valid question is whether observations could be found that support the simulation based evidence that regional land-conversion was driving decreases in precipitation at the case study sites. The intention of the observation is to identify a change in precipitation that is coincident with land-use. The best approximation to this, is to compare

precipitation at the same location before and after the lands of the region were converted. The difficulty is that this requires old records of rainfall. Any record implies the existence of humans and thus an impact on the land-surface near the measurement. It is impossible to have a site measurement without disturbance. Moreover, land conversion in South America did not happen instantaneously. Humans have been converting the lands of South America indigenously for millennia, European explorers and settlers have centuries old history. However, the major deforestation efforts in the eastern and southern boundaries of Amazon primary forests occurred roughly in the 1970s. Therefore the year 1970 can roughly distinguish a demarcation point of the era before and after deforestation.

Historical rain gauge measurements in Bolivia were compiled by Tom Cochrane (U. Canterbury NZ) and the World Meteorological Organization (WMO). The WMO collected historical rain gauge data from various original sources including the Servicio Nacional de Meteorologia e Hidrologia (SENAMHI) and the Administracion de Aeropuertos y Servicios Auxiliares a la Navegacion Aerea (AASANI). Several of these stations are in proximity to the case study at site 2. These location are provided in Figure 8-1. The locations of the measurement stations are plotted against the mean difference map in annual precipitation generated by the two scenarios (AV-PV) of coupled simulation. The mean annual rainfall and its standard deviation across these proximal measurement stations is provided in Figure 8-2. At the available sites, continuous records spanned from 1945 to 1987.

In addition to the historical precipitation record provided by the WMO, the Climatic Research Unit (CRU) Mitchell and Jones [2005] is a globally distributed historical climate product with a record dating back to 1901. The CRU dataset is based on an archive of global weather station data. Precipitation in the CRU dataset is mainly derived from the GHCN and Mike Hulme (originally cited as personal communication). Two maps of mean annual precipitation were assembled, a mean from 1940 to 1969 and a mean from 1970-2009. These two periods are intended to represent the era before wide-spread deforestation and the era during wide-spread deforestation. The difference in these means, subtracting the earlier period from the later, is provided in Figure 8-3.

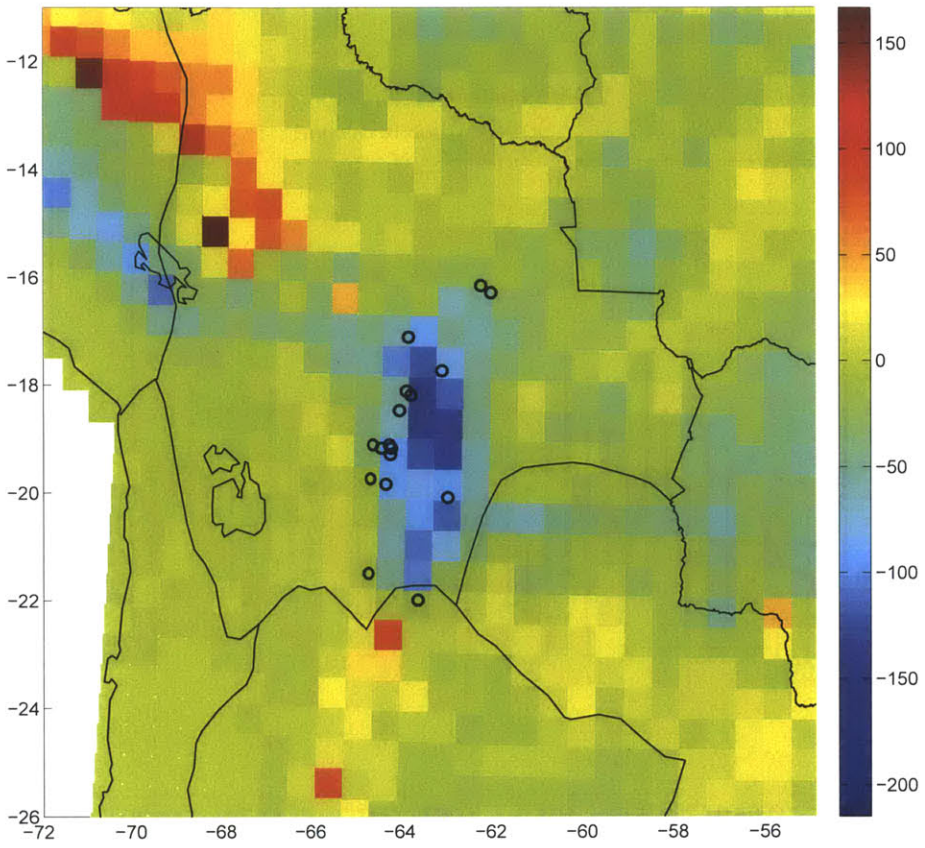


Figure 8-1: Locations of WMO historical precipitation records near the location of the site 2 case study in Bolivia. A map of the differences in mean annual rainfall from the two coupled simulation scenarios is provided for context regarding selection of stations.

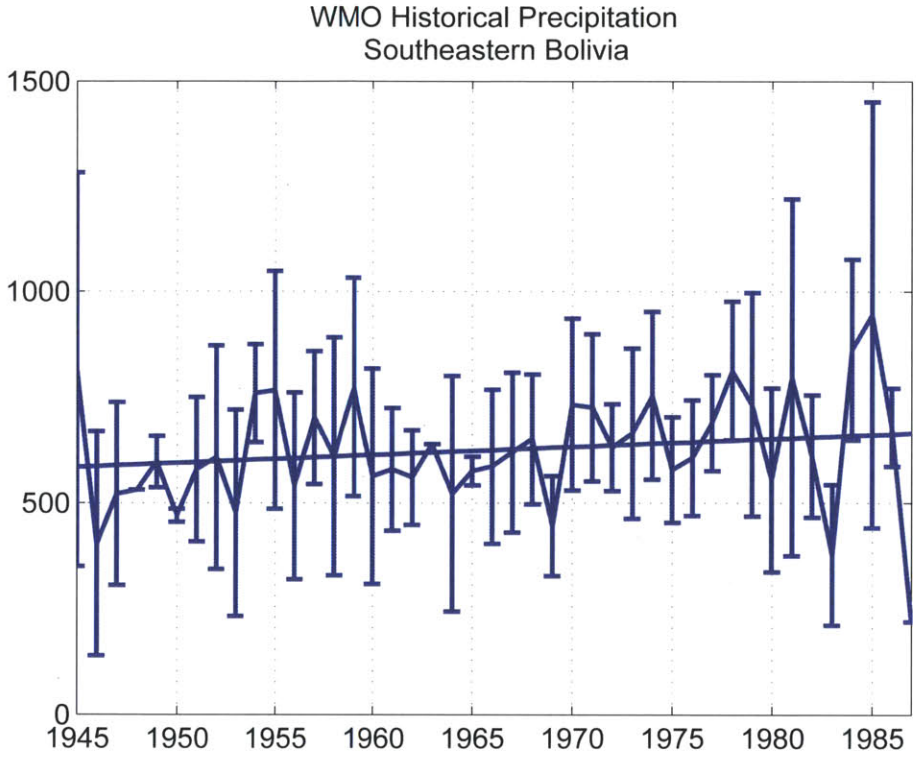


Figure 8-2: Mean annual precipitation at WMO measurement sites, southeastern Bolivia.

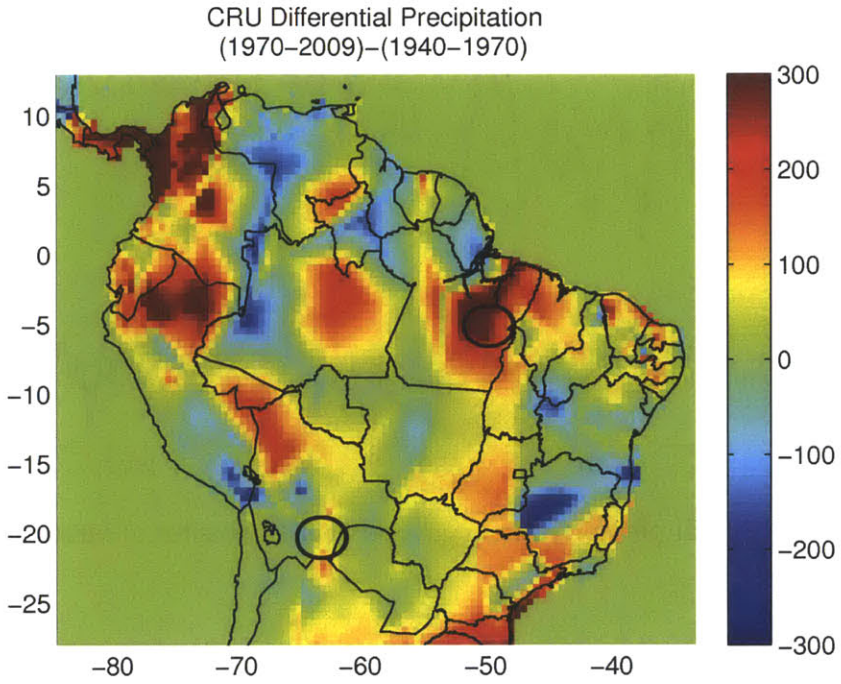


Figure 8-3: Map of the difference in annual precipitation averaged over two eras, 1940-1969 and 1970-2009, CRU 3.1.10. Black circles show the two case study areas discussed in Chapter 6.

A time series of the CRU precipitation at the two case study sites is also provided, see Figure 8-4. The plots also show a third order polynomial fit each of the time-series.

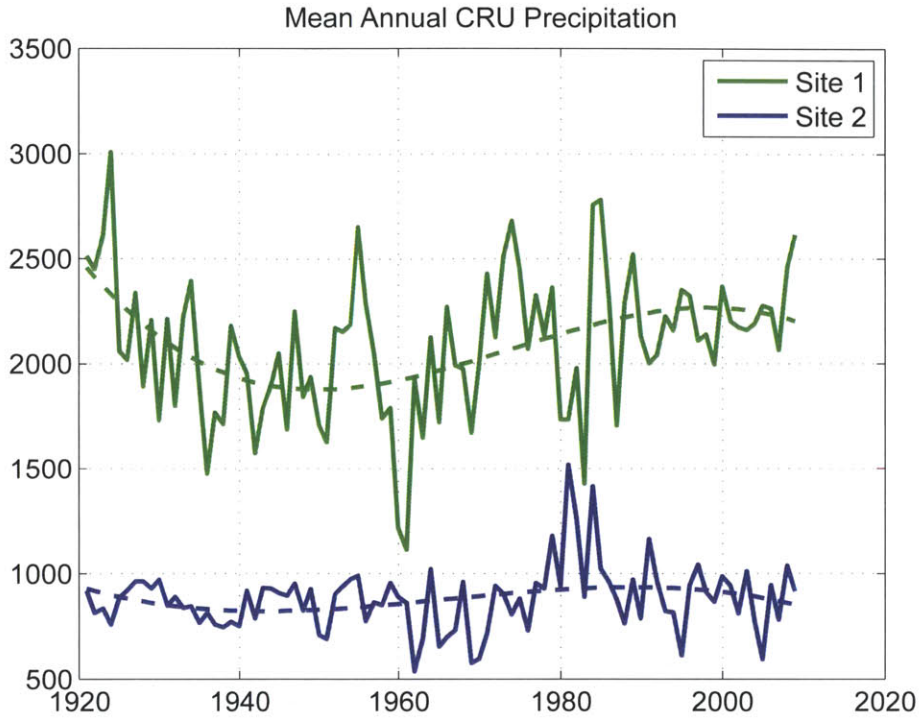


Figure 8-4: Annual precipitation estimated at the two sites of interest. CRU 3.1.10

### 8.1.2 Summary of Findings From The Observational Records

The time series measurements from the WMO and the CRU datasets relfect slight increase in precipitation at the two sites of interest over the last several decades. The increase in precipitation associated with these records is somewhat counter to the results found in the coupled model experiment. However, it can not be understated that the observations and the model experiment are showing two different things. The change in precipitation that is observed in the climate records must factor in many considerations; climate change, local effects at the measurement sites, measurement error, and model error in the case of the CRU data. The CRU dataset uses spatial interpolation procedures to map rainfall to locations without point measurements.

The coupled model experiment was motivated in part because the questions posed in this thesis simply cannot be answered through observation. It is impossible to find a real world precipitation signal that reflects a component attributed to hydrologic ramifications of land-conversion alone. On the other hand, the coupled simulation can isolate the precipitation signal that is a result of differential land-cover alone, because the initial and lateral boundary conditions of the system can be controlled. Likewise, physical processes that are not directly associated with land-conversion and the hydrologic cycle do not influence the results.

It was questioned if these historical records of climate could provide comparative evidence against the coupled simulation results. A slight trend indicates that precipitation has increased at the case study locations over the last several decades (coincident with the era of deforestation). It is also true that the signal is weak compared to the variability, and that there are other compelling factors that explain the increase in precipitation. In summary, the observational record is used to neither deny or substantiate the conclusions of this thesis.

## 8.2 Discussion on Continental Hydrology

The coupled simulation results indicate that land conversion in South America has not had a significant influence on continental mean precipitation. Continental mean precipitation with land conversion decreased in 3 out of the 4 years of simulation, but the differences were less than 5%. On the other hand, distinct patterns of differential precipitation emerged and were consistent from year to year. These patterns therefore reflected a re-distribution of precipitation.

Differences in mean continental moisture convergence, runoff and total evapotranspiration were consistent from year to year. Total evapotranspiration showed consistent decreases associated with the Actual Vegetation condition. The differences were correlated with the change in biomass. This is attributed to two mechanisms. Firstly, land conversion in forested regions decreased leaf area, which decreased the surface area of precipitation interception surfaces. Consequently, a larger fraction of precipitation penetrates the canopy. Consider that all of the leaf intercepted water is destined to evaporate back towards the atmosphere, but water that infiltrates the soil column can exit through runoff and therefore not all of the infiltrating water makes it back to the atmosphere as evaporation. Secondly, conversion of forested lands directly reduces transpiration. The total transpiration of a landscape is strongly influenced by the the stomatal density and leaf area, both of which are reduced with land-conversion and deforestation.

The comparison of coupled simulations confirmed that land-conversion promoted increased land-surface runoff. There are significant ecological impacts to increased runoff. Runoff directly influences bio-geochemical cycling. Runoff drives the mass transport inherent of the leaching of nutrients in soils.

## 8.3 Hydrologic Seasonality in Case Studies

The structure of the vegetation canopy influences the seasonal cycle of moisture distribution as well, this was conveyed in the case studies. Note that the fraction of rainfall

that penetrates a vegetated canopy is a function of both rainfall intensity and volume as well as the area of interception surface. As an example at site 2, transpiration was greater in the potential case during the wet season. But as the early dry season came, transpiration was greater in the actual vegetation condition, see Figure 6-14. By the end of the dry season both scenarios were virtually devoid of evapotranspiration and showed no difference. The soil moisture profiles show that the actual vegetation cases was getting enhanced wetting in the upper root zone during the wet season and early dry season, even through wet season precipitation generally decreased. This is explained by a combination of things. The potential vegetation both intercepted more precipitation bound for the soil column and also drew more soil water during the wet season to accommodate photosynthesis. This combination promoted a dryer soil column in the Potential scenario by the mid dry season (June).

The vegetation in the lowland dry forests of the site 2 potential scenario is described in model terms as a group of early successional tree species with accompanying c4 grasses. It must be realized that the model cohorts at this site are also used to describe tropical species in rainforests ecosystems as well, as the model parameters of these plants cannot be calibrated for every ecosystem.

The early successional competition strategy is fitting in dry forests to some extent, mostly in their ability to make opportunity out of a disturbance event. The southern Bolivian dry forests are indeed influenced by fire, and fitting for opportunists. But model vegetation parameters that are more closely associated with tropical vegetation may be adapted to shorter and less severe dry seasons. They may not regulate stomata in the late wet season or early dry season, because the climate guarantees water will be available again soon. A plant that is guaranteed to have a wet soil column in the future is not going to try to conserve moisture at the moment, it would be more advantageous for these plants to keep their stomata open in order to assimilate more carbon, be productive and more competitive for the limited available light. However, in the dry forest regions near site 2, plants are likely to have a different usage strategy for available root zone soil moisture. There are two arguments. One argument suggests that dry forest ecosystems regulate their stomata in the wet season when soil moisture is available, in

order to ensure soil moisture above wilting point is preserved through the dry season. On the other hand, the dry season in this region is long and according to the simulations, highly variable. Likewise, if a plant does not use moisture in the wet season to be productive, another plant will.

This is an important argument, because it hinges on the hydrometeorological dynamic of the local region. Total evapotranspiration during the transition from the late wet season to early dry season (April) at site 2 was significantly larger in the potential vegetation scenario. The difference was strong enough that the increased moist static energy released by the land-surface stimulated enhanced deep convection (although it is thought that increased moisture flux from the tropical forests in the north was also a contributing factor). At this time, the differential transpiration rates of the two scenarios was a significant component of the difference. Therefore, the resource usage strategy of the deep rooted vegetation place an impact in the coupled dynamic of the system.

At site 1, there was significant differential transpiration in the dry season as well. But in this case, transpiration showed a more persistent negative bias associated with land conversion and deforestation. This region received well over a meter of rainfall each year, which allowed a full saturation of the soil column during the wet season. This allows the deep rooted vegetation to access available water over the entire dry season at site 2. As a result, significantly more moist static energy was released by the forest canopies of the potential scenario during the entire dry season, and it was during this period that differential precipitation was the most pronounced, particularly in August through October.

## 8.4 Mechanisms of Differential Precipitation

The precipitation was primarily convective in areas where there was a strong differential rainfall signal between the two simulation scenarios (namely sites 1 and 2). The negative precipitation bias associated with land-conversion is attributed to weaker convective events. Weak convection is typified by buoyant updrafts that lack the moist static

energy to ascend several thousand meters. In deep convective events there is greater release of convective available potential energy and condensation of water vapor leading to increased rainfall. The decreases in moist static energy at Actual Vegetation case study sites were associated with a decrease in latent and total surface energy flux, brought on by decreases land surface albedo, leaf water interception and the ability to draw water from the lower soil column during dry season transpiration. The greatest differences in precipitation were observed during the dry season in regions experiencing divergence. Differences in the advection of precipitable water were evident when comparing the two scenarios, particularly regarding the case study in the bolivian lowlands. Nonetheless, convective precipitation biases appear to be strongly linked with localized differences in land-surface energy fluxes.

## 8.5 Ecosystem Response

There is evidence that climate perturbations associated with regional land conversion can influence the dynamics of the tropical forest canopies of eastern Para(site 1). The susceptability of the vegetation to respond to climate perturbations on this order is dependant on the the moisture stress regime. The strongest differential signals were related to growth rates as plant communities tended towards equilibrium. The influence on vegetation through this perturbation mechanism is limited though. In summary, the simulation results indicated that equilibrium levels of above ground biomass were not significantly different.

The vegetation response to perturbations in climate at the Bolivian lowlands is a more complex story. From an ecological perspective the Bolivian lowlands are an incredibly diverse region, considering floristic composition within its various ecosystems and the heterogeneity of ecosystem types. It has been described as the confluence of the three major biogeographical regions of South America, the Amazonian, Brazilian Paranense and Chaco [Toledo *et al.*, 2011a]. The region has been classified as having 7 distinctly different forest types, 5 Amazonian forests towards the north and two dry forests in the South, the Chiquitano which is central and eastern Bolivia and the Gran

Chaco in the south. The site at case study 2 $(-19.5N, -63.5E)$, is located on the western edge of the Gran Chaco dry forest, on its border with the Chaco Serrano. Photographs of the Chaco (upper panels) and Chaco Serrano (lower panels) are provided in Figure **??** (reprint permission from the Laboratorio de Plantas Vasculares, Departmento de Biologia y Farmacia, Universidad Nacional del Sur Argentina, *pending*).


Figure 8-5: Examples of vegetation in the Chaco (upper panels) and Chaco Serrano (lower panels) dry forests. (reprint permission pending, Laboratorio de Plantas Vasculares, Departmento de Biologia y Farmacia, Universidad Nacional del Sur Argentina).

The vicinity of case study at site 2 is characterized by strong gradients in mean annual rainfall. Figure 8-6 (courtesy [Cochrane, 2012]) shows the spatial variability of annual precipitation in the region throughout the 1990s. The site is located on a strong North-South gradient in annual precipitation. The northern Bolivian lowlands approach nearly 2 meters of rainfall where they meet the foothills of the Andean Altiplano. Precipitation in the Bolivian Chaco ranges from 600-800 millimeters of rainfall per year.

The precipitation for the control simulation accumulated 100 meters over the course of 125 years, approximately 800 millimeters per year. The perturbation climates pushed

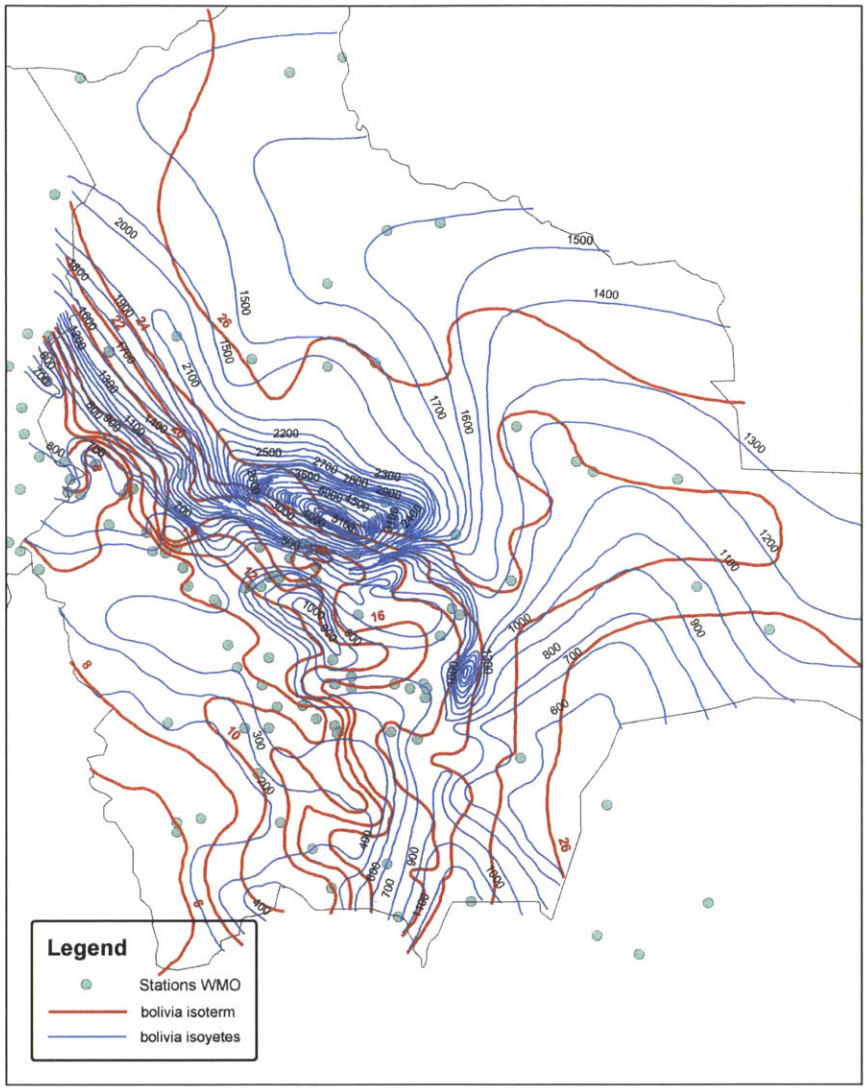


Figure 8-6: Isohyets taken from precipitation gauging stations compiled by the World Meteorological Organization. Figure is credited to T. Cochrane [Cochrane, 2012].

rainfall up to roughly 1 meter per year. The climate driving the simulations are very reasonable compared to the climate observed in the WMO record during the late 90's. Moreover, the estimation of a open canopy dry forest type forest structure is consistent

with the what exists in the Chaco/Chaco Serrano. This indicates that the climate and vegetation dynamic simulated in this area of Bolivia are plausible.

While studies on vegetation response and climactic variability are limited in the Chaco, Toledo and co-authors [Toledo *et al.*, 2011b] compared variability in Chiquitano forest structure and composition to variability in soil and climate. Principal Component Analysis of rainfall variability described 65% of the variability in structure and composition. The second most correlated variable, soil fertility explained 48% of the variability in forest structure and composition. In this vein, it is thought that climate change in this region, particularly mediated through change in precipitation would lead to "large changes in floristic composition in Bolivia" [Toledo *et al.*, 2011a]. There is evidence that the vegetation structure in the Gran Chaco dry forests are indeed sensitive to changes in seasonal precipitation. The differences in equlibrium vegetation structure that were simulated according to the different climate perturbations are consistent with a region that 1) has strong spatial gradients in rainfall, 2) strong seasonality and inter-annual variability and 3) heterogeneity of observed vegetation structure in the region.

The case study simulations of ecosystem response were based on possible alternative climates that would had existed if land-conversion never occurred. These perturbations carry a degree of uncertainty. The intention is to create perturbations that would had been plausible, though not necessarily definite. The results from these case study simulations were effective in demonstrating that precipitation biases generated by the differential land-cover can indeed have significant influences on ecosystem structure and composition, particularly in areas where there is ecotone transition. This was especially true of the mixed grasslands and dry forests in Bolivia.

## 8.6 Future Research

The continued development of biophysics and improvements to the numerical efficiency in the Ecosystem Demography Model 2 have positioned it to be used effectively in modeling terrestrial ecosystem dynamics over a broader range of space-time scales. This ecosystem tool could support global scale simulations as bound to general circulation

models of the atmosphere, as it would provide powerful predictive capabilities of ecosystems facing climate change. Such endeavors could benefit from new classes of cohorts that target dry tropical forests such as the Chaco or Chiquitano. Dry forests are well represented in the region but do not have cohort parameterizations specifically tuned for them. This sentiment is true for terrestrial biomes across the globe. A comprehensive database of plant functional parameters that specifically address the needs of dynamic biosphere models would be very beneficial for the entire modeling community.

The strength of the experimental design was undoubtedly the sophistication of the vegetation and land-surface scheme, as well as the ability to represent meso-scale atmospheric dynamics and convection. Future research could test regional hydrologic response with different boundary conditions, and/or include different approaches to modeling various processes such as methods of calculating mass flux and initiation of convective precipitation events.

# Appendix A

# Convective Parameterization - Grell Method

A convective parameterization is a numerical technique that approximates the convective cloud processes occuring at resolutions finer than that resolved by the equations of fluid motion on the model grid. Cumulus convective parameterization has been approached in various ways since the early 1970's. Examples are the seminal works by Kuo [Kuo, 1974], Arakawa and Schubert [Arakawa and Schubert, 1974], Houze et al. [Houze *et al.*, 1980], Kain and Fritsch [Kain and Fritsch, 1990], Fritsch and Chappel [Fritsch and Chappel, 1980], Emanuel [Emanuel, 1994] and Betts and Miller [Betts and Miller, 1986]. This thesis research uses the Grell method. This approach follows Arakawa-Shubert's idea of *Quasi-Equilibrium*, which holds that the atmosphere is in a constant cycle of radiatively driven destabilization and convectively driven restabilization. Emanuel describes it as statistical equilibrium, suggesting that the timescales of restabilization are small compared to the timescales of destabilization. This is clearly observed in nature: solar heating is a continuous process occurring over the period of daylight. In contrast, convective clouds can go through the processes of initiation, ascension and completion of its rain cycle over a period of tens of minutes.

The theory behind Grell's modified Arakawa-Schubert convection scheme is detailed in the NCAR Technical Notes TN-398+STR [Grell *et al.*, 1995]. A brief review of its strategy is discussed here for perspective, which hopefully will help shed some light on

how the land-surface processes may exert some mechanistic control over precipitation. For a more comprehensive treatment of the Grell implementation of Arakawa-Shubert convective parameterization, the reader is referred to Grell's Technical Notes.

The basic formulation behind Grell's scheme's (1993-current) and the modified Arakawa-Schubert (AS) variants are partitioned into three conceptual groups: static control, feedback to the environment, and dynamic control.

### A.0.1 Static Control

Static control suggests that convective clouds can be represented by columns of air, updrafts and downdrafts. The intensity of the drafts is determined by the mass flux $\dot{m}$ of moist air inside the column. Each of these columns has the possibility of entraining and detraining air from/to the environment outside. The rate at which the updrafts and downdrafts can entrain or detrain is controlled by the cloud radius (which governs the area of the flux boundary between cloud and environment). Fractional entrainment $\mu$ (which is per-unit mass of cloud air), is defined as the spatial derivative of mass flux, normalized by the mean rate of mass flux over that element; this is the *entrainment hypothesis*.

$$\mu = \frac{1}{\dot{m}_{(z)}} \frac{\partial \dot{m}_{(z)}}{\partial z} \approx f(radius) \tag{A.1}$$

It can be visualized as a cubic control volume at elevation $z$ in the buoyant column where mass is passing in the vertical direction at variable rates through the top and bottom of the cube. Some methods will assume constant area, some will grow or decay as a function of entrainment or detrainment from the top or sides. When the cubic control volumes are connected in a column, a system of equations form a functional relationship between the mass flux at the top and bottom of the column.

Cumulus parameterization creates a steady-state relationship between the column of moist air and the environment. The vertical positioning of the columns, their entrainment rates, and the mass flux guide an exchange of heat and moisture with the environment and the conversion of condensed cloud water into precipitation. It is the

entrainment driven exchange, also called feedback, which restabilizes the atmosphere.

The thermodynamic states inside the cloud drafts are defined by dry static energy, $H_{dry}$, total water mixing ratio (vapor and condensed water), $r_v + r_l$, and moist static energy, $H_{moist}$. Moist static energy is an analogue of virtual potential temperature and is defined as a function of geopotential (gravity $g$ and elevation $z$), the kinetic energy of the dry air (heat capacity of dry air $C_p$ and air temperature $T_a$) and the latent energy in the water vapor (latent heat of vaporization $L_{vap}$ and water vapor mixing ratio $r_v$):

$$H_{moist(z)} = gz + C_p T_{a(z)} + L_{vap} r_{v(z)} \tag{A.2}$$

The moist static energy of parcels ascending the column are assumed to be conserved under adiabatic displacements. Therefore, the change in moist static energy inside the column is only influenced by mixing with the outside air. Applying conservation of energy, the profile of moist static energy (normalized by mass) can be estimated as a function of fractional net entrainment. The moist static energy of the cloud updraft is denoted by subscript $up$. The moist static energy in the environment uses no subscript.

$$\frac{\partial h_{moist,up(z)}}{\partial z} = \mu_{up}(H_{moist(z)} - H_{moist,up(z)}) \tag{A.3}$$

When moist static energy is conserved inside an asecending parcel, the temperature will decrease as geopotential increases. At some point, temperature will drop below the dew point, and vapor will begin to condense and release heat. The column of air may become bouyant with respect to the outside air due to the added heat of condensation. There are two key points to consider in this process. First, entrainment of the outside air dilutes the difference between moist static energy of the updraft and the environment. Second, the updraft will not exist unless a parcel of air with high moist static energy can be adiabatically lifted to a location where it becomes bouyant.

Observing conservation of mass, the cloud entrainment governs the static profiles of water vapor and liquid water.

$$\frac{\partial (r_{v,up} + r_l)}{\partial z} = \mu_{up}(r_{v(z)} - r_{v,up(z)} - r_{l,up(z)}) + S_{l,up} \tag{A.4}$$

The sink term $S_{l,up}$ is the condensed cloud water that is sedimented into rainfall. Since there is no condensed water outside the plume, entrainment depletes condensed water and hence only the negative $r_l$ term. Similar processes govern the net fractional entrainment in the downdraft (secondary subscripts $dn$), with the exception that liquid water can be evaporated back into the air column as the source $S_{l,dn}$ from the falling precipitation.

$$\frac{\partial(r_{v,dn})}{\partial z} = -\mu_{dn}(r_{v(z)} - r_{v,dn(z)}) + S_{l,dn} \tag{A.5}$$

The total amount of precipitated water depends on total cloud mass, and the total mass and energy exchanged with the environment is dependent on cloud mass flux. The updraft and downdraft mass fluxes can be normalized by the mass flux at the base of the cloud. Where $\dot{m}_b$ and $\dot{m}_0$ are the mass fluxes at the bottom of the updraft and top of the downdraft respectively, and $\eta$ is the normalized mass flux profile:

$$\dot{m}_{up,(z)} = \dot{m}_b * \eta_{up(z)} \tag{A.6}$$

$$\dot{m}_{dn,(z)} = \dot{m}_0 * \eta_{dn(z)} \tag{A.7}$$

An important aspect of the AS column models is that the mass fluxes of the updrafts and downdrafts are functionally dependent, which reduces the number of unkown variables. Total sedimented condensate, $Q_{sc,up}$, is removed from the updraft as a sink term; the result is placed in the downdraft and partitioned into rainfall (that which reaches the surface and that which is re-evaporated, $E_{c,dn}$). The two are related by re-evaporation efficiency $\beta$.

$$E_{c,dn} = \beta \cdot Q_{sc,up} \tag{A.8}$$

The total sedimented condensate and evaporation can both be related to their mass flux profiles and the source/sink term.

$$Q_{sc,up} = \dot{m}_b \left( \int_{z_B}^{z_T} \eta_{up(z)} S_{l,up} dz \right) \equiv I_1 \dot{m}_b \tag{A.9}$$

$$E_{c,dn} = \dot{m}_0 \left( \int_0^{z_0} \eta_{dn(z)} S_{l,dn} dz \right) \equiv I_2 \dot{m}_0 \tag{A.10}$$

This connects the mass fluxes via the re-evaporation efficiency, where $I_1$ and $I_2$ are simply mass normalized rates of sedimentation and evaporation.

$$\dot{m}_0 = \frac{\beta I_1 m_b}{I_2} \tag{A.11}$$

The profiles of in-cloud moist static energy, as well as the total amount of mass and energy that fluxes from cloud to environment over the profile, is dependent on the choice of boundary conditions and the estimated mass through the base of the cloud. The calculation of feedback to the environment is very straight-forward: it is simply the total net entrainment of each layer times gradients in water vapor mixing ratio and moist static energy.

### A.0.2 Dynamic Control

The mass flux is estimated through the "dynamic control" process. Generally speaking, the end goal is to restabilize the atmosphere. One method of estimating instability, or potential for convection, is to evaluate the total bouyant energy of the column. One representation, the work function $A$, a column integration of the difference in moist static energy of cloud and environment. Here, $\gamma_{sat}$ is the slope of the saturation curve at a given temperature and pressure, and $H^*_{moist,env}$ refers to the moist static energy given the environment's (outside the cloud) air temperature and the condition of saturation.

$$A_{up} = \int_{z_B}^{z_T} \frac{g}{C_p T_{a(z)}} \frac{\eta_{up,(z)}}{1+\gamma_{sat}} (H_{moist,up(z)} - H^*_{moist,env(z)}) dz \tag{A.12}$$

Convection will seek to reduce the buoyant energy until the atmosphere is restabilized and the energy is used up. The available buoyant energy is calculated over a time and mass perturbation, and the rate of change is calculated to solve a system of equations. Explaining this system of equations in detail is outside the scope of this review.

### A.0.3 Boundary Assumptions

What is left is to make some assumptions on the boundary conditions, particularly the vertical placement of the up and downdraft end-points. Grell [1995] assumes that the moist static energy at the bottom of the downdraft is the maximum of that found in the environment at or below the updraft origin. The moist static energy at the top of the updraft is the equal to that found in the environment at saturated conditions. The moist static energy of the top of the downdraft is the minimum of that found in the environment over the same depth of the column.

Perhaps the trickiest parameter to find is the height of the base of the updraft, also known as level of updraft $z_{LOU}$. The location of the updraft is rather ambiguous, yet its placement can influence whether or not convection will happen. One could argue that the updraft starts at the elevation where eddies become large and energetic enough to lift a parcel to a potentially higher elevation where it will become positively bouyant, the level of free convection $z_{LFC}$. The choice of the location of the updraft dictates the moist static energy and water content of the parcel that is lifted through the column.

The choice of updraft base therefore influences the elevation at which the column may or may not become positively bouyant. In practice, the level of updraft base $z_{LOU}$ was defined as the layer in the atmospheric boundary layer with the maximum combination of vertical mean wind-speed and variance.

$$z_{LOU} = z \mid \text{MAX}(\overline{U}_z + \hat{U}_z) \tag{A.13}$$

The level of free convection $z_{LFC}$ can be found by adiabatically lifting and conserving the moist static energy (through moist phase changes) in the layer where the updraft is chosen. The bouyancy (density) of this parcel is compared to the environment. The level where the adiabatically lifted air first becomes less dense than the environment is the level of free convection.

If the level of free convection is not immediately above or at the level of updraft, convection may not happen unless turbulent conditions could mechanically lift the parcel from the updraft level to the level of free convection (where bouyancy takes over

and allows the parcel to ascend). This is sometime refered to as a "trigger" mechanism, and there are several ways to parameterize this. One method is to apply a force balance on the conceptual parcel as it leaves the updraft location. The parcel starts at the level of updraft $z_{LOU}$ with an assumed parcel velocity, explained next. The parcel is decelerated by the forces negative bouyancy and fluid drag, bringing it to a final resting level. If the final resting place is at or above the level of free convection, then the trigger has been satisfied and the process of calculating mass flux is allowed to happen.

Of course, the atmospheric model is not resolving boundary layer eddy motions, so an estimate of the vertical velocity of the parcel must be arrived at statistically. The user has some control over this. Operationaly, the parcel velocity has typically been defined as the $75 - 95$ percentile of the model grid's normally distributed vertical wind-speeds. This method relies heavily on the assumption of normaly distributed vertical wind-speeds and good estimates of the velocity variance and parcel force balance. A more simple approach is to define a constant that describes an acceptable level of separation between the two levels to warrant convection. The choice between these two trigger options is discussed in Çhapter 5.

Convective precipitation is undoubtedly a crucial pathway linking land-cover change with the feeding back of hydrologic energy. Understanding how it is parameterized in the model environment is necessary for understanding how this pathway changes or mitigates change in the land-atmosphere model system, a key question of this thesis research. It is clear that convective precipitation, as applied through Grell's scheme, is dependent on the tropospheric profiles of moist static energy and the turbulent transport of momentum, heat and water below the cloud layer. The ED2 land-surface model can mechanistically exert control over these variables. Some examples are through changes in albedo, roughness and bowen ratio.

# Appendix B

# EDM2.1: Vegetation System Mass and Energy Balance

From a thermodynamic perspective, the vegetation system refers to the collection of leaf tissue, leaf internal water, stem tissue, stem internal water and surface water. It is assumed that leaf tissue and leaf surface water are in constant thermal equilibrium, i.e., they always have the same temperature and combine for a total heat capacity and internal energy. The user has the option of including stems and stem water, and additionally whether to integrate their internal energy separately or to pool their internal energy and heat capacity with leaf and leaf water. For simplicity, this chapter will not consider stems. A simple diagram of the leaf and leaf-water control volume is provided in Figure B-1.

There are three modes through which vegetation surface water mass $m_v$ can flux through the vegetation system: 1) interception of precipitation, 2) vapor flux across the leaf surface and 3) leaf water overflow resulting in stem and drip flow. Vapor flux $\dot{m}_{vc}$ from the leaf surface to canopy air can occur as condensation, evaporation or sublimation. Intercepted precipitation, $\dot{m}_{int}$, like condensation, can also deposit water on the leaf surface. Leaf drip and stem flow, $\dot{m}_{ds}$, can only occur as overflowing precipitation. EDM2 assumes that once leaves are holding surface water at carrying capacity, precipitation will simply pass by the leaf. In the absence of precipitation events, surface water's only egress is via evaporation.

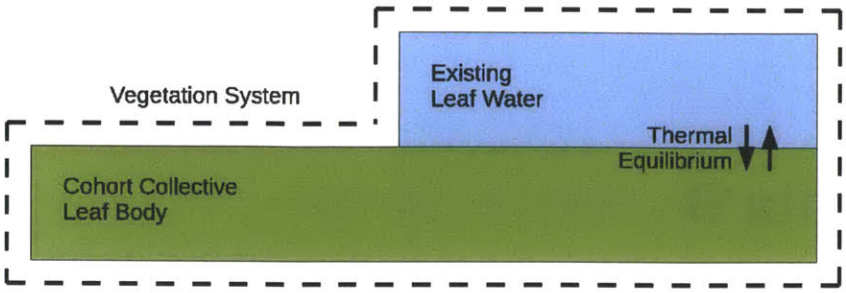


Figure B-1: Schematic of the vegetation system control volume, comprised of the leaf tissue and a dynamic surface water mass layer. Each cohort has a collective body of leaves with surface water. It is assumed that the leaf tissue and water are in constant thermal equilibrium. All energy fluxes through the control surface interact with the vegetation system as a single entity. Notice that the water surface does not cover the entire leaf, reflecting limited surface water holding capacity.

$$\frac{\partial m_v}{\partial t} = -\dot{m}_{vc} + \dot{m}_{int} - \dot{m}_{ds} \tag{B.1}$$

## B.1 Potential Leaf Vapor Flux

Condensation may only contribute to leaf surface water if it is below holding capacity. The maximum water mass per unit area $\gamma_l$ that a leaf can hold is plant functional trait. Evaporation may occur so long as leaf surface water exists. The rate of evaporation is controlled directly by the fractional area of water on the leaf surfaces $\sigma_w$ $[m^2/m^2]$ and an exponential function of the leaf water holding fraction.

$$\sigma_w = \min\left(1.0, \left(\frac{m_v}{\gamma_l \mathrm{LAI}}\right)^{0.6667}\right) \tag{B.2}$$

Leaf evaporation and condensation are both driven by the humidity gradient between the canopy air space and the leaf surface. If the vapor gradient, $\Delta_q$, is away from the leaf surface, the potential vegetation to canopy water vapor flux $\langle \dot{m}_{vc} \rangle$ will be positive and described by evaporation. Vapor gradient toward the leaf surface will yield

a negative term and condensation.

$$\Delta_q = \rho[q_{v,sat} - q_{can}] \tag{B.3}$$

The specific humidity of the canopy, $q_{can}$, is taken directly from its prognostic variable. The specific humidity at the leaf water surface, $q_{v,sat}$, is assumed saturated. The vapor pressure $p_{v,sat}$ is calculated via the Clausius-Clapeyron relationship following the fitting estimates of [Murphy and Koop, 2005]. Canopy air pressure $p_c$ is diagnostic and assumed to have insignificant deviation from the lowest layer of the atmospheric model.

$$q_{v,sat} = \epsilon_{av} \frac{p_{v,sat}}{p_c - p_{v,sat}} \tag{B.4}$$

The potential vegetation to canopy water vapor flux $\langle \dot{m}_{vc} \rangle$ is then calculated through a resistance formulation.

$$\langle \dot{m}_{vc} \rangle = \begin{cases} \text{Evaporation} \quad \Delta_q \text{LAI} \sigma_w / r_{av} & \text{if } \Delta_q > 0, \\ \text{Condensation} \quad \Delta_q \text{LAI} / r_{av} & \text{if } \Delta_q < 0. \end{cases} \tag{B.5}$$

The resistance $r_{av}$ of water vapor transport from the leaf surface boundary layer into the well-mixed canopy air space is estimated per the methods of Leuning and co-authors [Leuning *et al.*, 1995] adapted from formulations by Monteith. Some extra discussion of this term is provided in Appendix G.

## B.2 Interception and Throughfall

The leaf area index $(LAI)$ of a cohort is defined by the number density of its plants $np$ $[plants/m2]$, the amount of leaf carbon contained in each plant $b_l$ $[kgC/plant]$, the specific leaf area of the plant SLA $[m^2/kgC]$. Specific leaf area is a species specific parameter. Assume a patch with $N$ cohorts indexed by $i$.

$$\text{LAI}_{(i)} = \text{SLA} \cdot b_{l,(i)} \cdot np_{(i)} \tag{B.6}$$

The interception of precipitation is a slightly non-intuitive process in the ED2 model. First assume that the leaf surfaces are distributed uniformly over the entire patch's surface area at discrete vertical bands within the canopy. In reality, tree canopies exhibit clumping due to the non-uniformities of spacing in both stems and trunks. But recall that ED2's *Patches* conceptually encompass a tree gap. The horizontal homogeneity assumption does not conflict with breakages in a continuous canopy, as those would be represented by their own patches.

Despite the default assumption of uniformity some patches may represent open canopies. We use a conceptual model to approximate the areal fraction of land covered by clumped crowns cf and the fraction that is open. Precipitation can be divided by this fraction as the amount that hits canopy, and the remainder which is available to grass and soil following [Dietze and Clark, 2008]. Precipitation is split first into a fraction which bypasses the canopy completely according to cf. The fraction that hits the canopy is distributed among the leaves of each cohort based solely on their fraction of the patches Total Area Index TAI. Total area index merely considers the total plant surface per unit ground area, including leaf and stem tissues. The *potential* precipitation interception that each cohort can receive in each time-step is $\dot{m}_{pot(i)}$:

$$\dot{m}_{pot(i)} = \dot{m}_{pcp} \cdot \mathrm{cf} \cdot \frac{TAI_{(i)}}{\sum_{i=1}^{N} TAI_{(i)}} \tag{B.7}$$

The potential leaf precipitation either drips off or fills the leaf surface with water. If the leaf surfaces of the destination cohort have not completely filled with water, then the leaf intercepted precipitation $\dot{m}_{int(i)}$ will be equal to the potential precipitation interception on that target cohort $\dot{m}_{pot(i)}$. The leaf will accept all of the precipitation that is destined for it during that time step. Otherwise, the precipitation bypasses the water-filled leaf surface and is immediately directed towards the ground as drip and stem-flow $\dot{m}_{ds(i)}$.

Given that there are two leaf water states (overflow wet leaves and leaves with at least some dry space) and there are two leaf water flux conditions (evaporation and condensation), there are four possible groups that logically control the fluxes in and out of

the leaf. These four groups are covered in Table B.1. If the potential leaf water fraction exceeds maximum allowable, potential intercepted water and/or condensation will be shed into throughfall $\dot{m}_{ds}$. Shed water then contributes to ground surface interception. Table 1 shows the actual flux values given the combinations of threshold exceedance from potential fluxes and the existence of either evaporation or condensation.

| | $m_v > \gamma$LAI (overflown wet leaves) | $m_v < \gamma$LAI (partially dry leaves) |
|---|---|---|
| Evap. $\Delta_q > 0$ | $\dot{m}_{vc} = \langle \dot{m}_{vc} \rangle, \dot{m}_{int} = 0, \dot{m}_{ds} = \dot{m}_{pot}$ | $\dot{m}_{vc} = \langle \dot{m}_{vc} \rangle, \dot{m}_{int} = \dot{m}_{pot}, \dot{m}_{ds} = 0$ |
| Cond. $\Delta_q < 0$ | $\dot{m}_{vc} = 0, \dot{m}_{int} = 0, \dot{m}_{ds} = \dot{m}_{pot} + \langle \dot{m}_{vc} \rangle$ | $\dot{m}_{vc} = \langle \dot{m}_{vc} \rangle, \dot{m}_{int} = \dot{m}_{pot}, \dot{m}_{ds} = 0$ |

Table B.1: Logical controls of leaf water mass accumulation.

The flux terms that appear in the mass derivative of vegetation surface water, Equation B.1, are now defined.

## B.3 A Mass Based Approach to Leaf Heat Capacity

The heat capacity of the vegetation is the connection between the vegetation internal energy and its temperature. Temperature feeds back on internal energy by controlling the gradients of heat and vapor flux as well as emitted thermal radiation.

| | | |
|---|---|---|
| $C_{vb}$ | $[J/K]$ | Total heat capacity of the vegetation biomass (tissue and internal water) |
| $c_i$ | $[J/kg/K]$ | Specific heat capacity of frozen water |
| $c_l$ | $[J/kg/K]$ | Specific heat capacity of liquid water |
| $L_{F(T_3)}$ | $[J/kg]$ | Latent heat of fusion for water at the freezing point ( 6mb) |
| $H_{melt}$ | $[J]$ | Internal energy of leaves when surface water first melts |
| $H_{freeze}$ | $[J]$ | Internal energy of leaves when surface water first freezes |
| $T_3 = 273.15$ | $[K]$ | Freezing temperature of water at the triple point ( 6mb) |
| $c_{dgl} = 3281$ | $[J/kg/K]$ | Specific heat capacity of leaf tissue |
| $C2B = 2.0$ | $[kg/kg]$ | Ratio of total leaf biomass per unit leaf carbon |
| $B2W = 1.7$ | $[kg/kg]$ | Ratio of interstitial leaf water per unit biomass |

Table B.2: Variables associated with leaf thermodynamic calculations.

### B.3.1 Heat Capacity of the Vegetation Tissue

The internal energy of the vegetation system, $H_v$, can be calculated directly from vegetation temperature, $T_v$, liquid fraction of surface water, $f_l$, vegetation surface water mass, $m_v$, and the heat capacity of the vegetation biomass, $C_{vb}$. This system of accounting uses an absolute datum where zero Kelvin is zero energy. The freezing temperature $T_3$ and the latent heat of fusion $L_{F(T_3)}$ are assumed to occur at the triple point (roughly 6 millibars). Freezing temperature varies insignificantly between 1 atmosphere and 6 millibars. The specific heat capacity of liquid water $c_l$ and ice water $c_i$ vary insignificantly with temperature, and reference values at the triple point are used there as well. Equation B.8 provides ED2.1's multi-phase definition of total vegetation internal energy. This is equivalent to vegetation enthalpy, which is conserved in the canopy air space and land-surface model as a whole.

$$\begin{aligned} H_v = \quad & f_l \left( (m_v c_i) T_3 + m_v L_{F(T_3)} + (T_v - T_3)(m_v c_l) \right) + \\ & (1 - f_l) \left( (m_v c_i) T_v \right) + \\ & T_v C_{vb} \end{aligned} \tag{B.8}$$

Conversely, if leaf temperature and liquid water fraction are to be diagnosed from leaf internal energy, two critical energy points must be identified: the total energy when the leaf water *starts* to melt, $H_{melt}$, when being warmed as ice, and the total energy when the leaf water *starts* to freeze, $H_{freeze}$, when being cooled as a liquid:

$$H_{melt} = \left( C_{vb} + m_v c_i \right) T_3 \tag{B.9}$$

$$H_{freeze} = H_{melt} + m_v L_{F(T_3)} \tag{B.10}$$

When using explicit forward stepping integration techniques, the vegetation internal energy is updated based on the forward stepping of the time derivative, at which point it is compared to these two critical energy levels. If the internal energy is greater than

the energy of first freeze, the liquid fraction $f_l$ is 1. If the internal energy is less than the energy of first melt then the liquid fraction is 0. In Hybrid stepping, the leaf temperature is the prognostic variable (see Appendix H).

$$T_v = \begin{cases} \text{(Frozen)} \quad H_v / \left(c_i m_v + C_{vb}\right) & \text{if } H_v < H_{melt}, \\ \text{(Mixed Phase)} \quad T_3 & \text{if } H_{freeze} > H_v > H_{melt}, \\ \text{(Liquid)} \quad \frac{H_v - m_v c_i T_3 + m_v c_l T_3 - m_v L_{F(T_3)}}{C_{vb} + m_v c_l} & \text{if } H_v > H_l \end{cases} \tag{B.11}$$

If the internal energy is between the melt and the freeze energies, the liquid fraction is linearly related to the internal energy level between the two.

$$f_l = \left(H_v - H_{melt}\right) / \left(H_{freeze} - H_{melt}\right) \tag{B.12}$$

The current formulation bases the extensive heat capacity of plant tissue directly on carbon and water content. Leaf biomass is a constant scale of carbon, using a biomass multiplier $C2B$ (which is typically around 2). It uses literature derived estimates of specific heat capacity of dry green leaf biomass, $c_{dgl}$, and a constant multiplier for water to dry biomass in the leaf tissue $B2W$. It also assumes that the interstitial water inside the leaf tissue does not freeze and that the internal energy of the interstitial water scales linearly with temperature as a function of liquid water heat capacity, $c_{liq}$. For $n_p$ plants with $b_l$ biomass each:

$$C_{vb}(new) = n_p b_l \text{C2B}(c_{dgl} + \text{B2W}c_l)) \tag{B.13}$$

Values for the specific heat capacity of dry green leaf biomass and the biomass to water multiplier were retrieved from Gu and co-authors [Gu *et al.*, 2007]. They used a similar method as the one proposed above, incorporating the specific heat capacity of dry green leaf biomass from [Jones, 1992].

# Appendix C

# EDM2.1: Enthalpy Flux and Conservation in the Canopy Air Space

## C.1 Path Independent Equations of State

Latent heat can be defined as the change in specific enthalpy between two states of conserved mass through a phase change. We use this definition to conceptually explore equivalent change in enthalpy through a sublimative phase change. If heat is added to a frozen and closed system such that sublimation occurs at two different intermediate states yet the resulting vapor ends up at the same temperature, the total change in specific enthalpy should be the same. We will assume that all processes occur at the pressure associated with the triple point. There is no reason this exercise should not be transferable assuming constant atmospheric pressure. The two changes in specific enthalpy are designated $\Delta h_1$ and $\Delta h_2$ and are equivalent:

$$\Delta h_1 = \Delta h_2 \tag{C.1}$$

Path 1 assumes that the ice is warmed to the triple point and is then sublimated via phase change energy, $L_S$, to a final temperature at the triple point. Path 2 assumes the ice sublimes at a temperature below the triple point and is then warmed to the triple point.

*Let us also assume that the specific heat capacity of water vapor at constant pressure, $c_{pv}$, does not itself change as a function of temperature. The change of enthalpy disregarding phase change becomes linear with temperature.*

$$\Delta h_1 = \text{warming ice} + \text{phase change} = c_i(T_3 - T) + L_{S(T_3)} \tag{C.2}$$

$$\Delta h_2 = \text{phase change} + \text{warming vapor} = L_{S(T)} + c_{pv}(T_3 - T) \tag{C.3}$$

Equating these two changes in enthalpy yields a relationship between the latent heat of sublimation at any temperature $T$ and the sublimation at the triple point $T_3$. Combining the first three equations.

$$L_{S(T)} = L_{S(T_3)} + c_i(T_3 - T) + c_{pv}(T - T_3) \tag{C.4}$$

The same path equivalence can be applied to a vaporization process of liquid, changing phase either before or after the water increases in temperature. With phase change energy, $L_V$, at variable temperature:

$$\Delta h_1 = \text{phase change} + \text{warming vapor} = L_{V(T_3)} + c_{pv}(T - T_3) \tag{C.5}$$

$$\Delta h_2 = \text{warming liquid} + \text{phase change} = c_l(T - T_3) + L_{V(T)} \tag{C.6}$$

$$L_{V(T)} = L_{V(T_3)} + c_l(T_3 - T) + c_{pv}(T - T_3) \tag{C.7}$$

## C.2 Applying Path Independence to a Datum

Using the above relationships, we can start to form a conservative state equation for the enthalpy of ice, liquid and vapor phases that uses a consistent datum. Let's define the final enthalpy of a system, $h_f$, in vapor phase, that started at some enthalpy, $h_0$, in ice phase at temperature $T_0$ below the triple point. It can reach the final enthalpy via two

paths, one is sublimated below the triple point, the other is vaporized as liquid above the triple point.

$$h_f = h_0 + \Delta h_1 = h_0 + \Delta h_2 \tag{C.8}$$

If we define the specific enthalpy of our starting position with a base at zero Kelvin, then $h_0 = c_i T_0$. Following the first path, the final specific enthalpy can be defined as follows:

$$h_f = c_i T_0 + L_{S(T_0)} + c_{pv}(T_f - T_0) \tag{C.9}$$

Likewise, for path 2 where the ice is heated to liquid phase above the triple point prior to evaporation:

$$h_f = c_i T_0 + c_i(T_3 - T_0) + L_{F(T_3)} + c_l(T_f - T_3) + L_{V(T_f)} \tag{C.10}$$

By substituting in the linearized and temperature dependent definitions of latent heat of vaporization and sublimation we see that the final enthalpy of the two paths are equivalent. First define $L_{S(T_0)}$ in terms of $L_{S(T_3)}$. Rewrite, path 1:

$$h_f = c_i T_0 + \left[L_{S(T_3)} + c_i(T_3 - T_0) + c_{pv}(T_0 - T_3)\right] + c_{pv}(T_f - T_0) \tag{C.11}$$

which results in:

$$h_f = c_i(T_3 - T_0 + T_0) + L_{S(T_3)} + c_{pv}(T_0 - T_3 + T_f - T_0) \tag{C.12}$$

By substituting the linearized and temperature dependent definition of vaporization in path 2:

$$h_f = c_i T_0 + c_i(T_3 - T_0) + L_{F(T_3)} + c_l(T_f - T_3) + \left[L_{V(T_3)} + c_l(T_3 - T_f)c_{pv}(T_f - T_3)\right] \tag{C.13}$$

which results in:

$$h_f = c_i(T_3 - T_0 + T_0) + L_{F(T_3)} + c_l(T_f - T_3 + T_3 - T_f) + L_{V(T_3)} + c_{pv}(T_f - T_3) \quad \text{(C.14)}$$

Recalling that sublimation energy is equivalent to fusion and vaporization energy at constant temperature, the state equation for water vapor over both paths reduces to:

$$h_f = c_i T_3 + L_{S(T_3)} + c_{pv}(T_f - T_3) \quad \text{(C.15)}$$

The specific enthalpy of water vapor is here defined in linear equations of temperature and constants.

## C.3 Total Enthalpy of Moist Air

The total enthalpy of moist air, $H$, is an intensive property and considers both the mass $m$ and specific enthalpies of of dry air, $h_{dry}$, and water vapor, $h_{vap}$.

$$H_c = m_{dry} h_{dry} + m_{vap} h_{vap} \quad \text{(C.16)}$$

Considering an air space with variable depth, we can then calculate the enthalpy per square meter of ground surface by defining the mass of dry air via $m_{dry} = z_c(1 - q_v)\rho$ where $z_c$ is the depth of the control volume (canopy height), $\rho$ is the density of the moist air, $c_{pd}$ is the specific heat capacity of dry air, and $q_v$ is the specific humidity of the moist air. The total enthalpy of moist air in the canopy air-space can be defined in terms of its temperature, humidity, volume and density:

$$H_c = z_c\rho(1 - q_v)c_{pd}T_c + z_c\rho q_v \left(c_i T_3 + L_{S(T_3)} + c_{pv}(T_c - T_3)\right) \quad \text{(C.17)}$$

## C.4 Enthalpy and Mass: Flux and Conservation in Canopy Air and Vegetation

Enthalpy is a conservative variable, so the change in storage must balance the flux of enthalpy through the boundaries of the control volume and any source or sink terms inside the control volume. Assuming that radiation has minimal heating on the air directly, compared to the sensible and latent sources on its boundaries, the storage of enthalpy is dependent on the fluxes of enthalpy from the ground to canopy, $\dot{H}_{gc}$, the atmosphere to canopy, $\dot{H}_{ac}$, and the vegetation to canopy, $\dot{H}_{vc}$, and on transpiration, $\dot{H}_{TR}$. Note that there may be more than one cohort representing the vegetation surfaces, and the enthalpy flux coming from vegetation must be integrated over all cohorts.

$$\frac{\partial H_c}{\partial t} = \dot{H}_{gc} + \dot{H}_{ac} + \int \dot{H}_{vc} + \int \dot{H}_{TR} \tag{C.18}$$

The flux of enthalpy in all cases must account for both sensible and latent fluxes of energy and consider that the system is open (mass is fluxing through the control surfaces). The sensible enthalpy flux from the ground surface is modeled as a resistance temperature gradient. The latent component incorporates the mass flux of the water vapor and phase change at ground temperature. Using Equation C.15 to calculate the enthalpy contained in the water vapor leaving the ground surface:

$$\begin{aligned} \dot{H}_{gc} &= \dot{H}_{gc,sensible} + \dot{H}_{gc,latent} \\ &= g_{gc}\rho c_{pd}(T_g - T_c) + \dot{m}_{gc}\left(c_i T_3 + L_{S(T_3)} + c_{pv}(T_g - T_3)\right) \end{aligned} \tag{C.19}$$

The flux of enthalpy from the atmosphere to the canopy air is very similar. It considers both sensible heat and latent heat in the vapor flux. The vapor mass flux can be in either direction; the internal energy of that mass flux will assume the temperature of its starting point. If $\dot{m}_{ac}$ is positive, then $T_e = T_a$, otherwise $T_e = T_c$. Alternatively, one could argue that the average of the two temperatures would provide comparable

results, i.e. $T_e = \frac{1}{2}(T_c + T_a)$.

$$\begin{aligned}\dot{H}_{ac} &= \dot{H}_{ac,sensible} + \dot{H}_{ac,latent} \\ &= g_{gc}\rho c_{pd}(T_a - T_c) + \dot{m}_{ac}\left(c_i T_3 + L_{S(T_3)} + c_{pv}(T_e - T_3)\right)\end{aligned} \tag{C.20}$$

The flux of enthalpy from the leaf surface, ignoring transpiration, is handled almost exactly the same way. The surface area of the leaf is not equal to the unit surface area of ground and must be scaled by a function of $LAI$. The simple model of effective surface area, $\sigma_H$, of sensible heating is $\sigma_H = 2LAI$. There are multiple plant cohorts modeled independently in the shared air-space, identified with indices $i$.

$$\begin{aligned}\dot{H}_{vc(i)} &= \dot{H}_{vc(i),sensible} + \dot{H}_{vc(i),latent} \\ &= g_{vc(i)}\sigma_H \rho c_{pd}(T_{v(i)} - T_c) + \dot{m}_{vc(i)}\left(c_i T_3 + L_{S(T_3)} + c_{pv}(T_{v(i)} - T_3)\right)\end{aligned} \tag{C.21}$$

Transpiration enthalpy is a three body problem. The enthalpy of liquid water mass must be removed from the soil and deposited in the canopy air. The energy of the phase change where the liquid water is converted to vapor must be removed from the vegetation and deposited in the canopy air as well. Since the plant draws water up from different parts of the soil column, the total enthalpy flux is a sum over the root water extraction drawn from each of those layers. These fluxes must be calculated independently because the different soil layers have different temperatures and internal energies. The enthalpy flux of liquid water from soil layer $k$ to cohort $i$ with soil temperature $T_{soil(k)}$ is defined as:

$$\dot{H}_{TR(i),soil(k)} = \dot{m}_{TR(i),soil(k)}\left(c_i T_3 + L_{F(T_3)} + c_l(T_{soil(k)} - T_3)\right) \tag{C.22}$$

The water is brought to the temperature of the leaf $T_{v(i)}$ and vaporized. The leaf either donates or receives the heat necessary for bringing it to vaporization temperature and donates the heat for the phase change itself. The heat transfer is associated with

the water drawn up from each independent soil layer.

$$\dot{H}_{TR(i),veg:soil(k)} = \dot{m}_{TR(i),soil(k)} \left( c_l (T_{v(i)} - T_{soil(k)}) + L_{V(T_v(i))} \right) \tag{C.23}$$

The latent heat of vaporization at the leaf temperature, $T_v$, can be related to the heat of vaporization at the triple point, and the total flux of enthalpy from one soil layer to the canopy air-space is the sum of that drawn from the soil layer and energy donated by the leaf. For $K$ soil layers over the rooting depth, the enthalpy deposited into the canopy air from each cohort $i$ is the sum of the enthalpy contained in the liquid mass transfered and the energy that was donated to change its phase to vapor:

$$\begin{aligned}
\dot{H}_{TR(i)} &= \dot{H}_{TR(i),soil(k)} + \dot{H}_{TR(i),veg:soil(k)} \\
&= \sum_{k=1}^{K} \dot{m}_{TR(i),soil(k)} \left( c_i T_3 + L_{F(T_3)} + c_l (T_{v(i)} - T_3) + L_{V(T_v)} \right) \\
&= \sum_{k=1}^{K} \dot{m}_{TR(i),soil(k)} \left( c_i T_3 + L_{F(T_3)} + c_l (T_{v(i)} - T_3) + L_{V(T_3)} + c_l (T_3 - T_v) + c_{pv} (T_v - T_3) \right) \\
&= \sum_{k=1}^{K} \dot{m}_{TR(i),soil(k)} \left( c_i T_3 + L_{S(T_3)} + c_{pv} (T_{v(i)} - T_3) \right)
\end{aligned} \tag{C.24}$$

The leaf internal energy of individual cohorts, $H_{v(i)}$, is balanced via conservation of energy with the sum of leaf energy fluxes.

$$\frac{\partial H_{v(i)}}{\partial t} + F = 0 \tag{C.25}$$

This group of fluxes, $F$, is composed of net absorbed shortwave radiation, $R_s$, and longwave radiation, $R_l$, total vegetation to canopy enthalpy flux, $\dot{H}_{vc}$, enthalpy losses from the cooling of transpiration, $\dot{H}_{TR}$, enthalpy gains from root uptake liquid water, $\sum \dot{H}_{TR,soil(k)}$, the deposition of liquid water internal energy via intercepted precipitation, $\dot{H}_{pint}$, and the losses from stem flow and dripping, $\dot{H}_{ds}$.

$$F = R_{S,net} + R_{L,net} - \dot{H}_{vc} - \dot{H}_{TR} + \sum_{k=1}^{K} \dot{H}_{TR,soil(k)} + \dot{H}_{pint} - \dot{H}_{ds} \qquad \text{(C.26)}$$

| | | |
|---|---|---|
| $R_{Sv,net}$ | $[Watts/m^2]$ | Total absorbed short wave radiation |
| $R_{Lv,net}$ | $[Watts/m^2]$ | Net long wave or thermal radiation |
| $\dot{H}_{pint}$ | $[W/m^2]$ | Internal energy gains through precipitation intercepted by leaves |
| $\dot{H}_{ds}$ | $[W/m^2]$ | Internal energy losses from stem flow and drip flow by leaves |
| $\dot{H}_{vc}$ | $[W/m^2]$ | Enthalpy flux from the vegetation to the canopy air space (sensible and latent) |
| $\dot{H}_{TR}$ | $[W/m^2]$ | Enthalpy losses from transpired water flux from the leaf stomata |
| $\sum \dot{H}_{TR,soil(k)}$ | $[W/m^2]$ | Enthalpy gains from root uptake liquid water coincident with transpiration loss |

Table C.1: Components of leaf energy flux.

# Appendix D

# The Photosynthetic Pathway and Transpiration Demand

Solar and thermal radiation entering the top of the canopy are modeled via a two stream scattering process [Sellers *et al.*, 1992]. The vegetation and soil skin simultaneously absorb and reflect both longwave and shortwave radiation, while emitting thermal radiation and gaining/losing heat. The process has separate scattering coefficients for near infrared and visible portions of the shortwave spectrum and therefore accounts for them separately.

Net longwave radiation is modeled as the balance between absorbed longwave radiation $R_{la}$ (based on leaf level and soil surface albedo/scattering parameters in the two-stream process) and the brightness emission of the leaf. The canopy elements (leaves, soil surface and possible standing water) emit longwave radiation based on their brightness temperature $T_B$.

$$R_l = R_{la} - \epsilon\sigma T_B^4 \tag{D.1}$$

## D.1 The Photosynthetic Pathway and Transpiration Demand

At the cellular level, the plants have two modes of gas exchange with the environment. One mode is when the stomata are closed to conserve moisture. The other mode is when the plant is not under stress and the stomata are open. Starting with the assumption that the plant is in an un-stressed state and the stomata are open for gas exchange (the plant is under no water or nutrient stress ), the photosynthesis process is driven by two factors: 1) absorbed photosynthetically active radiation (PAR), and 2) the gradient between canopy and interstitial leaf carbon. The process is modeled after the methods of Farquhar, Ball, Berry, Grivet, Kirchbaum and Collatz (see [Farquhar *et al.*, 1980], [Kirchbaum and Farquhar, 1984], [Collatz *et al.*, 1991] for the original papers). Farquhar explains that carbon assimilation is estimated as the minimum of several rate limiting steps: light rate limitation $J_E$, ribulose phosphate rate limitation $J_C$ and sucrose synthesis rate limitation $J_S$. In the EDM2.1 model, the sucrose limitation is ignored. Net carbon assimilation $A_o$ during photosynthesis considers the limited uptake rate and the simultaneous respiration of photosynthesis $R_d$:

$$A_o = min(J_e, J_c) - R_d \tag{D.2}$$

The rate limitation functions are described in detail in Farquhar (1980) and Collatz (1991). They generally have the following functional dependencies, defined by the rate of PAR incident on the leaf $R_{par}$, leaf absorbance of PAR $a_{par}$, maximum calatytic capacity of Rubisco $V_M$, partial pressure of interstitial leaf carbon $ca_i$ and leaf temperature $T_v$:

$$\begin{cases} J_E = f(Q_p, aPAR, p_i, T_v) \\ J_C = f(V_m, ca_i, T_v) \\ R_d = f(T_v, V_m) \end{cases} \tag{D.3}$$

The carbon assimilation rate is connected to the transpiration rate by determining

the exchange rate of vapor through open stomata for a given carbon assimilation rate $A_o$. This is reflected in the stomatal conductance term $g_{sw}$, defined by boundary layer $CO_2$ content $C_s$, photosynthesis compensation point $\Gamma(T_v)$, vapor pressure deficit $D_s$ and water vapor molecular diffusivity $D_0$. The stomatal slope $M_{st}$ linearly scales the relative proportion of water vapor that escapes per unit carbon assimilated $A_o$.

$$g_{sw} = \frac{M_{st} A_o}{(C_s - \Gamma)(1 + \frac{D_s}{D_o})} + b \tag{D.4}$$

Collectively, the transport of water vapor from the open stomata $\dot{m}_{TRO}$ into the turbulent air space is regulated by two resistances in series. The first resistance is the inverse of the stomatal conductance just described. The second resistance is the aerodynamic resistance of the boundary layer $r_{bw} = 1/g_{bw}$ between the stomatal opening and the turbulent well mixed canopy air space. The transport is driven by the vapor pressure gradient:

$$\dot{m}_{TRO} = \frac{D_s}{\frac{1}{gsw} + \frac{1}{gbw}} \tag{D.5}$$

Stomatal conductance is not, however, controlled only by the demand to assimilate carbon and boundary conductance. Water and nutrient stresses regulate the opening and closing of the stomata, a limitation imposed on top of the limitations imposed by the boundary layer resistance and carbon exchange. Actual transpiration $\dot{m}_{TR}$ takes into account the external stresses of drought and nutrient limitation. If the fraction of time $f'_o$ the stomata are in an "open status" can be determined, the actual transpiration is a linear combination of open state stomatal transpiration rate and the cuticular transpiration rate $\dot{m}_{TRC}$ which is a plant specific parameter.

$$\dot{m}_{TR} = f'_o \dot{m}_{TRO} + (1 - f'_o)\dot{m}_{TRC} \tag{D.6}$$

The stomatal opening frequency is dependent on the supply of water available in the root zone, and water demand of the vegetation. The *supply* of water available to the plant is the vertical integration of available liquid water above the wilting point, scaled

by the capacity of the root tissue biomass $b_r$ and conductance $K_{br}$. The available water in each soil layer is determined by scaling the difference in field capacity water content $w_{fc}$ and wilting point water content $w_{wp}$ by the soil water potential's $\Psi$ linear position between the two.

$$Supply = K_{br} b_r \rho_l \sum_{k=1}^{KR} \Delta_{z(k)} f_{l(k)} \frac{\Psi_{(k)} - \Psi_{wp}}{\Psi_{fc} - \Psi_{wp}} (w_{fc} - w_{wp}) \tag{D.7}$$

The water demand is simply the open stomata transpiration rate.

$$Demand = \dot{m}_{TRO} \tag{D.8}$$

The open stomata time fraction $f'_o$ is calculated as follows.

$$f'_o = \frac{1}{1 + \frac{Demand}{Supply}} \tag{D.9}$$

As the ratio of demand over supply approaches infinity, the time fraction of open stomata approaches zero to compensate. Likewise, if the demand/supply ratio is zero, the plant will leave its stomata open all of the time. If plant photosynthesis demands as much water as is available in the root zone, the stomata will be allowed open half the time.

# Appendix E

# EDM2.1: Soil System Mass and Energy Balance

Soil moisture and internal energy are modeled through a one-dimensional layered soil column representing vertical transport of moisture within each patch. Soil texture is treated as homogeneous in each patch. Due to limitations in the availability of soil texture information, soil parameters used in this thesis are also uniform in the vertical dimensions. The total depth of the soil column is set by a combination of run-time parameters and a map defining the depth to bedrock. The user sets a vector describing the depth of the vertical soil layers down to the lowest layer index $N_{zg}$. This controls layer thicknesses $\Delta z(k)$. If the bedrock map defines that bedrock is found at a shallower depth than the depth at index $N_{zg}$, a no-flow condition is set at the depth of bedrock. Otherwise, flux is allowed through the lowest layer. This thesis work uses a free drainage (gravity) boundary condition. The user can also opt for no-flow or half drainage conditions through the lowest soil layer in cases where bedrock is not found.

The formulation for water flux between soil layers is taken directly from legacy code in the LEAF-2 model (see [McCumber and Pielke, 1981], [Tremback and Kessler, 1985], [Walko *et al.*, 2000]) where the change in soil moisture storage is a function of the second order derivative of water potential with respect to depth. A comprehensive explanation of the soil moisture and energy mechanics covered here can be found in [Walko *et al.*, 2000]. This section is mostly a review of their work and how it interfaces

into the ED2 model.

Volumetric soil moisture $w_{g(z)}$ $[m^3/m^3]$ is solved via forward explicit integrtion, whos time derivative is governed by the vertical gradient in soil moisture flux $\dot{w}_{gg}$ $[m^3/m^2 s]$ (subscript gg implies ground-ground) and transpiration $\dot{m}_{TR,soil(k)}$. Symbol $\rho_l$ is the density of liquid water.

$$\frac{\partial w_{g(z)}}{\partial t} = \frac{\partial \dot{w}_{gg(z)}}{\partial z} - \dot{m}_{tr(z)}/\rho_l \tag{E.1}$$

Flux is driven by the vertical gradient in water potential, the combination of matric potential (tension) $\Psi$ and elevation head $z$:

$$\dot{w}_{gg(z)} = -\rho_l K_\eta \frac{\partial(\Psi + z)}{\partial z} \tag{E.2}$$

where hydraulic conductivity $K_\eta$ is an exponential function of the relative soil moisture content that scales saturated hydraulic conductivity $K_{0\eta}$, and $\rho_l$ is the density of liquid water.

$$K_\eta = K_{0\eta} \left( \frac{w_{g(z)}}{w_{g(z),sat}} \right)^{2b+3} \tag{E.3}$$

The saturated hydraulic conductivity and the $b$ term are soil texture dependent parameters. The soil moisture potential is likewise a direct function of relative soil moisture.

$$\Psi = \Psi_{sat} \left( \frac{w_{g(z)}}{w_{g(z),sat}} \right)^{-b} \tag{E.4}$$

The prognostic internal energy in the soil column is defined using the same datum as the internal energy of the leaf system (i.e., zero energy is zero kinetic motion) and is likewise defined by liquid fraction $f_l$, water mass $m_{gw} = \Delta z w_g/\rho_g$ $[kg]$ and soil mass $m_{gs}$. (Note that enthalpy and internal energy are synonymous in an in-compressible system). The total internal energy (enthalpy) of the soil bulk $H_g$ is easily broken into the energy of the water bound in the pore spaces $H_{gw}$ and the energy of the non-water matrix material $H_{gm}$. The specific heat capacity of this matrix is defined by $c_g$. The

forward equation for diagnosing internal energy from water content and temperature in each soil layer is defined as follows:

$$H_{gw(z)} = f_{l(z)}((w_{g(z)}c_i/\rho_g)T_3 + m_{gw(z)}L_{F(T_3)} + (T_{g(z)} - T_3)(m_{gw(z)}c_l))+ \\ (1 - f_{l(z)})((m_{gw(z)}c_i)T_{g(z)}) \tag{E.5}$$

$$H_{gm(z)} = T_{g(z)}c_{g(z)}m_{gs} \tag{E.6}$$

$$H_{g(z)} = H_{gw(z)} + H_{gm(z)} \tag{E.7}$$

Soil internal energy is prognostic and is based on the vertical flux of heat and local sinks to root water uptake.

$$\frac{\partial H_g}{\partial t} = \frac{\partial}{\partial z}(\dot{H}_{gg}) - \dot{H}_{TR,soil} \tag{E.8}$$

The flux from one layer to another accounts for both the diffusive heat flux through the moist soil matrix (first term group) and also the advective heat flux bound in the internal energy of mobile liquid water.

$$\dot{H}_{gg(z)} = \dot{H}_{gg(z),sensible} + \dot{H}_{gg(z),water} \tag{E.9}$$

$$\dot{H}_{gg(z),sensible} = -K_H\frac{\partial T_{g(z)}}{\partial z} \tag{E.10}$$

The energy flux associated with the water mass flux is calculated by substituting $\dot{m}_{gg}$ for $m_g$ (see Equation E.5). Likewise, the temperature of the water in the soil bulk can be diagnosed by inverting the internal energy equation E.5 after the prognostic step.

The bulk thermal transfer coefficient $K_H$, describes the thermal diffusivity and conductivity of the soil matrix and is naturally a function of the bulk's composition and connectivity. Thermal diffusivity is only represented in the liquid water portion of the

matrix. Conduction is a function of the solid phase (matrix and solid water). The bulk thermal transfer coefficient is calculated as a second order polynomial of relative soil moisture content $\theta_g = w_g/w_{g,sat}$ with sub-coefficients $K_{0H}$,$K_{1H}$ and $K_{2H}$. The first coefficient $K_{0H}$ represents the matrix grain conductivity, and the latter terms $K1H$ and $K2H$ represent the moist conductivity.

$$K_H = K_{0H} + K_{1H}\theta_g + K_{2H}\theta_g^2) \tag{E.11}$$

## E.1 Surface Water Boundary Conditions - Ponded Water/Snow

Precipitation and dew deposition may stay ponded above the soil surface in liquid and frozen states. The model can predict ponded surface water as multi-phase transient layers, accounted for in a five step process. Multiple layers are possible and may be useful when dealing with multiple phases, which have variable qualities such as albedo and density.

1. Add throughfall $\dot{m}_{pcp}(1 - \text{cf})$, drip and stem-flow $\dot{m}_{ds}$ to the surface water pool.
2. Add or remove surface water mass via evaporation/condensation/sublimation $\dot{m}_{gc}$.
3. Check surface layers for computational stability and total number. Liquid layers should always be fused together, combining mass, depth and energy. Layers that are too thin for computational stability of thermal properties are placed in a virtual pool until enough mass accumulates and they can be accounted for with stability.
4. Remove liquid water in the lowest surface layer via infiltration $\dot{m}_{inf}$.
5. Remove liquid water in the top surface layer due to run off $\dot{m}_{ro}$.

The ED2.1 model provides an option of two simple methods for calculating the mass flux of infiltration $\dot{m}_{inf}$. Method one suggests that all unsaturated pore spaces in the top soil layer can be filled over the next time-step $\Delta t$. Infiltration is therefore the minimum

of how much liquid water mass exists in the transient surface layer $m_{sfc}$ (above the top soil layer $N_{zg}$) and how much pore space remains free in the top soil lyaer $\rho_l(w_{g(N_{zg}),sat} - w_{g(N_{zg})})$. Recall that $f_l$ is the liquid fraction.

$$\dot{m}_{inf} = \text{MIN}\left[(w_{g(N_{zg}),sat} - w_{g(N_{zg})})\rho_l \Delta z_{(N_{zg})}, m_{sfc} f_l\right] / \Delta t \tag{E.12}$$

The second option scales the surface water that is available to infiltrate by a parameterized polynomial, refer to [Anderson, 1976]. For surface runoff, the model uses an e-folding time-scale $\epsilon_{ro}$. After infiltration has been calculated at the current time-step, the mass of water leaving the surface pool $m_{sfc}$ as runoff $m_{ro}$ is scaled based on the time-step and the e-folding time-scale:

$$\dot{m}_{ro} = -\text{MIN}\left(\frac{m_{sfc}}{\epsilon_{ro}}, \frac{m_{sfc}}{\Delta t}\right) \tag{E.13}$$

An e-folding time-scale equal to or less than the land-surface model's primary integration step assumes that all surface water will be runoff during that step. An e-folding time-scale that is double the time-step assumes that half the water will be removed.

## E.2 Soil Column Boundary Conditions

If surface water exists ($m_{sfc} > 0$), the mass balance on the top soil layer $\left(\frac{\Delta w_{g(N_{zg})}}{\Delta t}\right)$ is influenced by infiltration $\dot{m}_{inf}$. Otherwise, it is governed by evaporation and condensation $\dot{m}_{gc}$ (gc denotes ground-¿canopy). These processes cannot happen simultaneously.

$$\frac{\Delta w_{g(N_{zg})}}{\Delta t} = \begin{cases} -\frac{1}{\Delta z}(\dot{w}_{gg(N_{zg}-1)} + \dot{m}_{gc}/\rho_w) & \text{if } m_{sfc} = 0, \\ -\frac{1}{\Delta z}(\dot{w}_{gg(N_{zg}-1)} - \dot{m}_{inf}/\rho_w) & \text{if } m_{sfc} > 0 \end{cases} \tag{E.14}$$

Keep in mind that these equations represent vapor fluxes originating from both liquids or solid surface water. If two phases exist simultaneously, the vapor mass fluxes are calculated independently for both phases and then summed by a linear combination of their liquid fraction.

The change in the enthalpy $\left(\frac{\Delta H_{g,(N_{zg})}}{\Delta t}\right)$ of the top soil layer uses the same binary

logical constraint as its change in water mass. Enthalpy can be added or lost through the mutually exclusive, evaporative $\dot{H}_{gc}$ and infiltration $\dot{H}_{inf}$ processes. Enthalpy can leave the top soil layer through the percolation of liquid mass and heat diffusivity $\dot{H}_{gg(N_{zg}-1)}$ (see equation E.10). New terms are added to include the energy gained or lost due to net shortwave ground $R_{sgn}$ and net longwave ground $R_{lgn}$ radiation.

$$\frac{\Delta H_{g,(N_{zg})}}{\Delta t} = \begin{cases} \frac{1}{\Delta z}(-\dot{H}_{gg(N_{zg}-1)} + R_{sgn} + R_{lgn} - \dot{H}_{gc}) & \text{if } m_{sfc} = 0, \\ \frac{1}{\Delta z}(-\dot{H}_{gg(N_{zg}-1)} + R_{sgn} + R_{lgn} + \dot{H}_{inf}) & \text{if } m_{sfc} > 0 \end{cases} \tag{E.15}$$

The enthalpy gained from infiltration, $\dot{H}_{inf}$, is defined by the liquid internal energy of the infiltration mass flux at the temperature of the surface water in the lowest surface layer (see equation E.5).

The directionality of surface vapor fluxes $\dot{m}_{gc}$ are mutually exclusive and are controlled much in the same way as the leaf surface water evaporation, i.e., by comparing the specific humidity of the canopy air $q_c$ with that of the the boundary layer vapor pressure above the soil or surface water $q_g^*$. The bulk resistance to scalar transport is $r_{gc}$ and is discussed in Appendix F.

$$\dot{m}_{gc} = \rho_c(q_g^* - q_c)/r_{gc} \tag{E.16}$$

The calculation of the vapor pressure at the soil surface requires special attention because the micro topography of the soil surface has a complex saturation condition. A partially saturated surface condition presents liquid water to the canopy air space via surfaces that are recessed in soil pore spaces and have partial exposures. Therefore, the boundary layer vapor pressure must be calculated with a parameterization technique. Using a saturation mixing ratio $R_{sat(T_{gs})}$ and saturation specific humidity $q_{sat(T_{gs})}$ at the ground surface, defined by the top soil layer's temperature $T_{gs}$, the following method was proposed by [Lee, 1992]:

$$q_g^* = \begin{cases} q_{sat(T_{gs})} e^{\left(\frac{g\psi}{R_{sat(T_{gs})}}\right)} q_c \beta(1-\beta) & \text{if } m_{sfc} = 0, \\ q_{sat(T_{sfc})} & \text{if } m_{sfc} > 0 \end{cases} \tag{E.17}$$

The beta term estimates the exposure level of the water in the soil pores to the boundary layer. It essentially scales the boundary layer specific humidity between a maximum saturation level and that of the canopy air above. If the soil water is dry compared to field capacity $w_{FC}$, it assumes that the water in the soil pores are fully recessed and locked into their residual cavities, therefore the air in the boundary layer is going to match the saturation content of the air in the canopy, receiving little to no exchange with liquid water. From Lee (1992):

$$\beta = \frac{1}{4}(1 - cos(\pi \cdot min(1, \frac{w_{g(N_{zg})}}{w_{FC}})))^2 \tag{E.18}$$

The moisture flux boundary condition at the bottom of the soil column is assumed to be a free drainage condition. Under this assumption, the water potential below the last layer of the soil column is assumed to be equal to that of the lowest layer, thus only the gravity component in the flux differential drives flow. In the case where a soil layer interfaces with bedrock, $\dot{w}_{gg} = 0$. For gravity flow:

$$\dot{w}_{gg,(z=1)} = -\rho K \tag{E.19}$$

# Appendix F

# EDM2.1: Turbulent Canopy Processes and Aerodynamic Resistance - Methods of Massman, Weil, Sauer and Norman

The theory behind canopy transport processes was taken from a literature review of Brutsaert and Garratt [Brutsaert, 1982] [Garratt, 1992]. Specific modifications to the ED2.1 model will be discussed. These modifications follow the work of Massman, Weil, Sauer and Norman; see [Massman, 1997], [Massman and Weil, 1999] and [Sauer and Norman, 1995].

There exists a "dynamic sub-layer" between the troposphere and the top of the canopy. It is characterized by a distribution of turbulent length scales associated with a range of eddies that extend to the depth of the atmospheric boundary layer itself to include eddies generated by shear produced by the rough wall at the surface. The ground surface or vegetation canopy acts as a rough wall boundary imposing drag on the sub-layer creating a logarithmic decay of momentum from a reference point in the free atmosphere to the rough wall. This holds so long as the rough wall elements imposing the drag on the dynamic sub-layer are greater than the ratio of the air's viscosity and the friction velocity of the flow, $(\nu/u_*)$.

## F.1 The Dynamic Sub-layer

The standard log profile of mean wind velocity $\overline{u}$ was derived by observing the dimensionless relationship between friction velocity $u_*$ (an analogue of shear), elevation $z$ and the derivative of wind speed with respect to elevation $d\overline{u}/dz$. This is Von Karman's constant $k$.

$$\frac{u_*}{zd\overline{u}/dz} = k \tag{F.1}$$

Integrating this equation between two elevations $z_2$ and $z_1$ generates a bounded logarithmic wind profile.

$$\overline{u}_2 - \overline{u}_1 = \frac{u_*}{k} ln\left(\frac{z_2}{z_1}\right) \tag{F.2}$$

If a no slip-condition is assumed at the rough wall boundary, the wind speed will approach zero near the ground surface at an elevation defined by the roughness length $z_{om}$, which also describes the decay rate of the wind-speed. However, in the case of a dense vegetation canopy, momentum and eddies of the ABL can not penetrate all the way to the earth's surface. Therefore, the surface of the lower boundary condition now becomes displaced above the un-penetrable zone. This displaced elevation is the zero-plane displacement height $d_0$.

$$\overline{u}_{(z)} = \frac{u_*}{k} ln\left(\frac{z - d_0}{z_{om}}\right) \tag{F.3}$$

The log wind profile becomes zero, when $z - d_0 = z_{om}$. The displacement and the roughness are parameters associated with the surface characteristics. Given a known velocity $U_{(z_{ref})}$ at a reference height $z_{ref}$, one can solve for the friction velocity $u_*$, and then solve for the wind profile from the reference height to the top of the canopy.

$$u_* = \frac{U_{(z_{ref})} \cdot k}{ln\left(\frac{z_{ref} - d_0}{z_{om}}\right)} \tag{F.4}$$

## F.2 A Conventional Approach to Estimating Friction Velocity and the Turbulent Transport in the Canopy Sub-Layer

Several land surface modeling systems use a linear scaling to approximate the displacement height and the roughness length. The original assumption in the ED2 model follows the suggestion of Brutsaert[Brutsaert, 1982], that the displacement height and roughness length are constant fractions of maximum height of the vegetation canopy $z_c$.

$$d_0 = 0.63 \cdot z_c \tag{F.5}$$

$$z_{om} = 0.13 \cdot z_c \tag{F.6}$$

In this formulation the wind velocity profile is dependent on the height of the vegetation canopy, and the wind speed at reference height. The wind speed at the top of the canopy $U_{(z_c)}$ can be estimated by solving for the friction velocity and substituting it in Equation F.3.

$$U_{(z_c)} = U_{(z_{ref})} * \frac{ln\left(\frac{z_c - 0.63z_c}{0.13z_c}\right)}{ln\left(\frac{z_c - 0.63z_c}{0.13z_c}\right)} \tag{F.7}$$

Brutsaert[Brutsaert, 1982] and Bonan[Bonan, 1996], explain that K-theory is one method to approximate coefficients of turbulent transfer. The momentum flux $\overline{u'w'}$ is approximated by the diffusivity $K$ and the derivative of the wind profile at the point of interest.

$$\overline{u'w'} = -K\frac{d\overline{u}}{dz} \tag{F.8}$$

Turbulent diffusivity $K$ is often estimated from the friction velocity and the length scale of the eddies passing through the point of interest. These eddies are represented by

a mixing length, which is the maximum length at which a parcel of air can be transferred inside an eddy at the point of interest. At the top of the vegetation canopy, the diffusivity term can be parameterized with an estimate of the eddy length scale $L_M$ and the friction velocity.

$$K_{(z_c)} = k \cdot u_* \cdot L_M \tag{F.9}$$

A first approximation to mixing length is the eddy length scale is as deep as the roughness elements imposed above the zero-plane $l_M = z_c - d_0$. Diffusivity at the canopy top is then estimated in terms of canopy height, reference height and wind-speed at reference height.

$$K_{(z_c)} = \frac{U_{(z_c)} \cdot k^2 (z_c - 0.63 z_c)}{ln\left(\frac{z_c - 0.63 z_c}{0.13 z_c}\right)} \tag{F.10}$$

Brutsaert showed through review of field measurements, that the decay of wind speed inside the canopy can be modeled via an exponential fit. Therefore, since winds decay exponentially, and there derivative decays exponentially, then diffusivity decays exponentially with the derivative of wind speed (shear). The ED2 model, along with other canopy models of similar design, use an attenuation coefficient of 2.5.

$$K_{(z)} = K_{(z_c)} \cdot e^{-2.5(1 - z/z_c)} \tag{F.11}$$

The resistance of turbulent transport of scalars between two elevations can be estimated by integrating the inverse of the diffusivity profile.

$$r_{a->b} = \int_{z=a}^{b} \frac{1}{K_{(z)}} dz \tag{F.12}$$

The integration bounds differ slightly across the models. The Community Land Model version 2 used a bare soil roughness length $z_{os}$ as a lower bound and canopy height as the upper bound.

$$r_{z_{os}->z_c} = \frac{e^a \cdot z_c \cdot ln\left(\frac{z_c - 0.63z_c}{0.13z_c}\right)}{U_{(z_c)} \cdot k^2 \cdot (z_c - 0.63z_c)}(e^{-z_{os}/z_c} - e^{-z_c/z_c}) \tag{F.13}$$

The relationships for wind speed, friction velocity, diffusivity and surface conductance can be re-evaluated in terms of a reference wind-speed and a normalized component. The value in this exercise is to observe how these four variables react to different surface parameters such as canopy height $z_c$, irrespective of the reference wind-speed. Unit normalized quantities are denoted with primes.

$$u_* = U_{z_{ref}} \cdot u'_* \tag{F.14}$$

$$u'_* = \frac{k}{ln\left(\frac{z_{ref} - 0.63z_c}{z_{om}}\right)} \tag{F.15}$$

$$\overline{U}_{(z_c)} = U_{z_{ref}} \cdot \overline{U}'_{(z_c)} \tag{F.16}$$

$$\overline{U}'_{(z_c)} = \frac{ln\left(\frac{z_{ref} - 0.63z_c}{0.13z_c}\right)}{ln\left(\frac{z_c - 0.63z_c}{0.13z_c}\right)} \tag{F.17}$$

$$K_{(z_c)} = U_{z_{ref}} \cdot K'_{(z_c)} \tag{F.18}$$

$$K'_{(z_c)} = \frac{ln\left(\frac{z_{ref} - 0.63z_c}{0.13z_c}\right) k^2 (z_c - 0.63z_c)}{ln\left(\frac{z_c - 0.63z_c}{0.13z_c}\right)^2} \tag{F.19}$$

Surface to canopy conductance, $g_{z_{os}->z_c}$, is by definition inverse resistance. For simplicity, the change is related to unit wind speed at the canopy top and not at reference height.

$$c_{z_{so}->z_c} = U_{(z_c)} \cdot c'_{z_{so}->z_c} \tag{F.20}$$

$$c'_{z_{so}->z_c} = \frac{k^2 \cdot (z_c - 0.63 z_c)}{e^a \cdot z_c \cdot ln\left(\frac{z_c - 0.63 z_c}{0.13 z_c}\right)} \frac{1}{(e^{-z_{om}/z_c} - e^{-z_c/z_c})} \tag{F.21}$$

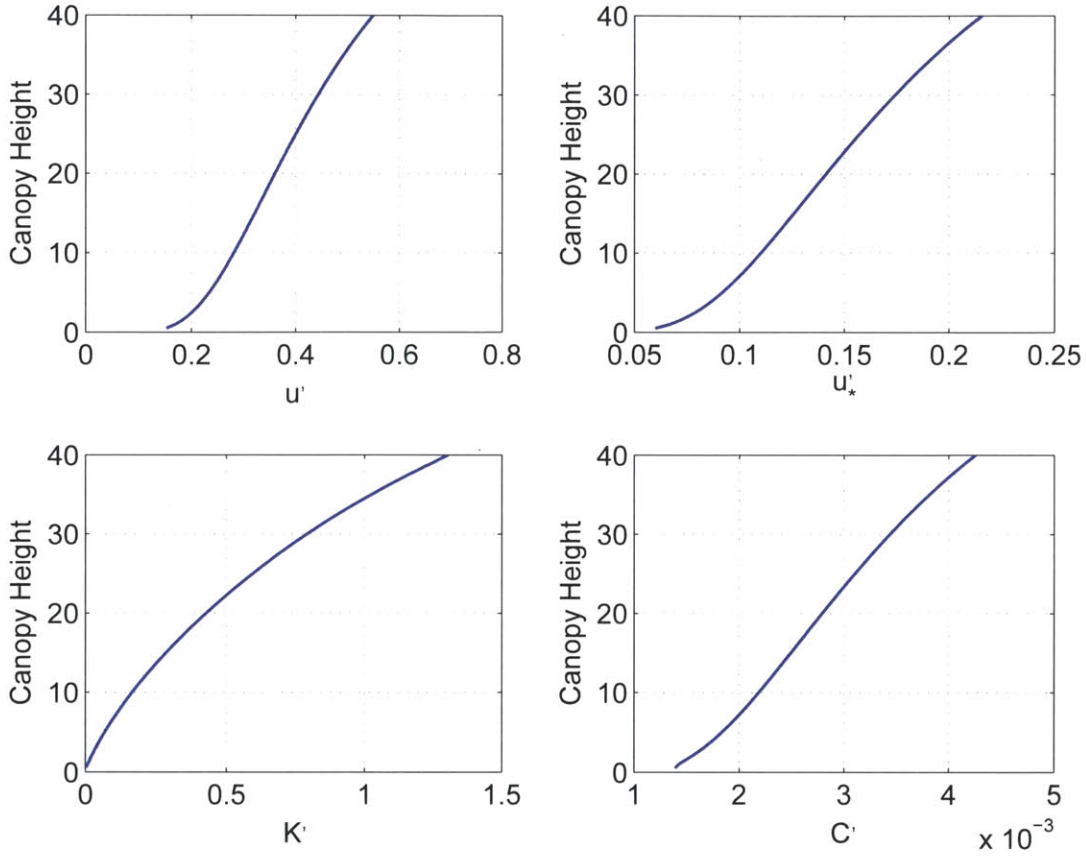


Figure F-1: Variables of unit turbulent transfer as a function of canopy height; wind speed at the canopy top $u'$, diffusivity at the canopy top $K'$, friction velocity $u'_*$ and soil to canopy conductance $C'$.

The diffusivity at the canopy top varies monotonically as a function of canopy height, see Figure F-1. Subsequently the scalar conductance from the ground to canopy top is controlled by the diffusivity at the canopy top and likewise increases monotonically as canopy height is increased.

There may be environments where this general type of phenomena exists. Vegetation that is taller may indeed have larger roughness elements, promoting a "rougher" rough-wall. Perhaps variability in crown emergents is related to canopy height. This model

ignores the vertical density of the foliage elements in the canopy, information which is not usually present in land-surface models.

Leaves in closed canopy forests are found in higher densities closer to the tree tops due to competition for light, this was observed in Central Amazonia. This creates a condition where the drag surfaces imposed on the winds in the dynamic sub-layer are densely packed and continuous at the canopy top. Using canopy depth alone to scale in-canopy turbulent exchange ignores a great deal of available information that could potentially be provided by the EDM model. Information on the vertical drag profile could enable more realistic in-canopy turbulent conditions and wind-profiles.

A poor estimate of turbulent resistance may have significant consequences to the modeled biophysical dynamics. Consider the flux of energy and mass through the three control surfaces of the land-surface model; the interface with the atmosphere above, surface runoff of heat and water, and subsurface drainage of heat and water. The resistances that control the flux rates between the soil and vegetation elements with the air effect the partitioning of energy between these three control surfaces. Even if there was only one flux surface and runoff and base-flow were ignored, changes in aerodynamic resistance would influence the equilibrium water masses and vegetation temperatures of the canopy. This would have direct impact on the ecological dynamics of the system.

## F.3 A Canopy Drag Density Approach to Scaling Wind Speed and Calculating Sub-layer Shear - Massman 1997

This section outlines the theory and application of the Massman methods of scaling wind speeds in EDM2. Massman's [Massman, 1997] (M97) first assumption is that the normalized wind-speed inside the vegetation canopy decays as a function of accumulated drag from bottom up.

$$u_{(z)}/u_{(z_c)} = e^{-n(1-\zeta_{(z)}/\zeta_{(z_c)})} \tag{F.22}$$

The cumulative leaf drag $\zeta$ is calculated as the integral of fluid drag on the leaf surface $C_d$, total frontal area of the drag elements $a$ per volume of air, and the sheltering factor $P_m$. The sheltering factor accounts for the effects of leaves hiding other leaves from seeing the viscous flow. An example of extreme sheltering would be two leaves immediately adjacent to each other, acting as the same roughness element, but accounting for twice the area. Massman tested the sensitivity of his results to variable sheltering factors and found that while the functional relationship of sheltering did influence results, they were not the most significant mode of variability.

$$\zeta_{(z)} = \int_o^z [C_{d(z')} a_{(z')} / P_{m(z')}] dz' \tag{F.23}$$

The in-canopy momentum equation assumes that shear balances with drag forces, hence:

$$d(-\overline{u'w'})/dz = \zeta_{(z)} u^2_{(z)} \tag{F.24}$$

The momentum balance is integrated over the canopy and combined with the equation for wind speed. The integrated momentum balance is then equated at the canopy top, and solved for $n$. Like the default method and most other Monin-Obukhov Similarity techniques, M97 assumes a constant shear layer above the canopy in the dynamic sub-layer, this allows us to define $-\overline{u'w'}(h)$ as the square of the friction velocity $u^2_*$.

$$n = \frac{\zeta_{(z_c)}}{2u^2_*/u^2_{(z_c)}} \tag{F.25}$$

There are still many unknowns in the current set of equations. Friction velocity $u_*$ and canopy top wind-speed $u_{(z_c)}$ are still required to calculate the in-canopy wind speed profile. M97 introduces a parameterization of surface drag which reduces the unknowns by 1. It is suggested that surface drag $C_{surf}$ is completely determined by the accumulated leaf area. Surface drag essentially transforms wind speed into shear. High values of drag will produce large friction velocities per unit wind speed.

$$u_*/u_{(z_c)} = \sqrt{C_{surf}} = c_1 - c_2 e^{-c_3 \zeta_{(z_c)}} \tag{F.26}$$

The constant shear layer assumption above the canopy still holds, Equation F.26 can be compared with the log wind equation from the canopy top to the reference elevation. Recall the log wind equation, which now contains a stability parameter $\Psi_M(\eta)$.

$$u_*/u(z) = k/[ln\left(\frac{z-d}{z_o}\right) - \Psi_M(\eta)] \tag{F.27}$$

The geometric parameters of displacement height and roughness length, as well as stability parameters are yet unknown. The stability parameter $\Psi_M(\eta)$ is analyzed as a function of the non-dimensional height $\eta$, defined as $\eta = z/L$ and $L$ is the Obukhov Length. For a treatment of stability analysis, see any boundary layer text including Garratt[Garratt, 1992], Brutsaert[Brutsaert, 1982] and Stull[Stull, 1988]. The calculation of the mixing length requires known momentum flux and sensible heat flux. The Obukhov length is a measure of the mechanical to the buoyant shear production, and because of this we must solve for stability simultaneously with the friction velocity $u_*$ and the potential temperature velocity (analogous with sensible heat flux) $\theta_*$. This solution requires an iterative method, which is time consuming and harbors issues of non-convergence. Estimating instability with the bulk Richardson number $Ri_B$ does not require iteration and can be used to derive the non-dimensional height $\eta$. The bulk Richardson number estimates stability by approximating heat and momentum flux from wind speed and temperature gradients.

$$Ri_B = (g/\theta_v)z(\theta_v - \theta_{v0})/(u^2) \tag{F.28}$$

The displacement height and roughness length are still unknown. For the displacement height, M97 advocates the center of drag method suggested by Thom[Thom, 1971]. The center of drag is the center of the vertical distribution of fluid drag in the canopy. With the assumption that unit drag force is unchanging at high Reynolds numbers the displacement height is determined geometrically. From Massman 97:

$$d/z_c = 1 - \int_0^{z_c} e^{-2n(1-\zeta_{(z)}/\zeta_{(z_c)})} d\zeta \tag{F.29}$$

The roughness length can be calculated algebraically by equating the log wind equation at the canopy top (F.27) to the surface drag parameterization (F.26).

$$z_o = (z_c - d)e^{-ku_{(z_c)}/u_*} \tag{F.30}$$

The set of equations defining in-canopy velocity is now closed.

### F.3.1 Estimating Drag Profiles from ED2 Cohorts

The ED2 model provides statistical distributions of vegetation cohorts. The cohorts have attributes of canopy height, leaf area index, crown width and number density. The model offers no information as to the spatial positioning of the cohorts' members, nor of the profiles of drag surfaces for each cohort. Therefore, the following assumptions are made:

- Cohort individuals are dispersed uniformly in their patch space, such that the leaf, stem and branch area index is considered to be homogeneous in the horizontal plane.
- The canopy leaves and stems constitute the drag surfaces and are distributed uniformly over the crown depth $z_c$.
- The crown depth $D_c$ is a constant scale of the cohort height. For grass species the depth of the cohort canopy is equal to the height.

As mentioned earlier, the fluid drag coefficient around the individual drag elements is held constant at 0.2. The drag surface frontal area $a(k)$ $[m2/m]$ per unit depth is estimated by summing the cohort conditional total area indices $TAI_C$ and the relative fraction of those areas found within discrete depth of air at elevation $k$.

$$a_{(k)} = \sum_{i=1}^{n} \frac{1}{\Delta z} TAI_{C(i,k)} \frac{\Delta z}{D_{c(i)}} \tag{F.31}$$

The "conditional" total area index is the total area index of only those cohorts with drag surface found at the elevation of interest.

$$TAI_{C(i,k)} \quad = \quad TAI_{(i)} \quad | \quad \left(z_{(k)} > (h_{(i)} - D_{c(i)}) \quad \& \quad z_{(k)} < h_{(i)}\right) \tag{F.32}$$

## F.4 Estimating Vertical Flux and Turbulent Transport Processes via Second Order Closure

The method of Massman (1997) estimates a wind-speed profile based on vertically distributed vegetation density. It also estimates the amount of shear in the sub-layer above the canopy, and the geometric attributes that define the drag on the fluid, see Figure F-2. However, the transport of scalar quantities such as the aerodynamic resistance that regulate heat an mass flux inside the canopy requires further interpretation. Seeking a better alternative than "K-theory", Raupach[Raupach, 1988] among others, explain that fluxes within the canopy can run counter gradient. For sensible heat flux, this gradient may be the temperature stratification, for momentum this gradient may be the mean velocity profile.

The use of K-theory is ubiquitous in simple LSM's, but its shortcomings can not be overstated. A gradient is only an approximation of the correlated perturbation of the vertical velocity and the scalar of interest. Having information of the turbulent energy may provide a closer analog to this correlation. Turbulent kinetic energy $TKE$ is the sum of the squared perturbations on mean wind-speed in each direction, in other words the sum variance.

$$TKE = \frac{1}{2} < \overline{u_i' u_i'} > \tag{F.33}$$

Raupach discusses the theoretical budget for how $TKE$ can be created, destroyed or transported into a point of interest [Raupach, 1988].

$$\frac{\partial(TKE)}{\partial t} = advection + P_s + P_w + P_b + T_t + T_p - D \tag{F.34}$$

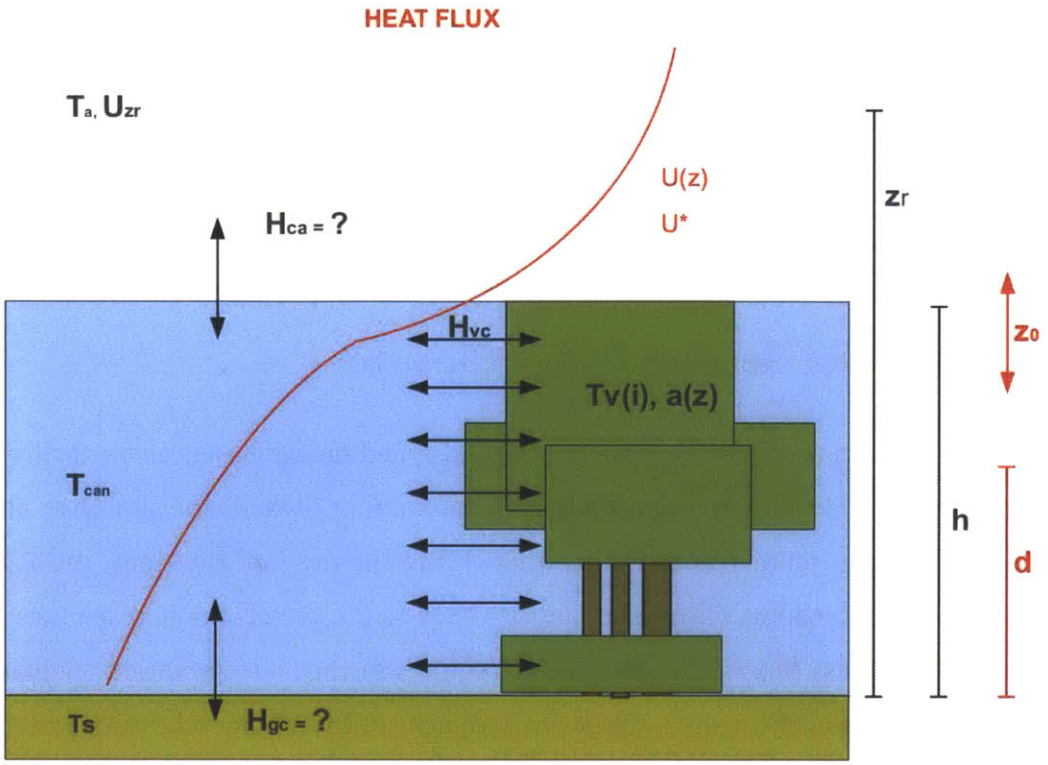


Figure F-2: Diagram of known and unknowns in the canopy modeling environment after the wind-profile is calculated. Variables such as roughness, displacement and drag profile are readily calculated based on cohort structure. An estimate of turbulent transport in the form of resistance is still required to calculate vertical enthalpy flux.

Assuming the system is in quasi-steady state ($\frac{\partial(TKE)}{\partial t} = 0$) and is horizontally homogeneous ($advection = 0$). the resulting terms balance and are described as follows by Raupach:

- shear production, $P_s = - < \overline{u'w'} > \frac{d\overline{u}}{dz}$, length scale $h$
- wake production, $P_w = - < \overline{u} > \frac{<\overline{u'w'}>}{dz}$, length scale $d << h$
- buoyant production, $P_b = \frac{g}{\theta_v} < \overline{w'\theta'_v} >$, (from Garratt)
- transport of TKE via velocity fluctuation, $T_t = -\frac{1}{2}\frac{d<\overline{w'u'_iu'_i}>}{dz}$
- transport of TKE via pressure fluctuation, $T_p = -(1/\rho)\frac{d<\overline{w'p'}>}{dz}$

- viscous heat dissipation, $D = \nu \overline{u_i' \frac{\partial^2 u_i'}{\partial x_j^2}}$

Raupach provides a compilation of the relative sources and sinks of these terms over the profile from observations. Figure F-3 is taken from [Raupach, 1988].

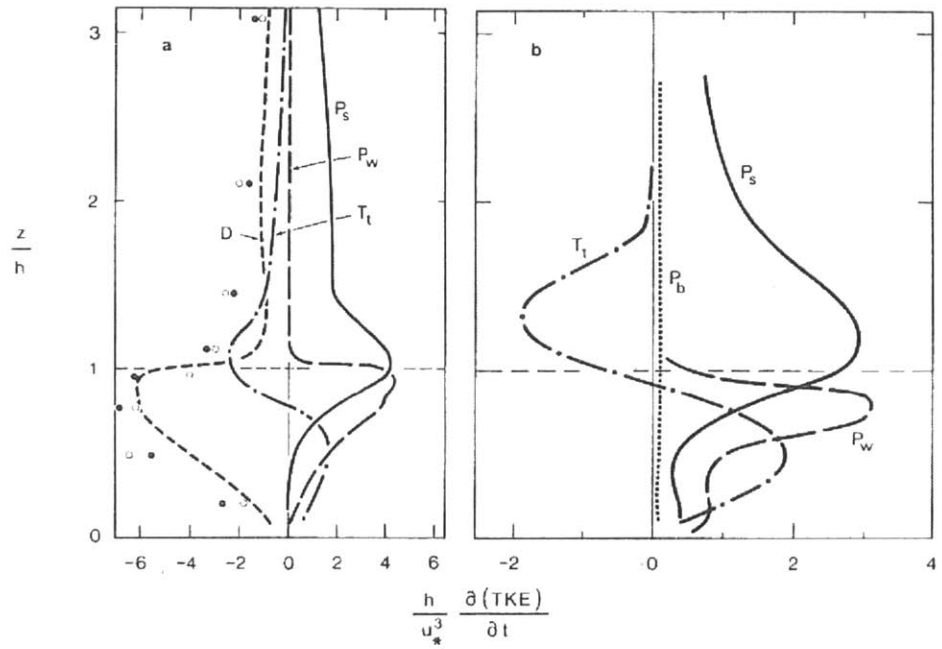


Fig. 9. Terms in the TKE budget, (22), for (a) the "strips" wind-tunnel model canopy (h = 60 mm) and (b) the Moga forest canopy (h = 12 m, $\bar{u} \approx 3.5$ m $s^{-1}$, slightly unstable daytime conditions). In (a), curve D is the residual - $P_s$ - $P_w$ - $T_t$; points are values of D from inertial-subrange spectral levels (open: u spectrum; solid: w spectrum).

Figure F-3: Taken from [Raupach, 1988].

Massman and Weil (MW99) [Massman and Weil, 1999] are able to resolve an analytical expression for the $TKE$ profile in a canopy by solving a reduced form of the $TKE$ budget equation, assuming horizontal homogeneity, proportional isotropy and boundary conditions. The horizontal homogeneity assumption matches the model construct in EDM2.1 nicely. The assumption of proportional isotropy means that the velocity variance in the three directions is proportional the the turbulent kinetic energy, and that the velocity variance in the vertical direction is likely the strongest of the three. Making a similar steady state assumption, they reduce the budget equation to five terms,

transport, viscous dissipation, return to isotropy, wake production and shear production shown in the following equation respectively (from MW99). Assuming velocity variance notation, in the horizontal plane along the direction of mean wind $u$, $\sigma_u = \overline{u'u'}$, the total energy variance is the sum over directions, $\sigma_e = \sigma_u + \sigma_v + \sigma_w$.

$$\frac{d}{dz}\left(\sigma_e \lambda_1 \frac{d\sigma_e^2}{dz}\right) - \frac{14\sigma_e^3}{9\lambda_3} + \frac{2\sigma_e}{9\lambda_2}\left(\sigma_w^2 - \sigma_e^2/3\right) + 2c(z)u^3 + 2\left(-\overline{u'w'}\right)\frac{du}{dz} = 0 \qquad \text{(F.35)}$$

The analytical solution and its expanded terms can be found by reading the original paper (MW99) and referencing equation 10. Ultimately, the velocity variance profile is dependent, on the canopy drag profile $c_{(z)}$, the canopy wind speed profile, the friction velocity at the canopy top and a tuning parameter we will call $\alpha_{99}$. This parameter assimilates several constant terms, among which is a joint eddy mixing length scale for both shear and wake driven turbulence. A range of potential values for $\alpha 99$ are evaluated in theoretical and experimental canopies and presented in MW99 and reproduced here, see Figure F-4. A sensitivity study of $\alpha_{99}$ using the ED2.1 model construct is shown in Figure F-5. While there is reduced sensitivity at ranges 0.03 through 0.01, 0.03 was chosen because it matches more closely to what MW99 ultimately advocated in their results (0.05).

Massman 1999 calculates a ground to canopy conductance term following methods outlined by Sauer and Norman [Sauer and Norman, 1995], who also adapted Monteith's application of the Nusselt Number to explain heat exchange. The heat transfer conductance, $g$ is related to the Nusselt number as a function of the mixing length of the eddies interacting with the ground $L$ and thermal conductivity of the fluid $k_f$. In the case of water vapor, the conductivity term is switched to a vapor diffusion term.

$$g = \frac{\mathrm{Nu} \cdot k_f}{L} \qquad \text{(F.36)}$$

The Nusselt number can be parameterized as a function of the Reynolds number $Re$ and the Prandtl number $Pr$.

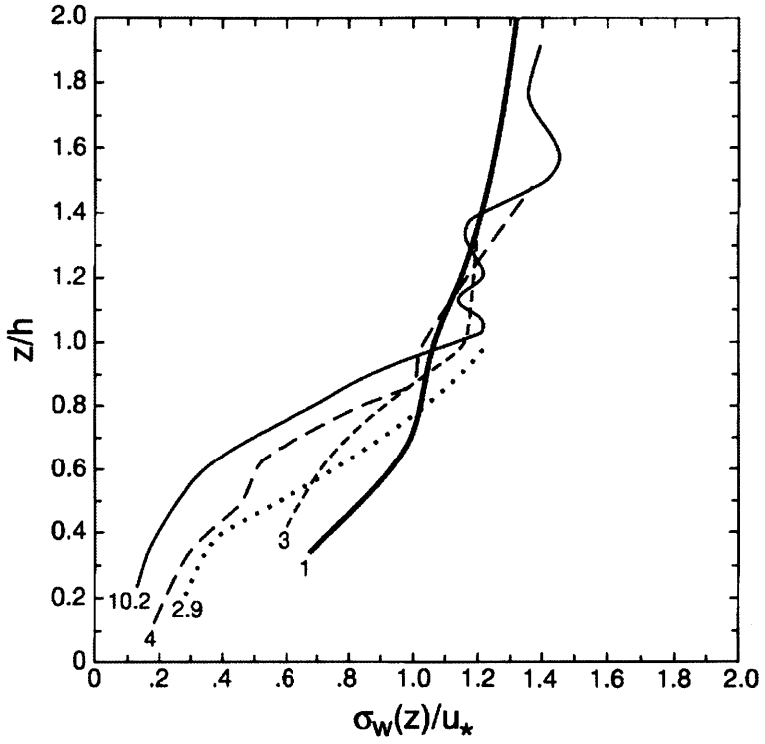


*Figure 3.* Observed profiles of $\sigma_w(z)/u_*$ for five different canopies. The canopy LAI is included below each curve. These profiles are taken from Gardiner (1994; LAI = 10.2, $C_d \approx 0.16$, spruce), Denmead and Bradley (1987; LAI = 4, pine), Shaw et al. (1974; LAI = 3, $C_d = 0.20$, corn), Wilson et al. (1982; LAI = 2.9, $C_d = 0.17$, corn), and Raupach et al. (1996; LAI = 1, eucalyptus).

Figure F-4: Synthetic and natural observations of normalized vertical wind variance profiles selected from [Massman and Weil, 1999].

$$\mathrm{Nu} = c\mathrm{Re}^a\mathrm{Pr}^b \tag{F.37}$$

$$g = (ck_f/L)\mathrm{Re}^a\mathrm{Pr}^b \tag{F.38}$$

Sauer and Norman then perform a fitting exercise based on a body of observational data in natural and laboratory settings to solve for the parameters a and b, as well as modify c to incorporate turbulent intensity $i$. This is the key step that invokes the utility of second order closure effects from MW99.

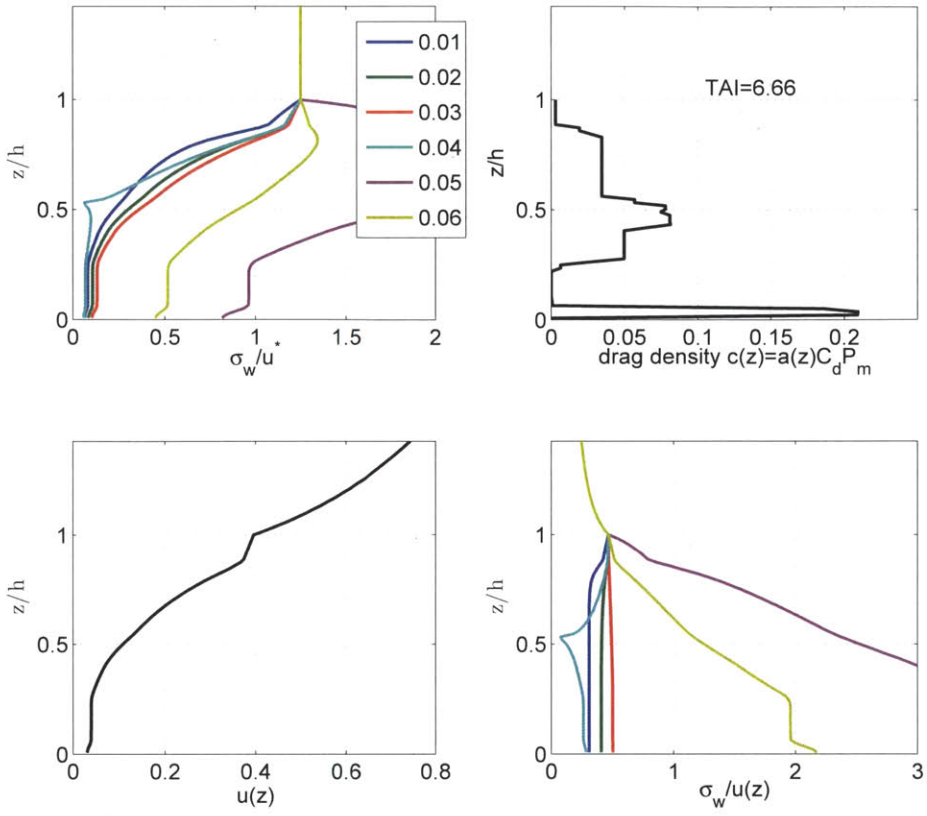


Figure F-5: Estimated profiles of the normalized vertical wind variance $\sigma_w/u^*$ for a selection of tuning parameters $\alpha_{99}$. The wind speed and frontal area profiles are provided for reference. The vertical drag and frontal area profile was selected from an arbitrary EDM2.1 forest canopy.

$$c = c'(1 + 2i) \tag{F.39}$$

Having a second order closure scheme, turbulent intensity can readily be extracted as the mean of the velocity variances normalized by wind speed at the surface $i = \bar{\sigma_{z=0}}/u_{z=0}$.

$$g_{gc} = c' \left(k_f/L_{sfc}\right) (1 + 2i)\, Re^a Pr^b u_{h_T} \sqrt{u_0/u_{h_T}} \tag{F.40}$$

Massman and Weil suggest the mixing length scale $L_{sfc}$ is taken to be the roughness length $z_o$ of the canopy's rough wall approximation of drag on the dynamic sub-layer. While it can be argued (admittedly by M99) that the roughness length does not have a strong theoretical matching with the eddy length scale at the soil surface, the roughness length gives a stable and bounded range of potential mixing lengths.

### F.4.1 MW99 Validation Test

The three model formulations were also compared in an arbitrary ED2.1 simulation for the Manaus area to assess the relative impacts on flux variables. The forest structure and composition was created via spin-up using ERA40 climatology. The analysis simulation was conducted over a period of one week, using ERA40 weather forcing near Manaus for January 1st through 7th of 2000. Figures F-6 and F-7 show results from the open-canopy and grassland canopy structures respectively. This is a sensitivity analysis, not to be interpreted as validation. The fluxes are consistent with the synthetic results using unit winds as evidenced by large fluxes from the M97 scheme for the open canopy, and relative consistency with the grass canopy. These results show that the vapor fluxes can differ on the order of 100 watts at the surface and canopy top.

The final test is a validation of the results generated using the MW99 closure techniques in ED2.1. A simulation was conducted for January of 2000 in the Manaus region. The mean diurnal canopy to atmosphere flux estimates of sensible and latent heat, the net radiation and the in canopy temperatures are compared between the model and that observed at an eddy flux tower, see Figure F-8. Results indicate good agreement between the two, where in most cases the means fall within the confidence range of the other.

In summary, the M97 and MW99 scheme has been applied to the ED2 model and can produce stable land surface energy dynamics in tropical conditions, over a range of canopy structures including grasses. All canopy turbulent closure methods that are based off of Monin-Obukhov similarity theory make assumptions about canopy uniformity and isotropy, the M97/M99 method also makes these assumptions. It is also a

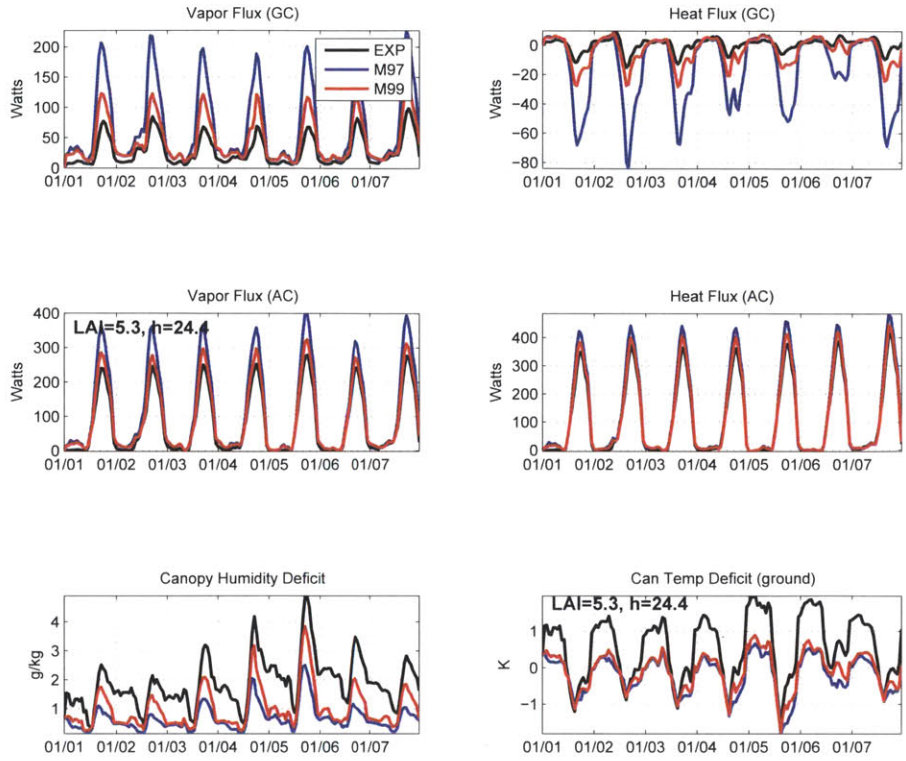


Figure F-6: Comparison of one week of ED2.1 flux estimates using the EXP, M97 and M99 schemes for the case of an *OPEN CANOPY*. Fluxes are estimated at either the interface between the ground and canopy (GC) or the ABL and canopy (AC). For reference, the canopy humidity deficit with the ABL, and the temperature deficit with the ABL is also provided in the lower panels.

method primarily appointed to closed tree-stands, not grasslands. There is treatment of this issue. When LAI becomes low, the model opts for a simplified surface roughness parameterization. It can be argued that the M97 method has a much more realistic aerodynamic response to the drag profiles generated by ED2.1 model canopies, as compared to the default method. In conceptual design, it is more physically defensible and makes use of the ED2 model's information on plant structure and composition.

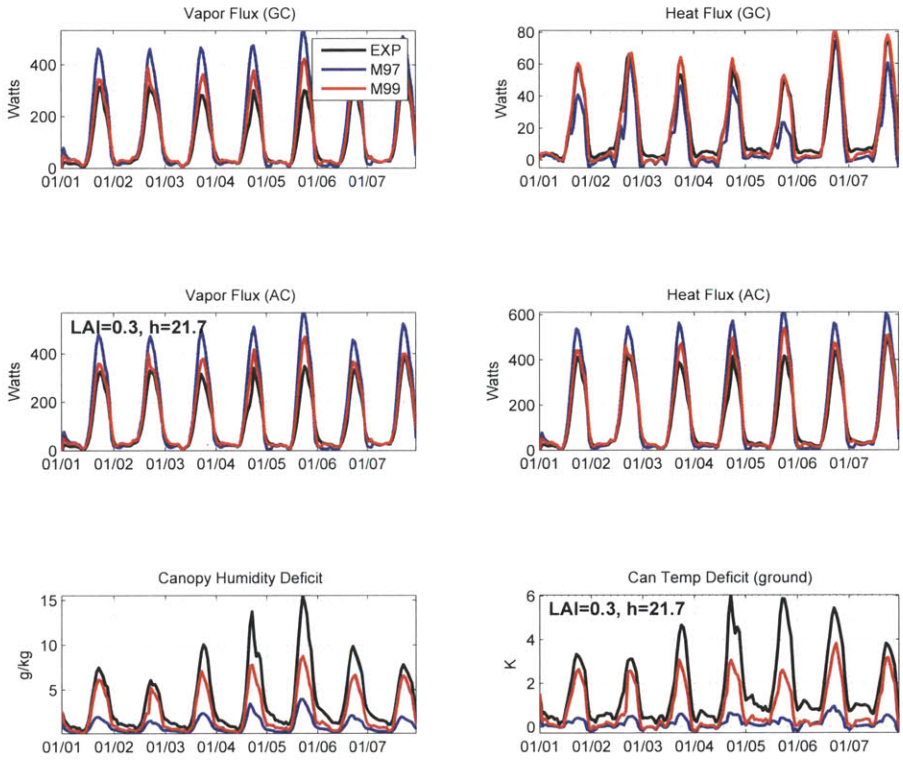


Figure F-7: Comparison of one week of ED2 flux estimates using the default, M97 and M99 schemes for the case of a *GRASSLAND CANOPY*.

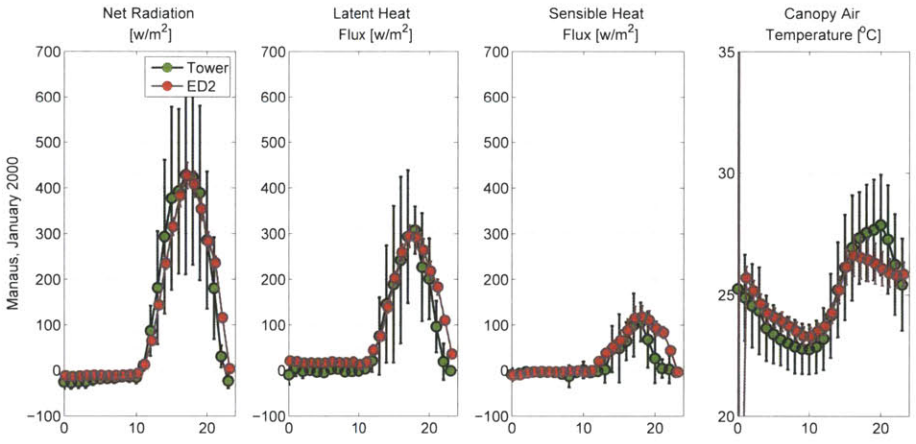


Figure F-8: Comparison of ED2 model estimates and tower measured diurnal mean flux data. Manaus January 2000.

# Appendix G

# Bulk Resistance of Scalar Transport from Leaf Surfaces

The transport of water vapor and heat (scalars) from leaf surface to the canopy air space is controlled by by a module derived from Monteithh's "Principles of Environmental Physics, 1973". Modifications to leaf-canopy resistance can have significant impacts on leaf temperature distributions, maximum leaf temperature and numerical integration time.

Conductance of scalar transport $c_s$ is the sum of mechanical (forced) $c_{sm}$ and buoyant (free) $c_{sb}$ components; dependent on leaf width $w_l$, mean wind speed incident on the leaf $U$, molecular diffusivity $D_H$ and the temperatures of the leaf and surrounding canopy air $T_l$ and $T_a$.

$$c_{sm} = 0.003 \cdot \sqrt{U/w_l} \tag{G.1}$$

$$c_{sb} = 0.5 \cdot \frac{1}{w_l} \cdot D_H \cdot G_R^{1/4} \tag{G.2}$$

Where $G_R$ is the Grashof number,

$$G_R = 1.6 \cdot 10^8 |T_l - T_a| w_l^3 \tag{G.3}$$

$$c_S = c_{SM} + c_{SB} \tag{G.4}$$

The resistance being the inverse,

$$r_s = 1/c_s \tag{G.5}$$

Some of the terms in this relationship will have differing sensitivities. For instance mechanical conductance is dependent on wind speed and leaf width only, and are dampened by a square root. Buoyant conductance is more complicated. The most influential parameter is the leaf width because it is inversely related to conductance. Temperature gradient is effectively a function of a $3/4$ power.

A persistent challenge in the continued development of ED2.1 has been the stable integration of leaf energy, particularly those leaves with low heat capacity and high heating rates (imagine grasses baking in dry lands with abundant solar radiation). It was not uncommon for leaves with small heat capacities to start oscillating due to high heating and cooling rates, and thus trigger step truncations in the Runge-Kutta process.

Assuming molecular diffusivity is relatively constant, for a given leaf type we can construct a range of wind speeds and temperature differences that encapsulate the variety of expected environmental conditions governing the scalar transport. Figure G-1 shows this variability space for a tropical palm of width 20 centimeters. Figure G-2 breaks down the range of conductances into their buoyant and mechanical terms.

The variability space for a 3 centimeter leaf width is shown in Figures G-3 and G-4.

The figures show two clear points. The first is that the range of leaf resistance changes nonlinearly and is relatively large. As wind speed decreases to nearly still conditions, the resistance gets extremely high.

The second and perhaps more important point, is that resistance is insensitive to temperature gradients. In other words, the buoyant conduction term has little to no effect. Transport is nearly always dominated by mechanical transport. The minimum forced conductance is greater than or approximately equal to the maximum free conductance term, for both leaf types. So while temperature gradients are generating buoyant

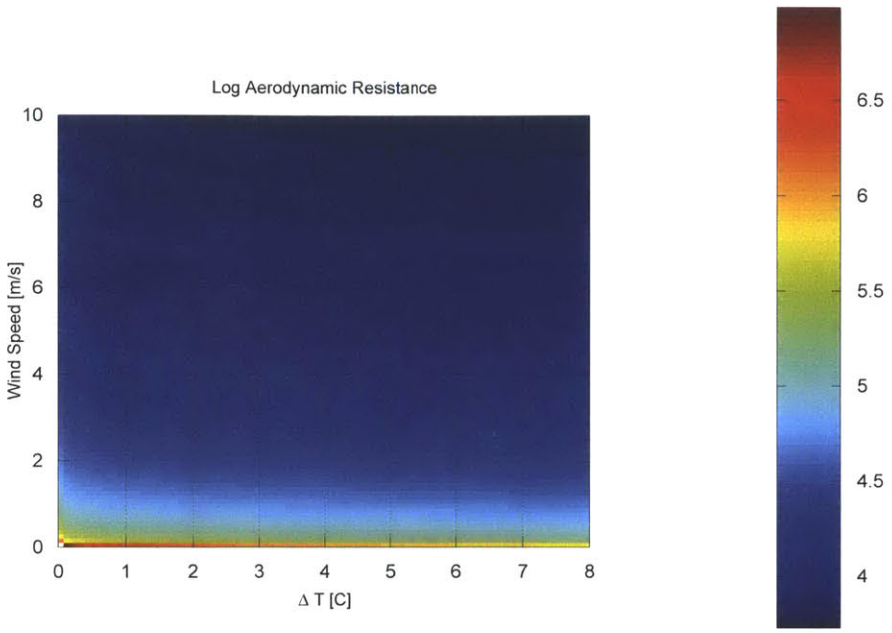


Figure G-1: The aerodynamic resistance [s/m] of scalar transport from a 20 centimeter wide leaf surface to canopy air for a range of mean incident wind speeds and leaf to air temperature differences.

transport, they are an order of magnitude lower that mechanical effects, and hence have no influence. An alternative approach to leaf aerodynamic conductance calculates the Nusselt number, much in the same way surface conductance was calculated with the Sauer and Norman method.

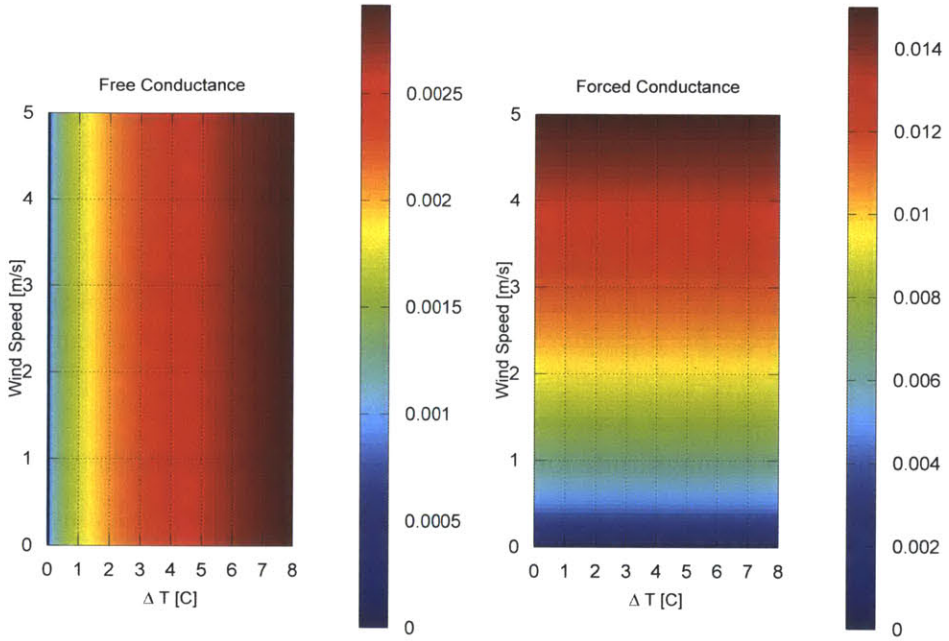


Figure G-2: The forced and free components of aerodynamic conductance [m/s] of scalar transport from a 20 centimeter wide leaf surface to canopy air for a range of mean incident wind speeds and leaf to air temperature differences.

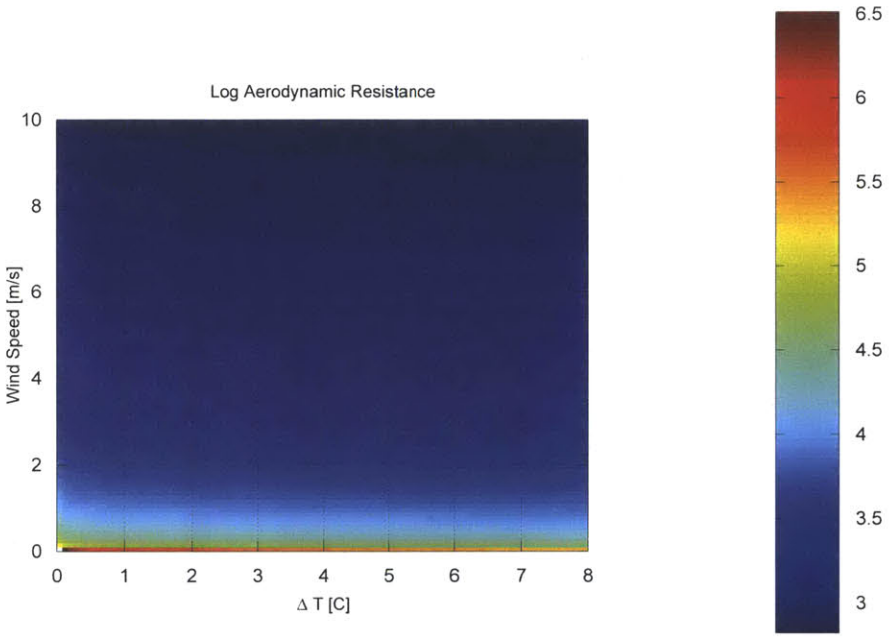


Figure G-3: The aerodynamic resistance [s/m] of scalar transport from a 3 centimeter wide leaf surface to canopy air for a range of mean incident wind speeds and leaf to air temperature differences.

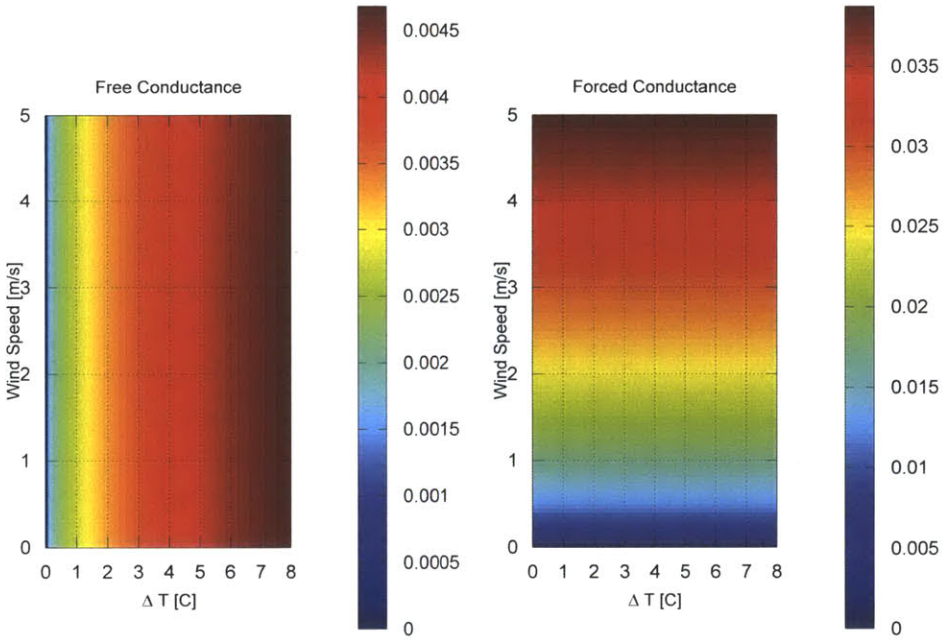


Figure G-4: The forced and free components of aerodynamic conductance [m/s] of scalar transport from a 3 centimeter wide leaf surface to canopy air for a range of mean incident wind speeds and leaf to air temperature differences.

# Appendix H

# EDM2.1: Mixed Forward Euler / Trapezoidal Backwards Euler (FE-BDF2) Numerical Integration in Canopy Biophysics

## H.1 Solver

The BDF2 method states that the discrete time derivative of the state vector can be approximated by a partial trapezoidal forward step from both current and previous time positions $(n-1)$ and $(n)$, as well as a full backward step using the derivative at the future step $(n+1)$. Let us assume that the state variables can be described as a vector quantity, denoted by $Y$. Like any numerical stepping procedure there is an assumption that state quantities at different points in time can be calculated by extrapolation using slopes, the slopes calculated by evaluating derivatives.

$$\frac{Y_{n+1} - Y_n}{\Delta t} + \frac{1}{2}\frac{Y_{n+1} - 2Y_n + Y_{n-1}}{\Delta t} \approx \frac{\partial Y}{\partial t}, t(n+1) \tag{H.1}$$

It may be possible to describe the time derivative of the state vector by a system of linear equations defined as follows:

$$\frac{\partial Y}{\partial t} = A \cdot Y + B \tag{H.2}$$

The system of linear equations only has a unique solution if it is fully determined, giving at least as many equations as unknowns. If the state equations can indeed be linearized by combining the previous two equations, we see that the forward state linear system can be solved simultaneously using information on the state from the current and previous steps. The tricky part, and computationally intensive part, is inverting $[3 - 2A\Delta t]$.

$$Y_{n+1} = [3I - 2A\Delta t]^{-1} [4Y_n - Y_{n-1} + 2B\Delta t] \tag{H.3}$$

The EDM2.1 model makes use of adaptive time-stepping. The time step $\Delta t$ between time $(n)$ and $(n+1)$ may not be the same as from $(n)$ to $(n-1)$. Lets accommodate the previous equation by allowing for the current step length $\Delta t_+$ and the previous step length $\Delta t_-$ to satisfy those two conditions respectively.

$$Y_{n+1} = [3I - 2A\Delta t_+]^{-1} \left[ \left( 3 + \frac{\Delta t_+}{\Delta t_-} \right) Y_n - \left( \frac{\Delta t_+}{\Delta t_-} \right) Y_{n-1} + 2B\Delta t_+ \right] \tag{H.4}$$

The first challenge is describing the system as a set of linear equations. There are roughly four state spaces in EDM2.1 that include and border the (1) canopy air space: (2) the vegetation elements enmeshed with the canopy air space, (3) a standing surface water pool (transient) and (4) the soil column. The moist soil and wet leaves are described by their moist internal energy, water mass and water phase. Prior to revision, the canopy air was described by specific humidity and air temperature. Since revision 77 of the ED2.1 code, the canopy air space was re-defined to prognose and conserve specific enthalpy, as well as specific humidity, see Appendix C.

The implicit solution requires linear equations. Soil heat and moisture transport is governed by the diffusion equation which is second order. Vapor flux from liquid or solids is governed by saturation vapor pressure which is usually described by a complex polynomial with temperature. Therefore we make the assumption that everything but the heat in the canopy air and leaves is solved with a normal Euler solution, and the

latter two exceptions use a coupled implicit solution.

The state vector for the implicit solver can only be described by the canopy temperature $T_c$, and the leaf temperatures $T_v$ inhabiting that air space:

$$Y = \begin{bmatrix} T_c \\ T_{v(1)} \\ T_{v(2)} \\ \cdots \\ T_{v(n)} \end{bmatrix} \tag{H.5}$$

*Note that the model accommodates wood temperature as an extension of the state vector, it is left out in this document for simplicity.

The forward solver will be performed first, because it relies on a derivative at the current model time step $(n)$. The Euler forward step is performed on the soil column, surface water, leaf water and canopy humidity states. This will provide a forward state and boundary conditions to enable the backward step on the canopy temperatures, which is performed second.

Here is the procedure itemized:

1. Forward Euler step via derivatives functional on current model state. Applies to soil moisture, soil surface water, canopy water and leaf water.

2. Identify boundary conditions to the implicit solver, including forward ground temperature, canopy moisture content, leaf thermal inertia, and temperature of the lower atmospheric boundary layer.

3. Approximate forward state stability factors and aerodynamic properties of the canopy based on current time-step thermal states and gradients.

4. Perform inverse step on canopy air temperature and leaf temperature.

5. Stability and error analysis resulting in continuation or re-step.

## H.2 Equation of State - Canopy Air

The total enthalpy in the canopy air $H_c$ can be described by its temperature $T_c$, specific humidity $q_c$, canopy depth $z_c$, total moist air density $\rho$, freezing temperature $T_3$, specific heat capacity of ice $c_i$ and the latent heat of sublimation $L_{S(T_3)}$. The ED2.1 model in its current release does not yet account for multi-phase (non-vapor) suspended water.

$$H_c = z_c\rho(1-q_c)c_{pd}T_c + z_c\rho q_c\left(c_iT_3 + L_{S(T_3)} + c_{pv}(T_c - T_3)\right) \tag{H.6}$$

We can re-write this equation in terms of air temperature simply by re-arranging terms.

$$T_c = \frac{H_c - z_c\rho q_c\left(c_iT_3 + L_{S(T_3)} - c_{pv}T_3\right)}{z_c\rho(1-q_c)c_{pd} + z_c\rho q_c c_{pv}} \tag{H.7}$$

For simplicity, we will create a new term, reference specific enthalpy $h_{ref} = c_iT_3 + L_{S(T_3)} - c_{pv}T_3$.

With general representation of air temperature in terms of enthalpy, lets calculate the derivative with respect to time. We assume that the volume, specific heat capacity and density of the air-space remains relatively constant over the integration window. We continue the assume that specific heat capacity of ice, liquid water, vapor and dry air at constant pressure are all invariable with temperature as well.

$$\frac{\partial T_c}{\partial t} = \frac{\partial}{\partial t}\left[\frac{H_c - z_c\rho q_c h_{ref}}{z_c\rho(1-q_c)c_{pd} + z_c\rho q_c c_{pv}}\right] \tag{H.8}$$

$$\frac{\partial T_c}{\partial t} = \frac{\partial}{\partial t}\left[\frac{H_c}{z_c\rho(1-q_c)c_{pd} + z_c\rho q_c c_{pv}} - \frac{z_c\rho q_c h_{ref}}{z_c\rho(1-q_c)c_{pd} + z_c\rho q_c c_{pv}}\right] \tag{H.9}$$

Derive via quotient rule:

$$\frac{\partial T_c}{\partial t} = \frac{\frac{\partial H_c}{\partial t}\left(z_c\rho(1-q_c)c_{pd}+z_c\rho q_c c_{pv}\right) - H_c\frac{\partial}{\partial t}\left(z_c\rho(1-q_c)c_{pd}+z_c\rho q_c c_{pv}\right)}{\left(z_c\rho(1-q_c)c_{pd}+z_c\rho q_c c_{pv}\right)^2} - \ldots$$
$$\frac{\frac{\partial}{\partial t}\left(z_c\rho q_c h_{ref}\right)\left(z_c\rho(1-q_c)c_{pd}+z_c\rho q_c c_{pv}\right) - \frac{\partial}{\partial t}\left(z_c\rho(1-q_c)c_{pd}+z_c\rho q_c c_{pv}\right)\left(z_c\rho q_c h_{ref}\right)}{\left(z_c\rho(1-q_c)c_{pd}+z_c\rho q_c c_{pv}\right)^2} \tag{H.10}$$

Enthalpy is a conservative variable, so the change in storage must balance the flux of enthalpy through the boundaries of the control volume and any source or sink terms inside the control volume. Assuming that radiation has minimal heating on the air directly compared to the sensible and latent sources on its boundaries, the storage of enthalpy is dependant on the fluxes of enthalpy from the ground to canopy $\dot{H}_{gc}$, the atmosphere to canopy $\dot{H}_{ac}$, vegetation to canopy $\dot{H}_{vc}$ and transpiration $\dot{H}_{TR}$. These fluxes were defined earlier in the chapter.

$$\frac{\partial H_c}{\partial t} = \dot{H}_{gc} + \dot{H}_{ac} + \int \dot{H}_{vc} + \int \dot{H}_{TR} \tag{H.11}$$

With the enthalpy fluxes defined, the temperature derivative is expanded into a linear equation dependant on boundary conditions, canopy air temperature and leaf temperature. To simplify these equations, we introduce a constant, $X_c = z_c\rho(1-q_c)c_{pd} + z_c\rho q_c c_{pv}$.

$$\begin{aligned}\frac{\partial T_c}{\partial t} = & \frac{g_{gc}\rho c_{pd}(T_g - T_c) + \dot{m}_{gc}\left(h_{ref} + c_{pv}T_g\right)}{X_c} \\ & + \frac{g_{ac}\rho c_{pd}(T_a - T_c) + \dot{m}_{ac}\left(h_{ref} + c_{pv}\frac{1}{2}(T_a + T_c)\right)}{X_c} \\ & + \frac{\sum_{i=1}^{N}\left[g_{vc(i)}\sigma_{(i)}\rho c_{pd}(T_{v(i)} - T_c) + \dot{m}_{vc(i)}\left(h_{ref} + c_{pv}T_{v(i)}\right)\right]}{X_c} \\ & + \frac{\sum_{i=1}^{N}\left[\dot{m}_{TR(i),soil(k)}\left(h_{ref} + c_{pv}T_{v(i)}\right)\right]}{X_c} \\ & - \frac{\left(z_c\rho(1-q_c)c_{pd}T_c + z_c\rho q_c\left(h_{ref} + c_{pv}T_c\right)\right)\frac{\partial}{\partial t}\left[z_c\rho(1-q_c)c_{pd} + z_c\rho q_c c_{pv}\right]}{X_c^2} \\ & - \frac{\frac{\partial}{\partial t}\left[z_c\rho q_c h_{ref}\right]}{X_c} \\ & + \frac{\frac{\partial}{\partial t}\left[z_c\rho(1-q_c)c_{pd} + z_c\rho q_c c_{pv}\right]\left(z_c\rho q_c h_{ref}\right)}{X_c^2} \end{aligned} \quad \text{(H.12)}$$

Making algebraic substitutions, the final form follows the same construct as $\frac{\partial Y}{\partial t} = A \cdot Y + B$:

$$\begin{aligned}\frac{\partial T_c}{\partial t} = & \frac{1}{X_c}\left[g_{gc}\rho c_{pd}T_g + \dot{m}_{gc}\left(h_{ref} + c_{pv}T_g\right) + g_{ac}\rho c_{pd}T_a + \dot{m}_{ac}h_{ref} + \dot{m}_{ac}c_{pv}\frac{1}{2}T_a\right] \\ & + \frac{1}{X_c}\left[\sum \dot{m}_{vc(i)}h_{ref} + \sum \dot{m}_{TR(i)}h_{ref} - z_c\rho h_{ref}\frac{\partial q_c}{\partial t}\right] \\ & + \frac{T_c}{X_c}\left[-g_{gc}\rho c_{pd} - g_{ac}\rho c_{pd} + \frac{1}{2}\dot{m}_{ac}c_{pv} - \sum g_{vc(i)}\sigma_{(i)}\rho c_{pd}\right] \\ & - \frac{T_c}{X_c^2}\frac{\partial q_c}{\partial t}\left[z_c\rho(1-q_c)c_{pd} + z_c\rho q_c c_{pv}\right]\left[z_c\rho c_{pv} - z_c\rho c_{pd}\right] \\ & + \sum \frac{T_{v(i)}}{X_c}\left[g_{vc(i)}\sigma_{(i)}\rho c_{pd} + \dot{m}_{vc(i)}c_{pv} + \dot{m}_{TR(i)}c_{pv}\right] \end{aligned} \quad \text{(H.13)}$$

## H.3 Equation of State - Leafy Vegetation

A similar argument is used when constructing the linear equations for change in vegetation temperature. The internal energy $H_v$ of a moist leaf with water mass $m_v$, tissue total heat capacity $C_v$, and liquid fraction $f$.

$$U_v = f\left[m_v c_i T_3 + m_v L_f + (T_v - T_3)(m_v c_l)\right] + \\ (1-f)\left[m_v c_i T_v\right] + \\ T_v C_v \tag{H.14}$$

The change in leaf internal energy is simply the balance of solar $\dot{R}_s$ and thermal $\dot{R}_l$ net radiation, the heat deposited by interception $\dot{H}_{int}$, heat lost by shedding $\dot{H}_{shed}$, the heat gained form drawing up root extracted liquid water $\dot{H}_{s->l,TR}$ and the vapor phase enthalpy fluxes $\dot{H}_{vc}$ and $\dot{H}_{l->a,TR}$.

$$\frac{\partial U_v}{\partial t} = \dot{R}_s + \dot{R}_l - \dot{H}_{vc} - \dot{H}_{l->a,TR} + \dot{H}_{s->l,TR} + \dot{H}_{int} - \dot{H}_{shed} \tag{H.15}$$

Rearrange so that leaf temperature is the independent variable, then take the partial derivative. Note that heat flux of root uptake is independent of leaf temperature.

$$\begin{aligned} \frac{\partial T_v}{\partial t}\left(f c_l m_v + (1-f) c_i m_v + C_v\right) = \\ \dot{R}_S + \dot{R}_L - \sigma_h \mathrm{LAI} g_h c_{pd}\left(T_v - T_c\right) \\ -\left(\dot{m}_{vc} + \dot{m}_{TR}\right)\left(c_i T_3 + L_{S(T_3)} - c_{pv} T_3 + c_{pv} T_v\right)\Big) \\ -\dot{H}_{SH} + \dot{H}_{s->l,TR} + \dot{H}_{INT} \\ -\left(f c_i T_3 + f L_{F(T_3)} - f T_3 c_l + f T_v c_l + T_v c_i - f T_v c_i\right)\frac{\partial m_v}{\partial t} \end{aligned} \tag{H.16}$$

Make a substitution for the re-occurring denominator, $X_v = f c_l m_v + (1-f) c_i m_v + C_v$.

$$\frac{\partial T_v}{\partial t} = \frac{1}{X_v}\left[\dot{R}_S + \dot{R}_L - h_{ref}\dot{m}_{vc} - h_{ref}\dot{m}_{TR} - \dot{H}_{SH}\right] + \frac{1}{X_v}\left[\dot{H}_{s->l,TR} + \dot{H}_{INT} + \left(fc_l T_3 - fc_i T_3 - fL_F\right)\frac{\partial m_v}{\partial t}\right] + \frac{T_c}{X_v}\left[\sigma_h \mathrm{LAI} g_h c_{pd}\right] + \frac{T_v}{X_v}\left[\left(fc_i - fc_l - c_i\right)\frac{\partial m_v}{\partial t} - \sigma_h \mathrm{LAI} g_h c_{pd} - \left(\dot{m}_{vc} + \dot{m}_{TR}\right) c_{pv}\right] \quad \text{(H.17)}$$

## H.4 The Directionality Problem

Leaf internal energy is defined as a function of temperature, water mass and liquid fraction. Water mass is prognosed by the forward euler step. And leaf temperature is progrnosed by the implicit step, but in order to do so requires and estimate of the liquid fraction, which is co-dependent with temperature. The assumption is made when manipulating the ordinary differential equation for change in enthalpy into change in temperature, that liquid fraction is constant. The hybrid solver calculates the forward leaf temperature (via implicit stepping) using the liquid-fraction diagnosed by the forward Euler temperature estimate. After the implicit step, the forward liquid fraction is diagnosed again based on the improved prediction of leaf temperature based on the implict solution.

We know that in truth, as the leaf temperature approaches the freezing point via warming, some extra energy is required for the melting process. Alternately, approaching via cooling, energy is released through the freezing process. Ideally, at the instant the leaves approach the freezing point, the derivative for leaf internal energy is dependant only on phase change and not temperature change.

The effect of using this method is that while the temperature of the leaves shows a continuous and smooth transition across steps, the leaf internal energy will jump slightly as temperatures cross the freezing point. Future implementations could allow for the inclusion of the forward state phase change derivative as a component in the leaf energy derivative. The method may harbour complications though, the forward time es-

timate of the phase change derivative would necessarily have to be approximated by the current phase change derivative. Likewise, phase change has hard boundaries at fully liquid and fully solid states, which is inconsistent with the continuous functions describing change in leaf energy. The other alternative is to implicitly solve for enthalpy directly. This is also complicated because the sensible heat flux component of the enthalpy change is based on temperature. Sensible heat flux could be represented in terms of enthalpy, and this sytem of equations may be linear.

## H.5 Sparse Gaussian Elimination

Recall that the solution requires matrix inversion. To simplify the explanation of this process, the major terms are grouped such that:

$$\hat{Y} = \left(3 + \frac{\Delta t_+}{\Delta t_-}\right) Y_n - \left(\frac{\Delta t_+}{\Delta t_-}\right) Y_{n-1} + 2B\Delta t_+ \tag{H.18}$$

and

$$\hat{A} = 3I - 2A\Delta t_+ \tag{H.19}$$

$$Y_{n+1} = \hat{A}^{-1}\hat{Y} \tag{H.20}$$

The matrix destined for inversion is strangely sparse. The top row of the matrix is non-zero. Every other row of the matrix is populated only by entries in the left column, and the diagonal. This is advantageous because it can be solved via simple Gaussian elimination using only two unested loops of matrix edge length. This is fast, and ultimately, the matrix inversion and therefore the implicit step takes an insignificant amount of computational time compared to the forward step. The first loop calculates the forward canopy temperature.

$$Y_{n+1,(1)} = \frac{\hat{Y}_{n,(1)} - \sum_{i=2}^{N} \hat{A}_{(1,i)}\hat{Y}_{n,(i)}/\hat{A}_{(i,i)}}{\hat{A}_{1,1} - \sum_{i=2}^{N} \hat{A}_{(1,i)}\hat{A}_{(i,1)}/\hat{A}_{(i,i)}} \tag{H.21}$$

The second loop calculates the leaf temperatures, which is a trivial problem now because they are two body solutions.

$$Y_{n+1,(i)} = \frac{\hat{Y}_{n,(i)} - \hat{A}_{(i,1)} Y_{n+1,(1)}}{\hat{A}_{(i,i)}} \tag{H.22}$$

## H.6 Validation - Energy Closure

As a first order test of the hybrid solution, the energy and mass conservation variables were compared. If energy is conserved, the integrated enthalpy flux into the land-surface model through the atmosphere should equal the total change in the system's internal energy. Similiarly, this applies to mass. The results of this check are shown in Figures H-1 and H-2.

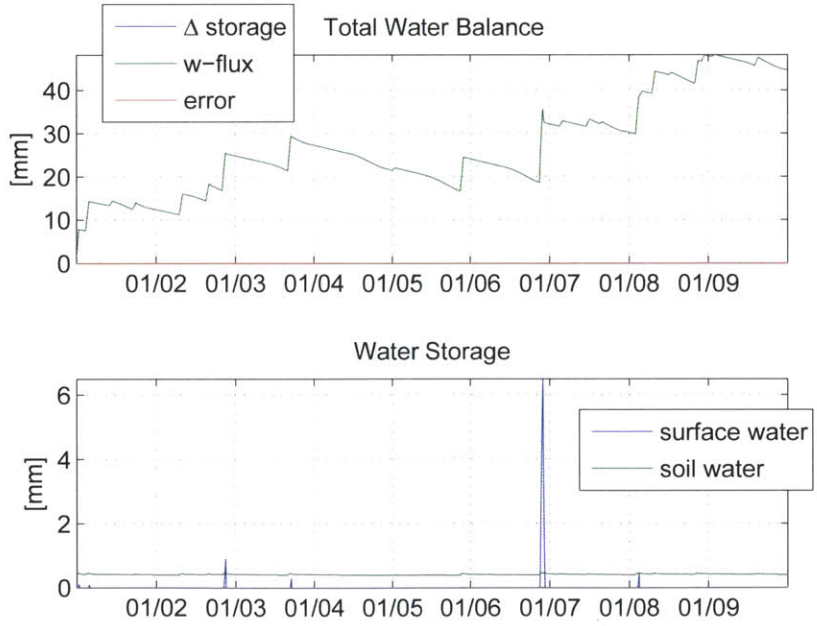


Figure H-1: Water balance check on the hybrid solver for a 28 year old forest site in and around Manaus. Climate forcing is arbitrary DS314 data.

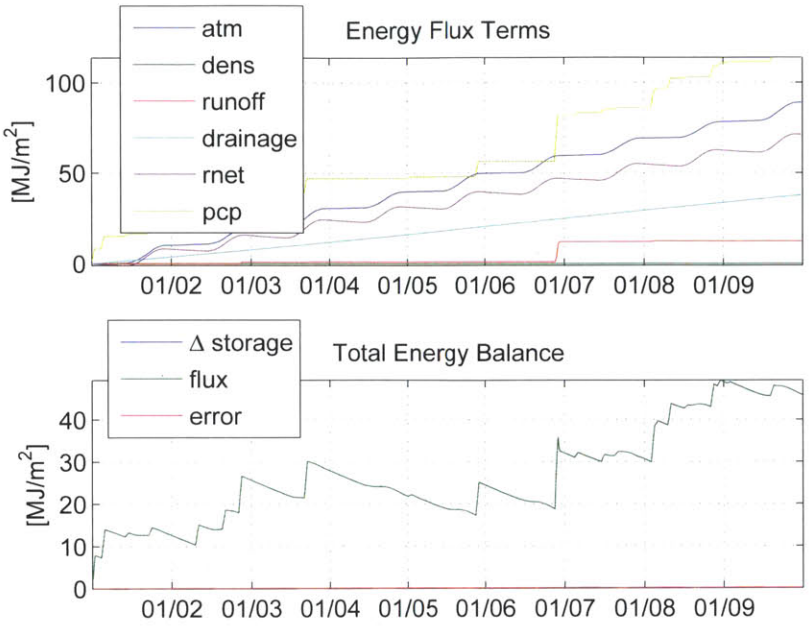


Figure H-2: Energy balance check on the hybrid solver for a 28 year old forest site in and around Manaus. Climate forcing uses arbitrary DS314 data.

## H.7 Validation - Comparison with RK4 Results

The high frequency flux and state biophysics variables estimated by hybrid and the Runge-Kutta integration methods are compared. The Runge-Kutta, being a multi-step solver provides an error acceptance measure. Therefore, RK4 biophysics estimates (when forced to an error tolerance of $0.1\%$) can provide a comparison base-line for the results of the hybrid solver. Figures H-3 through H-6 encapsulate the differences in the two methods for leaf temperature, air temperature, specific humidity and carbon dioxide concentrations. The results differ modestly at their peaks. The hybrid solution typically underestimates the dynamic range. This type of phenomenon is anticipated because the forward solution is based off of the forward derivative. The concept can be illustrated by imagining the numerical solution to a sine wave. Using forward derivatives to project steps from a current position will always have a dampening effect. Ultimately the validation indicated that the hybrid solver provides a stable and comparable alternative to the Runge Kutta integration method. The hybrid solver, performs

significantly faster than the RK4. The exact performance increase generally depends on how long the LSM step size is, and if the canopy conditions are such that the RK4 integrator continually shortenes its step. Comparisons have shown that at a minimum the hybrid is at least twice as fast as the RK4 scheme, and can show speed increases up to four or five times as fast.

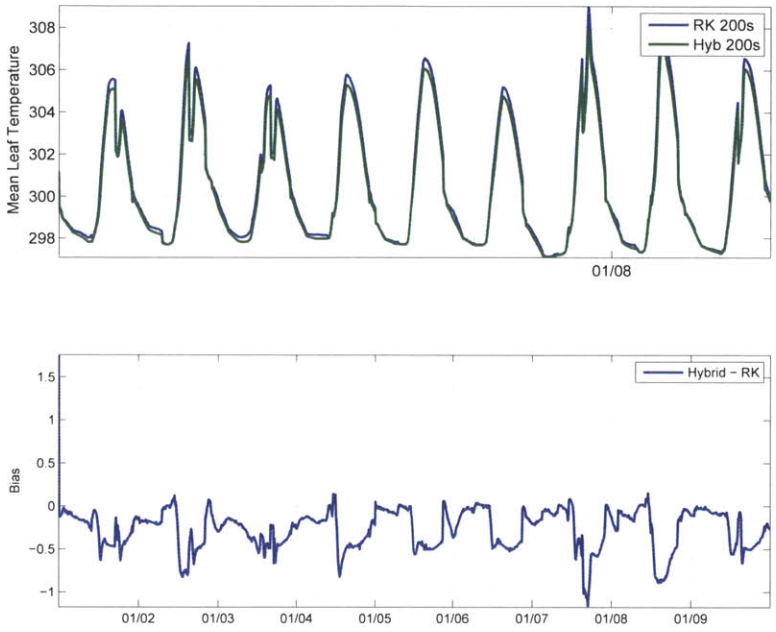


Figure H-3: Comparison of patch average leaf temperature time series for Hybrid and RK4 solvers, in a 28 year old forest site in and around Manaus.

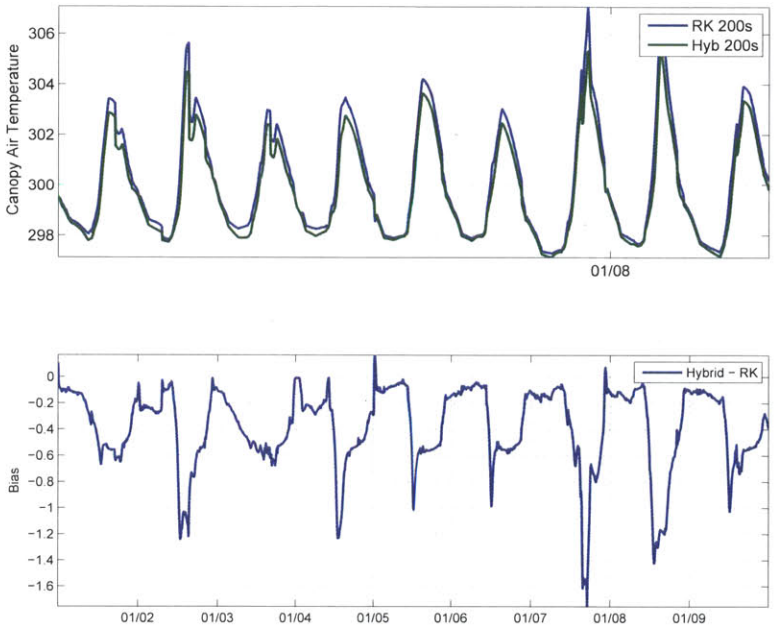


Figure H-4: Comparison of canopy air temperature time series for Hybrid and RK4 solvers, in a 28 year old forest site in and around Manaus.

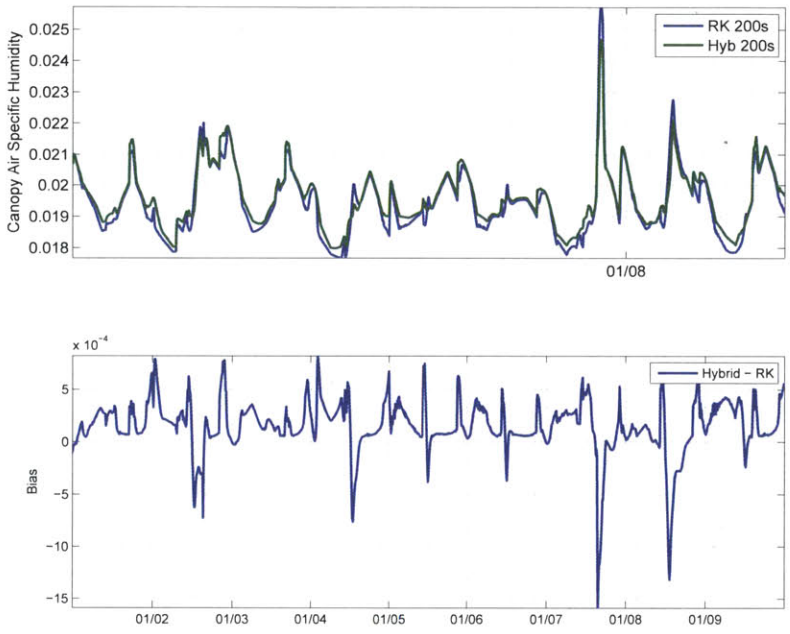


Figure H-5: Comparison of canopy specific humidity time series for Hybrid and RK4 solvers, in a 28 year old forest site in and around Manaus.

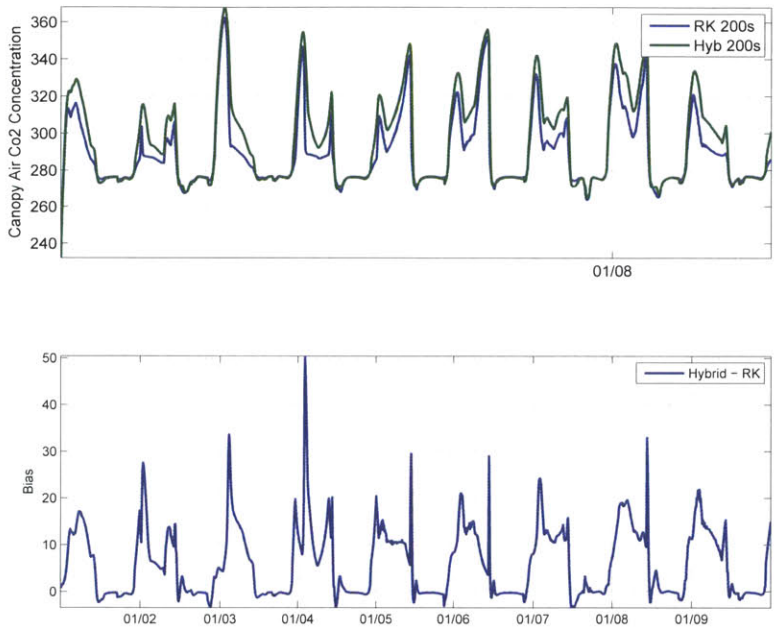


Figure H-6: Comparison of canopy carbon dioxide time series for Hybrid and RK4 solvers, in a 28 year old forest site in and around Manaus.

# Bibliography

ANDERSON, E. A Point Energy and Mass Balance Model of a Snow Cover. *Journal of Geophysical Research*, 114(D24) [1976].

ANTHES, R. A. Enhancement of convective precipitation by mesoscale variations in vegetative covering in semiarid regions. *J. of Climate and Applied Meteorology*, 23(4):pages 541–554 [1984].

ARAKAWA, A. and W. SCHUBERT. Interaction of a cumulus cloud ensemble with the large scale environment. Part I. *Journal of Atmospheric Science*, 31:pages 674–701 [1974].

ATKINSON, B. W. *Meso-Scale Atmospheric Circulations*. Academic Press [1981].

AVISSAR, R. and Y. LIU. Three-dimensional numerical study of shallow convective clouds and precipitation induced by land surface forcing. *Journal of Geophysical Research-Atmospheres*, 101(D3):pages 7499–7518 [1996].

AVISSAR, R. and D. WERTH. Global hydroclimatological teleconnections resulting from tropical deforestation. *Journal of Hydrometeorology*, 6:pages 134–146 [2004].

BALDI, M., G. A. DALU and R. A. PIELKE. Vertical velocities and available potential energy generated by landscape variability - theory. *J. of Applied Meteorology and Climatology*, 47(2):pages 397–410 [2008].

BEINROTH, F. Relationships between US soil taxonomy, the Brazilian system and FAO/UNESCO soil units. In BORNEMISZA, E. and A. ALVARADO, eds., *Soil Management*

*in Tropical America: Proceedings of a Seminar held at CIAT, Cali, Columbia, February 10-14, 1974*, pages 97–108. North Carolina State University [1975].

BETTS, A. and M. MILLER. A new convective adjustment scheme. Part I: Observational and theoretical basis. *Quarterly Journal of the Royal Meteorological Society*, 112:pages 677–692 [1986].

BONAN, G. A Land Surface Model (LSM version 1.0) for Ecological, Hydrological and Atmospheric Studies: Technical Description and User's Guide. *NCAR Technical Note. National Center for Atmospheric Research, Boulder Colorado*, NCAR/TN-417STR [1996].

BOTTA, A. and J. FOLEY. Effects of Climate Variability and Disturbances on the Amazonian Terestrial Ecosystems Dynamics. *Global Biogeochemical Cycles*, 16(4) [2002].

BRUTSAERT, W. *Evaporation into the atmosphere, Environmental Fluid Mechanics Series*. D. Reidel Publishing Company, Dordrecht Holland [1982].

CARDILLE, J. and J. FOLEY. Agricultural Land-use Change in Brazilian Amazonia Between 1980 and 1995: Evidence from Integrated Satellite and Census Data. *Remote Sensing of Environment*, 87:pages 551–562 [2003].

CHAGNON, F. and R. BRAS. Contemporary Climate Change in the Amazon. *Geophysical Research Letters*, 32(L13703) [2005].

CHAGNON, F., R. BRAS and J. WANG. Climatic Shift in Patterns of Shallow Clouds Over the Amazon. *Geophysical Research Letters*, 31(L24212) [2004].

CHAMBERS, J., T. ELDIK, J. SOUTHON and N. HIGUCHI. Tree age structure in tropical forests of Central Amazonia. In BIERREGAARD, R., C. GASCON, T. LOVEJOY and R. MESQUITA, eds., *Lesons from Amazonia*, pages 68–78. Yale University Press [2001].

CHARNEY, J. Dynamics of Desert and Draught in the Sahel. *Q. J. Royal Meteorological Soc.*, 101:pages 193–202 [1975].

CHAUVEL, A., Y. LUCAS and R. BOULET. On the genesis of the soil mantle of the region of Manaus, Central Amazonia, Brazil. *Experimentia*, 43:pages 234–240 [1987].

CHEN, C. and W. COTTON. A One-Dimensional Simulations of the Stratocumulus-Capped Mixed Layer. *Boundary Layer Meteorology*, 25(3):pages 289–321 [1983].

COCHRANE, T. Personal Web-page on historical climate data of South America [2012].

COLLATZ, G., J. BALL, C. GRIVET and J. BERRY. Physiological and Environmental Regulation of Stomatal Conductance, Photosynthesis and Transpiration: A Model That Includes a Laminar Boundary Layer. *Agricultural and Forest Meteorology*, 54:pages 107–136 [1991].

COX, P., R. BETTS, C. JONES, S. SPALL and I. TOTTERDELL. Acceleration of Global Warming Due to Carbon-Cycle Feedbacks in a Coupled Climate Model. *Nature*, 408(9) [2000].

CUTRIM, E. M., D. W. MARTIN and R. M. RABIN. Enhancement of cumulus clouds over deforested lands in Amazonia. *Bulletin of the American Meteorological Society*, 76(10):pages 1801–1805 [1995].

D'ALMEIDA, C. and CO AUTHORS. The effects of deforestation on the hydrological cycle in Amazonia: a review on scale and resolution. *International Journal of Climatology*, 27(5):pages 633–647 [2007].

DALU, G. A. and R. A. PIELKE. Vertical heat fluxes generated by mesoscale atmospheric flow induced by thermal inhomogeneities in the planetary boundary layer. *Journal of Atmospheric Science*, 50(6):page 919926 [1993].

DALU, G. A., R. A. PIELKE, M. BALDI and X. ZENG. Heat and momentum fluxes induced by thermal inhomogeneities. *J. of Atm. Sci*, 53(22):pages 3286–3302 [1996].

DICKINSON, R. and A. HENDERSON-SELLERS. Modeling Tropical Deforestation: A Study of GCM Land-Surface Parameterization. *Q. J. Royal Meteorological Soc.*, 114 [1998].

DIETZE, M. and J. CLARK. Changing the gap dynamics paradigm: vegetative regeneration control on biodiversity response to disturbance. *Ecological Monographs*, 78:pages 331–347 [2008].

DIXON, R., S. BROWN, R. HOUGHTON, A. SOLOMON, M. TREXLER and J. WISNIEWSKI. Carbon pools and Flux of Global Forest Ecosystems. *Science*, 263:pages 185–190 [1994].

ELTAHIR, E. Role of Vegetation in Sustaining Large-Scale Atmospheric Circulations in the Tropics. *J.G.R. Atmospheres*, 10(D2) [1996].

ELTAHIR, E. and R. BRAS. On the Response of the Tropical Atmosphere to Large-Scale Deforestation. *Q.J.R. Meteorol. Soc.*, 119:pages 779–793 [1993].

EMANUEL, K. *Atmospheric Convection*. Oxford University Press, New York [1994].

FARQUHAR, G., S. VON CAEMMERE and J. BERRY. A biochemical model of phosynthetic CO2 assimilaiton in leaves of C3 plants. *Planta*, 149:pages 78–90 [1980].

FIGUEROA, S., P. SATYAMURTY and P. S. DIAS. Simulations of the summer circulation over the south american region with an eta coordinate model. *Journal of the Atmospheric Sciences*, 52:pages 1573–1584 [1995].

FRITSCH, J. and C. CHAPPEL. Numerical prediction of convectively driven mesoscale pressure systems. Part I: Convective parameterization. *Journal of Atmospheric Science*, 37:pages 1722–1733 [1980].

FRITSCH, J. and C. CHAPPELL. Numerical Prediction of Convectively Driven Mesoscale Pressure Systems 1. Convective Parameterization. *Journal of the Atmospheric Sciences*, 37(8):pages 1722–1733 [1980].

FU, Q., K. LIOU, M. CRIBB, T. CHARLOCK and A. GROSMAN. Multiple Scattering Parameterization in Thermal Infrared Radiative Transfer. *J. Atm. Sci.*, 54:pages 2799–2812 [1997].

GAN, M., V. KOUSKY and C. ROPELEWSKI. The South American Monsoon Circulation and Its Relationship to Rainfall over West-Central Brazil. *Journal of Climate*, 17:pages 47–66 [2004].

GARRATT, J. *The Atmospheric Boundary Layer.* Cambridge University Press, Cambridge UK [1992].

GEIST, H. and E. LAMBIN. Proximate Causes of Underlying Driving Forces of Tropical Deforestation. *Bioscience*, 52(2) [2002].

DE GONCALVES, L., N. RESTREPO-COUPE, H. DA ROCHA, S. SALESKA and R. STOCKLI. LBA-ECO CD-32 LBA Model Intercomparison Project (LBA-MIP) Forcing Data. Data set [NA].

GRELL, G., J. DUDHIA and D. STAUFFER. A Description of the Fifth-Generation Penn State/NCAR Mesoscale Model (MM5). *NCAR/Technical Note*, 398+STR [1995].

GU, L., T. MEYERS, S. PALLARDY, P. HANSON, B. YANG, M. HEUER, K. HOSMAN, Q. LIU, J. RIGGS, D. SLUSS and S. WULLSCHLEGER. Influences of biomass heat and biochemical energy storages on the land surface fluxes and radiative temperature. *Journal of Geophysical Research*, 112(D02107):pages 1–11 [2007].

HARRINGTON, J. and P. OLSSON. A Method for the Parameterization of Cloud Optical Properties in Bulk and Bin Microphysical Models. Implications for Arctic Cloud Boundary Layers. *Atmospheric Research*, 57:pages 51–80 [2001].

HASLER, N. and R. AVISSAR. What controls evapotranspiration in the amazon basin? *Journal of Hydrometeorology*, 8(3):pages 380–395 [2007].

HENDERSON-SELLERS, A., R. DICKINSON, T. DURBRIDGE, P. KENNEDY, K. MCGUFIE and A. PITMAN. Tropical Deforestation: Modeling Local to Regional Scale Climate Change. *Journal Geophysical Research*, 98:pages 7289–7315 [1993].

HOUZE, R., C. CHENG, C. LEARY and J. GAMACHE. Diagosis of cloud mass and heat fluxes from radar and synoptic data. *Journal of Atmospheric Science*, 37:pages 754–773 [1980].

HURTT, G., S. FROLKING, M. FEARON, B. M. III, E. SHEVIALOKOVA, S. MALYSHEW, S. PACALA and R. HOUGHTON. The underpinnings of land-use history: three centuries

of global gridded land-use transitions, wood harvest activity and resulting secondary lands. *Global Change Biology*, 12:pages 1–22 [2006].

HUTYRA, L., J. MUNGER, S. SALESKA, E. GOTTLIEV, B. DAUBE, A. DUNN, D. AMARAL, P. DE CAMARGO and S. WOFSY. Seasonal Controls on the Exchange of Carbon and Water in an Amazonian Rainforest. *Journal of Geophysical Research Biosciences*, 112(G03008):pages 1–16 [2007].

JONES, H. *Plant Microclimate: A Quantatative Approach to Environmental Plant Phsyciology, 2nd ed.*. Cambridge Univ. Press, New York [1992].

KAIN, J. The Kain-Fritsch Convective Parameterization: An Update. *Journal of Applied Meteorology*, 43(1):pages 170–181 [2004].

KAIN, J. and J. FRITSCH. A One-Dimensional Entraining-Detraining Plume Model and Its Application in Convective Parameterization. *Journal of Atmospheric Science*, 47(23):pages 2784–2802 [1990].

KALNAY, E. and CO AUTHORS. The NCEP/NCAR 40-year reanalysis project. *Bull. Amer. Meteor. Soc.*, 77:pages 437–471 [1996].

KIM, Y., R. KNOX, M. LONGO, D. MEDVIGY, L. HUTYRA, E. PYLE, S. WOFSY, R. BRAS and P. MOORCROFT. Seasonal Carbon Dynamics and Water Fluxes in an Amazon Rainforest. *Global Change Biology*, 18(4):page 2012 [2012].

KIRCHBAUM, M. and G. FARQUHAR. Temperature dependenc of whole-leaf photosynthesis in Eucalyptus pauciflora. *J. Plant Physiology*, 11:pages 519–538 [1984].

KLEIDON, A. and M. HEIMANN. Assessing the Role of Deep Rooted Vegetation in the Climate System with Model Simulations: Mechanism, Comparison to Observations and Implications for Amazonian Deforestation. *Climate Dynamics*, 16:pages 183–199 [2000].

KOUSKY, V. Pentad Outgoing Longwave Radiation Climatology for the South American Sector. *Review of Brasilian Meteorology*, 3:pages 217–231 [1988].

KUMMEROW, C., W. BARNES, T. KOZU, J. SHIUE and J. SIMPSON. The Tropical Rainfall Measurement Mission (TRMM) Sensor Package. *Journal of Atmospheric and Oceanic Technology*, 15:pages 809–817 [1998].

KUO, H. Further studies of the influence of cumulus convection on large-scale flow. *Journal of Atmospheric Science*, 31:pages 1232–1240 [1974].

LAMMERING, B. and I.DWYER. Improvement of Water Balance in Land Surface Schemes by Random Cascade Disaggregation of Rainfall. *International Journal of Climatology*, 20:pages 681–695 [2000].

LAURANCE, W. The Hyper-Diverse Flora of the Central Amazon. In R.O. BIERREGAARD, T. L., C. GASCON and R. MESQUITA, eds., *Lessons from Amazonia*, pages 47–53. Yale University Press [2001].

LAURANCE, W., M. COCHRANE, S. BERGEN, P. FEARNSIDE, P. DELAMONICA, C. BARBER, S. D'ANGELO and T. FERNANDES. The future of the Brazilian Amazon. *Science*, 291(5503) [2001].

LAURANCE, W., L. FERREIRA, J. R. DE MERONA and S. LAURANCE. Rain Forest Fragmentation and the Dynamics of Amazonian Tree Communities. *Ecology*, 79(6) [1998].

LEAN, J. and D. WARRILOW. Simulation of the Regional Climatic Impact of Amazon Deforestation. *Nature*, 342:pages 411–413 [1989].

LEE, T. *The impact of vegetation on the atmospheric boundary layer and convective storms*. Ph.D. thesis, Dept. Of Atmospheric Science, Colorado State University, Fort Collins, CO [1992].

LEUNING, R., F. KELLIHER, D. D. PURY and E. SCHULZE. Leaf Nitrogen, Photosynthesis, Conductance and Transpiration: Scaling from Leaves to Canopies. *Plant, Cell and Environment*, 18:pages 1183–1200 [1995].

LEVINE, N. and CO AUTHORS. The Role of Short and Long-Term Climate Variability in Governing Amazonian Biomass Dynamics. *In Preparation* [2012].

LIMA, M. A. and J. W. WILSON. Convective storm initiation in a moist tropical environment. *Monthly Weather Review*, 136(6):pages 1847–1864 [2008].

MARENGO, J., V. KOUSKY, N. FILIZOLA and L. WAINER. Onset and End of the Rainy Season in the Brazilian Amazon Basin. *Journal of Climate*, 14:pages 1109–1123 [2001].

MASSMAN, W. An Analytical One-Dimensional Model of Momentum Transfer by Vegetation of Arbitrary Structure. *Boundary Layer Meteorology*, 83:pages 407–421 [1997].

MASSMAN, W. and J. WEIL. An Analytical One-Dimensional Second-Order Closure Model of Turbulence Statistics and the Lagrangian Time Scale Within and Above Plant Canopies of Arbitrary Structure. *Boundary Layer Meteorology*, 91:pages 81–107 [1999].

MCCUMBER, M. and R. PIELKE. Simulation of the effects of surface fluxs of heat and moisture in a mesoscale numerical model, Part I: Soil layer. *Journal of Geophysical Research*, 86(C10):pages 9929–9938 [1981].

MEDVIGY, D. *The State of the Regional Carbon Cycle: Results from a Constrained Coupled Ecosystem-Atmosphere Model.* Ph.D. thesis, Harvard University, Cambridge MA [2006].

MEDVIGY, D., R. WALKO, M. OTTE and R. AVISSAR. The Ocean-Land-Atmosphere-Model: Optimization and Evaluation of Simulated Radiative Fluxes and Precipitation. *Monthly Weather Review*, 138(5):pages 1923–1939 [2010].

MEDVIGY, D., S. WOFSY, J. MUNGER, D. HOLLINGER and P. MOORCROFT. Mechanistic Scaling of Ecosystem Function and Dynamics in Space and Time: Ecosystem Demography Model Version 2. *Journal of Geophysical Research*, 114 [2009].

MITCHELL, T. and P. JONES. An improved method of constructing a database of monthly climate observations and associated high-resolution grids. *International Journal of Climatology*, 25:pages 693–712 [2005].

MOORCROFT, P., G. HURTT and S. PACALA. A Method for Scaling Vegetation Dynamics: The Ecosystem Demography Model. *Ecological Monographs*, 71(4):pages 557–586 [2001].

MURPHY, D. and T. KOOP. Review of the vapour pressures of ice and supercooled water for atmospheric applications. *Q. J. Royal Meteor. Soc.*, 31:pages 1539–1565 [2005].

MURPHY, P. and A. LUGO. Ecology of a tropical dry forest. *Annual Review of Ecology and Systematics*, 17:pages 67–88 [1986].

NEGRI, A., T. BELL and L. XU. Sampling of the diurnal cycle of precipitation using TRMM. *Journal of Atmospheric and Oceanic Technology*, 19:pages 1333–1344 [2002].

NEPSTAD, D. and CO AUTHORS. The effects of partial throughfall exclusion on canopy processes, aboveground production, and biogeochemistry of an Amazon Forest. *Journal of Geophysical Research*, 107(D20):pages LBA 53 1–18 [2002].

NEPSTAD, D., C. DE CARVALHO, E. DAVIDSON, P. JIPP, P. LEFEBVRE, H. NEGREIROS, E. DAL SILVA, T. STONE, S. TRUBORE and S. VIEIRA. The Role of Deep Roots in the Hydrological and Carbon Cycles of Amazonian Forests and Pastures. *Nature*, 372:pages 666–669 [1994].

NEPSTAD, D., G. CARVALHO, A. BARROS, A. ALENCAR, J. CAPOBIANCO, J. B. AMD P. MOUTINHO, P. LEFEBVRE, U. L. SILVA and E. PRINS. Road paving, Fire Regime Feedbacks and the Future of Amazon Forests. *Forest Ecology and Management*, 154:pages 395–407 [2001].

NEPSTAD, D. and M. COE. Conference: Workshop on Amazonian Savannization. Manaus, Brazil [2008].

NOBRE, C., P. SELLERS and J. SHUKLA. Amazonian Deforestation and Regional Climate Change. *Journal of Climate*, 4 [1991].

OLIVEIRA, A. and S. MORI. A Central Amazonian terra firme forest. *Biodiversity and Conservation*, 8:pages 1219–1244 [1999].

OLSON, J. *Global ecosystem framework-definitions*. USGS EROS Data Center Internal Report, Sioux Falls, SD [1994].

PEILKE, R. Land Use and Climate Change. *Science*, 310:pages 1625–1626 [2005].

DE PESQUISAS ESPACIAIS INPE, I. N. *Monitoring of the Amazon forest by satellite 2001-2002*. Technical Paper, Sao Jose Dos Campos, Brazil [2003].

PHILLIPS, O. L. and CO AUTHORS. Drought sensitivity of the Amazon rainforest. *Science*, 323(5919):pages 1344–1347 [2009].

PIELKE, R. Influence of the Spatial Distribution of Vegetation and Soils on the Prediction of Cumulus Convective Rainfall. *Reviews of Geophysics*, 39(2) [2001].

PIELKE, R., W. COTTON, R. WALKO, C. TREMBACK, W. LYONS, L. GRASSO, M. NICHOLLS, M. MORAN, D. WESLEY, T. LEE and J. COPELAND. A Comprehensive Meteorological Modeling System - RAMS. *Meteorological Atmospheric Physics*, 49(1-4):pages 69–91 [1992].

PIELKE, R. A. *Mesoscale Meteorological Modeling*. Academic Press [1984].

PINKER, R. and I. LASZLO. Modeling Surface Solar Irradiance for Satellite Applications on a Global Scale. *J. Appl. Meteor.*, 31(2):pages 194–211 [1992].

RABIN, R. M. and CO AUTHORS. Observed effects of landscape variability on convective clouds. *Bulletin of the American Meteorological Society*, 71(3):pages 272–280 [1990].

RAIA, A. and I. DE ALBUQUERQUE CAVALCANTI. The life cycle of the south american monsoon system. *Journal of Climate*, 21:pages 6227–6246 [2008].

RAUPACH, M. Canopy Transport Processes. In STEFFEN, W. and O. DENMEAD, eds., *Flow and Transport in the Natural Environment: Advances and Applications*. Springer-Verlag [1988].

RENNO, N. and A. INGERSOLL. Natural convection as a heat engine: a theory for CAPE. *J. of Atm. Sci.*, 53(4):pages 572–585 [1996].

ROGERS, R. and M. YAU. *A Shrt Course in Cloud Physics*. Pergamon Press, University of California, CA [1989].

ROSENFELD, D. TRMM Observed First Direct Evidence of Smoke from Forest Fires Inhibiting Rainfall. *Geophys. Res. Lett.*, 26:pages 3105–3108 [1998].

ROZANTE, J., D.S.MOREIRA, L. DE GONCALVES and D. VILA. Combining TRMM and surface observations of precipitation: Technique and validation over South America. *Weather and Forecasting*, 25:pages 885–894 [2010].

SALATI, E. and P. VOSE. Amazon Basin: A System in Equilibrium. *Science*, 225:pages 129–138 [1984].

SALIO, P., M. NICOLINI and E. ZIPSER. Mesoscale Convective Systems over Southeastern South America and Their Relationship with the South American Low-Level Jet. *Monthly Weather Review*, 135:pages 1290–1301 [2007].

SAMANTA, A., Y. KNYAZIKHIN, L. XU, R. DICKINSON, R. FU, M. COSTA, S. SAATCHI, R. NEMANI and R. MYNENI. Seasonal changes in leaf area of Amazon forests from leaf flushing and abscission. *Journal of Geophysical Research - Atmospheres*, 117(G1) [2011].

SATYAMURTY, P., C. NOBRE and P. S. DIAS. South America. In TBA, ed., *Meteorology of the Southern Hemisphere*, pages 119–139. American Meteorological Society [1998].

SAUER, T. and J. NORMAN. Simulated Canopy Microclimate Using Estimated Below Canopy Soil Surface Transfer Coefficients. *Agricultural and Forest Meteorology*, 75:pages 135–160 [1995].

SELLERS, P., J. BERRY, G. COLLATZ, C. FIELD and F. HALL. Canopy Reflectance, Photosynthesis, and Transpiration III. A Reanalysis Using Improved Leaf Models and a New Canopy Integration Scheme. *Remote Sensing of Environment*, 42:pages 187–216 [1992].

SHEFFIELD, J., G. GOTETI and E. WOOD. Development of a 50-Year High-Resolution Global Dataset of Meteorological Forcings for Land Surface Modeling. *Journal of Climate*, 19:pages 3088–3111 [2006].

SHUKLA, J., C. NOBRE and P. SELLERS. Amazon Deforestation and Climate Change. *Science*, 247:pages 1322–1325 [1990].

SILVA, R. R. D., D. WERTH and R. AVISSAR. Regional impacts of future land-cover changes on the Amazon basin wet-season climate. *Journal of Climate*, 21(6):pages 1153–1170 [2008].

SILVER, W., J. NEFF, M. MCGODDY, E. VELDKAMP, M. KELLER and R. COSME. Effects of soil texture on belowground carbon and nutrient storage in a lowland Amazonian forest ecosystem. *Ecosystems*, 3:pages 193–209 [2000].

SKOLE, D. and C. TUCKER. Tropical Deforestation and Habitat Fragmentation in the Amazon: Satellite Data from 1978 to 1988. *Science*, 260(5116):pages 1905–1910 [1993].

SOARES-FILHO, B., D. NEPSTAD, L. CURRAN, G. CERQUEIRA, R. GARCIA, C. RAMOS, E. VOLL, A. MCDONALD, P. LEFEBVRE and P. SCHLESINGER. Modelling Conservation in the Amazon Basin. *Nature*, 440(23):pages 520–523 [2006].

SOLOMON, S., D. QIN, M. MANNING, Z. CHEN, M. MARQUIS, K. AVERYT, M.TIGNOR and H. MILLER, eds. *IPCC, Climate Change 2007: The Physical Science Basis. Contribution of Working Group I to the Fourth Assessment Report of the Intergovernmental Panel on Climate Change*. Cambridge University Press, Cambridge, United Kingdom and New York, NY, USA [2007].

SOUZA, E. P., N. O. RENNO and M. A. F. SILVA-DIAS. Convective circulations induced by surface heterogeneities. *J. of Atm. Sci.*, 57(17):pages 2915–2922 [2000].

STULL, R. *An Introduction to Boundary Layer Meteorology*. Springer [1988].

THOM, A. Momentum Absorbtion by Vegetation. *Quarterly Journal Roy. Met. Society*, 97:pages 414–428 [1971].

TOLEDO, M., L. POORTER, I. PENA-CLAROS, M. ALARCON, A. BALCAZAR, J. CHUVINA, J. LEANO, C. LICONA, J. T. STEEGE and H. BONGERS. Patterns of determinants of floristic variation across lowland forests of Bolivia. *Biotropica*, 43 [2011a].

TOLEDO, M., L. POORTER, M. PENA-CLAROS, A. ALARCON, J. BALCAZAR, C. LEANO, J. LICONA and F. BONGERS. Climate and soil drive forest structure in Bolivian lowland forests. *Journal of Tropical Ecology*, 27:pages 333–345 [2011b].

TREMBACK, C. and R. KESSLER. A surface temperature and moisture parameterization for use in mesoscale models. *Seventh Converence on Numerical Weather Prediction,Montreal,PQ,Candad*, pages 355–358 [1985].

UPPALA, S. and CO AUTHORS. The ERA-40 re-analysis. *Quart. J. R. Meteorol. Soc.*, 131:pages 2961–3012 [2005].

VERA, C. and CO AUTHORS. The South American Low-Level Jet Experiment. *Bulletin of the American Meteorological Society*, 87(1) [2006].

WALKO, R., L. BAND, J. BARON, T. KITTEL, R. LAMMERS, T. LEE, D. OJIMA, R. PIELKE, C. TAYLOR, C. TAQUE, C. TREMBACK and P. VIDALE. Coupled Atmosphere-Biophysics-Hydrology Models for Environmental Modeling. *Journal of Applied Meteorology*, 39(6):pages 931–944 [2000].

WANG, G. and E. ELTAHIR. Ecosystem Dynamics and the Sahel Drought. *Geophysical Research Letters*, 27(6):pages 795–798 [2000a].

—. The Role of Ecosystem Dynamics in Enhancing the Low-Frequency Variability of the Sahel Rainfall. *Water Resources Research*, 36:pages 1013–1021 [2000b].

WANG, J. and CO AUTHORS. The impact of deforestation in the Amazon basin on cloud climatology. *Proceedings of the National Academy of Science*, 106(10):page 3670 3674 [2009].

WANG, J., R. BRAS and E. ELTAHIR. The Impact of Observed Deforestation on the Mesoscale Distribution of Rainfall and Clouds in Amazonia. *Journal of Hydrometeorology*, 1(3):pages 267–286 [2000].

WANG, J., R. L. BRAS and E. A. B. ELTAHIR. A stochastic linear theory of mesoscale circulation induced by the thermal heterogeneity of the land surface. *Journal of the Atmospheric Sciences*, 53(20):pages 3349–3363 [1996].

WANG, J. and D. WOLFF. Evaluation of TRMM ground-validation radar-rain errors using rain gauge measurements. *Journal of Applied Meteorology and Climatology*, 49:pages 310–324 [2010].

ZOU, J. and K. LAU. Does a Monsoon Climate Exist Over South America? *Journal of Climate*, 11:pages 1020–1040 [1998].